BULGARIAN CHEMICAL COMMUNICATIONS

2019 Volume 51 / Number 1

Journal of the Chemical Institutes
of the Bulgarian Academy of Sciences
and of the Union of Chemists in Bulgaria

Bulgarian Chemical Communications, Volume 51, Issue 1 (pp. 5-9) 2019

Iron, manganese, vanadium, copper and zinc of the Cretaceous-paleogene boundary fish clay at the Kirkevig site (Højerup, Stevns Klint, Denmark)

M. G. Đorđević, P. I. Premović*

Laboratory for Geochemistry, Cosmochemistry & Astrochemistry, University of Niš, P.O. Box 224, 18000 Niš, Serbia

Received, July 21, 2018; Revised, July 30, 2018

The marine shallow Cretaceous–Paleogene boundary (KPB) sections at Kirkevig consist of a very thin reddish smectite-rich carbonate-poor ejecta layer overlain by black marl. Similar sections with a thin reddish layer are found in other KPB sites at Stevns Klint. The metal oxide fractions of the ejecta layer have a relatively high Fe concentration (0.03 %) and trace concentrations of: Mn (30 ppm), Cu (45 ppm) and Zn (850 ppm). Most of these metals are located in this fraction: Fe (90 %), Mn (85 %), Cu (80 %) and Zn (90 %). Trace Mn, Cu and Zn were probably absorbed on the Fe oxides present. It is speculated that most of the Fe oxides were sourced by the chondritic component of the impact fallout. The smectite fraction includes lower Fe (10 %), Mn (15 %), Cu (10 %) and Zn (5 %) contents but a high V (90 %) content. This component is most likely of local (marine or terrestrial) provenance and was probably redeposited, after its formation, from the original site to its present location. The carbonate fraction of the ejecta layer shows minor concentrations of these metals.

Keywords: Cretaceous–Paleogene boundary, Ejecta layer, Trace metals, Smectite

INTRODUCTION

In their seminal paper, Alvarez *et al.* [1] reported anomalously high Ir in the Cretaceous-Paleogene boundary (KPB) clays from Italy (Gubbio), Denmark (Stevns Klint) and New Zealand (Woodside Creek). According to these authors, this enhanced Ir concentration was produced by a large asteroid impact in the late Cretaceous that was probably largely responsible for one of the greatest biological extinctions in Earth history. It has been suggested that the impactor was a C1 chondrite-type body [2] and the impact occurred at Chicxulub (Yucatan Penninsula, Mexico) [3].

The Fish Clay is a thin grey-to-black marl forming KPB at Stevns Klint (eastern Denmark), Fig.1a. Here it occurs in small marine basins between the Cretaceous white chalk and the overlying calcareous Tertiary formation. The most prominent sites of the Fish Clay at Stevns Klint are near village of Højerup. Alvarez *et al.* [1] studied this clay from the most famous site near the Højerup old Church.

The Kirkevig boundary section is similar to the neighboring Højerup Church section in lithology. The Kirkevig boundary section is comprised of a dark clay with a basal Fe-rich (ejecta) red layer (Fig. 1b).The lower "reddish" unit (red layer) of this clay would be informally called the "ejecta layer" and the upper overlying "darkish" unit (black marl) - the "boundary layer". The ejecta and boundary layers at Kirkevig are up to about 0.5 cm and up to 3 cm thick, respectively, (Fig. 1b). The contact between these two layers is generally sharp and records a significant change in depositional regime. Ejecta layer is underlain by a Maastrichtian bryozoan-rich chalk and the boundary layer is overlain by the lower Danian (Cerithium) limestone. In general, the Ir anomaly of the prominent marine and continental KPB clays is largely concentrated in the ejecta layers. Our preliminary results indicate that Ir is relatively abundant (ca. 15 ppm) in the ejecta layer of Kirkevig.

In this paper we focus our attention on Fe, Mn, V, Cu and Zn in the ejecta layer of the Kirkevig boundary section (hereinafter KEL) for which otherwise there are no previously published geochemical data. Essentially, this paper is complementary to our previous studies [5-7].

EXPERIMENTAL

Spectrochemical instrumentation

Inductively coupled plasma–optical emission spectroscopy (ICP–OES) analysis. The various fractions of KEL were analyzed for Fe, Mn, V, Cu and Zn by a Spectroflame ICP–OES instrument using Ar as the plasma gas.

* To whom all correspondence should be sent:
E-mail: pavle.premovic@yahoo.com

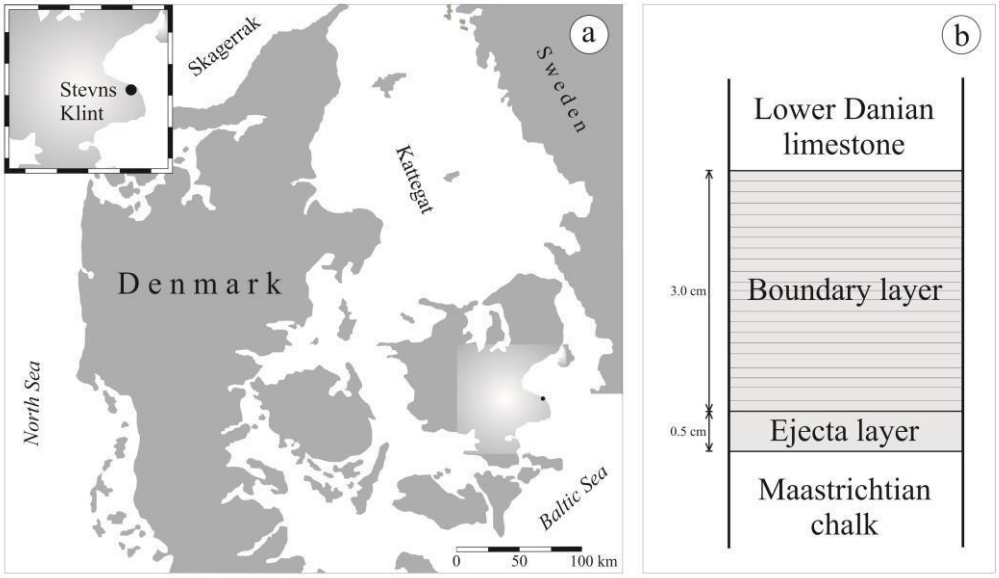

Figure 1. a) Geographic location map of the Fish Clay samples from Stevns Klint; b) a simplified lithological column of the KPB section at Kirkevig.

Relative error in the precision of the analyses ranged from 5 to 10 %. Total uncertainties (including accuracy errors) were up to 20 %.

X-Ray diffraction (XRD) analysis. XRD patterns were obtained with a Siemens D500 vertical goniometer using CoKα radiation (35 kV, 20 mA). Powder diffractograms were acquired in the 4-75 °C 2θ range, with 7–20 s counting per 0.02° 2θ step. The samples were prepared using the back-loading procedure according to Moore and Reynolds [6], which provides significant disorientation of the clay layers.

Fourier transform infrared (FTIR) spectrometry. FTIR spectra were recorded in the absorbance mode using a BOMEM Michelson Series MB FTIR spectrometer set to give undeformed spectra. The resolution was 4 cm^{-1} in the 400–4000 cm^{-1} analyzed range. The spectra were obtained at room temperature from KBr pressed pellets prepared by mixing 1.5 mg of a KEL fraction (see below) sample with 150 mg of KBr.

Scanning electron microscopy (SEM)-energy dispersive spectrometry (EDS). All SEM-EDS work was carried out using a scanning microscope Philips XL 30 ESEM/TMP, coupled to an energy-dispersive spectrometer (EDAX type Sapphire).The backscattered electron (BSE) mode was done before microprobing. Analytical conditions were as follows: accelerating voltage 15 or 20 kV, probe current 60 nA, working distance *ca*. 1 cm, counting time 100 s. Individual parameters: acceleration of electron beam and magnification are printed on the photos. Samples were coated with gold and stuck to a carbon tape.

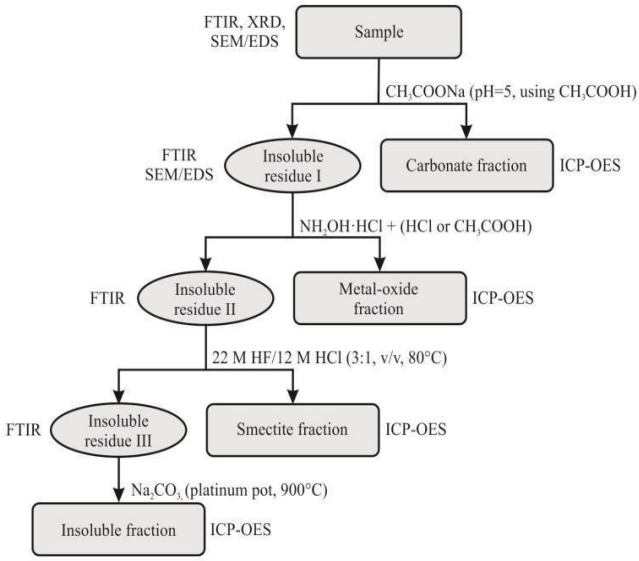

Figure 2. Flow chart of the selective extraction procedure.

Analysis and fractionation

The modified fractionation procedure (selective extraction) of KEL was similar to that used by Premović [8], Tessier *et al*. [9] and Zakiri [10]. The flow chart in Fig. 2 outlines the major steps in preparing its four fractions.

Thus, powdered sample (1 g) was treated (room temperature, 12 h) with Na acetate using acetic acid (1 M, pH 5.0) to remove most of the carbonates. The soluble material constitutes the carbonate fraction. Carbonate removal was checked by FTIR/SEM-EDS analyses.

The insoluble residue (II) was demineralized with boiling hydrofluoric/hydrochloric acid HF/HCl

(22 and 12M, respectively, 3:1 v/v, 80 °C, 12 h). This acid mixture removes SiO_2 and $A1_2O_3$.

The removal of SiO_2 and Al_2O_3 was checked by FTIR analysis. The soluble part constitutes the smectite fraction or phase.

The insoluble residue (III) was demineralized by annealing using sodium carbonate at high temperature (900 °C). The soluble part constitutes the insoluble fraction.

RESULTS AND DISCUSSION

Demineralization and ICP–OES analysis. The first demineralization step (CH_3COONa) removed only 10 wt. % of KEL. This mass loss was due to the total dissolution of carbonates. The second demineralization step (NH_2OH-HCl) removed 35 wt. % of the sample, mainly Fe oxides. SiO_2 and Al_2O_3, the dominant constituents of the sample seem to have been unaffected by the demineralization steps. Geochemical analysis also indicated that 50 wt. % of the sample is the smectite fraction which was removed by the HF/HCl step.

Iron. Simple chemical analyses showed that KEL is composed of carbonate (10 %), metal oxide (35 %), smectite (50 %) and insoluble (5 %) components. The distribution of Fe among these four fractions is also given in Table 1. This table shows that Fe was relatively abundant (0.03 %) and that about 90 wt. % of this metal was associated with the metal oxide phase. Indeed, the SEM-EDS analyses of KEL show also abundant presence of Fe oxides, probably hematite, Fig. 3.

The insoluble residue (I) was further demineralized by repeated treatment with hydroxylammonium chloride ($NH_2OH{\cdot}HCl$) in 0.25 M HCl and 25 % CH_3COOH. This treatment removed metal oxides, including amorphous and crystalline Fe-oxides. The soluble part constitutes the metal-oxide fraction.

Table 1. Geochemical distribution of Fe, Mn, V, Cu and Zn in the sample fractions

Metal		Total	Carbonate	Oxide	Smectite	Insoluble
		[%]	[ppm]	[%]	[%]	[ppm]
Fe	ppm	0.03	<1	0.03	0.003	<1
		100	<1	90	10	<1
		Total	Carbonate	Oxide	Smectite	Insoluble
	%	100	<1	90	10	<1
Mn	ppm	35	<1	30	5	<1
	%	100	<1	85	15	<1
V	ppm	110	<1	10	100	<1
	%	100	<1	10	90	<1
Cu	ppm	55	<1	45	5	5
	%	100	<1	80	10	10
Zn	ppm	940	40	850	45	5
	%	100	5	90	5	<1

Abundant Fe oxides in KEL indicate that its deposition probably occurred under well (aerated) oxygenated conditions.

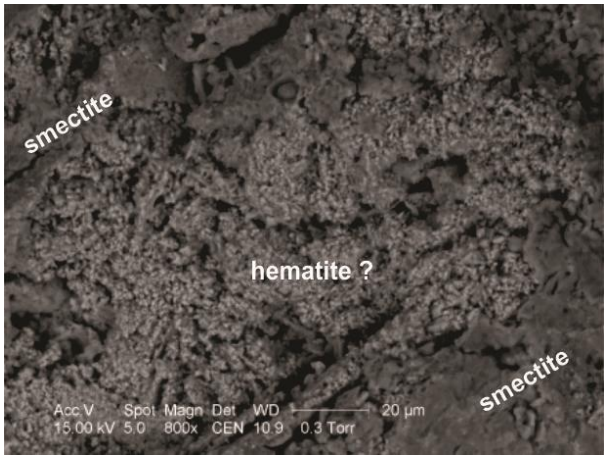

Figure 3. SEM micrographs of Fe oxide (probably hematite) and smectite phase.

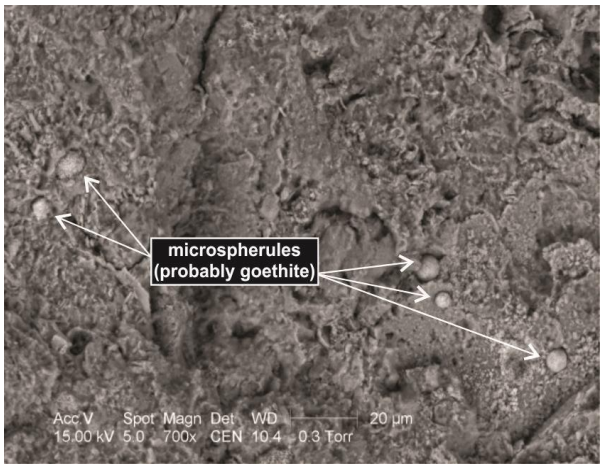

Figure 4. SEM micrographs of probably goethite-rich microspherules.

Premović [11] hypothesized that the massive amount of Fe oxides of the ejecta fallout is generated by the Chicxulub chondritic impactor. Indeed, SEM-EDS analyses of KEL show a presence of few Fe-oxide (probably goethite) microspherules, Fig. 4. Similar microspherules were found in Fish Clay near the Højerup Old Church which is interpreted to be derived from the Chicxulub impact fallout [12].

Premović [11] estimated that global fluency of Fe-oxides derived from the chondritic Fe was approximately 20 g cm^{-2}. He speculated that most of these oxides were probably originally deposited on the local (topographically high) oxic soils and then laterally transported to the KPB sites by the impact induced surface (acid?) waters. Indeed, Schmitz [13] reported that the ejecta layers at two of the worldwide most prominent KPB sites at Caravaca (Spain) and at Woodside Creek (N. Zealand) contain about 5 % of Fe. As KEL, both of these layers are formed under well oxygenated conditions. For comparison, KEL contains about 8 % of Fe. This is about 10 times higher than in their underlying decarbonated latest Maastrichtian and overlying lower Danian limestone.

Manganese. Mn range in KEL is predominantly (85 %) associated with the metal oxide fraction. In a well oxygenated environment Mn geochemically behaves similar to Fe [14]. In this case, Mn shows only IV oxidation state, forming mainly oxide MnO_2. It is highly likely that in this form Mn is associated with the metal oxide fraction of KEL probably absorbed by its Fe oxides.

Vanadium. KEL contains a relatively high concentration (110 ppm) of V, Table 1. Most of this V (90 %) is incorporated within the smectite structure. The KEL vanadium content is comparable to the vanadium contents of ejecta layers of other Danish boundary rocks [5]. The study by Premović *et al*. [11] indicates that the smectite component of these rocks is most likely of local (marine or terrestrial) provenance and was probably redeposited, after its formation, from the original site to its present location. So there is no reason to believe that smectite of the Kikevig boundary section would be of different origin.

Copper and Zinc. We primarily selected to analyze KEL for Cu and Zn because of their distinctive (but relatively simple) geochemical activities and properties. Indeed, Zn and Cu show a similar geochemical behavior in sedimentary environments, which is distinctively different from the geochemical behavior of Fe and V [14].

Table 1 lists the KEL concentrations of Cu (55 ppm) and Zn (940 ppm). The concentration of Zn is much higher than the Zn content in the sedimentary rock which ranges from 100 to 120 ppm [14]. This table also shows that most of Cu (80 %) and Zn (90 %) reside in the metal oxide fraction containing mainly Fe oxides. They are most likely absorbed on these oxides.

CONCLUSIONS

Main carrier of Mn, Cu and Zn in KEL is its metal oxide component enriched with Fe (0.03 %). These trace metals were probably adsorbed on the Fe oxides. Most V is associated with the KEL smectite component. This component is most likely of local (marine or terrestrial) origin and was probably redeposited, after its formation, from the original site to its present location.

Acknowledgement: *Authors thank to Dr. Tove Damholt for providing KPB samples from Kirkevig and to Dr. Jesper Milan for his help and useful information related to this research. We also thank*

Dr. Justyna Ciesielczuk for the qualitative SEM-EDS analysis. Also, our thanks go to Dr. Mirjana S. Pavlović (for the ICP-OES analyses) and Dr. Branko Z. Matović (for the X-ray analyses).

REFERENCES

1. L.W. Álvarez, W. Álvarez, F. Asaro, H. V. Michel, *Science*, **208**, 1095 (1980).
2. A. Shukolyukov, G. W. Lugmair, *Science*, **282**, 927 (1998).
3. A. R. Hildebrand, G. T. Penfield, D. A. Kring, M. Pilkington, A. Y. Camargo, S. Jacobsen, W. V. Boynton, *Geology*, **19**, 867 (1991).
4. P. I. Premović, *Geochem. Int.*, **49** (1), 55 (2011).
5. P. I. Premović, N. Z. Pavlović, M. S. Pavlović, N. D. Nikolić, *Geochim. Cosmochim. Acta*, **57**, 1433 (1993).
6. P. I. Premović, N. D. Nikolić, I. R. Tonsa, M. S. Pavlović, M. P. Premović, D. T. Dulanović, *Earth Planet. Sc. Lett.*, **177** (1-2), 105 (2000).
7. P. I. Premović, M. G. Đorđević, J. Ciesielczuk, M. V. Frontasyeva, S. Pavlov, M. Aničić Urošević, ISINN-25, Dubna, Russia, 2017.
8. P. I. Premović, *Geochim. Cosmochim. Acta*, **48**, 473 (1984).
9. A. Tessier, P. G. C. Campbell, M. Bisson, *Anal. Chem.*, **51**, 844 (1979).
10. H. M. Zakir, N. Shikazono, *J. Environ. Chem. Ecotoxicol.*, **3**, 116 (2011).
11. P. I. Premović, *Open Geoscience*, **1**, 721 (2016).
12. P. I. Premović, *Int. J. Astrobiol.*, **8** (3), 193 (2009).
13. B. Schmitz, *Geology*, **16**, 1068 (1988).
14. A. Kabata-Pendias, H. Pendias, Trace Elements in Soils and Plants, CRC Press, Florida, 2001.

Bulgarian Chemical Communications, Volume 51, Issue 1 (pp. 10-15) 2019

Effect of ultrasound waves intensity on the removal of Congo red dye from the textile industry wastewater by Fe_3O_4@TiO_2 core-shell nanospheres

H. Ghaforyan[1*], T. Ghaffary[2], S. Mohammadibilankohi[1], M. Hasanpour[1], M. Ebrahimzadeh[1], R. Pincak[3,4], M. Farkhan[1]

[1]*Department of Physics, Payame Noor University, P.O.BOX 19395-3697 Tehran, I.R. of Iran*
[2] *Department of Science, Shiraz Branch, Islamic Azad University, Shiraz, Iran*
[3] *Institute of Experimental Physics, Slovak Academy of Sciences, Watsonova 47,043 53 Kosice, Slovak Republic*
[4]*Bogoliubov Laboratory of Theoretical Physics, Joint Institute for Nuclear Research, 141980 Dubna, Moscow region, Russia*

Received, April 29, 2018; Revised, July 23, 2018

In this study, Fe_3O_4@TiO_2 core-shell nanospheres synthesized by a ultrasound-assisted co-precipitation method and their performance in removal of Congo red dye from industrial wastewater under ultrasonic waves were investigated. The structural and morphological properties of the nanospheres were studied by X-ray diffraction (XRD) and transmission electron microscopy (TEM). The XRD analysis confirmed the high purity of the nanospheres synthesized under ultrasound assistance. According to the TEM images, the diameters of Fe_3O_4@TiO_2 nanospheres were about 5 - 15 nm. The adsorption rate of the Congo red dye using these nanoparticles is significantly dependent on the sonicator power and the adsorption rate reached 100% at a power above 30 W.

Keywords: Ultrasound waves, Water treatment, Congo red, Nanoparticles, Core-shell nanospheres, Fe_3O_4@TiO_2.

INTRODUCTION

In recent years, shortage of water resources and the ever-increasing development of industrial units has increased the production of industrial wastewater and contaminated water resources, which is considered a major socioeconomic problem [1]. Chemicals affect water quality indices such as color, taste and smell. It is necessary to control such compounds because they may produce undesired carcinogenic substances such as trihalomethanes. Among various industries, textile, pulp and paper, pharmaceutical, and leather industries are major producers of dye pollutants due to the consumption of thousands of tons of dyes [2-4]. Most dyes are resistant to biodegradation processes. The presence of dyes in the wastewater from such industries prevents the sunlight from penetrating into the water and consequently reduces the rate of photosynthetic processes in surface water [5]. The removal of organic compounds from aqueous environments has been widely studied [6-10]. The most common methods for the removal of such compounds include ozonation [11], coagulation [12], ion exchange [13], biodegradation [14], use of membranes [15], and adsorption [16]. The high cost of advanced oxidation and membrane processes, the need for a large amount of coagulants and production of large volumes of sludge in the coagulation process to remove humic acids, and the low degradation efficiency are among the disadvantages of these methods. Therefore, the use of inexpensive and cost-effective methods for the removal of dyes from the wastewater of textile and dye manufacturing plants is of special importance in developing countries to maintain human and environmental health [17]. The use of adsorption process has received much attention as a simple and cost-effective method [18]. The adsorption process is known as the most suitable method for removing dye pollutants and improving the quality of industrial wastewater because of low cost, simple design, simple operation, and insensitivity to toxic materials [19]. Recently, magnetic particles have been extensively used as a new adsorbent due to magnetic properties and separability by magnets, large number of active surface adsorption sites, and high pollutant removal efficiency [20-22]. In this regard, iron oxide nanoparticles are known as an effective adsorbent for the removal of pollutants from aqueous environments and are widely used for the removal of organic pollutants and heavy metals from such environments [23]. Absalan *et al*. studied the removal of a reactive red dye from aqueous medium using surfactant-modified iron oxide nanoparticles. According to their results, more than 98% of the dye was removed using this method [24].

* To whom all correspondence should be sent:
E-mail: pasiran@gmail.com

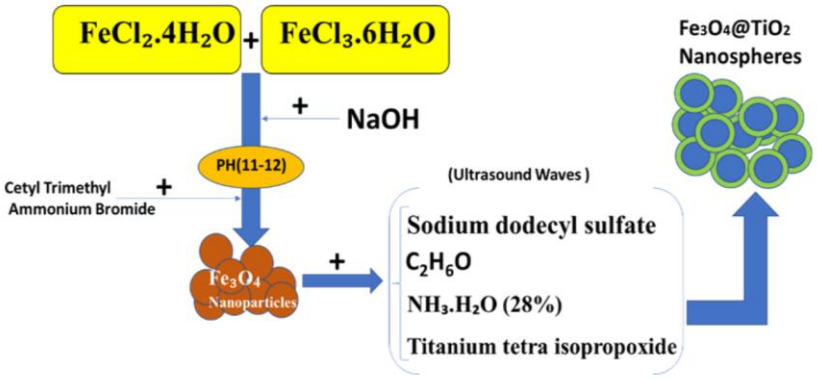

Figure 1. Schematics of the ultrasonic-assisted synthesis of Fe_3O_4@TiO_2 core-shell nanospheres.

Shen *et al*. conducted a study on the removal of nickel, copper, cadmium, and chromium ions and obtained a removal efficiency of more than 90% using iron oxide nanoparticles [25].The aim of the present study is to remove Congo red dye from the textile industry wastewater by synthesized Fe_3O_4@TiO_2 core-shell nanospheres in the presence and absence of ultrasound waves.

EXPERIMENTAL

Materials

All chemical reagents were purchased from Merck Chemical Co. $FeCl_3.6H_2O$, $FeCl_2.4H_2O$, cetyl trimethyl ammonium bromide (CTAB), sodium dodecyl sulfate (SDS), titanium tetra-isopropoxide (TTIP), 28% ammonium hydroxide solution, Congo red (CR), ethanol, hydrochloric acid and sodium hydroxide were used as received. Double distilled water (DDW) was used in all experiments.

Methods

First, 2.01 g of $FeCl_3.6H_2O$ and 0.7923 g of $FeCl_2.4H_2O$ were added to 40 ml of deoxygenated water purged with argon gas for 15 min. Once a transparent solution was obtained, 45.1 ml of 0.1 M sodium hydroxide solution was added to the mixture. Finally, the pH was adjusted in the range of 11-12. After precipitation, 0.1 g of CTAB was added to the solution as a surfactant. The resulting mixture was stirred using a magnetic stirrer at ambient temperature under continuous argon purge (Figure 1). After 20 min, the precipitate was separated using a magnet and washed firstly with water and dilute nitric acid and then with ethanol to remove impurities and reach neutral pH (7.0). The resulting precipitate was dried in an oven at 130°C for 30 min. Then, 0.7 g of CTAB or SDS was added to a mixture of 90 ml ethanol, 35 ml deionized water, and 3 ml 28% ammonium hydroxide. After that, 0.7 g of Fe_3O_4 prepared in the previous step was added to the resulting mixture. The mixture was further treated using a sonicator for 20 min. The sonication power was maintained at 20 W during mixing. A certain amount of TTIP was added to the mixture and further sonicated for an hour. The resulting precipitate was separated using a magnet and then washed several times with water and ethanol to remove impurities. The nanoparticles were then dried in an oven at 55°C for 5 h. Figure 1 shows schematically the ultrasonic-assisted synthesis of Fe_3O_4@TiO_2 core-shell nanospheres.

RESULTS

Figure 2 shows the XRD spectrum of the synthesized nanoparticles. The XRD analysis confirms the inverse spinel cubic structure of Fe_3O_4. The peaks appeared at 2θ = (220), (311), (400), (422), (511), and (440) are fully consistent with the standard cubic structure of the magnetic iron oxide (JCPDS, No. 19-0629). Obviously, Fe_3O_4 is the only phase detected in the XRD spectra and no characteristic peaks of ɣ-Fe_2O_3, another co-precipitation product with peaks very close to this structure, are observed. The Fe_3O_4 crystalline lattice consists of tetrahedral and octahedral sites in which iron ions are surrounded by 4 and 6 ions of oxygen, respectively. As can be seen, the peaks only correspond to the Fe_3O_4 structure, but the intensity of peaks is reduced due to overlapping of peaks. However, since no characteristic peaks of TiO_2 crystalline structure are observed, it can be concluded that amorphous titanium dioxide nanoparticles cover the Fe_3O_4 surface.

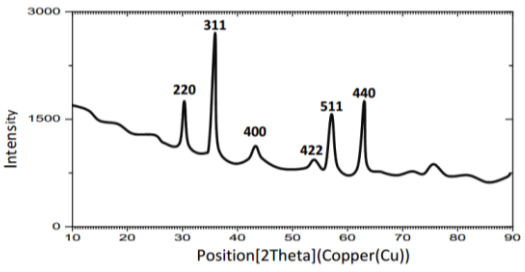

Figure 2. X-ray diffraction spectrum of iron oxide-titanium dioxide core-shell nanospheres.

Figure 3 shows the TEM image of Fe_3O_4@TiO_2 nanoparticles. Most particles are spherical with a mean diameter of 5-15 nm. It can be stated that the ultrasonic-assisted synthesis results in smaller Fe_3O_4@TiO_2 nanospheres showing a good agreement with XRD results.

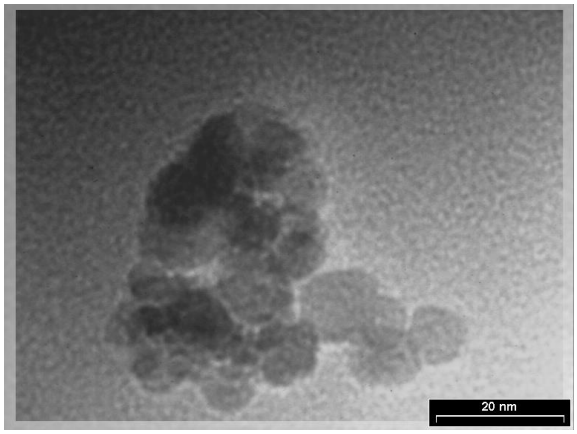

Figure 3. TEM micrograph of Fe_3O_4@TiO_2 nanoparticles synthesized under ultrasound assistance.

Removal of dye pollutants by Fe_3O_4@TiO_2 nanoparticles

To evaluate the performance of Fe_3O_4@TiO_2 nanospheres synthesized under ultrasound assistance in the removal of dye pollutants, a certain amount of the adsorbent was poured into the cell and mixed by a sonicator at a certain pH and temperature. Each experiment was repeated three times to verify the results. Figure 4 shows the chemical structure of Congo red dye. Dye removal was carried in different conditions. It is noteworthy that Congo red is one of the most widely used dyes in the textile industry. Because of its chemical structure, Congo red is among the stable and very toxic dyes in terms of degradability.

Effect of ultrasonic waves' intensity

The effect of various factors on the removal of Congo red dye from an aqueous solution of 150 mgr/l Congo red dye in deionized water (with an initial pH of 9-9.5) using the Fe_3O_4@TiO_2 adsorbent was studied. As clearly seen in Figure 5, dye removal decreases at low intensities but increases at intensities higher than 28 W. An increase in the number of bubbles at high ultrasonic intensities improves the cavitation process, which in turn significantly affects the mass transfer from the adsorbent surface. Therefore, the effect of other factors on the dye removal was studied at the optimal intensity of 28 W. The following chart was plotted using the sonicator power calculated by calorimetry.

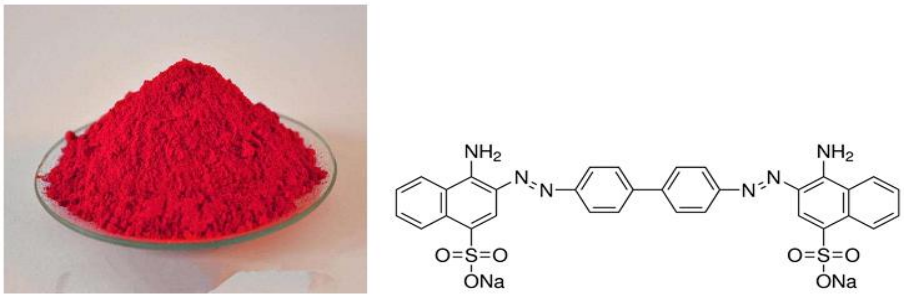

Figure 4. Chemical structure of Congo red dye

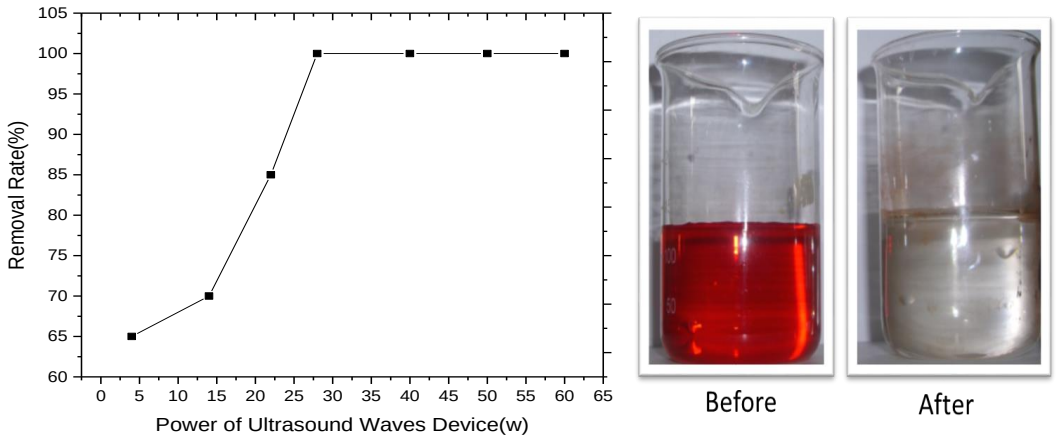

Figure 5. Effect of ultrasonic intensity on the removal of Congo red dye (concentration: 150 mg/l, adsorbent: 0.09 g, temperature: 21-24°C, time: 3 min).

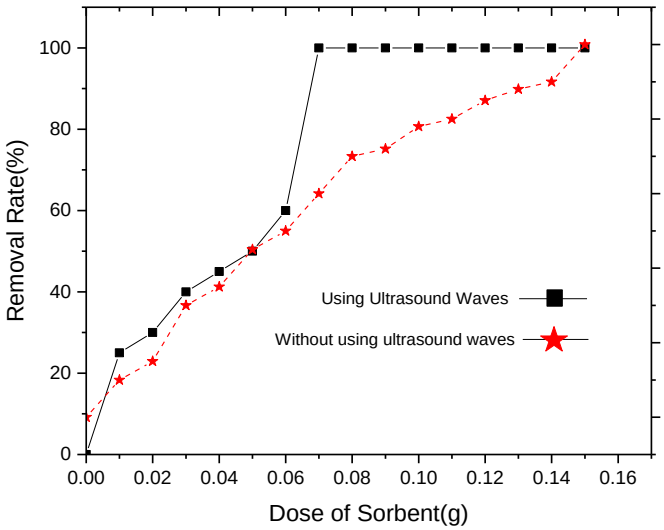

Figure 6. Effect of adsorbent concentration on Congo red dye removal (concentration: 150 mg/l, temperature: 21-24°C, time: 3 min)

The effect of different concentrations of the adsorbent (0.01 to 0.15 g) on the removal of Congo red dye from 65 ml of a 150 mg/l dye solution was studied at the initial pH of the dye for 3 min. As shown in Figure 6, with increasing the adsorbent level up to 0.15 g, the reaction rate in the classical method increases resulting in a dye removal percentage of 99.55%. The reaction rate also increases in the ultrasonic-assisted dye removal method with increasing the adsorbent level, but a dye removal rate of 99.7% was obtained with 0.09 g of Fe_3O_4@TiO_2 nanoparticles.

Since the amorphous structure of titanium dioxide contains Ti^{4+} and O^{2-} ions (based on the XRD results), the surface atoms cannot be fully coordinated leading to an increase in the degree of coordination unsaturation. Furthermore, surfactants may affect the arrangement of this configuration. The minimum configuration energy for the surface atoms occurs when they are in close contact with the surroundings at the atomic scale. With increasing degree of unsaturation, driving forces for chemical and physical adsorption will increase. The main driving forces for molecular adsorption include: (1) coordination of surface atoms with the surrounding atoms and (2) interaction of the surface charges with counter-ions. Obviously, an increase in the adsorbent level leads to an increase in the adsorption rate due to the increased contact surface of the adsorbent. With increasing adsorbent level, the contact surface of the adsorbent particles will increase. As a result, a larger number of dye molecules can be accomodated on the adsorbent surface leading to an increase in the adsorption rate. Moreover, the burst of cavitation bubbles causes the formation of high-pressure turbulent currents and high-speed microjets which reduce the size of larger particles. This in turn increases the contact surface and surface reactivity. In addition, the mass transfer process is improved by ultrasonically induced turbulence due to the mechanical pressures. Bubble bursting can also affect the surface diffusion and structure in this system. Therefore, an optimal adsorbent level of 0.1 g was used to investigate the effect of other factors.

DISCUSSION

According to the results, the initial intraparticle diffusion rate in the stirring method is higher than that of the ultrasonic method. This can be attributed to the larger thickness of the boundary layer in the ultrasonic method due to the increased number of dye molecules on the external surface of the adsorbent. Moreover, as temperature increases in the stirring method, intraparticle diffusion rate decreases due to increased ion mobility and eventually increased number of dye molecules in the boundary layer and on the external surface. In contrast, the intraparticle diffusion rate increases in the ultrasonic method because of accelerated mass transfer into the pores as a result of mechanical pressures.

CONCLUSION

It can be concluded that with increasing temperature, layer diffusion becomes the dominant mechanism in the presence or absence of ultrasonic waves. However, intraparticle diffusion is faster in the stirring method than in the ultrasonic method considering the boundary layer thickness. Nonetheless, the adsorption rate in these steps is very low compared to that on the surface. This can

be attributed to interactions between the dye molecules and the adsorbent surface. It is noteworthy that the dye-adsorbent interactions are stronger in the ultrasonic method.

Acknowledgements: *Thanks are due to the Payame Noor University in Iran for the financial support. Also, the work was partly supported by VEGA Grant No. 2/0009/16. R. Pincak would like to thank the TH division in CERN for hospitality.*

The authors declare no conflict of interests regarding the publication of this article.

REFERENCES

1. P. Rao, I. M. Lo, K. Yin, S. C. Tang, Removal of natural organic matter by cationic hydrogel with magnetic properties, *Journal of environmental management*, **92**(7), 1690 (2011).
2. T. A. Saleh, V. K. Gupta, Column with CNT/magnesium oxide composite for lead (II) removal from water, *Environmental Science and Pollution Research*, **19**(4), 1224 (2012).
3. J. Rivera-Utrilla, M. Sánchez-Polo, M. Á. Ferro-García, G. Prados-Joya, R. Ocampo-Pérez, Pharmaceuticals as emerging contaminants and their removal from water. A review, *Chemosphere*, **93**(7), 1268 (2013).
4. E. M. Dias, C. Petit, Towards the use of metal–organic frameworks for water reuse: a review of the recent advances in the field of organic pollutants removal and degradation and the next steps in the field, *Journal of Materials Chemistry* A, **3**(45), 22484 (2015).
5. S. M. Bilankohi, M. Ebrahimzadeh, T. Ghaffary, M. Zeidiyam, Scattering, Absorption and Extinction Properties of Al/TiO_2 Core/Shell Nanospheres, *Indian Journal of Science and Technology*, **8**(S9), 27 (2015).
6. I. Ali, Z. A. Alothman, A. Al-Warthan, Sorption, kinetic and thermodynamic studies of atrazine herbicide removal from water using iron nano-composite material, *International Journal of Environmental Science and Technology*, **13**(2), 733 (2016).
7. B. Wang, G. H. Huang, L. Liu, W. Li, Y. L. Xie, Integrated planning of urban water resources and water pollution control management: Case of Urumqi, China. *Journal of Water Resources Planning and Management*, **142**(6), 05016001 (2016).
8. N. Shah, F. Claessyns, S. Rimmer, M. Balal Arain, T. Rehan, A. Wazwaz, M. Wasi Ahmad, M. Ul-Islam, Effective Role of Magnetic Core-Shell Nanocomposites in Removing Organic and Inorganic Wastes from Water, *Recent Patents on Nanotechnology*, **10**(3), 202 (2016).
9. F. Meng, Q. Liang, H. Ren, X. Guo, Low-cost solvothermal synthesis of hierarchical structure γ-AlOOH and its application to remove Cr (VI), methyl orange and Congo red from contaminated water, *Current Nanoscience*, **11**(4), 434 (2015).
10. T. Huang, Adsorption of Trace Selenium on Nano-Ti2 from Natural Water Samples, *Current Analytical Chemistry*, **11**(3), 193 (2015).
11. D. Gümüş, F.Akbal, A comparative study of ozonation, iron coated zeolite catalyzed ozonation and granular activated carbon catalyzed ozonation of humic acid, *Chemosphere*, **174**, 218 (2017).
12. Y. Zhao, Y. Sun, C. Tian, B. Gao, Y. Wang, H. Shon, Y. Yang, Titanium tetrachloride for silver nanoparticle-humic acid composite contaminant removal in coagulation-ultrafiltration hybrid process: floc property and membrane fouling, *Environmental Science and Pollution Research*, **24**(2), 1757 (2017).
13. G. J. Millar, S. J. Couperthwaite, S. Papworth, Ion exchange of sodium chloride and sodium bicarbonate solutions using strong acid cation resins in relation to coal seam water treatment, *Journal of Water Process Engineering*, **11**, 60 (2016).
14. E. Baginska, A. Haib, K. Kümmerer, Biodegradation screening of chemicals in an artificial matrix simulating the water–sediment interface, *Chemosphere*, **119**, 1240 (2015).
15. J. M. Dickhout, J. Moreno, P. M. Biesheuvel, L. Boels, R. G. Lammertink, W. M. de Vos, Produced water treatment by membranes: A review from a colloidal perspective. *Journal of Colloid and Interface Science*, **487**, 523 (2017).
16. M. Chandrasekar, M. R. Ishak, S. M. Sapuan, Z. Leman, M. Jawaid, A review on the characterisation of natural fibers and their composites after alkali treatment and water absorption, *Plastics, Rubber and Composites*, **46**(3), 119 (2017).
17. L. Song, B. Zhu, V. Jegatheesan, G. Stephen, D. Mikel, S. Muthukumaran, A hybrid photocatalysis and ceramic membrane filtration process for humic acid degradation: Effect of pore size and transmembrane pressure, *Desalination and Water Treatment*, **69**, 102 (2017).
18. M. Y. Gaouar, B. Benguella, Efficient and eco-friendly adsorption using low-cost natural sorbents in waste water treatment, *Indian Journal of Chemical Technology (IJCT)*, **23**(3), 204 (2016).
19. L. Lin, X. Xu, C. Papelis, P. Xu, Innovative use of drinking water treatment solids for heavy metals removal from desalination concentrate: Synergistic effect of salts and natural organic matter, *Chemical Engineering Research and Design*, **120**, 231 (2017).
20. A. S. Adeleye, J. R. Conway, K. Garner, Y. Huang, Y. Su, A. A. Keller, Engineered nanomaterials for water treatment and remediation: costs, benefits, and applicability, *Chemical Engineering Journal*, **286**, 640 (2016).
21. M. Khan, I. M. Lo, Removal of ionizable aromatic pollutants from contaminated water using nano γ-Fe_2O_3 based magnetic cationic hydrogel: Sorptive performance, magnetic separation and reusability, *Journal of Hazardous Materials*, **322**, 195 (2017).

22. D. H. K. Reddy, Y. S. Yun, Spinel ferrite magnetic adsorbents: alternative future materials for water purification, *Coordination Chemistry Reviews*, **315**, 90 (2016).
23. L. Wang, C. Kim, Z. Zhang, Q. Hu, T. Sun, X. Hu, Adsorption Behavior of Lysozyme on Carbon-Coated Fe_3O_4 Nanoparticles, *Current Nanoscience*, **13**(2), 159 (2017).
24. A. Gharaati, M. Ebrahimzadeh, Enhanced Microwave Absorption Properties of FeCo@TiO_2 Core-Shell Nanoparticles, *Current Nanoscience*, **14**(6), 1 (2018).
25. A. M. Gutierrez, T. D. Dziubla, J. Z. Hilt, Recent advances on iron oxide magnetic nanoparticles as sorbents of organic pollutants in water and wastewater treatment, *Reviews on Environmental Health*, **32**(1-2), 111 (2017).

Bulgarian Chemical Communications, Volume 51, Issue 1 (pp. 16-19) 2019

Determination of the pK_a values of some pyridine derivatives by computational methods

V. E. Atalay

Üsküdar University, Bioengineering Department, Üsküdar, Istanbul, Turkey

Received August 25, 2018; Accepted December 24, 2018

In this study, pK_a values are determined relying on density functional theory, its related methods such as WB97XD, M062X, B3LYP with 6-31+Gdp and 6-311++Gdp basis sets for three pyridine derivatives, namely isoniazid, nicotinamide and pyridoxine. When investigating the obtained values, the most accurate values are found to be obtained *via* the WB97XD method with 6-31+Gdp basis set in water phase. The pK_a values calculated in the gas phase were not satisfactory enough to compare with the experimental results.

Keywords: pK_a, DFT, M06-2X, WB97XD, B3LYP, pyridine

INTRODUCTION

Pyridine with C_5H_5N chemical formula is a basic heterocyclic aromatic compound [1]. Pyridine became a much interested compound in 1930s with the importance of its role in the disease treatment [2]. It's derivatives have been reported for a variety of biological activities and were used in clinical uses, such as anti-microbial [3-5], anti-viral [6-8], antioxidant [9], anti-diabetic [10] anti-cancer activities [11], anti-malarial agents [12], psychopharmacological antagonistic [13], iron overload disease [14], anti-amoebic agents [15], anti-inflammatory agents [16]. Pyridine derivatives in these fields also have increasing importance for modern medicinal applications, especially they have an important role to develop human medicine. There are more than hundred drugs in the market containing pyridine compounds [1]. In this study, three heterocyclic pyridine derivatives, namely isoniazid, pyridoxine hydrochloride and nicotinamide were investigated (Figure 1).

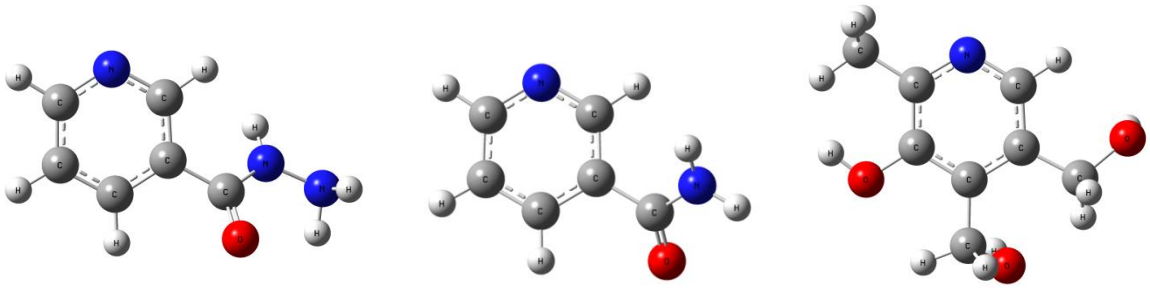

(a) (b) (c)

Figure 1. Investigated drug molecules: (a) isoniazid, (b) nicotinamide, (c) pyridoxine

Acid dissociation constants, K_a, are essential for understanding many fundamental reactions in chemistry and biochemistry of a drug precursor, such as tautomeric equilibrium, activity searches and determination of certain physical parameters. Especially determination of pK_a values of drugs gains paramount significance from the perspective of dosage form formulation, pharmaceutical analysis, and studying of drug pharmacokinetics. Solubility, lipophilicity, protein binding and membrane permeability of a given drug are also influenced by its pK_a value [17]. Several techniques have been used for pK_a determinations, such as potentiometric titration, spectrophotometric method, NMR titration, liquid chromatography (LC), capillary electrophoresis (CE) and computational methods [18]. Experimental measurements are generally less simple, as there would be considerable synthesis and purification efforts prior to the pK_a measurement. The ability of accurate computational calculating pK_a values is important for scientific advancements in biochemistry, medicinal chemistry, and other related fields [19]. In this study, the pK_a values of

* To whom all correspondence should be sent:
E-mail: vildan.enisoglu@uskudar.edu.tr

three active drug compounds were determined by a theoretical approach in order to compare computationally obtained values with the experimental values.

Method

Firstly, conformer search was performed with the Spartan14 [20] with a semi-empirical PM6 method [21, 22]. Geometry optimizations were performed for the obtained most stable structures in gas and water phases. The Gaussian 09 software [23] was used for all theoretical calculations, and all visulalizations were done with GaussView5 [24]. In the literature there are several studies on pKa detemination with density functional theory (DFT) [25-29]. DFT's ability to accurately compute ground-state observable properties has given its remarkable ease of use and its ability to effectively balance accuracy with computational speed when compared to traditional high-accuracy *ab initio* methods [30-32]. B3LYP [33], M062X [34] and WB97XD [35] were preferred as calculation methods with 6-31+Gdp and 6-311++Gdp basis sets in the gas and water phases for the investigated isoniazid, nicotinamide and pyridoxine molecules. IEF-PCM method [36] was applied to solvent phase calculation.

Determination of pK_a values

First principles computations have historically relied on thermodynamic cycles, taking advantage of the fact that the Gibbs energy is a state function, and therefore any convenient cycle that connects the initial reactants to the final products provides a way to calculate the Gibbs energy change for the reaction of interest [37]. The quality of calculated pK_as depends on the accuracy of the computed protonation energies and the reliability of the estimated solvation energies [28]. The pK_a values were calculated by the following Scheme 1 and Eqs.1-4:

$A + H^+ \leftrightarrow AH^+$ (protonation reaction)

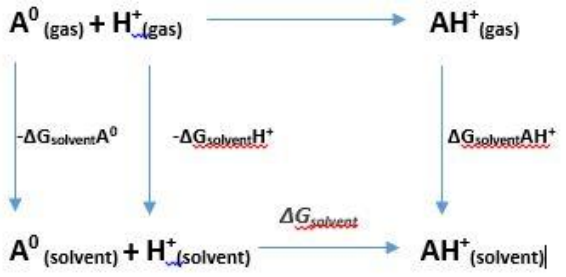

Scheme 1. Thermodynamic cycles of the Gibbs free energies in gas and solvent phases [38].

The Gibbs free energy (ΔG) for the investigated compounds in the gas phase was determined by Eq.1 [39]:

$$\Delta G = \Delta H - T\Delta S \qquad \text{Eq. 1}$$

The pK_a values for the gas phase were calculated by Eq. 2:

$$pK_a = \Delta G/R/T/2.303 \qquad \text{Eq. 2}$$

On the other side, for the solvent phase, ΔΔG values were calculated *via* Eq. 3 and the obtained values were used to determine the pK_a values *via* Eq. 4 [37]:

$$\Delta\Delta G = \Delta G_{solvent} + \Delta G_{gas} + \text{correction factor } (R*T*In\ (24.46)) \qquad \text{Eq. 3}$$

$$pK_a = \Delta\Delta G/R/T/2.303 \qquad \text{Eq. 4}$$

RESULTS AND DISCUSSION

The calculated and literature data based pK_a values for the nicotinamide, isoniazid and pyridoxine compounds are listed in Table 1. The calculated results are compared with the literature data. The comparison results show that the choice of method was quite adequate. However, the pK_a values in the gas phase are somewhat different from the water phase calculations and experimental values with almost 0.2-0.9 difference in all studied methods and basis sets. The calculated pK_a value for nicotinamide with WB97XD method 6-31+Gdp basis set in water is the same (pK_a=3.35) as the literature value. In the literature, the same method has been found to provide the best correlation with the experimental data for the thiol molecules [37]. For the pyridoxine compound, the WB97XD method calculated the relevant value (pK_a=5.25) with the slightest difference (0.05) as compared to the literature value (pK_a=5.20). When the WB97XD method results are compared with experimental NMR results, we can observe that especially for the pyridoxine molecule, the experimental values (pK_a=5.24) are closer to the obtained value by the WB97XD method and this result is consistent with the literature [27]. When we look for the best pK_a value for the isoniazid compound, WB97XD/6-311++Gdp level of theory gives pK_a=3.36 (nearest obtained value through computational methods), whereas the corresponding pK_a value in the literature is 3.50. The obtained results show that WB97XD is a more suitable method for this kind of molecules.

On the other hand, M062X methods provide accurate results for the investigated molecules, especially with 6-31+Gdp basis set in water phase. For nicotinamide, the calculated pK_a value (3.39) is lower than the literature value with a small

difference (0.04) which is a quite good result in the water phase. For isoniazid molecule, the computationally obtained value by the same method is 3.23, as compared to the 3.20 value through the web-based calculation method.

The B3LYP/6-31+Gdp method has also given close results with the NMR methods for the nicotinamide molecule, pK_a= 3.57 and pK_a=3.54, respectively. The results of this method are closer to the web-based calculation results for other investigated compounds in water phase obtained as pK_a=3.29 (calculated) and pK_a=3.20 (web-based); pK_a=5.65 (calculated) and pK_a=5.60 (web-based) for isoniazid and pyridoxine compounds, respectively. In general sense, the B3LYP method has not given good matching performance with respect to other studied experimental methods in the literature.

Table 1. The calculated pK_a values with the DFT theory B3LYP, WB97XD and M062X methods, 6-31+Gdp and 6-311++Gdp basis sets in the gas and water phases

	Compound		
Method/phase	Nicotinamide	Isoniazid	Pyridoxine
B3LYP/6-31+Gdp/gas	4.17	4.12	4.98
B3LYP/6-31+Gdp/water	3.57	3.29	5.65
B3LYP/6-311++Gdp/gas	4.18	4.13	4.98
B3LYP/6-311++Gdp/water	3.42	3.30	5.64
WB97XD/6-31+Gdp/gas	4.08	4.03	4.88
WB97XD/6-31+Gdp/water	**3.35**	3.22	**5.25**
WB97XD/6-311++Gdp/gas	4.09	4.03	4.87
WB97XD/6-311++Gdp/water	3.47	**3.36**	5.34
M062X/6-31+Gdp/gas	3.85	3.79	4.69
M062X/6-31+Gdp/water	3.39	3.23	5.30
M062X/6-311++Gdp/gas	3.87	3.82	4.72
M062X/6-311++Gdp/water	3.45	3.25	5.33
NMR Method [40]	3.54	3.65	5.24
Literature	3.35 [41]	3.50 [42]	5.20 [43]
Web-Based Calculation [44]	3.60	3.20	5.60

CONCLUSION

In this study, three pyridine derivatives, namely nicotinamide, isoniazid and pyridoxine were investigated to determine the pK_a values and compare them with the experimental data. DFT theory was chosen with WB97XD, M062X and B3LYP methods using 6-31+Gdp and 6-311++Gdp basis sets. According to the obtained results the WB97XD/6-31+Gdp method has given more accurate computational values that are consistent with the experimental values in the literature. On the other hand, M062X and B3LYP methods have not reached satisfactory convergence performance to the experimental values. As an important emphasis, condensed phase results are significantly better than gas phase results. The essential result is that the WB97XD method was found as an excellent option to determine the pK_a values of pyridine family derivatives through theoretical approaches, as demonstrated by the fact that our computational findings very closely match the experimental data.

REFERENCES

1. A. A. Altaf, A. Shahzad, Z. Gul, *Jour. of Drug Des. and Med. Chem.*, **1**, 1 (2015).
2. G. D. Henry, *Tetrahedron*, **60**, 6043 (2004).
3. M. M. Mashaly, Z. H. Abd-Elwahab, A. A. Faheim, *Jour. Chin. Chem. Soc.*, **51**, 901 (2004).
4. R. Sabet, A. Fassihi, B. Moeinifard, *Res. in Pharm. Sci*., **2**, 103 (2009).
5. Y. Zheng, Z. Ma, X. Zhang, N. Yang, G. Yang, *Int. Jour. of Chem.*, **3**, 42 (2011).
6. E. Abele, R. Abele, E. Lukevics, *Chem. of Heteroc. Comp.*, **39**, 825 (2003).
7. S. A. M. El-Hawash, A. E. Abdel Wahab, M. A. El-Demellawy, *Archiv der Pharmazie*, **339**, 14 (2006).
8. M. Vrábel, M. Hocek, L. Havran, M. Fojta, I. Votruba, B. Klepetářová, R. Pohl, *Eur. Jour. of Inorg. Chem.*, 1752 (2007).
9. A. Worachartcheewan, S. Prachayasittikul, R. Pingaew, C. Nantasenamat, T. Tantimongcolwat, S. Ruchirawat, V. Prachayasittikul, *Med. Chem. Res.*, **21**, 3514 (2012).
10. S. Firke, B. Firake, R. Chaudhari, V. Patil, *Asian Jour. of Res. in Chem.*, **2**, 157 (2009).

11. X. T. Yang, H. Wu, S. J. Ma, J. J. Hu, Y. Wang, *Trans. Met. Chem*., **1** (2011).
12. B. Narayan Acharya, D. Thavaselvam, M. Parshad Kaushik, *Med. Chem. Res*., **17**, 487 (2008).
13. E. Kita, R. Lisiak, *Trans. Met. Chem*., **35**, 441 (2010).
14. T. B. Chaston, D. R. Richardson, *Jour. of Biol. Inorg. Chem.*, **8**, 427 (2003).
15. N. Bharti, M. R. Maurya, F. Naqvi, A. Azam, *Bioorg. Medi. Chem. Lett.*, **10**, 2243 (2000).
16. Y. K. Márquez-Flores, M. E. Campos-Aldrete, H. Salgado Zamora, J. Correa-Basurto, M. E. Meléndez-Camargo, *Med. Chem. Res*., (2011).
17. M. Khattab, F.Wang, A. H. Clayton, *Scientific Reports*, **7**, 16271 (2017).
18. S. Babić, A. J, Horvat, D. M, Pavlović, M. Kaštelan-Macan, *Talanta*, **70**, 732 (2007)
19. G. C. Shields, P. G. Seybold, Computational Approaches for the Prediction of pKa Values, CRC Press, 2010.
20. W.J. Hehre, W. W. Huang, Chemistry with Computation: An introduction to SPARTAN. Wavefunction, Inc., 1995.
21. J. J. P. Stewart, *J. Mol. Model.*, **14**, 499 (2008).
22. J. J. P. Stewart, *J. Mol. Model*., **15**, 765 (2009).
23. M. J. Frisch, G. W. Trucks, H. B. Schlegel, & H. Nakatsuji, Gaussian 09, revision D. 01, 2009.
24. GaussView, Version 5, Dennington, R., Keith, T., Millam, J. Semichem Inc., Shawnee Mission KS, 2009.
25. S. Çalış, H. Berber, Ü. D. Uysal, C. Öğretir, *Anadolu University Journal Of Science And Technology –B Theoretical Sciences*, **2**, 149 (2011).
26. T. N. Brown, N. Mora-Diez, *The Jour. of Phys. Chem B*, **110**, 41, 20546 (2006).
27. B. Thapa, H. Bernhard Schlegel, *The Jour. of Phys. Chem. A*, **119**, 21 (2014).
28. B. Thapa H. Bernhard Schlegel, *The Jour. of Phys. Chem. A*, **120**, 44, (2016).
29. D. O. Kashinski, G. M. Chase, R. G. Nelson, O. E. Di Nallo, E. F. C. Byrd, *The Journal of Physical Chemistry A*, **121**, 2265 (2017).
30. P. G. Seybold, G. C. Shields, *Comp. Molec. Sci.*, **5**, 3, 290 (2015).
31. P. C. Hariharan, J. A. Pople, *Theoret. Chim. Acta (Berl.)*, **28**, 3, 213(1973).
32. P. C. Hariharan, J. A. Pople, *Mol. Phys.*, **27**, 1, 209 (1974).
33. A. D. Becke, *J. Chem. Phys*., **98**, 2, 1372 (1993)
34. D. G. Truhlar, Y. Zhao, *Theor. Chem. Acc*., **120**, 215 (2006).
35. A. J. Garza, O. I. Osman, N. A. Wazzan, S. B. Khan, G. E. Scuseria, A. M. Asiri, *Theor. Chem. Acc*., **9**, 132 (2013).
36. A. V. Marenich, C. J. Cramer, D. G. Truhlar, *J. Phys. Chem. B*, **113**, 6378 (2009).
37. B. Thapa, H. B. Schlegel, *J. Phys. Chem*. A, **120**, 28, 5726 (2016).
38. R. Casasnovas, J. Ortega Castro, J. Frau, J. Donoso, F. Munoz, *Int. Jour. of Quant. Chem*. **114**, 20, 1350 (2014).
39. J. Reijenga, A. Van Hoof, A. Van Loon, B. Teunissen, *ACI*, **8**, 12304 (2013).
40. A. Zivkovic, J. J. Bandolik, A. J. Skerhut, C. Coesfeld, M. Raos, N. Zivkovic, V. Nikolic, H. Stark, *Magnetochemistry*, **3**, 29 (2017).
41. D.D. Perrin, *Pure Appl. Chem.*, **20**, 133 (1969).
42. C. Becker, J.B. Dressman, G.L. Amidon, H.E. Junginger, *J. Pharm. Sci.*, **96**, 522 (2007).
43. T.D.A.D.D. Santos, D.O. Da Costa, S. S. Da Rocha Pita, F. S. Semaan, *Eclet. Quim*., **35**, 81(2010).
44. http://epoch.ukyedu/ace/public/pKa.j

Bulgarian Chemical Communications, Volume 51, Number 1 (pp. 20 – 24) 2019

Protecting effect of vitamin U against amiodarone-induced hepatic damage via its antioxidative activity

I. B. Turkyilmaz*, R. Yanardag

Department of Chemistry, Faculty of Engineering, Istanbul University-Cerrahpasa , 34320, Avcilar-Istanbul, Turkey

Received, November 7, 2016; Revised, November 28, 2018

In this study, we aimed to investigate the protective effect of Vitamin U (Vit U) on amiodarone (AMD)-induced hepatotoxicity. Male Sprague-Dawley rats were grouped as control, Vit U given control (50 mg/kg, by gavage), AMD (100 mg/kg, by gavage) and Vit U given AMD (in same dose and time). AMD and Vit U were given for 7 days. On the 8th day, all animals were sacrificed. Serum aspartate and alanine aminotransferase, alkaline phosphatase activities and total lipid and total bilirubin levels, liver lipid peroxidation and protein carbonyl levels, lactate dehydrogenase, myeloperoxidase, xanthine oxidase, arginase, prolidase, DT-diaphorase activities were found to be increased and liver glutathione levels, paraoxonase and Na^+/K^+-ATPase activities were found to be decreased in AMD group. Administration of Vit U reversed these effects. Based on our results, we may suggest that Vit U has a protective effect on AMD-induced hepatotoxicity in rats.

Keywords: Vitamin U; amiodarone; liver; toxicity; rat

INTRODUCTION

Amiodarone (AMD), 2-butyl-3-(3',5'-diiodo-4-α-diethyl aminoethoxybenzoyl) benzofuran, is a class III antiarrhythmic drug, effective myocardial infarction or congestive heart failure treatment, which has been widely used in medicine [1]. This drug is effective in preventing ventricular and supraventricular tachyarrhythmias [2]. Despite having effective properties on cardiac arrhythmias, AMD is highly lipophilic in nature, has poor availability and also has a long half-life [3]. So these properties make this drug tend to accumulate in many organs and side effects and toxicity occur during therapy. Organs like the liver, lung, kidneys, gastrointestinal and neuromuscular systems make up the list of tissues adversely affected by AMD [4]. AMD-induced hepatotoxicity is characterized by steatosis, enlarged hepatocytes, inflammation, fibrosis and phospholipidosis [5]. In in vivo and in vitro studies, AMD has been shown to generate free radicals that may be involved in the pathogenesis of its toxicity [6].

Vitamin U (Vit U), S-methyl methionine sulphonium chloride, is a methionine derivative. It is reported that Vit U is present in the largest quantity in species belonging to the Brassicaceae family [7]. Vit U is found in cabbage and other green vegetables. This vitamin has a beneficial power action on gastric and intestinal functions [8]. Vit U is reported to have hypolipidemic effect, hepatoprotective, cytoprotective, anti-inflammatory and antidepressant actions, adipocyte differentiating and wound-healing properties [9].

In this study, we aimed to investigate the protective effect of Vit U on AMD-induced hepatotoxicity.

EXPERIMENTAL

Animals and experimental design

The experimental procedures were approved by the local Animal Care and Use Committee of Istanbul University, with the certification on the Application for the Use of Animals dated September 27, 2012 (approval ID: 2012 / 127). In this study, 3.5-4 months aged male Sprague-Dawley rats were used. Application of AMD dose and time were determined as Reasor *et al.* [10]. Vit U (Fluka 64382) dose were administered according to Sokmen *et al.* [9]. A total of twenty nine rats were divided into 4 groups as follows. The groups include: Group I, control animals receiving corn oil for 7 days (n=6); Group II, animals receiving Vit U (50 mg/kg) for 7 days (n=7); Group III; animals receiving AMD (100 mg/kg) for 7 days (n=8); and Group IV, animals receiving Vit U (50 mg/kg) for 7 days 1 h prior to administration of AMD (100 mg/kg) (n=8). AMD and Vit U were administered to rats by gavage. On the 8th day, blood samples were taken before sacrification and then all the animals were sacrificed.

* To whom all correspondence should be sent:
E-mail: burchemistry@gmail.com

Biochemical assays

Experiments were made in serum and liver tissues of all groups. Aspartate (AST) and alanine aminotransferase (ALT) activities [11], alkaline phosphatase (ALP) [12], total lipid levels [13], total bilirubin [14] were determined in serum. Liver samples were homogenized. Homogenates were centrifuged. Glutathione (GSH) [15], lipid peroxidation (LPO) [16], protein carbonyl (PC) levels [17], lactate dehydrogenase (LDH) [18], myeloperoxidase (MPO) [19], paraoxonase (PON1) [20], xanthine oxidase (XO) [21], arginase [22], Na^+/K^+-ATPase [23], prolidase [24], DT-diaphorase (DTD) activities [25], and protein content [26] were determined in the supernatant.

Statistical analysis

Biochemical analysis was performed by one-way ANOVA followed by Duncan's Newman-Keuls multiple comparison test. The values are expressed as the mean ± standard deviation (SD). *P* values less than 0.05 were considered to be significant.

RESULTS

AST, ALT and ALP activities ($P < 0.0001$, $P < 0.005$), lipid ($P < 0.005$) and bilirubin levels ($P < 0.05$) were significantly increased in AMD group when we compared to control group. Administration of Vit U reversed these effects in AMD group significantly, respectively ($P < 0.05$, $P < 0.0001$, $P < 0.005$) (Table 1).

Table 1. Serum AST, ALT and ALP activities, total lipid and total bilirubin levels of all groups.

Groups	AST (U/L)*	ALT (U/L)*	ALP (U/L)*	Total Lipid (mg/dL)*	Total Bilirubin (mg/dL)*
Control	21.68 ± 6.15	21.41 ± 8.35	58.08 ± 9.73	135.10 ± 39.69	0.281 ± 0.011
Control + Vit U	38.07 ± 16.76[a]	14.83 ± 8.12[a]	62.63 ± 20.61[a]	149.45 ± 9.57[a]	0.366 ± 0.103[a]
AMD	69.17 ± 14.23[b]	55.63 ± 21.16[d]	216.71 ± 11.13[b]	208.89 ± 24.75[d]	0.358 ± 0.039[f]
AMD + Vit U	38.12 ± 19.72[c]	31.72 ± 10.87[c]	155.15 ± 0.30[e]	159.60 ± 16.98[c]	0.260 ± 0.034[g]

*Mean ± SD, [a]p >0.05 *versus* control group, [b]$p < 0.0001$ *versus* control group, [c]$p < 0.05$ *versus* AMD group, [d]$p < 0.005$ *versus* control group, [e]$p < 0.0001$ *versus* AMD group, [f]$p < 0.05$ *versus* control group, [g]$p < 0.005$ *versus* AMD group.

Table 2. Liver GSH, LPO and PC levels of all groups.

Groups	GSH (nmol GSH/mg protein)*	LPO (nmol MDA/mg protein)*	PC (nmol carbonyl/mg protein)*
Control	14.13 ± 1.39	3.35 ± 0.32	8.34 ± 0.36
Control + Vit U	11.67 ± 2.10[a]	2.83 ± 0.58[a]	8.53 ± 1.85[a]
AMD	6.14 ± 1.79[b]	4.08 ± 0.49[a]	16.69 ± 5.21[e]
AMD + Vit U	8.60 ± 0.67[c]	2.88 ± 0.58[d]	10.39 ± 1.41[d]

*Mean ± SD, [a]p >0.05 versus control group, [b]$p < 0.0001$ versus control group, [c]p >0.05 versus AMD group, [d]$p < 0.05$ versus AMD group, [e]$p < 0.05$ versus control group

Table 3. Liver LDH, MPO, PON1 and XO activities of all groups

Groups	LDH (U/mg protein)*	MPO (U/g tissue)*	PON1 (U/g protein)*	XO (U/g protein)*
Control	13.08 ± 4.01	1.89 ± 0.68	10.83 ± 0.46	0.45 ± 0.06
Control + Vit U	23.08 ± 12.01[a]	2.00 ± 0.56[a]	7.91 ± 2.11[a]	0.34 ± 0.32[a]
AMD	61.52 ± 14.70[b]	3.04 ± 0.60[d]	5.92 ± 2.03[d]	1.24 ± 0.31[d]
AMD + Vit U	37.25 ± 5.55[c]	1.31 ± 0.42[e]	9.25 ± 2.37[c]	0.23 ± 0.10[c]

*Mean ± SD, [a]p >0.05 versus control group, [b]$p < 0.005$ versus control group, [c]$p < 0.05$ versus AMD group, [d]$p < 0.05$ versus control group, [e]$p < 0.005$ versus AMD group

GSH levels were found to be decreased significantly ($P < 0.0001$) and PC levels were found to be increased significantly in AMD group as compared to control group ($P < 0.05$). However, the increasing of LPO levels were not in a significant manner in AMD group when compared to control group ($P > 0.05$). Besides, administration of Vit U decreased LPO and PC levels in a significant manner in AMD group ($P < 0.05$). Decreased GSH levels were found to be increased insignificantly in AMD + Vit U as we compared to AMD group ($P > 0.05$) (Table 2).

Liver LDH, MPO and XO activities were increased and PON1 activity was decreased in AMD group in a significant manner as compared to control group ($P < 0.005$ and $P < 0.05$).

Table 4. The liver arginase, Na^+/K^+-ATPase, prolidase and DT-Diaphorase activities of all groups

Groups	Arginase (μmol urea/mg protein)*	Na^+/K^+- ATPase (nmol Pi/ mgproteinxh)*	Prolidase (U/g protein)*	DT-Diaphorase (μmol/min mg protein)*
Control	469.33 ± 20.81	2.50 ± 0.56	968.18 ± 374.77	179.75 ± 43.54
Control + Vit U	489.08 ± 290.05[a]	1.69 ± 0.43[a]	973.67 ± 571.86[a]	329.02 ± 71.55[c]
AMD	529.00 ± 134.56[a]	1.30 ± 0.52[c]	1884.06 ± 670.39[c]	240.86 ± 14.21[a]
AMD + Vit U	178.56 ± 98.51[b]	4.30 ± 1.05[d]	937.14 ± 480.42[d]	145.13 ± 20.92[d]

*Mean ± SD, [a]p >0.05 *versus* control group, [b]$p < 0.005$ *versus* AMD group, [c]$p < 0.05$ *versus* control group, [d]$p < 0.05$ *versus* AMD group; Na^+/K^+- ATPase: sodium potassium ATPase

When we applied Vit U to AMD group, we determined decreased activities for LDH, MPO, XO and increased activity for PON1 when we compared to AMD group ($P < 0.05$ and $P < 0.005$) (Table 3). The arginase and DTD activities were found to be increased insignificantly (P>0.05) while the increasing activity of prolidase was in a significant manner in AMD group as we compared to control group ($P < 0.05$). In addition to this, Na^+/K^+-ATPase activity was also found to be significantly decreased in AMD group as compared to control group ($P < 0.05$). Administration of Vit U reversed these activities in AMD group in a significant manner ($P < 0.005$ and $P < 0.05$) (Table 4).

DISCUSSION

The liver is a vital organ that regulates various biochemical processes and plays an important role in the metabolism of carbohydrates, lipids and proteins [27]. It also participates actively in the elimination and detoxification of drugs and in metabolic homeostasis during which a number of reactive oxygen species (ROS) generating reactions are involved [28]. Thus, its metabolic role and importance make the liver more vulnerable. Finding a solution for drug and chemical induced hepatotoxicity by using safer therapeutic agents became crucial.

Serum aminotransferases and phosphatases are both markers and gold standard enzymes which are usually used for determining the liver injury [29]. Elevated levels of the activities of these enzymes indicate cellular leakage and function loss of cell membrane. Various researchers reported elevated AST, ALT and ALP activities in patients who are treated with AMD [30]. In accordance with these results, we found elevated activities of AST, ALT and ALP in the AMD group. Administration of Vit U to the AMD group significantly decreased these activities. Vit U may have used its cellular repair function while decreasing these activities [7]. We may conclude that Vit U protects the liver against AMD induced injury.

AMD is a phospholipase inhibitor and causes lipid accumulation in the liver. The increased levels of serum lipid profile in AMD treated rats have been shown in literature [31]. In our study, we recorded increased levels of total lipid in AMD group. Besides, Sokmen *et al.* showed that Vit U has a hypolipidemic effect on valproic acid induced hepatotoxicity [9]. Seri *et al.* reported that Vit U has a hypolipidemic metabolism because of initiating an acceleration of fetal excretion of lipid molecules and its acidic metabolites [32]. In the light of these reports, we found decreasing levels of total lipid in AMD+Vit U group.

In this study, AMD treatment produced significantly increase in bilirubin as well as ALP activity. These results demonstrate that the toxin included insult to the liver could also precipitate biliary obstruction resulting in mild hyperbilirubinemia in addition to hepatocellular necrosis. But, administration of Vit U reversed this increase in the AMD group. This reverse effect of Vit U may be associated with protective effect on hepatocellular damage.

Cell culture hepatotoxicity studies done with AMD revealed that AMD decreases GSH levels and increases LPO levels [33]. These levels in AMD toxicity can be explained with this approach: AMD is also called as a cationic amphiphilic drug because of its nature. This nature provides it an elevation of substrates for LPO and also another elevation for ROS that oxidize these substrates. In addition to that GSH protects the membrane lipids from peroxidation and an increase in LPO levels means that the oxidation of reduced GSH by LPO products. In our study, we observed decreased GSH and increased LPO levels in AMD group compared to the control group in parallel to this approach. Administration of Vit U reversed these effects. The effect of Vit U on these levels may be directly elevation of GSH levels by the reversible effect on the sulfhydryl compounds. So elevation of GSH levels by Vit U indicate decreased LPO levels indirectly.

Curtis *et al.* reported that some liver pathologies like alcoholic liver disease, nonalcoholic fatty liver disease and steatohepatitis may involve PC formation [34]. In our study, we observed elevated

PC levels in AMD group. Administration of Vit U reversed this effect in AMD+Vit U group. The reversing effect of Vit U may be explained by this approach. A hydrophilic nature provides an easy interaction of sulfhydryl groups with injured protein structure [35]. Vit U can be dissolved in aqueous media which means it has a hydrophilic nature. By having this advantage, sulfhydryl group of Vit U shows a protective effect by repairing tissue damage.

An increase in serum and tissue LDH activities in AMD toxicity was reported in literature [36]. In our study, an increase in LDH activity was observed in the AMD group. Administration of Vit U decreased these effects in the AMD group. We may suggest that decreasing LDH activity and in turn decreasing levels of ROS are associated with antioxidant property of Vit U.

Increased levels of free radicals activate neutrophils and then activated neutrophils secrete MPO more than ever in the region of injured tissue [37]. PON1 has a thiol group at its active site and Navab *et al.* reported that PON1 synthesis is reduced under in vivo and in vitro oxidative stress conditions [38]. Increased activities of XO mean there is an injury in purine metabolism which may be due to ROS. We measured increased MPO and XO activities and decreased PON1 activity in AMD group. Administration of Vit U reversed these enzyme activities in AMD group. Salim reported that the substances which have sulfhydryl groups bind oxyradicals and this binding can enhance the tissue healing process by removing the harmful agents [39]. So as being a sulphur containing substance, Vit U may have shown its antioxidant effect by reversing MPO, PON1 and XO levels in AMD treated groups.

Abdel-Azeem *et al.* reported that arginase activity increases in chemical-induced hepatotoxicity model [40]. In the present study, we observed elevated arginase activity in the AMD group. In the AMD+Vit U group, we observed that the activity of this enzyme decreased compared to the AMD group. This reductive effect may be associated with antioxidant properties of Vit U.

Decreased Na^+/K^+-ATPase was reported in AMD induced small intestinal toxicity in rats [41]. In this study, a significant decrease was observed in the AMD group. Vit U increased this enzyme activity in AMD group. The reversing effect of Vit U may result due to two reasons. One of them is a probability of indirectly providing thiol group because Vit U is converted to methionine, later cysteine through many steps in vivo [42]. Second reason may be that Vit U fixes the membrane stability property [7].

An increase in prolidase activity was associated with many diseases in various studies including liver diseases [43]. In the present study, a significant increase was observed in the AMD group. However, a significant decrease was determined in the AMD+Vit U group compared to AMD group.

DTD activity was found to be increased in chemical-induced hepatotoxicity models [44]. In the present study, we observed a significant increase of DTD activity in the AMD group. In the AMD+Vit U group, DTD activity was found to be significantly decreased. This may be related to radical scavenging activity of Vit U.

Our results indicate that AMD-induced liver damage is associated with increased oxidative stress. Our results have important implications for the treatment of AMD-induced hepatotoxicity. Sulfhydryl compounds have been described to possess antioxidant, anticancer, antihepatotoxic and neurotropic properties [45]. Sulfur-methyl-methionine (Vit U) is one of the sulfhydryl compounds that have been reported to provide various biological functions including inhibition of free radical production, gastric motility disorder, vasolateral pressure and direct cellular damage [46].

In conclusion, our present results demonstrated the amendatory potential of Vit U against AMD-induced hepatocellular changes, cholestasis, hyperlipidemia and oxidative stress induced by AMD due to its antioxidant, free radical scavenger and membrane-stabilizing properties. The protective effect of Vit U may be due to its sulfhydryl group. This is the first study showing a protective effect of Vit U against AMD – induced hepatotoxicity. In heart patients receiving AMD therapy, our findings may be helpful for the prevention of these side effects of AMD before treatment or other conditions.

Acknowledgement: *This study was supported by The Scientific Research Projects Coordination Unit of Istanbul University. Project Number: 25537.*

REFERENCES

1. B.N. Singh, *Am. J. Cardiol.*, **78**, 41 (1996).
2. M. Nasser, T.R. Larsen, B. Waanbah, I. Sidiqi, P.A. McCullough, *Drug Healthc. Patient Saf.*, **5**, 191 (2013).
3. M. Babatin, S.S. Lee, P.T. Pollak, *Curr. Vasc. Pharmacol.*, **6**, 228 (2008).
4. E. Kapatou, A. Skyrlas, M.G. Agelaki, C. Pantos, T.M. Kolettis, V. Malamou-Mitsi, *J. Physiol. Pharmacol.*, **61**, 671 (2010).
5. J.H. Lewis, F. Mullick, K.G. Ishak, R.C. Ranard, B. Ragsdale, R.M. Perse, E.J. Rusnock, A. Wolke, S.B.

Benjamin, L.B. Seeff, H. J. Zimmerman, *Hum. Pathol.*, **21**, 59 (1990).
6. R.J. Ruch, S. Bandyopadhyay, P. Somani, J.E. Klaunig, *Toxicol. Lett.*, **56**, 117 (1991).
7. I. Racz, E. Paldi, G. Szalai, T. Janda, M. Pal, D. Lasztity, *J. Plant Physiol.*, **165**, 1483 (2008).
8. A.D. Patel, N.K. Prajapati, Review on biochemical importance of vitamin-U. *J. Chem. Pharm. Res.*, **4**, 209 (2012).
9. B.B. Sokmen, S. Tunali, R. Yanardag, *Food Chem. Toxicol.*, **50**, 3562 (2012).
10. M.J. Reasor, C.M. McCloud, T.L. Beard, D.C. Ebert, S. Kacew, M.F. Gardner, K.A. Aldern, K.Y. Hostetler, *Toxicology***, 106**, 139 (1996).
11. S. Reitman, S. Frankel, *Am. J. Clin. Pathol*., **28**, 56 (1957).
12. K. Walter, C. Schutt, in: Methods of Enzymatic Analysis, H.U. Bergmeyer (ed.), Verlag Chemie Weinheim, Academic Press. Inc., New York, USA, 1974; p. 856.
13. C.S. Frings, T.W. Fendley, R.T. Dunn, C.A. Queen, *Clin. Chem*., **18**, 673 (1972).
14. L. Jendrassik, P. Gróf, *Biochem. Z.*, **297**, 81 (1938).
15. E. Beutler, in: A manuel of biochemical methods, Grune and Stratton, New York, USA, 1975; p.112.
16. A. Ledwozyw, J. Michalak, A. Stepien, A. Kadziolka, *Clin. Chim. Acta***, 155**, 275 (1986).
17. R.L. Levine, D. Garland, C.N. Oliver, A. Amici, I. Climent, A.G. Lenz, B.W. Ahn, S. Shaltiel, E.R. Stadtman, *Methods Enzymol*., **186**, 464 (1990).
18. R. Bais, M. Philcox, *Eur. J. Clin. Chem. Clin. Biochem*., **32**, 639 (1994).
19. H. Wei, K. Frankel, *Cancer Res*., **51**, 4443 (1991).
20. C.E. Furlong, R.J. Richter, S.L. Seidel, A.G. Motulsky, *Am. J. Hum. Genet*., **43**, 230 (1988).
21. E.D. Corte, F. Stirpe, *Biochem. J*., **108**, 349 (1968).
22. J.W. Geyer, D. Dabich, *Anal. Biochem*., **39**, 412 (1971).
23. A.S. Ridderstap, S.L. Bonting, *Am. J. Physiol*., **217**, 1721 (1969).
24. F.P. Chinard, *J. Biol. Chem*., **199**, 91 (1952).
25. L. Ernster, L. Danielson, M. Ljunggren, *Biochim. Biophys. Acta*, **58**, 171 (1962).
26. O.H. Lowry, H.J. Rosebrough, A.L. Farr, R.J. Randall, *J. Biol. Chem.*, **193**, 265 (1951).
27. A. Omidi, N. Riahinia, M.B. Montazer Torbati, M.A. Behdani, *Avicenna J. Phytomed*. **4**, 330 (2014).
28. H.S. Wong, J.H. Chen, P.K. Leong, H.E. Leung, W.M. Chan, K.M. Ko, *Molecules***, 19**, 17649 (2014).
29. K. Vijayavel, C. Anbuselvam, B. Ashokkumar, *Biomed. Environ. Sci*., **26**, 295 (2013).
30. T. Merz, S.H. Fuller, *Am. J. Health Syst. Pharm.*, **64**, 1818 (2007).
31. T. Yamamoto, R. Kikkawa, H. Yamada, I. Horii, *J. Toxicol. Sci*., **31**, 49 (2006).
32. K. Seri, T. Matsuo, T. Taniguchi, K. Amemiya, M. Kudo, G. Saito, T. Kato, *Arzneimittelforschung*, **30**, 1694 (1980).
33. A. Ouazzani-Chahdi, A. Elimandi, A. Chabli, J. Spenard, P. Colin, P.S. Haddad, *Can. J. Physiol. Pharmacol*., **85**, 233 (2007).
34. J.M. Curtis, W.S. Hahn, E.K. Long, J.S. Burrill, E.A. Arriaga, D.A. Bernlohr, *Trends Endocrinol. Metab*., **23**, 399 (2012).
35. S.A. Salama, M.S. Al-Harbi, M.S. Abdel-Bakky, H.A. Omar, *Biochimie*, **115**, 203 (2015).
36. P.T. Pollak, S.L. Shafer, *Clin. Pharmacol. Ther*., **75**, 342 (2004).
37. I. Demiryilmaz, E. Sener, N. Cetin, D. Altuner, B. Suleyman, F. Albayrak, F. Akcay, H. Suleyman, *Med. Sci. Monit*., **18**, BR475 (2012).
38. M. Navab, S. Hama-Levy, B.J. Van Lenten, G.C. Fonarow, C.J. Cardinez, L.W. Castellani, M.L. Brennan, A.J. Lusis, A.M. Fogelman, B.N. La Du, *J. Clin. Invest*., **99**, 2005 (1997).
39. A.S. Salim, *J. Pharmaceut. Sci*., **80**, 539 (1991).
40. A.S. Abdel-Azeem, A.M. Hegazy, K.S. Ibrahim, A.R. Farrag, E.M. El-Sayed, *J. Diet. Suppl*., **10**, 195 (2013).
41. K.N. Sirajudeen, R.T. Selvi, Babakrishnan, H. Devaraj, N.S. Devaraj, *Drug Chem. Toxicol*., **23**, 387 (2000).
42. T. Watanebe, S. Ohara, S. Miyazawa, K. Saigenji, K. Hotta, *J. Gastroenterol. Hepatol*., **15**, 45 (2000).
43. G. Zanaboni, K.M. Dyne, A. Rossi, V. Monafo, G. Cetta, *Haematologica***, 9**, 13 (1994).
44. R. Arora, S. Bhushan, R. Kumar, R. Mannan, P. Kaur, A.P. Singh, B. Singh, A.P. Vig, D. Sharma, S. Arora, *Plos One*, **9**, 1 (2014).
45. H. Javed, M.M. Khan, A. Khan, K. Vaibhav, A. Ahmad, G. Khuwaja, M.E. Ahmed, S.S. Raza, M. Ashafaq, R. Tabassum, M.S. Siddiqui, O.M. El-Agnaf, M.M. Safhi, F. Islam, *Brain Res.*, **1389**, 133 (2011).
46. T. Watanabe, S. Ohara, T. Ichikawa, K. Saigenji, K. Hotta, *Dig. Dis. Sci*., **41**, 49 (1996).

Bulgarian Chemical Communications, Volume 51, Issue 1, (pp. 25 – 30) 2019

Degradation of sulfonamides in aqueous solution by an electro/Fe^{2+}/peroxydisulfate process

N. N. Wu[1*], Y. He[1], Y. C. Tan[1], Y. S. Wang[2], W. T. Fang[1]

[1] *School of Municipal and Environmental Engineering, Shenyang Jianzhu University, Shenyang 110168, China*
[2] *China Energy Engineering Corporation limited, Liaoning Institute, Shenyang 110179, China*

Received March 31, 2018; Revised August 30, 2018

Sulfonamide antibiotics with strong toxicity are difficult to degrade in aqueous media. In this study, electrochemical coupled with Fe^{2+} activation of peroxydisulfate (EC/Fe^{2+}/PS) was used to treat sulfamethoxazole (SMX). The removal efficiency of SMX was 89.4%. Acidic medium was favorable to the oxidative degradation of SMX. The best removal efficiency was at pH 3. Fe^{2+} concentration and plate spacing were optimized; too high or too low values were not beneficial to SMX degradation. To a certain extent, separately increasing the PS concentration, Na_2SO_4 concentration and current density could increase the removal rate of SMX. The free radical test showed that $SO_4^{\bullet-}$ played a leading role in acid conditions. It was found that the benzene ring structure of SMX was gradually destroyed. According to the data analysis, the kinetic model of the EC/Fe^{2+}/PS system was $C_t=C_0$ exp $(-8.9921\times10^{-4}$ $[Fe^{2+}]^{0.4383}$ $[PS]^{0.7747}$ $[Na_2SO_4]^{0.3382}$ $[\text{current density}]^{0.4095}$ $[\text{plate spacing}]^{0.8573}$ t). This study shows that the EC/Fe^{2+}/PS system can effectively degrade sulfonamide antibiotics in water. It provides an efficient and environmentally friendly treatment for removing sulfonamides from water.

Keywords: Electrochemistry; Fe^{2+}; Peroxydisulfate; Reaction kinetics; Sulfamethoxazole

INTRODUCTION

In recent years, a new type of pollutants, such as pharmaceuticals and personal care products (PPCPs), has been frequently detected in various kinds of water bodies. PPCPs include human and animal medicines, cosmetics, sunscreens, spices, etc., with the characteristics of low concentration, strong toxicity and difficult removal [1]. Antibiotics are some of the most important pollutants in PPCPs. Sulfonamides (SAs) with chemotherapeutic effects are the earliest and most widely used antibiotics [2]. SAs pollution is mainly harmful to the microorganisms, aquatic animals and human health. Therefore, one of the hot issues in water treatment is how to effectively control and remove SAs.

Advanced oxidation has the advantages of strong reaction speed, high removal efficiency, no secondary pollution. Thus, advanced oxidation methods are widely used in the field of antibiotic treatment [3]. Activated peroxydisulfate (PS) technology is a new advanced oxidation method. Electrochemical technology combined with activated PS is a technology of PS activation based on the introduction of an electric field [4]. In the process, on the one hand, the organic matter is oxidized through the electrochemical reaction and degraded into small molecules. On the other hand, the organic matter is oxidized by strongly active free radicals produced by the activated PS (Eq. (1) and Eq. (2)) [5]. Previous studies have shown that the presence of an electric field activates part of the persulfate and allows the persulfate catalyst to be reused (Eq. (3)) [6]. In the study of electrochemical and persulfate oxidation, Fe^{2+} is usually used as a catalyst. According to the different types of Fe^{2+} production, the process is divided into three types. (i) direct addition of Fe^{2+} catalyzing the decomposition of PS to produce $SO_4^{\bullet-}$. That is followed by the reduction of Fe^{3+} at the cathode to Fe^{2+} for reuse [7]; (ii) Fe^{2+} is added by external Fe^{3+} reduction on the cathode to reproduce Fe^{2+} in the solution [8, 9]; (iii) Fe^{2+} is generated by the Fe electrode as the anode, activating PS to produce $SO_4^{\bullet-}$ [10].

$$S_2O_8^{2-} + Fe^{2+} \rightarrow Fe^{3+} + SO_4^{\bullet-} + SO_4^{2-} \quad (1)$$
$$Fe^{2+} + SO_4^{\bullet-} \rightarrow Fe^{3+} + SO_4^{2-} \quad (2)$$
$$Fe^{3+} + e^- \rightarrow Fe^{2+} \quad (3)$$

At present, applying the electrochemical synergistic persulfate technology (EC/Fe^{2+}/PS) to treat sulfa antibiotics has not been reported. Sulfamethoxazole (SMX) has been frequently detected in the environment. The structural formula of the SMX is as follows:

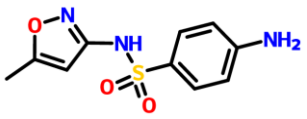

Formula 1.

* To whom all correspondence should be sent:
E-mail: nanawu0816@xmu.edu.cn

In this study, EC/Fe^{2+}/PS method was used to treat SMX in water. The effect and its impact factors were investigated. The reaction kinetics was also analyzed.

EXPERIMENTAL

SMX ($C_{10}H_{11}N_3O_3S$), PS ($Na_2S_2O_8$), 1, 2-naphthoquinone-4-sulfonic acid sodium salt ($C_{10}H_5NaO_5S$) and $FeSO_4 \cdot 7H_2O$ were purchased from Tianjin Kemiou Chemical Reagent Co., Ltd. All reagents were analytical grade. The electrochemical reactor was a glass beaker with an effective volume of 2000 mL. The anode was made of Ti/IrO_2-RuO_2-TiO_2 coated with ruthenium-titanium-iridium. The cathode was made of a stainless steel plate. The electrode plate size was 20 cm × 6 cm × 0.3 cm. Electric stirring method was adopted.

The initial concentration of SMX was 10 mg/L (40 μM). The removal of SMX was monitored at different conditions: PS, Fe^{2+}/PS, EC, EC/PS, and EC/Fe^{2+}/PS. The impact factors of the EC/Fe^{2+}/PS system were studied, such as SMX initial concentration, initial pH, Fe^{2+} concentration, PS concentration, electrolyte concentration, current density and plate spacing. The effect on PS residual rate was also studied. Excess *tert*-butanol and methanol were added to determine the types of free radicals [11]. In order to analyze the reaction product, samples were taken after a certain reaction time. Then the absorbance of the solution in a certain wavelength range was measured.

The concentration of SMX was determined by spectrophotometry using sodium 1, 2-naphthoquinone-4-sulfonate as the chemical derivative chromogenic reagent [12]. Removal efficiency was calculated as follows: removal efficiency (%) = $((C_0-C_t)/C_0) \times 100$, where C_0 and C_t are the concentrations of SMX at time 0 and t, respectively. The concentration of PS was determined using an iodometric titration method.

RESULTS AND DISCUSSION

Degradation efficiency of SMX in the EC/Fe^{2+}/PS process

The degradation of SMX was investigated under different conditions of PS, Fe^{2+}/PS, EC, EC/PS, EC/Fe^{2+}/PS. The results are shown in Fig. 1. As can be seen, SMX was hardly removed in the PS system. Comparatively, it was found that 23.28% of SMX was removed after 5 min of the reaction in the Fe^{2+}/PS system, but the removal efficiency did not further change. This suggested that Fe^{2+} could activate PS to produce $SO_4^{\bullet-}$, which would degrade the SMX. However, the degradation of SMX only occurred in the first few minutes of the reaction. The reason may be that Fe^{2+} was consumed in the reaction, indicated by the color change of the solution. No activating agent continued to activate PS in the system. In the EC system, the degradation efficiency of SMX was 50.45% after 60 min of reaction. The removal efficiency of SMX increased to 70.38% when PS was added to the system. This indicated that the electron transfer could activate PS to produce $SO_4^{\bullet-}$, which oxidized SMX [13].

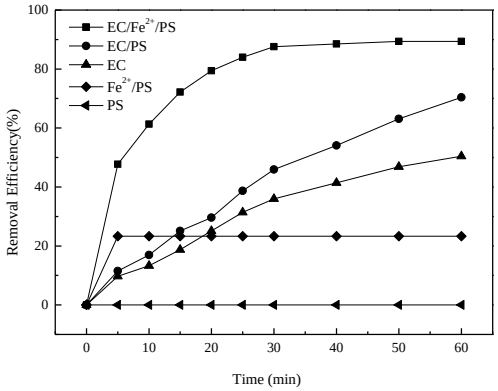

Fig. 1. Removal efficiency of SMX in the different systems

In the EC/Fe^{2+}/PS system, the degradation efficiency of SMX was 89.4%, which was higher than the sum of EC system (50.45%) and Fe^{2+}/PS system (23.28%). That suggested a synergistic effect between EC and Fe^{2+}/PS [7].

Effect of SMX initial concentration, initial pH, Fe^{2+} concentration and PS concentration

As can be seen from Fig. 2 (a), with the increase in SMX concentration, the degradation efficiency gradually decreased. When the concentration of PS was constant (2.5 mM), the number of active radicals generated by activation was limited (2.5 mM). When the concentration of SMX increased from 10 mg/L to 30 mg/L, a larger number of intermediate products were produced by oxidative degradation. Then the further degradation of intermediate products would consume the radicals. They would compete with the SMX, reducing the degradation efficiency of SMX.

The removal efficiency of SMX showed a downward trend as the initial pH value increased (Fig. 2 (b)). The highest degradation efficiency was at pH 3, reaching 87.59%. SMX removal efficiency was maintained at a high level when pH values were 3, 5, 7, 9. It was shown that the pH of the solution decreased to neutrality with the progress of the reaction [14]. This indicated that the PS activation system could apply to a wide range of initial pH values. At pH 11 the removal rate rapidly decreased. The remaining content of PS gradually increased as the pH increased from 3 to 11. That suggested that as the pH increased, less PS was decomposed in the system. The reason may be that in addition to the activation effect of Fe^{2+}, the PS was also catalyzed by acid to accelerate the $SO_4^{\bullet-}$ formation at low pH.

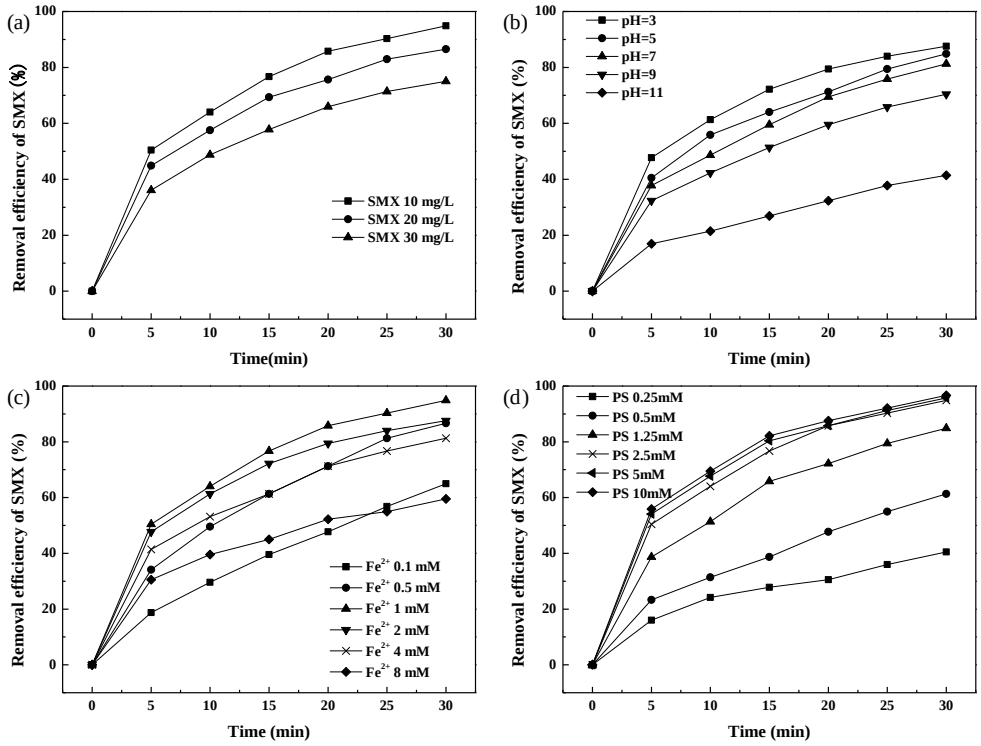

Fig. 2. Effect of the SMX initial concentration (a), initial pH (b), Fe^{2+} concentration (c) and PS concentration (d) on SMX removal efficiency in the EC/Fe^{2+}/PS system

A higher pH value was unfavorable for PS decomposition. Precipitation of Fe^{3+} would occur at the higher pH. That would weaken the reduction reaction of Fe^{3+}, dropping the generation rate of $SO_4^{\bullet-}$. Meanwhile, $SO_4^{\bullet-}$ would react with OH^- at the higher pH. Under alkaline conditions, the oxidation-reduction potential of $^{\bullet}OH$ (E_0 = 2.3) was lower than that of $SO_4^{\bullet-}$. $SO_4^{\bullet-}$ and $^{\bullet}OH$ also reacted and thus some active free radicals were consumed in the system with a higher pH. This suggested that at higher pH value the catalyst activity was reduced and, the concentration of active radicals in the solution decreased.

When the concentration of Fe^{2+} increased from 0.1 mM to 1.0 mM, the removal efficiency of SMX increased from 64.95% to 94.84% (Fig. 2 (c)). However, the removal rate of SMX showed a downward trend when the Fe^{2+} concentration changed from 2 mM to 8 mM. The remaining content of PS decreased as the concentration of Fe^{2+} increased. That implied that the catalytic reaction rate increased and the decomposition of PS was accelerated. Therefore, as the initial Fe^{2+} concentration increased from 0.1 mM to 1 mM, the removal rate of SMX significantly increased. When the concentration of Fe^{2+} was higher, the color of the reaction solution was deepened to brown. This may be because excessive Fe^{2+} was oxidized to Fe^{3+} by consuming sulfate radicals. Besides that a high concentration of $SO_4^{\bullet-}$ would undergo a self-quenching reaction, leading to inefficient use of $SO_4^{\bullet-}$. These results suggested that an appropriate amount of Fe^{2+} could promote SMX degradation, while excessive Fe^{2+} could inhibit SMX degradation. This conclusion was consistent with previous reports [15].

As the PS concentration increased from 0.25 mM to 2.5 mM, the SMX removal efficiency rapidly increased (Fig. 2 (d)). When the PS concentration went on increasing, the SMX removal efficiency little changed. It was found that increasing PS concentration decreased its own residual rate. PS residual rate was defined as (C_{ps-t}/C_{ps-0}), where C_{ps-t} and C_{ps-0} were the concentrations of PS at time t and 0, respectively. The reason may be that when the PS concentration was low, the probability of collision with the Fe^{2+} was relatively low. With the increase in PS concentration, the concentration of $SO_4^{\bullet-}$ gradually increased in the system. When the PS concentration reached to a certain range, increasing the PS concentration could reduce the PS residual rate, but the SMX oxidation rate was not obviously changed. This may be because the high concentration of PS could quickly produce a large number of free radicals. In addition to the self-quenching reactions, radicals also reacted with PS. Large amounts of PS were inefficiently degraded. The utilization efficiency of

PS and $SO_4^{\bullet-}$ was very low when PS was added in excess.

Effect of Na_2SO_4 concentration, current density and plate spacing

As shown in Fig. 3 (a), when Na_2SO_4 concentration was 0 mM, the removal efficiency of SMX was very low. When Na_2SO_4 concentration was 6 mM, the removal efficiency of SMX was obviously improved. When the concentration of Na_2SO_4 went on increasing, the removal efficiency of SMX gradually increased. When the Na_2SO_4 concentration was greater than 25 mM, the removal efficiency of SMX slightly increased.

As the current density increased, the removal efficiency of SMX also increased (Fig. 3 (b)). The reason may be that the electrochemical reaction between the electrodes would be more intense with the greater current density. Enhancement of electron transfer could promote the production of $SO_4^{\bullet-}$ by PS and increase the degradation rate of SMX [16].

The removal rate of SMX firstly increased and then decreased with the increase of plate spacing (Fig. 3 (c)). The removal rate reached 94.84% when the spacing reached 9 cm. After that, the removal rate showed a downward trend. The reason may be that the solution resistance became larger when the spacing increased to a certain value. Then the mass transfer efficiency decreased, leading to the downfall of the reaction rate [17].

Identification of oxidizing species and reaction products

The results suggest that reactive oxidizing species are produced in the EC/Fe^{2+}/PS system, leading to the enhanced degradation of SMX. To identify the generation of $^{\bullet}OH$ or $SO_4^{\bullet-}$, radical quenchers of *tert*-butanol and methanol were added to the system. *Tert*-butanol is an effective quencher of $^{\bullet}OH$, while methanol is a good quencher of both $SO_4^{\bullet-}$ and $^{\bullet}OH$ [18, 19].

It can be seen from Fig. 4 (a) that adding a quencher to the EC/Fe^{2+}/PS system has a significant effect on SMX degradation. When no quencher was added to the system, the removal rate of SMX was 94.84% in 30 min. The removal rate of SMX decreased to 83.06% as an excess of *tert*-butanol was added. This indicated the presence of $^{\bullet}OH$ in the system and played a role in the oxidation of SMX. The removal rate of SMX was 43.21% when adding excess methanol. The inhibition of SMX oxidation by methanol was much stronger than that by *tert*-butanol. These results indicated the presence of $SO_4^{\bullet-}$ in the system and $SO_4^{\bullet-}$ played a leading role in the process of SMX. The solution had a distinct absorption peak at a wavelength of 256 nm (benzene ring B) before the reaction (Fig. 4 (b)). The absorption peak decreased until it disappeared with the reaction. This indicated that SMX was oxidized and the benzene ring structure was gradually destroyed.

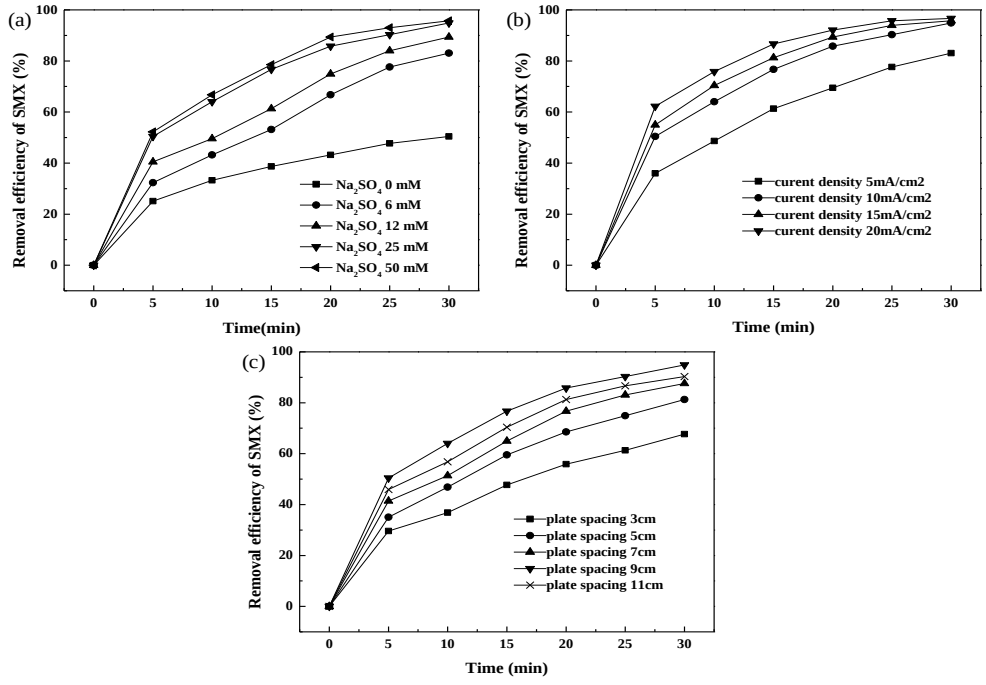

Fig. 3. Effect of Na_2SO_4 concentration (a), current density (b) and plate spacing (c) on SMX removal efficiency in the EC/Fe^{2+}/PS system

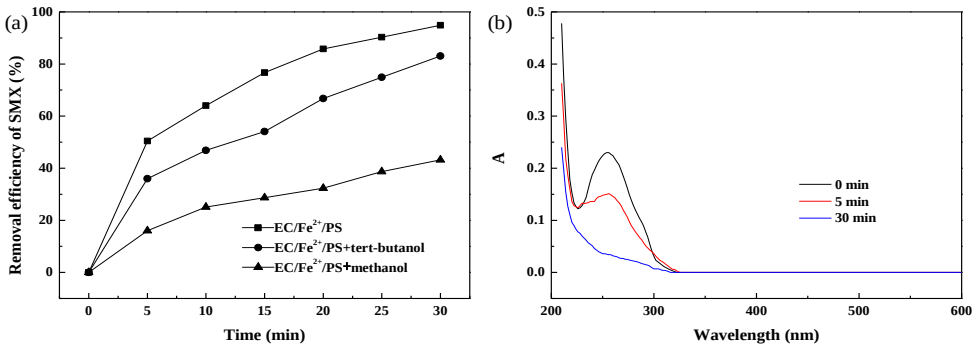

Fig. 4. Effect of quenchers on SMX degradation (a) and UV-vis spectrum during the reaction (b) in the EC/Fe^{2+}/PS system

Reaction kinetics of the EC/Fe^{2+}/PS system

The first-order kinetic equation was best to fit the reaction kinetics of the EC/Fe^{2+}/PS system. The reaction rate constant k is affected by several factors, such as [Fe^{2+}], [PS], [Na_2SO_4], [current density] and [plate spacing] at certain SMX concentration and pH conditions. Then the apparent correlation could be established:

$k=\mu[Fe^{2+}]^a\ [PS]^b\ [Na_2SO_4]^c\ [\text{current density}]^d\ [\text{plate spacing}]^e$

where μ, a, b, c, d, e are constants. In order to obtain these constants, the above results were subjected to statistical analysis. Then the reaction rate constant of k can be expressed as:

$k=8.9921\times10^{-4}[Fe^{2+}]^{0.4383}[PS]^{0.7747}[Na_2SO_4]^{0.3382}\ [\text{current density}]^{0.4095}[\text{plate spacing}]^{0.8573}$

So, the kinetic equation of SMX degradation in EC/Fe^{2+}/PS system can be expressed as:

$C_t=C_0\ \exp\ (-8.9921\times10^{-4}\ [Fe^{2+}]^{0.4383}\ [PS]^{0.7747}\ [Na_2SO_4]^{0.3382}\ [\text{current density}]^{0.4095}\ [\text{plate spacing}]^{0.8573}\ t)$.

From the above equation, the order of factors affecting the reaction rate is as follows: plate spacing > PS concentration > Fe^{2+} concentration > current density > Na_2SO_4 concentration under certain reaction conditions. Comparison between kinetic model and experimental data shows that the actual value was well fitted to this dynamic model.

CONCLUSIONS

The main results of this study showed that:

1. The EC/Fe^{2+}/PS system could effectively degrade SMX in aqueous medium. The acidic conditions were favorable to SMX degradation. The optimal values of Fe^{2+} concentration and plate spacing were 1 mM and 9 cm, respectively. When the values were higher than the optimal values, the removal efficiency decreased and the processing cost increased. The removal efficiency increased with the separate increase in PS concentration, Na_2SO_4 concentration and current density.

2. The results of the free radical test showed that $SO_4^{\bullet-}$ played a leading role in the EC/Fe^{2+}/PS system. The benzene ring structure of SMX was destroyed in the reaction. The reaction kinetic equation was obtained:

$C_t=C_0\ \exp\ (-8.9921\times10^{-4}\ [Fe^{2+}]^{0.4383}\ [PS]^{0.7747}\ [Na_2SO_4]^{0.3382}\ [\text{current density}]^{0.4095}\ [\text{plate spacing}]^{0.8573}\ t)$.

These results show that sulfonamide antibiotics could be effectively oxidized in the EC/Fe^{2+}/PS system. This study provides an efficient and environmentally friendly treatment for removing sulfonamides in water.

Acknowledgement: *This work was financially supported by Doctoral Research Start Fund Project of Liaoning Province (201501070), Department of Education Scientific Research General Project of Liaoning Province (L2015451), and Scientific Research Project of Shenyang Jianzhu University (2017023). We would like to thank Timothy R. Filley for language correction.*

REFERENCES

1. E. N. Evgenidou, I. K. Konstantinou, D. A. Lambropoulou, *Sci. Total Environ.*, **505**, 920 (2015).
2. Z. Q. Ye, H. S. Weinberg, *Anal. Chem.*, **79**, 1140 (2007).
3. F. S. Souza, S. V. Da, C. K. Rosin, L. Hainzenreder, A. Arenzon, *Environ. Technol.*, **39**, 552 (2017).
4. K. P. de Amorim, L. L. Ronmaldo, L. S. Andrade, *Sep. Purif. Technol.*, **120**, 323 (2013).
5. Y. F. Ji, C. Fen'onato, A. Salvador, X. Yang, J. M. Chovelon, *Sci. Total Environ.*, **472**, 804 (2014).
6. Y. R. Wang, W. Chu, *Water Res.*, **45**, 3886 (2011).
7. J. Wu, H. Zhang, J. Qiu, *J. Hazard. Mater.*, **215-216**, 140 (2012).
8. H. Lin, H. Zhang, L. Hou, *J. Hazard. Mater.*, **276**, 188 (2014).

A. Ledjeri, I. Yahiaoui, F. Aissani-Benissad, *J. Environ. Manage.*, **184**, 249 (2016).

9. S. Yuan, P. Liao, A. N. Alshawabkeh, *Environ. Sci. Technol.*, **48**, 656 (2014).
10. Y. Zhou, J. Jiang, Y. Gao, J. Ma, S. Y. Pang, J. Li, X. T. Lu, L. P. Yuan, *Environ. Sci. Technol.*, **49**, 12948 (2015).
11. Q. Li, Z. Yang, *Chinese J. Anal. Chem.*, **1**, 84 (2006).
12. P. C. Xie, J. Ma, W. Liu, J. Zou, S. Y. Yue, X. C. Li, M. R. Wiesner, J. Y. Fang, *Water Res.*, **69**, 228 (2015).
13. M. Ahmad, A. L. Teel, R. J. Watts, *Environ. Sci. Technol.*, **47**, 5868 (2013).
14. H. V. Lutze, S. Bircher, I. Rapp, N. Kerlin, R. Bakkour, M. Geisler, C. von Sonntag, T. C. Schmidt, *Environ. Sci. Technol.*, **49**, 1678 (2015).
15. H. Zhang, J. Wu, Z. Wang, D. Zhang, *J. Chem. Technol. Biot.*, **85**, 1440 (2010).
16. D. Molognoni, S. Chiarolla, D. Cecconet, A. Callegari, A. G. Capodaglio, *Water Sci. Technol.*, doi: 10.2166/wst.2017.532 (2017).
17. R. C. Zhang, P. Z. Sun, T. H. Boyer, L. Zhao, C. H. Huang, *Environ. Sci. Technol.*, **49**, 3060 (2015).
18. M. M. Huber, S. Korhonen, T. A. Ternes, V. U. Gunten, *Water Res.*, **39**, 3610 (2005).

Bulgarian Chemical Communications, Volume 51, Issue 1, (pp. 31 – 37) 2019

Anticorrosive potential of ethanol extract of *Delonix elata* for mild steel in 0.5 M H_2SO_4 - a green approach

D. Mahalakshmi[1a], C. B. N. Unnisa[1], V. Hemapriya[1], E. P. Subramaniam[2], S. M. Roopan[3], S. Chitra[1], I.- M. Chung[4a], S.-H. Kim[4], M. Prabakaran[4*]

[1]*Department of Chemistry, PSGR Krishnammal College for women, Coimbatore, India*
[2]*Department of Chemistry, Coimbatore institute of Technology, Coimbatore, India*
[3]*Chemistry of Heterocycles & Natural Product Research Laboratory, Department of Chemistry, School of Advanced Sciences, VIT University, Vellore, India*
[4]*Department of Crop Science, College of Sanghur Life Science, Konkuk University, Seoul 05029, South Korea*

Received July 16, 2018; Revised August 30, 2018

The phytochemical constituents of *Delonix elata*, characterized by gas chromatography-mass spectroscopy (GC-MS) and their inhibitive action on mild steel in 0.5 M H_2SO_4 medium, are discussed in the present study. The impedance and polarization techniques showed a similar trend as regards concentration and inhibition efficiency. The optimized concentration of *D. elata* (10 % v/v) resulted in high inhibition efficiency (85.96%). To confirm the adsorption of inhibitors on the mild steel surface, morphological studies of the latter were carried out by means of scanning electron microscopy (SEM), energy dispersive spectroscopy (EDX) and atomic force microscopy (AFM) techniques for both uninhibited and inhibited specimens. The electrochemical measurements and surface studies were well associated with each other.

Keywords: *Delonix elata*, GC-MS, Inhibitive action, SEM-EDX-AFM

INTRODUCTION

The supreme properties of metals and alloys have gained vast attention from earlier days. Among the existing metals, low cost and remarkable functional properties of iron and its alloys had made it to enter the construction fields and industrial sectors [1]. The extent of its usage in industrial sectors without proper remedial measures leads to huge economical loss. In specific, mild steel is extensively used in various fields such as construction, automobile, petroleum and oil industries due to its low cost and excellent mechanical strength [2, 3]. When such metal is subjected to pickling, cleaning and descaling processes [4] in presence of mineral acids like hydrochloric acid and sulphuric acid, undoubtedly base metal dissolution takes place in addition to the removal of oxide coatings and corrosion products. Such deterioration of metals is a serious problem which should be taken care of to find a solution to minimise the loss where complete elimination is impossible. As a remedy, usage of inhibitors is a low-cost method which can slow down or prevent the metal loss when added in acid solutions [5]. In this regard, organic inhibitors have gained long-term attention in minimising the corrosion rate to the maximum extent due to their heteroatoms such as S, O and N and their π electron density, which could behave as adsorption centres. Though the organic compounds are acknowledged with good inhibition efficiency, their cost, synthetic methodology and toxicity limit their usage [6]. Thus, recent researches are turning towards exploring the green and eco-friendly corrosion inhibitors originating from plant sources. The plant extracts, boosted with phytochemical constituents such as amino acids, terpenoids, flavonoids, alkaloids, polyphenols, tannins, etc., along with their simple preparative methods, low cost, easy availability and renewable resources, are environmentally acceptable ones [7]. To strengthen the platform of green inhibitors, lot of research work has been carried out by various researchers using different plant sources as corrosion reducers for different metals in various aggressive media, which is evident from the reports documented using extracts of watermelon rind [8], *Justicia gendarussa* [9], *Ligularia fischeri* [10], *Phyllanthus amarus*, *Oxandra asbeckii*, *Phyllanthus amarus* [11], *Zenthoxylum alatum* [12], *Tragia plukenetii* [13], *Tripleurospermum auriculatum*, *Teucrium oliverianum* [14], *Silybum marianum* [15], *Egyptian licorice* [16], *Ginkgo biloba* [17], etc. In order to highlight the potential of green inhibitors, in the present work *Delonix elata* was chosen, a hermaphroditic, deciduous tree originating from Caesalpinioideae family. Its leaves and barks are widely used in Siddha and Ayurveda. It is known for its anti-inflammatory [18], anti-rheumatic, anti-microbial [19] and antioxidant [20] activities. As reported by Singh *et al*. [21], leaf extracts of

* To whom all correspondence should be sent:
E-mail: prabakarannitt@gmail.com; prabakaran@konkuk.ac.kr
[a]D. Mahalakshmi and I.-M. Chung have equally contributed to this work.

Delonix elata were found to possess active ingredients like tannins, saponins, quinones, terpenoids, steroids, flavonoids, phenols, alkaloids and coumarins. Its active ingredients rich in heteroatoms and aromaticity are expected to provide good protection for metals. In order to check this expectation, an ethanol extract of leaves of *Delonix elata* was prepared to study its inhibition efficiency for mild steel in 0.5 M H_2SO_4 medium using electrochemical and non-electrochemical techniques. Surface characterization studies were made by SEM, EDX, and AFM analysis and are discussed in the forthcoming sections.

EXPERIMENTAL METHODS

The mild steel samples were machined in to appropriate dimensions of 3 × 1 × 1 cm followed by pickling with hydrochloric acid to remove impurities. The samples were abraded with various grades of emery sheets for polished surface and stored in a desiccator for further usage. The electrolytic solution of 0.5 M H_2SO_4 was prepared with double distilled water. The leaves of *Delonix elata* were collected, washed several times with double distilled water, shade dried and finally made into powder. About 1 g of powder was allowed to reflux with 100 ml of ethanol for 3 h. Later the cooled extract was filtered and refrigerated for further use.

Gas chromatography-mass spectroscopy (GC-MS)

The required amount of sample was diluted with ethanol and was analyzed by GC-MS using Perkin Elmer Clarus 60 instrument equipped with a DB 5-MS capillary standard non-polar column (30 m × 0.25 i.d., film thickness 0.25 µm). An electron ionization system with 70 eV ionization energy was used for the detection of components along with helium gas (99.999 % purity), and operating parameters like sample volume (1 µL), delay time (2 min) and running time (40 min).

Electrochemical measurements

An electrochemical work station, IVIUM compactstat potentiostat/galvanostat was used. The measurements were carried out in a three-electrode cell assembly comprising a mild steel rod of 0.785 cm^2 exposure, platinum and calomel electrode as working, counter and reference electrodes. The open circuit potential (OCP) was measured after stabilizing the system. An electrochemical impedance spectroscopy (EIS) test was carried out in the frequency range of 10 KHz to 0.01 Hz using superimposed sine wave amplitude of 10 mV. From the plots obtained for the selected concentrations of the inhibitors (2, 6 and 10 % v/v), impedance parameters like charge transfer resistance (R_{ct}) and constant phase element (CPE) for uninhibited and extract-inhibited medium were sorted from which inhibition efficiency was calculated using the equation below:

$$\text{Inhibition efficiency}(\%) = \frac{R_{ct(inh)} - R_{ct(Blank)}}{R_{ct(inh)}} \times 100 \quad (1)$$

where, $R_{ct(inh)}$ and $R_{ct(Blank)}$ are the charge transfer resistances of inhibited and uninhibited samples, respectively. Followed by impedance measurements, potentiodynamic polarization measurements were carried out by applying a potential range of -200 mV to +200 mV at a scan rate of 1 mV/sec under similar experimental set up. From the resulting Tafel plots, polarization parameters like corrosion current (I_{corr}), corrosion potential (E_{corr}) and Tafel slopes (b_a and b_c) were drawn:

$$\text{Inhibition effeciency}(\%) = \frac{I_{corr(blank)} - I_{corr(inh)}}{I_{corr(blank)}} \times 100 \quad (2)$$

where, $I_{corr(blank)}$ and $I_{corr(inh)}$ correspond to the corrosion current of uninhibited and inhibited medium, respectively.

Surface analysis (SEM-EDX and AFM)

The extent of a metal to undergo corrosion in uninhibited and inhibited (10 % v/v) medium can be additionally evidenced by SEM analysis. The elemental composition of the samples can be retrieved from the EDX analysis. SEM analysis coupled with EDX was done with a biomedical research microscope (Mumbai, India). Multimode scanning probe microscope (NTMDT, NTEGRA prima, Russia) with cantilever length, width and thickness of 135, 30 and 2 µm, respectively and 0.35-6.06 N/m force constant assisted with NOVA software was used to record the AFM images for both inhibited and uninhibited samples.

RESULTS AND DISCUSSION

Gas chromatography-mass spectroscopy (GC-MS)

Fig. 1 shows the GC-MS spectra representing the phytochemical constituents of the ethanol extract of *Delonix elata.* Fig. 2a shows the structure of 9 major peaks (based on their retention times) corresponding to the phytoconstituents: a) propane-1-1-3-triethoxy (RT=5.40), b) DL-homocystine (RT = 7.64), c) melezitose (RT=10.76), d) l-(+)-ascorbic acid 2,6-dihexadecanoate (RT=21.48), e) 1,2,3,4-tetrahydro-N-(1-methylethyl)-N-(phenylmethyl) 2-naphthalenamine, (RT=24.29), f) L-ascorbic acid-6-octadecanoate (RT=25.2), g) 1-vinyl-1-hydroxycholestane (RT=30.18), h) 2-(3-acetoxy-4,4,14-trimethylandrost-8-en-17-yl) propanoic acid

(RT=33.55) and i) 9-hexadecenoic acid eicosyl ester (Z) (RT=35.95). On the other hand, the presence of smaller peaks could be due to small quantities of disintegrated major components. Fig. 2b shows the major components of the extract. Similarly, compounds elicited at lower retention time could be low-polar plant constituents. It is worth noting that all 9 compounds shown in Fig. 2a are a mixture of organic moieties containing O, N or π-electrons [22], electron-rich multiple bonds [23] which is a necessary criterion for the present discussion. Since the retention times of the majority of the compounds are close to each other and owing to the complex hetero systems, it is difficult to reveal individual actions rendered by the phytoconstituents. Thus, the ethanol extract was used as such for the forthcoming studies.

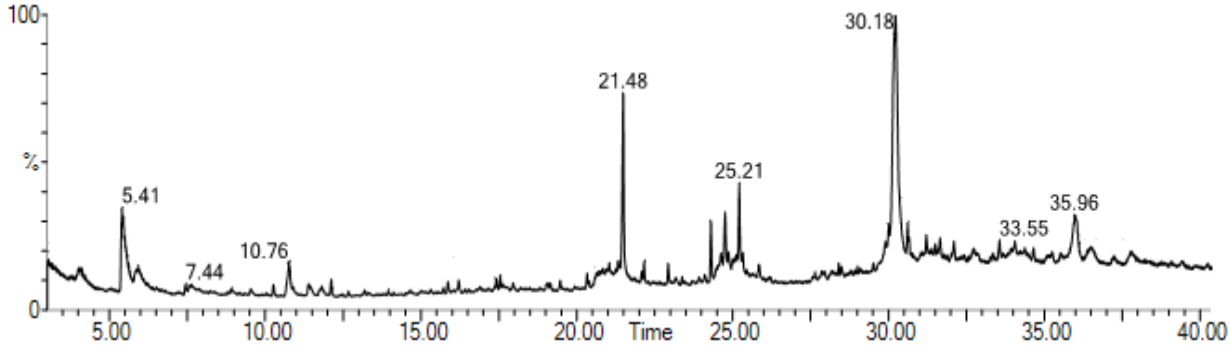

Fig. 1. GC-MS chromatogram of *Delonix elata.*

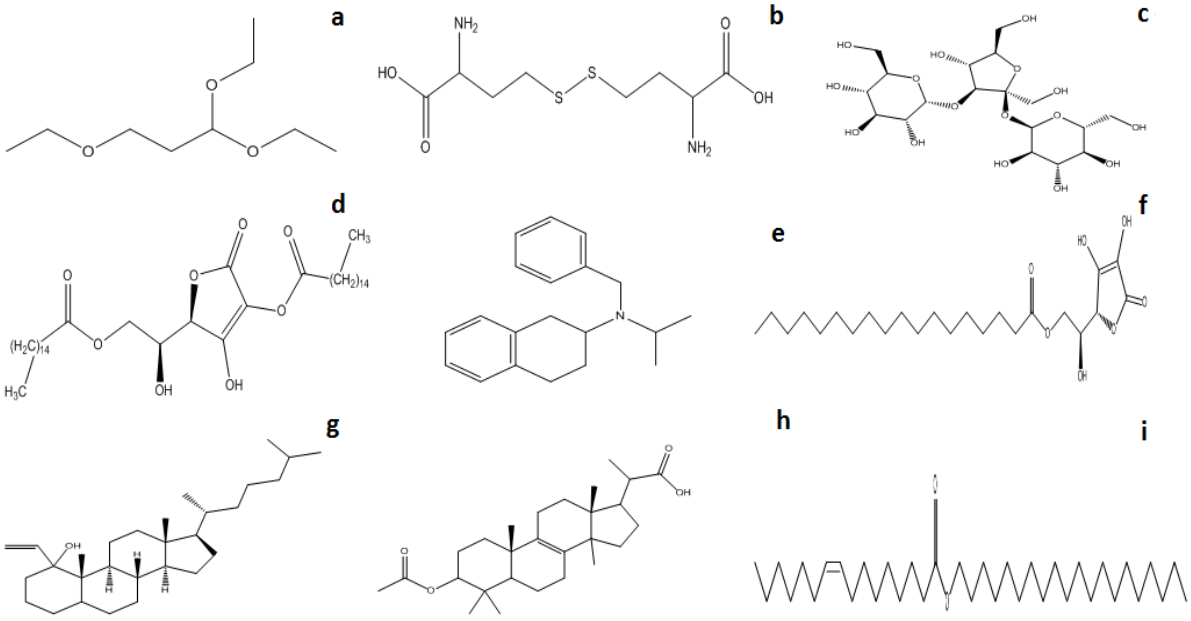

Fig. 2a) Structures of the major phytoconstituents elucidated by GC-MS.

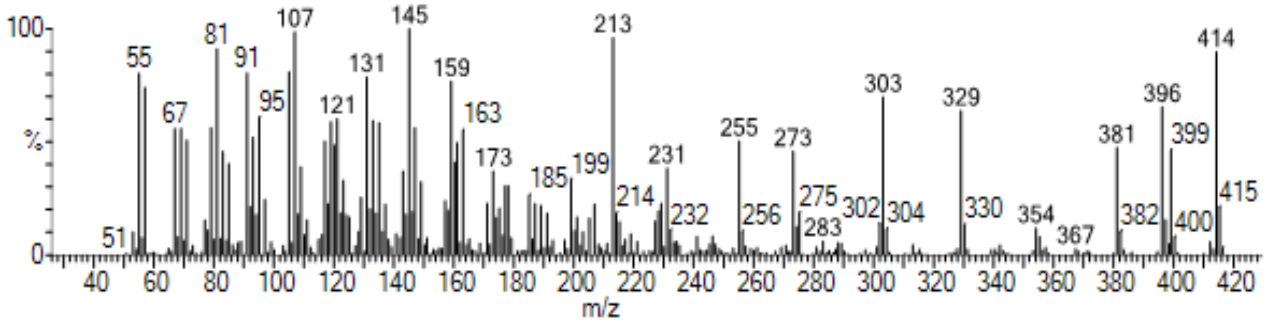

Fig. 2b. Mass spectrum of 1-vinyl-1-hydroxycholestane.

Electrochemical impedance spectroscopy (EIS)

The electrochemical response and reactivity of metal specimens in 0.5 M H_2SO_4 medium was measured after attaining steady-state potential, represented in the form of open circuit potential (OCP). Fig. 3 shows the OCP image of selected concentrations (2, 6, 10 % v/v) of the inhibited test medium.

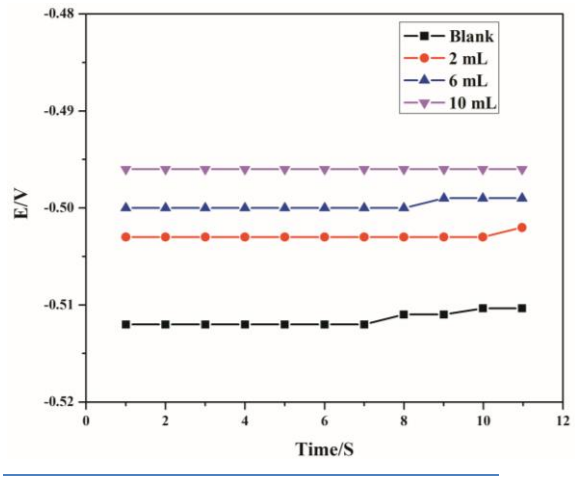

Fig. 3. OCP measurement of the corrosion of mild steel in 0.5 M H_2SO_4.

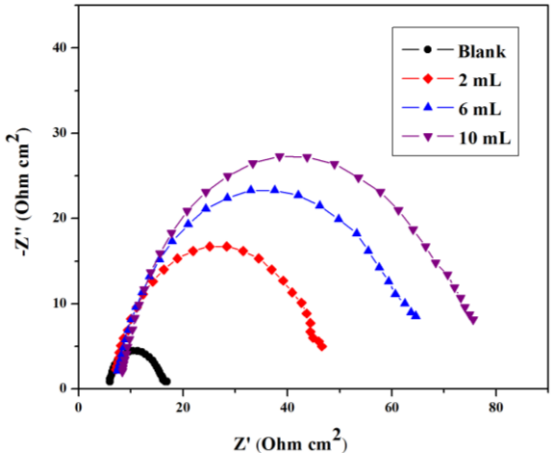

Fig. 4. Nyquist plots for the corrosion of mild steel in 0.5 M H_2SO_4.

From the OCP image, the adsorption of inhibitors on the mild steel surface is evidenced by the shift towards negative potential in presence of inhibitors with reference to uninhibited medium [24, 25]. The EIS technique is a most powerful tool to understand the reactions occurring at the electrochemical interface leading to the adsorption of inhibitor molecules [26]. The EIS measurements for the selected concentrations of inhibitors are reflected in the form of Nyquist plots, as displayed in Fig. 4. The impedance response for the uninhibited and inhibited systems is exhibited in the form of single depressed capacitive loops owing to the fact that the corrosion process on the mild steel surface is controlled by charge transfer [27]. However, the imperfection in semicircle would be attributed to the inhomogeneity or roughness of the metal surface. On increasing the concentration of the ethanol extract of *Delonix elata* as 2, 6, 10 % v/v, a successive increase in the diameter of the semicircles [28] was found compared to that of uninhibited test medium thereby retaining the shape of the loops [29], suggesting a similar mechanism. This could be correlated with the charge transfer resistance (R_{ct}) values displayed in Table 1.

Table 1. AC-impedance parameters for corrosion of mild steel for selected concentrations of the inhibitors in 0.5 M H_2SO_4.

C % (v/v)	R_{ct} (ohm cm^2)	CPE ($\mu F/cm^2$)	IE (%)
Blank	10.12	22.4	-
2	46.98	14.8	78.46
6	63.90	13.7	84.16
10	72.09	12.7	85.96

Table 2. Corrosion parameters for corrosion of mild steel with selected concentrations of the inhibitors in 0.5 M H_2SO_4 by potentiodynamic polarization method.

C % (v/v)	Tafel slopes (mV/dec)		$-E_{corr}$ (mV)	I_{corr} ($\mu A/cm^2$)	IE (%)
	b_a	b_c			
Blank	83	139	471	850	-
2	78	145	489.5	477	43.88
6	71	168	482.1	311	63.41
10	66	185	478.8	268	68.47

The increased R_{ct} values from 10.12 Ohm cm^2 (Blank) to 72.09 Ohm cm^2 (10 % v/v) reveal the formation of a layer on the metal surface by the phytoconstituents of the added extract thereby retarding the dissolution of metal in acid medium. On the other hand, decreased constant phase element (CPE) from 22.4 (uninhibited) to 12.7 $\mu F/cm^2$ (inhibited) due to the decrease in local di-electric constant or replacement of already adsorbed ions by the added inhibitor molecules or decreased thickness of double layer [30, 31] also suggested the formation of a barrier at the metal/solution interface. The constant phase element (CPE) can be determined with the help of the representation below where the frequency at which the imaginary component of the impedance is considered maximum:

$$Z_{(CPE)} = \frac{1}{Q.(j\omega)^n} \quad (3)$$

where $Z_{(CPE)}$ is the impedance of CPE, Q is a proportional factor, ω is the angular frequency and n is a factor which takes values between 0 and 1 indicating the inhibitor adsorption. The obtained

experimental data were fitted into Randle's equivalent circuit, as displayed in Fig. 5, to deduce the electrochemical parameters. The increased pattern of R_{ct} values obtained on addition of the extract clearly demonstrates that the system has undergone resistance towards corrosion thereby blanketing the metal surface by the added inhibitor. It is noteworthy to discuss the inhibition efficiency rendered by the extract of *Delonix elata*.

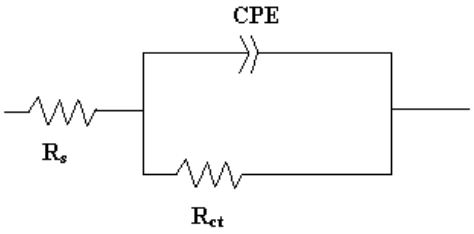

Fig. 5. Randle's equivalent circuit.

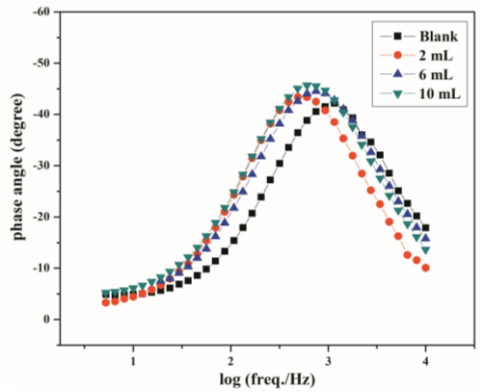

Fig. 6. Bode plot for the corrosion of mild steel in 0.5 M H_2SO_4.

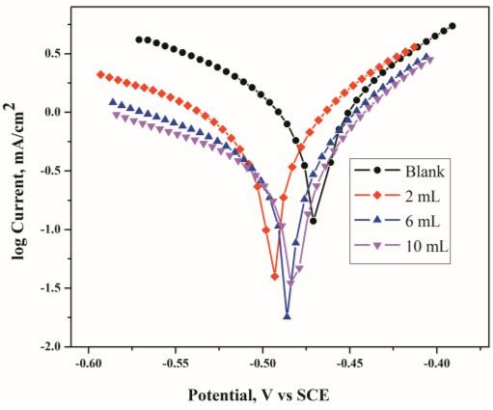

Fig. 7. Potentiodynamic polarization plot for the corrosion of mild steel in 0.5 M H_2SO_4.

Since the extract is a complex mixture of heteroaromatic compounds it is quite difficult to identify the behavior of the individual components. Thus it is assumed that all components elucidated based on their retention times could interact synergistically thereby providing a combined inhibition effect on the mild steel surface. The representation of Nyquist plot could be still better understood by correlating Bode phase angle and modulus plot. The Bode plots shown in Fig. 6, represent the single time constant with increased phase angle for the addition of 2, 6, 10 % v/v extract compared to blank, providing a confirmation that the added extract has acted synergistically on the mild steel surface in forming a protective layer to minimize corrosion.

Potentiodynamic polarization technique

Influence of the inhibitors on the partial cathodic and anodic reaction mechanisms could be well understood with the help of potentiodynamic polarization measurements. Potentiodynamic polarization parameters such as corrosion current densities (I_{corr}), corrosion potential (E_{corr}), cathodic Tafel slope (b_c) and anodic Tafel slope (b_a) were deduced from the Tafel curves, as shown in Fig. 7 and displayed in Table 2. The obtained polarization curves show that both cathodic and anodic reactions are inhibited by the addition of inhibitors. From the parameters listed in Table 2 it could be noticed that there appears a decreased corrosion current density from 850 (blank) to 268 μA/cm^2 (inhibited) thereby minimizing the corrosion rate in the presence of inhibitors. However, the added inhibitors alter both cathodic and anodic reactions from whose curves Tafel slopes b_a and b_c could be determined. Tafel constants b_a and b_c are both affected by the addition of inhibitors, b_c to a slightly higher extent. The shifting trend in E_{corr} values was found to be 18.5 mV/sec which is less than 85 mV, suggesting mixed type of inhibition with predominant cathodic inhibition [32]. Thus, the added inhibitors can either retard cathodic hydrogen evolution or anodic dissolution of mild steel providing a mixed mode of inhibition on the mild steel surface.

Surface analysis (SEM-EDX-AFM)

Fig. 8 shows the SEM-EDX images of mild steel specimens immersed in an aggressive acid medium, as well as in a *Delonix elata* (10 % v/v) inhibited medium which confirm the formation of protective layer after immersion. The image of the blank specimen exhibited rough surface [33] with pit-like appearance confirming that the metal has undergone dissolution whereas the smooth surface shown by the inhibited specimen confirms the adsorption of phytochemical constituents on the metal surface thereby retarding corrosion. On the other hand, the corresponding EDX images shown in Fig. 8 along with the elemental composition shown in Table 3, still make the adsorption of components more precise. Comparing the images and data represented, some of the elements of lower proportion present in the blank disappeared in the

inhibited specimen giving a confirmation that the added inhibitor forms a layer on the metal surface. Additional peaks corresponding to S, N and O confirm the adsorption of multiple components of the phytochemical constituents on the metal surface where it is again a difficult task to determine the action of individual components. To study the progress of adsorption of inhibitors on the mild steel surface, AFM was used as a powerful technique nowadays which has the capability of revealing the morphology from nano to micro scale. The three-dimensional images of uninhibited and inhibited specimens are shown in Fig. 8. From the average roughness (Ra), root-mean-square roughness (Rq), and the maximum peak-to-valley (P-V) height values obtained from AFM processing, relevant information can be secured. The obtained Ra and Rq values of (198.38 nm, 258.103 nm) blank and (80.7398 nm,102.026 nm) for 10 % v/v inhibited plate coincided well with P-V height values of 2089.77 nm for blank and 686.106 nm for inhibited medium. All the three parameters for inhibited specimens were found to be less than those of the blank specimen, confirming the smooth surface due to the adsorption of inhibitors [33].

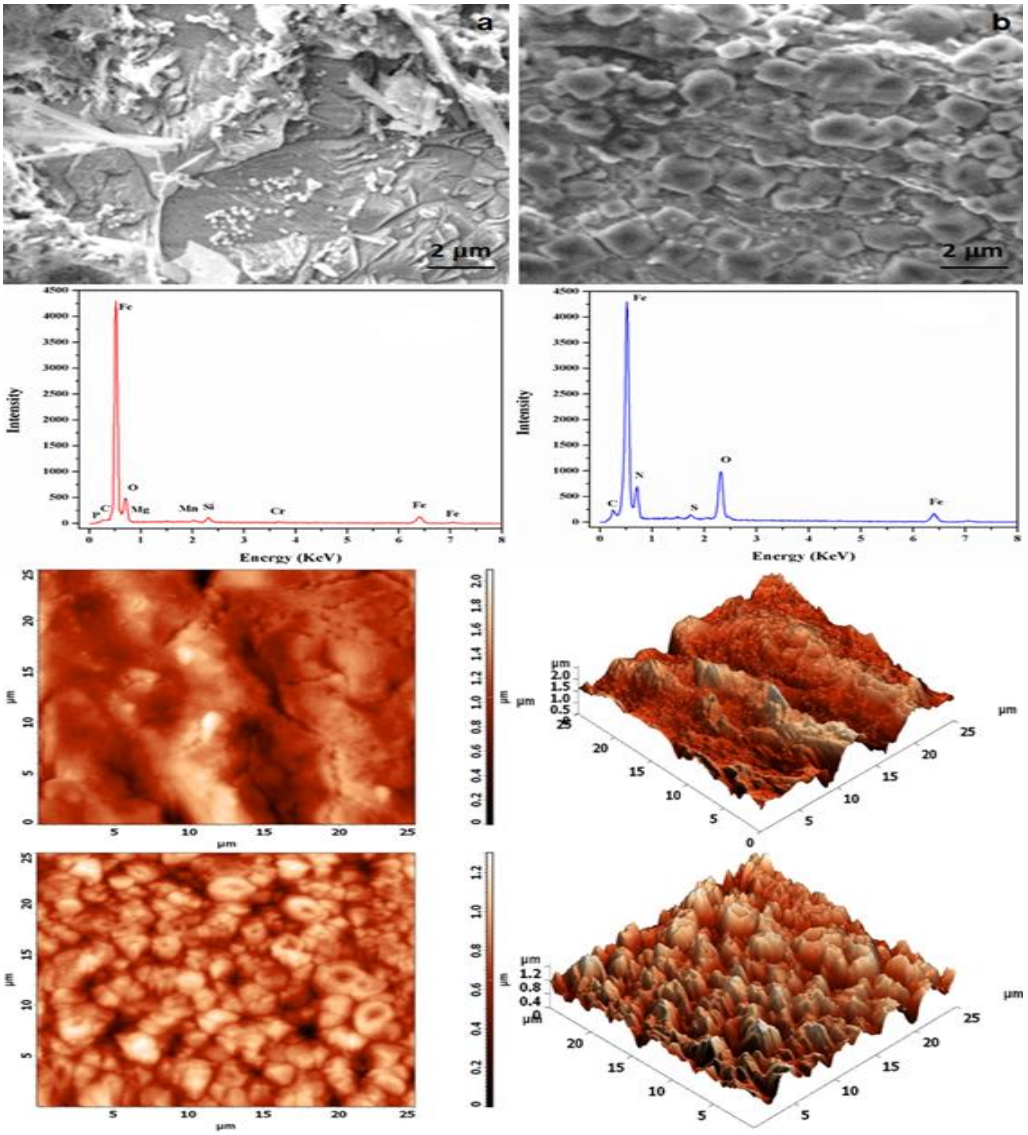

Fig. 8. SEM-EDX and AFM images of mild steel in 0.5 M H_2SO_4 a) blank, and b) 0.5M H_2SO_4 + 10% v/v *D. elata*.

Table 3. Percentage compositions of elements present on the mild steel surface.

Elements	Composition (Atomic %)	
	Blank	Inhibited
C	0.03	0.37
Fe	64.04	55.66
O	26.03	35.6
S	-	2.38
N	-	5.99
Mn	2.27	-
Cr	0.53	-
Mg	1.71	-
P	0.38	-
Si	5.01	-

CONCLUSIONS

The conclusions of the present study are as follows: (i) The phytochemical constituents of the ethanol extract of *Delonix elata* were identified by GC-MS analysis. (ii) Increased charge-transfer resistance and decreased corrosion current density were obtained from impedance and polarization techniques. Both methods correlate well with each other. (iii) The surface studies carried out using SEM, EDX, and AFM techniques confirmed the adsorption of inhibitors on the mild steel surface.

***Acknowledgement**: This paper was supported by the KU Research Professor Program of Konkuk University.*

REFERENCES

1. G. Ji, P. Dwivedi, S. Sundaram, R. Prakash, *Res. Chem. Intermed.*, **42**, 439 (2016).
2. O. K. Abiola, A. O. James, *Corros. Sci*., **52**, 661 (2010).
3. E. E. Oguzie, C. K. Enenebeaku, C. O. Akalezi, S. C. Okoro, A. A. Ayuk, E. N. Ejike, *J. Colloid Interface Sci.*, **349**, 283 (2010).
4. M. Prabakaran, S. H. Kim, V. Hemapriya, I. M. Chung, *J. Ind. Eng. Chem.*, **37**, 47 (2016).
5. S. Bilgic, *Mater. Chem. Phys.*, **76**, 52 (2002).
6. M. Gopiraman, P. Sakunthala, R. Kanmani, A. R. Vincent, N. Sulochana, *Ionics*, **17**, 843 (2011).
7. R. M. A. Shahba, A. E. E. Fouda, A. E. El-Shenawy, A. S. M. Osman, *Materials Sci. Appl.*, **7**, 654 (2016).
8. N. A. Odewunmi, N. A. Umoren, Z. M. Gasem, *J. Ind. Eng. Chem.*, **21**, 239 (2015).
9. A.K. Satapathy, G. Gunasekaran, S. C. Sahoo, K. Amit, P. V. Rodrigues, *Corros. Sci.*, **51**, 2848 (2009).
10. M. Prabakaran, S. H. Kim, K. Kalaiselvi, V. Hemapriya, I. M. Chung, *J. Taiwan Inst. Chem. Eng.*, **59**, 553 (2016).
11. M. S. Nooshabadi, M.S . Ghandchi, *J. Ind. Eng. Chem.*, **31**, 231 (2015).
12. L. R. Chauhan, G. Gunasekaran, *Corros. Sci.*, **49**, 1143 (2007).
13. M. Prabakaran, S. H. Kim, V. Hemapriya, I. M. Chung, *Res. Chem. Intermed.*, **42**, 3703 (2016).
14. M. S. A. Otaibi, M. A. Mayouf, M. Khan, S. A. A. Mazroa, H. Z. Alkhathlan, *Arabian J. Chem.*, **7**, 340 (2014).
15. N. Soltani, N. Tavakkoli, M. K. Kashani, A. Mosavizadeh, E. E. Oguzie, M. R. Jalali, *J. Ind. Eng. Chem.*, **20**, 3217 (2014).
16. M. A. Deyab, *J. Ind. Eng. Chem.*, **22**, 384 (2015).
17. Y. Singh, E. E. Ebenso, W. Liu, J. Pan, B. Huang, *J. Ind. Eng. Chem.*, **24**, 219 (2015).
18. M. G. Sethuraman, N. Sulochana, *Curr. Sci.*, **55**, 343 (1986).
19. M. Vijayasanthi, V. Kannan, *Afr. J. Microbiol. Res.*, **8**, 697 (2014).
20. P. Krishnappa, K. Venkatarangaiah, Venkatesh, S. K. S. Rajanna, *IJNPR*, **8**, 47 (2017).
21. S. Singh, S. N. Kumar, *WJPPS*, **3**, 2042 (2014).
22. M. S. Al-Otaibi, A. M. Al-Mayouf, M. Khan, A. A. Mousa, S. A. Al-Mazroa, H. Z. Alkhathlan, *Arab. J. Chem.*, **7**, 340 (2012).
23. N. O. Eddy, *Portugaliae Electrochim. Acta*, **27**, 579 (2009).
24. E. M. Sherif, *Int. J. Electrochem. Sci.*, **6**, 3077 (2011).
25. K. M. Zohdy, *Int. J. Electrochem. Sci.*, **10**, 414 (2015).
26. F. Mansfeld, *Electrochim. Acta*, **35**, 1533 (1990).
27. F. Bentiss, C. Jama, B. Mernari, H. El Attari, L. El Kadi, M. Lebrini, M. Traisnel, M. Lagrenee, *Corros. Sci.*, **51**, 1628 (2009).
28. N. A. Negma, N. G. Kandile, E. A. Badr, M. A. Mohammed, *Corros. Sci.*, **65**, 94 (2012).
29. N. Labjar, M. Lebrini, F. Bentiss, N. E. Chihib, S. El Hajjaji, C. Jama, *Mater. Chem. Phys.*, **119**, 330 (2010).
30. A.K. Singh, M. A. Quraishi, *Corros. Sci.*, **52**, 152 (2010).
31. F. Bentiss, M. Traisnel, M. Lagrenee, *Corros. Sci.*, **42**, 127 (2000).
32. S. B. Tutunaru, *J. Therm. Anal. Calorim.*, **127**, 863 (2016).
33. P. Mourya, S. Banerjee, M. M. Singh, *Corros. Sci.*, **85**, 352 (2014).

Bulgarian Chemical Communications, Volume 51, Issue 1, (pp. 38 – 47) 2019

Extraction of zinc and copper from a contaminated soil by using organic acids

D. Paliulis

Department of Environmental Protection and Water Engineering, Vilnius Gediminas Technical University, Saulėtekio al. 11, Vilnius, Lithuania, LT-10223

Received April 24, 2018; Revised November 13, 2018,

Numerous studies reveal that chemical extraction of heavy metals is one of the most effective soil treatment methods and it is often applied to cleaning polluted areas. Chemical extraction is used as an *ex-situ* approach, so the price is higher compared to the *in-situ* (most of the price consists of plowing, transporting and warehousing of contaminated soil). Despite the higher price, chemical extraction method is not only effective but also fast – >80% of cleaning efficiency can be achieved in a few hours. Although the method is characterized by high efficiency, chemical extraction has not yet been applied for heavy metal contaminated soil treatment in Lithuania. The dependence of chemical extraction efficiency on variable parameters – organic acid type, concentration and temperature are analyzed. The optimum extraction parameters are set by cost-benefit analysis and highest metal removal efficiency. The aim of this work was to optimize the process of zinc and copper removal from contaminated soil using biodegradable organic acids (citric acid, tartaric acid, acetic acid). The calculated sorption capacity of soil for Cu, Zn was 95.5% and 44.8%, respectively. It was found using the X-ray fluorescence spectrometry method that 0.05 M tartaric acid and 0.5 M citric acid are the most effective acids among the tested organic acids (acetic acid, citric acid, tartaric acid) for removal of Cu and Zn from contaminated sand soils; extraction efficiency was up to 86% for removal of Cu and up to 94.7% for removal of Zn (temperature - 20 ^{o}C, extraction time - 2 h). The maximum extraction efficiency of Cu (95.1%) and Zn (97.7%) was determined using citric acid (C= 0.5 M, t = 2 h) when the extraction was carried out at 80±2°C. Studies have shown that, from a cost-effective point of view, the most effective way to clean contaminated with Cu and Zn soil is extraction with 0.05 M tartaric acid. Extraction should be carried out at 20°C for 2 h. In this case, the highest common unit cost efficiency (~ 86.02%) was achieved at the least cost (temperature, acid concentration).

Keywords: Soil, Extraction, Zinc, Copper, Organic acids, Citric acid, Acetic acid, Tartaric acid.

INTRODUCTION

Heavy metals (HM) are natural components of the soil [1, 2]. The sources of heavy metals are of natural or anthropogenic origin. Under natural conditions soil is supplemented with heavy metals by rock desertification and sedimentation processes. In the natural environment, under the influence of a complex of environmental conditions (humidity, temperature changes, erosion, etc.), rock depression and soil formation processes take centuries; while heavy metals do not locally concentrate in this case, their concentrations in soil remain low.

Anthropogenic pollution with heavy metals is characterized by high concentrations of heavy metals, mostly locally or regionally. Soils are significantly supplemented with heavy metals by human activities: metallurgy, galvanizing industry, mining, transport, waste incineration, fertilizer and pesticide use in agriculture. Heavy metals entering the soil should not always be a problem - stable compounds are not dangerous, but not all heavy metals found in the soil form persistent compounds, it depends on the physical and chemical conditions of the environment. The amount of heavy metal in the soil depends on the amount of moisture and other parameters [3]. Soil contamination with heavy metals is a topical problem, as the change in physical or chemical properties of soil (in the case of more intensive irrigation, low pH), heavy metals are able to migrate to the environment - to pollute groundwater and to enter and accumulate in plants and living organisms [4]. In ionic states, or when combined with organic compounds, heavy metals can be absorbed by algae, plants, and through the dietary chain can reach the primary and secondary consumers, thus peak heavy metal concentrations accumulate in the tissues of end-users [5,6]. Various components of the living environment often fail to adapt to such sudden changes of environmental pollution - this causes degradation of the ecosystem. The pollution of soils with heavy metals and their compounds raises concern and danger due to the durability of metals, their accumulation in the physical environment and persistence in the living organisms. Heavy metals can enter the human body in several ways, with food or fluids, by direct contact and by inhalation [7]. Due to the toxicity and effects on living

* To whom all correspondence should be sent:
E-mail: dainius.paliulis@vgtu.lt

organisms, lead (Pb), cadmium (Cd), arsenic (As), mercury (Hg), copper (Cu), zinc (Zn) and nickel (Ni) are classified by USEPA (United States Environmental Protection Agency) as pollutants that are subject to monitoring of their changes in the environment [4]. Settled heavy metals tend to accumulate in the soil, this geological formation is a good indicator of environment pollution with heavy metals. Soil contamination studies often detect concentrations of heavy metals that exceed the limit values - pollution poses a risk to all ecosystem components, including humans [6, 8, 9].

Territories polluted with heavy metals in most European countries, if concentrations of heavy metals are above the permissible limit values, must be cleaned. Soil treatment can be carried out using two principles: *in-situ* and *ex-situ.* Chemical extraction of metals is based on the *ex-situ* principle, therefore its cost is higher than *in-situ* (the major part of price consists of soil excavation, transportation and storage work, the part of chemical reagents is very small). In spite of the higher price, this method of soil treatment is efficient and fast – studies of heavy metal extraction have shown that more than 80% of treatment efficiency can be achieved within a few hours. 88% copper and 86% zinc elimination efficiency after 1 hour contact time at room temperature was reached with sulfuric acid [10]. Application of strong acids for extraction of heavy metals from contaminated soil is not aceptable due to the fact that strong acid reduces the content of organic matter in the soil.

EDTA, nitric acid and hydrochloric acid were used to remove heavy metals from contaminated soils [11]. The efficiency over 70% for lead removal was achieved during extraction of soil with the tested acids - 0.05M EDTA, 1.7% HCl and 10 % HNO_3 using optimized extraction time and acid volumes. Many scientists carried out studies on the extraction of heavy metals from contaminated soils using different chemicals (sulfuric acid, nitric acid, chelators and organic acids – citric acid, PESA, EDTA, EDDS, PDTA, BDTA, IDSA, NTA, HEDTA and EGTA, CDTA, etc. [12-21]. The trivalent heavy metal ions, iron and chromium, were more difficult to be removed than the divalent ions, copper, zinc, nickel, and cadmium. More than 99.9% of heavy metals can be removed from the sludge by treating with 0.5 M sulfuric acid in 2 h [12]. It was found that the extraction of Cr using PESA was more efficient than that using ethylenediaminetetraacetic acid (EDTA) and *S,S*-ethylenediaminedisuccinic acid (EDDS) under similar conditions. The extraction efficiency reached 58% [14]. The removal efficiencies of Zn, Ni, Cr and Cu reached 53.5%, 40.2%, 35.4% and 13.1%, respectively, using citric acid [15].

The removal efficiencies of Cu, Zn and Pb reached 9.5%, 82.2%, and 87.3%, respectively, at the optimal 0.325 M concentration of nitric acid assisted by ultrasound for 20 min [16]. Zinc and nickel were the heavy metals having the best removal efficiency with citric acid. EDTA gives better results for extraction of copper, cadmium and lead from biosolids [17]. Citric acid was more active than H_2SO_4 for leaching heavy metals (Mo, V, Ni, and Co) from a spent catalyst [18]. The combined application of EDTA and EDDS significantly increased the extraction of heavy metals (especially Pb) from the soil [19]. 0.05 M EDTA and 0.1 M citric acid were tested for the simultaneous extraction Cu, Pb and Zn from an Italian harbour sediment. Best extraction efficiency was achieved using 0.05 M EDTA solution [20]. Soil washing using EDTA and three of its derivatives: CDTA (trans-1,2-cyclohexanediaminetetraacetic acid), BDTA (benzyldiaminetetraacetic acid), and PDTA (phenyldiaminetetraacetic acid) was tested for extracting Cu^{2+}, Zn^{2+}, Ni^{2+}, Pb^{2+}, and Fe^{3+} from a contaminated soil [21]. It was determined that the best extractant was PDTA, worse extractants were EDTA and CDTA. BDTA was the least effective extractant [21]. Removal of Cu, Ni and Pb from soil was achieved using IDSA, NTA, HEDTA and EGTA. Metal extractions ranged between 80 and 97% using IDSA as the best extractant [22]. The extraction of heavy metals from soil can be carried out using EDDS [23]. Different chemicals have been used to remove zinc from the soil: EDTA, NTA, citrates, tartrates, oxalates, and EDTA, citrates, DTPA, sulfides, EDDS – for removal of copper from the soil. A hybrid method involving chelating agents and microorganisms can be applied for removal of heavy metals from electronic waste [24]. Chelating agent GLDA was tested for removal of cadmium, nickel, copper and zinc from industrial sludge [25]. About 89 % cadmium, 82 % nickel, 84 % copper and less than 50 % zinc elimination efficiency was achieved from industrial sludge applying GLDA [25]. Pb removal from contaminated soils applying low molecular weight organic acid (LMWOA) – citric acid (CA), malic acid and nanoscale zero-valent iron (nZVI) were investigated. The maximum Pb removal efficiencies reached 72% for mine soil and 87% for farmland soil after 4 h by the mixed solutions of CA and nZVI, respectively [8].

Low molecular weight organic acids such as acetic acid, oxalic acid and citric acid could be used for removal of heavy metals from polluted soil [26]. During chemical extraction of heavy metals from the contaminated soil it is important to remove both forms of metals - mobile and immobile. The extraction of metals from soil with organic ligands depends on the competition between the metal-binding functional groups from the sludge structure and the organic chelator [15]. Physical and chemical extraction reaction conditions can be changed for increasing of effectiveness of contaminated soil treatment.

The aim of this work was to optimize the process of zinc and copper removal from contaminated soil using biodegradable organic acids.

METHODOLOGY

Scheme of experiment:

1. Sampling of soil.
2. Determination of soil type and pH before pollution.
3. Determination of total carbon quantity in soil.
4. Contamination of soil with aqueous solutions of zinc and copper nitrates.
5. Determination of zinc and copper concentrations in conaminated soil samples and pH determination.
6. Extraction of heavy metals from soils applying organic acids.
7. Determination of the effect of temperature and acid concentration unit efficiency on the removal of copper and zinc.

All reagents used in the research were of analytical reagent grade, deionized water meets the requirements of LST EN ISO 3696: 1996 standard.

Instruments used in the study:

X-ray fluorescence spectrometer Niton XL2;
TOC Analyzer Shimadzu TOC V;
Elution shaker C. Gerhardt GmbH and Co.KG - Rotoshake RS12;
Mettler Toledo pH meter;
Electric chopper-homogenizer;
Radwag AS60/220 laboratory balance.

Collection of soil samples

Soil samples were taken from an unbuffered, natural area - in the meadow near the coniferous forest in the territory of Ukmergė town. The nearest industrial or energetic company was more than 2 km away from the sampling point. The chosen area is near to the Bugeniai village (coordinates X-546828, Y-612062). The sample locations are arranged in a grid of 20 meters (120 meters from the road and 100 meters from the nearest building) (see Fig. 1).

Fig. 1. Soil sampling points

Samples were taken with a steel rack at a depth of 10 cm, and about 650 g of soil were taken from each point. The total mass of soil was about 10 kg. The collected samples were placed in the same container to form a composite sample. Soil was transported to the laboratory, dryed at 38 ºC temperature for 24 h, sieved through 3 sieves - 2 mm, 0.25 mm and 0.125 mm for determination of soil type. Soil fraction with a size smaller than 2 mm was selected for pH determination and pollution with the investigated heavy metal salts (nitrates).

Determination of soil type, pH and metals concentrations before pollution

The type of soils that are predominant in the territory of Lithuania was chosen for the study. According to standards EN ISO 14688-1:2002 and

EN ISO 14688-2:2004 was determined as sand soil type.

pH of the soil was determined according to standard LST ISO 10390: 2005. 20 g of analysed soil was mixed with 100 ml of 0.1 M KCl solution, shaken for 1 h with the Elution shaker C. Gerhardt GmbH and Co.KG - Rotoshake RS12 and filtered through a 0.45 μm filter. pH of the separated suspension was measured with a Mettler Toledo pH meter; pH of the suspension was 7.9. Deionised water (5 l) of was mixed with 3 kg of soil. The soil was stirred for 30 min with an electric grout mixer, after which the soil was filtered through a 0.45 μm filter. The filtered soil was dried at 38 °C for 24 h. Five samples of 30 g of soil were collected and background concentrations of heavy metals (Cu and Zn) were measured with the X-ray fluorescence spectrometer Niton XL2. Concentration of copper was 15.45±3 mg/kg, concentration of zinc was 42.22±2 mg/kg.

Determination of total carbon quantity in soil

Quantity of total carbon in soil was 2.5-3.0 %. It was determined using the TOC Analyzer Shimadzu TOC V.

Pollution of soil with aqueous solutions of zinc and copper nitrates

Limit values for metals in soil according to Lithuanian hygiene norm HN 60:2015 are these: 75 mg/kg (Cu) and 300 mg/kg (Zn). Salts of the investigated heavy metals were dissolved in 600 ml of deionised water (2.85 g $Cu(NO_3)_2 \times 3H_2O$ and 13.5 g $Zn(NO_3)_2 \times 6H_2O$). Ratio of solution: soil was 2:1 (v:w).

Determination of zinc and copper concentrations in polluted soil samples and pH determination

Before the soil extraction tests were carried out, the condition was raised: in the contaminated soil the concentrations of Cu and Zn should be at least 2 times higher than set in the Lithuanian Hygiene Norm HN 60:2015. After contamination with heavy metals, the soil and solution were mixed with the Elution shaker C. Gerhardt GmbH and Co.KG - Rotoshake RS12 for 2 h. After mixing, the soil was filtered through a 0.45 μm filter. The filtered soil was dried at 38 °C for 24 h. The values of heavy metals in the polluted soil were determined with the X-ray fluorescence spectrometer Niton XL2. Concentration of copper in the polluted soil was 9.54 times and concentration of zinc in polluted soil was 4.47 times higherthan the limit values presented in the Lithuanian Hygiene Norm HN 60:2015, it means that raised condition was achieved. Ater contamination of soil with heavy metals salts pH decreased to 3.9.

Extraction of heavy metals from soils applying organic acids

The research was based on Wang's proposed methodology [15], which used the best-case method in metal extraction studies. The method is based on the fact that the optimal solution to the problem is determined using less resources: all possible variants are not examined, some of them disappear at the initial stage of the study, for example, if the dependence of the extraction efficiency on a single variable parameter, e.g., acid concentration, is investigated, after studies with 3 variables the most effective option found in the next step is the best-defined option (see Table 1).

Table 1. Extraction study using the best-case method.

Acid	Acid concentration [M]	Temperature [°C]
Tartaric acid, Acetic acid, Citric acid	0.05, 0.1, 0.2, 0.35, 0.5	20, 40, 60, 80

The effects of the three variables on the effectiveness were investigated in extraction studies. The main variable was the extractant (organic acid), secondary variables - acid concentration [M] and temperature [°C]. Three organic acids were used in the experiments: tartaric acid, acetic acid and citric acid. The following acid concentrations were used in the studies: 0.05 M, 0.1 M, 0.2 M, 0.35 M and 0.5 M [12,15]. After determination of two optimal organic acids, experiments were carried out with selected concentrations of acids, variable – temperature.

According to the literature review, the maximum extraction efficiency is achieved within the first 2 hours, so the extraction tests were carried out from 0.5 to 24 h (0.5, 2, 8, 24 h). Based on the primary extraction results, the extraction efficiency is practically constant after 2 h; therefore the selected extraction time was 2 h.

Optimal extraction conditions and parameters were found during experiments.

Determination of the effect of temperature and acid concentration unit efficiency on the removal of copper and zinc

The unit efficiency calculation was used for evaluation of efficiency of acid concentration unit and temperature unit. This indicator shows what performance could be achieved with a part of a particular parameter. In this case the obtained efficiency is divided by a certain parameter, the highest value equals 100%, and all other calculations are carried out according to the principle of proportionality. This method is effective for comparing completely different parameters (different acid concentrations, temperatures) if their values are known. This parameter also helps researchers to achieve the best result with the lowest cost. For example with X acid of 0.5 M concentration it was achieved 80% extraction efficiency and with Y acid 0.01 M - 60% efficiency. The highest value is equal to 100%, in this case unit efficiency of Y acid is 100%, and X acid unit efficiency is just 2.6%. In the analysed case it is better to use Y acid if the cost of acid concentration is estimated. The maximum efficiency is achieved with X acid and reaches 80%. Efficiency of acid unit is higher for Y acid, but overall efficiency is only 60%.

RESULTS AND DISCUSSION

Cu and Zn salts (nitrates) were used for artificial contamination of soil with the investigated heavy metals. The concentration of the metals in the soil was determined by X-ray fluorescence spectrometry. According to the measured concentration of metals in the artificially contaminated soils, the amount of metals absorbed by the soil was calculated. The results of soil absorption capacity are presented in Table 2.

Table 2. The absorption capacity of heavy metals in the test soil and other parameters

Metal	Metal concentration in soil, mg/kg	Limit value according to HN 60:2015	Soil absorption efficiency,%	Exceeding the limit value, times
Cu	715.23	75	95.49	9.54
Zn	1341.03	300	44.85	4.47

It shows that the main condition for soil contamination was achieved - all metal concentrations exceeded the limit value set in the Lithuanian Hygiene Norm HN 60:2015 more than 2 times. Soil mostly effectively absorbed copper - soil absorption efficiency was more than 95%, soil absorption efficiency for zinc was near 45% (Table 2).The investigated soil was homogeneous - the distribution of the metal concentration in different soil samples around the mean value was ± 3.6% for Cu and ± 5.7% for Zn, accordingly. The homogeneous distribution of metal concentrations in soils is important for extraction studies, as it leads to lower errors of research results.

Dependence of Cu extraction efficiency on acid type and concentration

45 units of contaminated soil (10 g) were used for determining the effect of acid type and concentration on heavy metals extraction efficiency. The extraction time and temperature were constants (2 h, 20±2 °C). Three different organic acids (tartaric, acetic, citric) and 5 different concentrations (0.05 M, 0.1 M, 0.2 M, 0.35 M, 0.5 M) were used for extraction.

After extraction with organic acids soil pH was in the range from 1.9 to 3.7 depending on acid type and concentration – with tartaric acid (1.9-2.5), with citric acid (2.1-2.5), with acetic acid (2.8-3.7). Dependence of residual Cu concentration in soil on extractant type and concentration is presented in fig. 2.

Figure 2 shows that copper from the contaminated soil was most effectively eliminated by tartaric acid. With all concentrations of tartaric acid, the copper removal efficiency remained similar – it increased with increasing of tartaric acid concentration from 80% to 86.0%.

Citric acid was also effective in removing copper from soil, but at low concentrations (0.05 M and 0.1 M), it was not as effective as tartaric acid. Extraction efficiency was in thr range from 67.7% to 85.4 %.

Acetic acid was the least effective on the extraction of copper from contaminated soil. Applying this acid the efficiency of copper extraction ranged from 34.2% to 69% with increasing acetic acid concentration.

Deionised water reduced copper concentration in the control contaminated soil sample by only

14.5%. It can be argued that copper forms solid insoluble complexes with soil particles and is difficult to be removed if the medium is not acidified.

Dependence of Zn extraction efficiency on acid type and concentration

Dependence of residual Zn concentration in soil on extractant origin and concentration is presented in fig. 3.

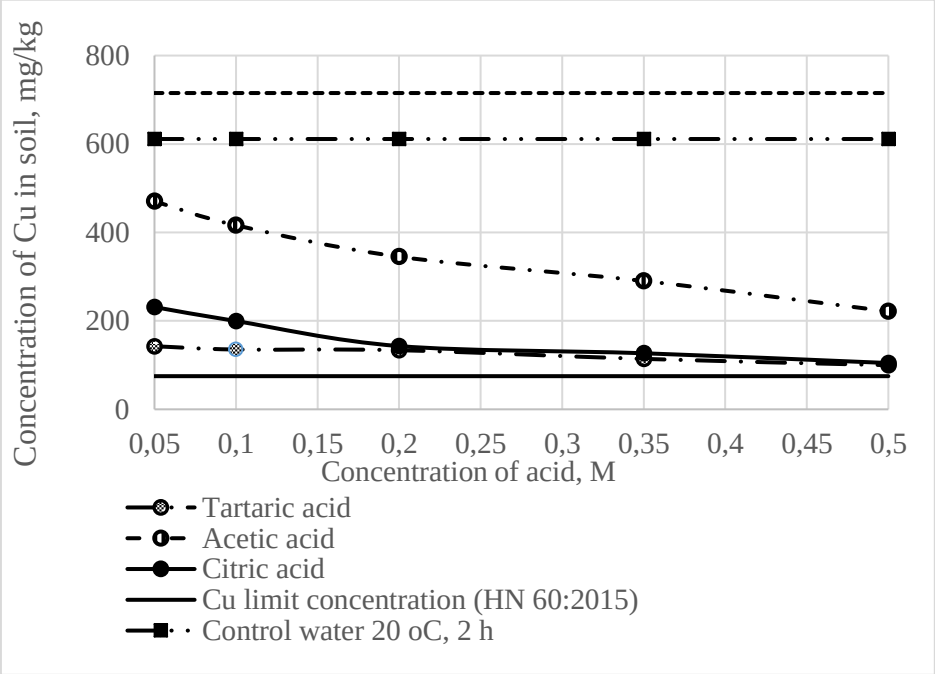

Fig. 2. Dependence of residual Cu concentration in soil on extractant type and concentration, temperature 20 ºC± 2 °C, extraction time 2 h.

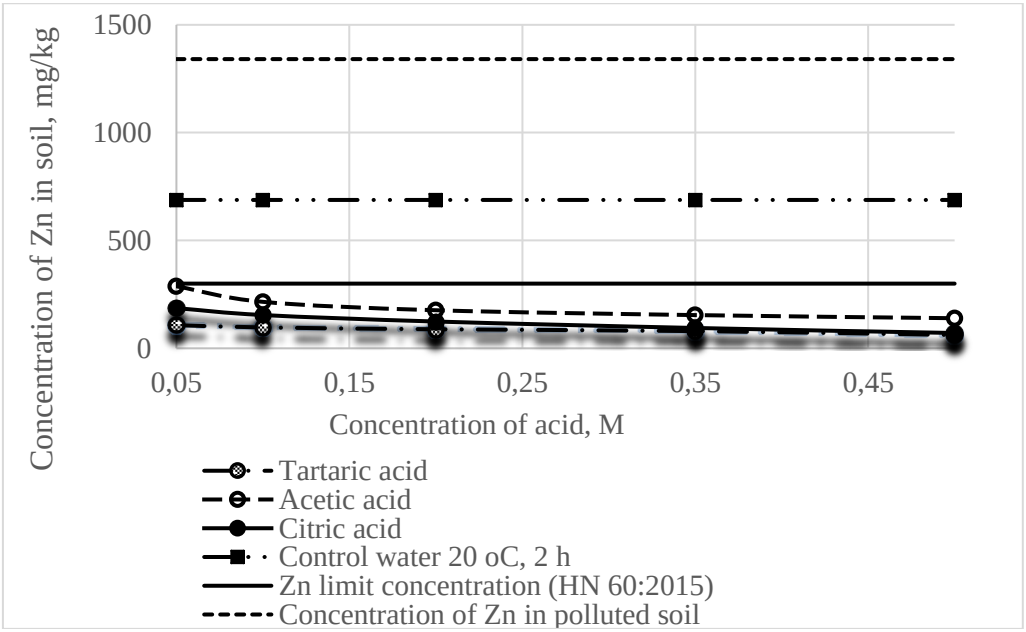

Fig. 3. Dependence of residual Zn concentration in soil on extractant type and concentration, temperature 20 ºC± 2 °C, extraction time 2 h.

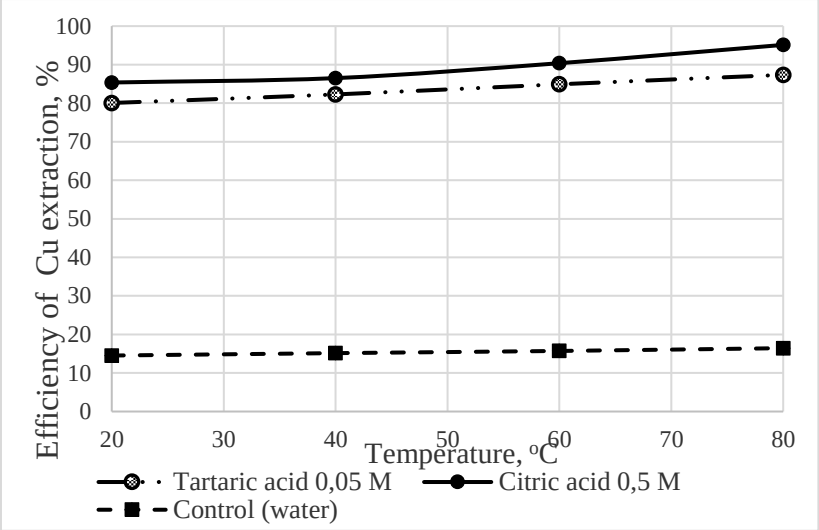

Fig. 4. Dependence of Cu extraction efficiency on the soil temperature, extraction time 2 h.

All three investigated organic acids were very effective for extraction of zinc from contaminated soil (fig. 3). The most effective extractant for removal of zinc from contaminated soils (like in case of copper) was tartaric acid.

With all investigated concentrations of tartaric acid copper removal efficiency was similar - it increased with increasing tartaric acid concentration from 92% to 95.4%.

Citric acid was also effective in removing zinc, but slightly less compared to tartaric acid. The effectiveness of citric acid with increasing acid concentration ranged from 86.1% to 94.7%.

Acetic acid proved to be the least effective. With this acid zinc removal efficiency increased from 78.6% to 89.6% with increasing acid concentration.

Deionised water reduced zinc concentration in the control contaminated soil sample by 48.7%, therefore, in the case of soil contamination with zinc, the primary soil treatment method (taking into account the extent of exceeding the limit value) may be a method of soil washing with water.

Dependence of Cu extraction efficiency on temperature

The efficiency of extraction also depends on the temperature of the solution. Contaminated soil samples (10 g) were used to determine the efficiency of extraction with temperature. In the study of extraction efficiency with temperature, the most effective first-stage acids and their concentrations were used - 0.05 M tartaric acid and 0.5 M citric acid.

Extraction with both mentioned acids was carried out at different temperatures – 20 ºC, 40 ºC, 60 ºC and 80 ºC. After extraction soil samples were dried and analyzed using XRF spectrometer. The obtained data on the concentrations of Cu remaining in the soil samples after rinsing are presented in Fig. 4.

Increasing the temperature from 20 ± 2ºC to 80 ± 2ºC resulted in a slight increase in the removal efficiency of copper from the soil using 0.05 M tartaric acid - only by 7.3%. The maximum removal efficiency was 87.4% at 80 ± 2ºC.

The use of 0.5 M citric acid at higher temperature increased the efficiency of copper removal by 9.7%. The maximum copper removal efficiency with citric acid was achieved at a temperature of 80 ± 2 °C and reached 95.1%.

Removal of copper on applying deionised water increased from 14.5% to 16.4% on increasing temperature (Fig. 4). Increasing of temperature had no significant effect on the effectiveness of copper removal from contaminated soil using organic acids.

Dependence of Zn extraction efficiency on temperature

The obtained data on the concentrations of Zn remaining in the soil samples after rinsing are presented in Fig. 5.

With an increase in temperature from 20 ± 2 ºC to 80 ± 2 ºC, the removal of zinc from the contaminated soil with the use of 0.05 M tartaric acid slightly increased as for copper - only by 4% (Fig. 4). The maximum removal efficiency was 96% at 80 ± 2 °C.

Using 0.5 M citric acid a slight increase in zinc elimination efficiency was noted with increasing temperature by just 3%. The maximum zinc removal efficiency applying citric acid was achieved at a temperature of 80 ± 2 ºC and was 97.7%.

The efficiency of zinc removal from the the control sample of soil with deionised water with increasing temperature increased from 48.7% to 50.6% (Fig. 5).

Increasing of temperature had no significant effect on the efficiency of zinc removal from contaminated soil using organic acids.

It is very important to estimate which acid is more effective for the removal of the selected metals. The most effective was 0.5 M citric acid for extraction of zinc and copper from contaminated soil, but with 0.05 M tartaric acid comparable metal removal efficiency was achieved, 10 times lower tartaric acid concentration being effective enough.

Determination of temperature and acid concentration unit efficiency on removal of copper and zinc

The efficiency of acid concentration and temperature units on copper and zinc common extraction efficiency is presented in fig. 6.

The results of extraction efficiency according to acid concentration unit and temperature unit are quite different, because the tartaric acid concentration is 10 times lower (lower costs) but extraction efficiency is similar to that with 0.5 M citric acid.

In this case the maximum rational efficiency was achieved with 0.05 M tartaric acid at the lowest temperature - 20 ° C (higher cost does not compensate for the benefit of metals removal and it is seen from the above presented results that the temperature does not significantly affect the efficiency of Cu and Zn removal from contaminated soil).

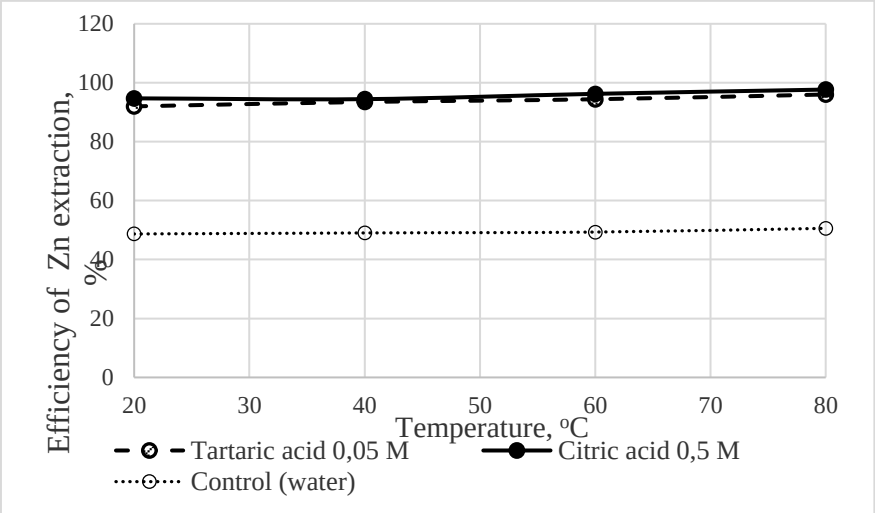

Fig. 5. Dependence of Zn extraction efficiency from the soil on temperature, extraction time 2 h.

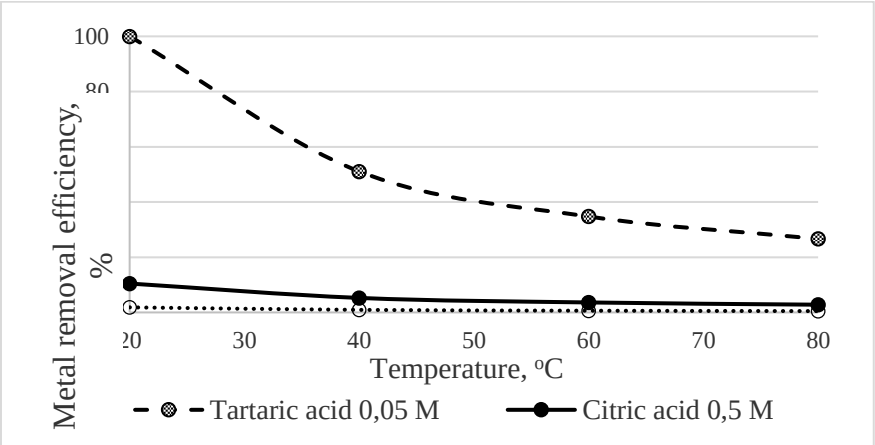

Fig. 6. Efficiency of temperature and concentration unit, % on removal of copper and zinc, extraction time 2 h

The obtained results of the study are ambiguous and should be evaluated depending on the objectives of the application:

Condition 1 – if evaluation is carried out according to the highest metal removal efficiency - in this case 0.5 M citric acid and 80 °C temperature should be used.

Condition 2 - if evaluation is carried out according to the practical application possibilities (in terms of unit temperature and unit efficiency) - in this case it is best to use 0.05 M tartaric acid and 20 ± 2 °C temperature.

Better extraction efficiency was achieved for zinc removal from polluted soil compared to copper using citric acid as extractant. Similar results were obtained by other scientists - the removal efficiencies of Zn and Cu reached 53.5% and 13.1% using citric acid [15]; zinc was the heavy metal having better removal efficiency from biosolid with citric acid, compared to copper [17].

It can be concluded that tartaric acid offers similar extraction efficiency as citric acid. Similar results were obtained by other scientists - citrate removed 80 to 99.9% of all metals (Cd, Pb, Cu and Zn) within 24 h at pH from 2.3 to 7.5. Tartarate removed 84 to 99.9% of all metals from soil within 24 h at pH from 2.1 to 6.7 [27].

It can be concluded that acetic acid is the worst extractant among the tested organic acids.

The efficiency of heavy metals extraction from polluted soil depends on extraction time, type of heavy metals (soluble or not soluble in water), type of organic acid and its concentration, process temperature, quantity of organic carbon and other parameters. Low molecular organic acids such as tartaric and citric are better chelating agents compared to acetic acid and can be applied for removal of heavy metals from soil. These organic acids are environment-friendly and can be decomposed by bacteria.

CONCLUSIONS

1. It has been found using X-ray fluorescence spectrometry that 0.05 M tartaric acid and 0.5 M citric acid are the most effective acids among the tested organic acids (acetic acid, citric acid, tartaric acid) for removal of Cu and Zn from contaminated sand soils; extraction efficiency was up to 86% for Cu removal and up to 94.7% for Zn removal (temperature - 20 °C, extraction time - 2 h).

2. The maximum extraction efficiency of Cu (95.1%) and Zn (97.7%) was found using citric acid (C= 0.5 M, t = 2 h) when the extraction was carried out at 80±2 °C.

3. Studies have shown that, from a cost-effective point of view, the most effective way to clean contaminated with Cu and Zn soil is the extraction with 0.05 M tartaric acid. Extraction should be carried out at 20 °C for 2 h. In this case, the highest common unit cost efficiency (~ 86.02%) was achieved at the least cost (temperature, acid concentration).

REFERENCES

1. Y. Hu, H. Cheng, Application of stochastic models in identification and apportionment of heavy metal pollution sources in the surface soils of a large-scale region, *Environ. Sci. Technol.*, **47**, 3752 (2013).
2. H. Chen, Y. Teng, S. Lu, Y. Wang, J. Wang, Contamination features and health risk of soil heavy metals in China, *Science of the Total Environment*, **512**, 143 (2015).
3. M. S. R. Sharma, , N. S. Raju, Correlation of heavy metal contamination with soil properties of industrial areas of Mysore, Karnataka, India by cluster analysis, *International Research Journal of Environmental Sciences*, **2**(10), 22 (2013).
4. S. M. Rodrigues, N. Cruz, C. Coelho, Risk assessment for Cd, Cu, Pb and Zn in urban soils: chemical availability as the central concept, *Environmental Pollution*, **183**, 234 (2013).
5. L. Wang, Y. Wang, ,C. Xu, Z. An, S. Wang, Analysis and evaluation of the source of heavy metals in water of the River Changjiang, *Environ. Monitoring and Assessment*, **173**, 301 (2011).
6. A. Maceda-Veiga, M. Monroy, E. Navarro, G. Viscor, A. de Sostoa, Metal concentrations and pathological responses of wild native fish exposed to sewage discharge in a Mediterranean river, Science *of the Total Environment*, **449**, 9 (2013).
7. C. Qu, Z. Ma, J. Yang, Y. Lie, J. Bi, L. Huang, Human Exposure Pathways of Heavy Metal in a Lead-Zinc Mining Area, Jiangsu Province, China, *PloS one*, **7**(11), 1 (2012).
8. G. Wang, S. Zhang, X. Xu, T. Li, Y. Li, O. Deng, *G*. Gong, Efficiency of nanoscale zero-valent iron on the enhanced low molecular weight organic acid removal Pb from contaminated soil, *Chemosphere*, **117**, 617 (2014).
9. Y. B. Yohannes, Y. Ikenaka, S. M. M. Nakayama, A. Saengtienchai, K. Watanabe, M. Ishizuka, Organochlorine pesticides and heavy metals in fish from Lake Awassa, Ethiopia: Insights from stable isotope analysis. *Chemosphere*, **91**(6), 857 (2013).
10. S. Bisone, J. F. Blais, P. Drogui, G. Mercier, Toxic metal removal from polluted soil by acid extraction. Water, Air, and Soil Pollution, **223**(7), 3739 (2012).
11. H. Jeon, S. Park, Simplified acid extraction methods of heavy metal ions from contaminated soils, *International Journal of Geomate*, **13**(36), 70 (2017).
12. Y. C. Kuan, I. H. Lee, J. M. Chern, Heavy metal extraction from PCB wastewater treatment sludge

by sulfuric acid, *Journal of Hazardous Materials*, **177**(1–3), 881 (2010).
13. W. H. Zhang, L. Z. Tong, Y. Yuan, Z. Y. Liu, H. Huang, F.F. Tan, R.L. Qiu, Influence of soil washing with a chelators on subsequent chemical immobilization of heavy metals in a contaminated soil, *Journal of Hazardous Materials*, **178**(1), 578 (2010).
14. L. H. Zhang, Z. L. Zhu, Chromium extraction from sewage sludge using polyepoxysuccinic acid, *Pedosphere*, **22**(1), 131 (2012).
15. X. Wang, J. Chen, X. Yan, X. Wang, J. Zhang, J. Huang, J. Zhao, Heavy metal chemical extraction from industrial and municipal mixed sludge by ultrasound-assisted citric acid, *Journal of Industrial and Engineering Chemistry*, **27**, 368 (2015).
16. J. Deng, X. Feng, X. Qiu, Extraction of heavy metal from sewage sludge using ultrasound-assisted nitric acid, *Chemical Engineering Journal*, **152**(1), 177 (2009).
17. M. Gheju, R. Pode, F. Manea, Comparative heavy metal chemical extraction from anaerobically digested biosolids, *Hydrometallurgy*, **108**(1), 115 (2011).
18. M. Marafi, A. Stanislaus, Waste Catalyst Utilization: Extraction of Valuable Metals from Spent Hydroprocessing Catalysts by Ultrasonic-Assisted Leaching with Acids, *Industrial and Engineering Chemistry Research*, **50**(16), 9495 (2011).
19. G. Mancini, M. Bruno, Enhanced phytoextraction of Pb and other metals from contaminated soils and associated risks, in: BIC 2010 2nd International Conference on Industrial Biotechnology, 20, 1-10. Enrico Bardone Aurelio Viglia, 2010.
20. L. Di Palma, R. Mecozzi, Heavy metals mobilization from harbor sediments using EDTA and citric acid as chelating agents, *J. Hazard. Mater*., **147**(3), 768 (2007).
21. T. Zhang, J. M. Liu, X. F. Huang, B. Xia, C. Y. Su, G. F. Luo, Y. W. Xu, Y. X. Wu, Z. W. Mao, R. L. Qiu, Chelant extraction of heavy metals from contaminated soils using new selective EDTA derivatives, *Journal of Hazardous Materials*, **262**, 464 (2013).
22. M. A. Mohamed, A. Efligenir, J. Husson, J. Persello, P. Fievet, N. F. Rouge, Extraction of heavy metals from a contaminated soil by reusing chelating agent solutions, *Journal of Environmental Chemical Engineering*, **1**(3), 363 (2013).
23. T. C. Yip, D. C. Tsang, K. T. Ng, I. M. Lo, Empirical modelling of heavy metal extraction by EDDS from single- metal and multi-metal contaminated soils, *Chemosphere*, **74**(2), 301 (2009).
24. D. Pant, D. Joshi, M. K. Upreti, R. K. Kotnala, Chemical and biological extraction of metals present in E waste: a hybrid technology, *Waste Management*, **32**(5), 979 (2012).
25. Q. Wu, Y. Cui, Q. Li, J. Sun, Effective removal of heavy metals from industrial sludge with the aid of a biodegradable chelating ligand GLDA, *J. Hazard. Mater*., **283**, 748 (2015).
26. E. Zaleckas, V. Paulauskas, E. Sendžikienė, Fractionation of heavy metals in sewage sludge and their removal using low-molecular-weight organic acids, *Journal of Environmental Engineering and Landscape Management*, **21**(3), 189 (2013).
27. R. A. Wuana, F. E. Okieimen, J. A. Imborvungu, Removal of heavy metals from a contaminated soil using organic chelating acids, *International Journal of Environmental Science and Technology*, **7**(3), 485 (2010).

Bulgarian Chemical Communications, Volume 51, Issue 1, (pp. 48 – 53) 2019

The effects of epoxyacrylate coating on printability of bio/synthetic-based fabrics in a thermal transfer printing system

S. Sönmez[1*], Z. Yıldız[2], A. Akgül[1]

[1]*Marmara University, School of Applied Sciences, Printing Technologies Department, İstanbul– Turkey*
[2]*Marmara University, Technology Faculty, Textile Engineering Department, İstanbul – Turkey*

Received December 27, 2017; Accepted October 25, 2018

This study was aimed to determine the effect of epoxyacrylate oligomer on the print quality. For this purpose, the test print image, transferred on polyester film using a digital printing system, was applied on three different textile fabrics using thermal transfer printing system at three different temperatures. Then, epoxyacrylate based coating formulation was applied on the printed textile fabrics. In order to determine the printability parameters, print colors L*, a*, b* and gloss values were measured on uncoated and epoxyacrylate coated printed textile fabrics. Then a standard washing process was applied on uncoated and epoxyacrylate coated printed textile fabrics in order to estimate the washing fastness of the coating and printing processes. Results showed that print chroma values of epoxyacrylate coated fabrics decreased whilst print gloss values increased. But, after the washing step, print gloss values of uncoated and epoxyacrylate coated printed textile fabrics all remained unchanged. Furthermore, epoxyacrylate coating has no significant effect on print lightness values of printed textile fabrics. The change in textile fabrics' structures did not show a distinct effect on printability parameters.

Keywords: Epoxyacrylate coating, Thermal transfer printing, Print gloss

INTRODUCTION

Epoxy polymers exhibit excellent chemical stability and thermal resistance, showing good adhesion properties on a great variety of surfaces. They have good mechanical properties and can be used in composite materials as the matrix phase. Although having all these advantages, epoxies have some drawbacks such as low impact resistance, high brittleness, and poor UV-resistance. In order to eliminate these drawbacks, epoxies should be modified using some chemical reactions or inorganic fillers. The most widely used method in modification of epoxies is the acrylation process. The reaction of an epoxy with acrylic acid gives the epoxyacrylate (EA) oligomer which can be used for various coating purposes such as corrosion and UV protection, resistance to flame, acid and organic solvents, etc. [1-7]. In the literature there are just a few studies considering the usage of EA based coatings in printing industry. In a previous study, a urethane acrylate oligomer has been synthesized and used in a blue light curable ink formulation for jet printing on cotton fabrics [8].

Today, an aspect of graphic industry that is becoming more and more interesting is printing of textile materials. Printing of textile materials can be most appropriately described as an art and a science of desired design transfer onto the textile surface. Textile materials can be printed using screen-printing technique, digital printing technique, and thermal transfer printing [9]. In thermal transfer printing, firstly the image is transferred onto the transfer paper using digital printing technique, then a binder is printed on the printed transfer paper using digital or screen printing system. Finally, the images on prepared test samples are transferred onto textile fabric by using heat in the range of 140-220°C depending on textile fabric structure [10].

In this study, EA oligomer was synthesized and then applied on printed textile fabrics by dip-coating for protection of the image quality in a thermal transfer printing system. The effects of EA coating layer on print lightness, print chroma, and print gloss values were investigated. Printed and EA coated fabrics were also tested after double washings to assess the water resistance of printing color and EA layers.

MATERIALS AND METHODS

Materials

In this study, three different kinds of textile fabrics (cotton 113 g/m^2, 30 warp/cm, 22 weft/cm, polyamide 168 g/m^2, knitted fabric, polyester 84 g/m^2, 64 warp/cm, 40 weft/cm) were used. Bisphenol-A based epoxy (EPIKOTE 162, EEW:167-171 g/equiv.), triphenyl phosphine (TPP), acrylic acid (AA), methyl ethyl ketone (MEK), hydroquinone (HQ), photoinitiator

* To whom all correspondence should be sent:
E-mail: ssonmez@marmara.edu.tr

(Irgacure-184), and dipropylene glycol diacrylate (DPGDA) were all purchased from Sigma-Aldrich.

Preparation and Application of the Printing Master Film via Thermal Printing System

Printing master films were prepared and then they were printed on polyester film by an HP Indigo 5500 digital printing machine. In order to prevent spreading of the image, the surfaces of printed polyester films were coated with white dye using a semi-automatic screen-printing machine. The mesh number was 140 threads/cm (tpc). After print, they were dried at 60°C. Then, they were coated with water-based adhesive for giving binder feature using a screen-printing system. The mesh number was 68 threads/cm (tpc) [11-13]

The obtained printing master films were transferred on cotton, polyamide and polyester textile fabrics using Sahok Sh 49BD thermal transfer printing machine at 140°C, 170°C and 200°C. In this process, printing pressure and printing time were kept constant.

Epoxyacrylate Synthesis and Coating Process on Printed Fabrics

The synthesis of EA oligomer was carried out according to previous studies [12,13]. 300 ppm of HQ and 1000 ppm of TPP (out of the total AA and epoxy resin) were dissolved in AA by ultrasonication, then included in a round-bottom flask having the epoxy resin. The molar radio of AA and epoxy was set as 1:1. Magnetic stirrer condenser, and air inlet were used during the reaction. 10 % DPGDA was included in the reaction in order to decrease the viscosity of the resin. The reaction was performed at 100ºC for 2 h and another 2 h at 120ºC. At the end of the reaction phosphonium betaine was formed *via* the ring opening reaction of epoxide group which is initiated by the nucleophilic attack of the catalyst (TPP). The obtained betaine group abstracts a proton from AA by giving a carboxylate anion that is effective on the electrophilic carbon of phosphorus, resulting an ester bonding.

The obtained EA oligomer was included in coating formulations with 3 % photoinitiator, and MEK. MEK was used to lower the viscosity of the resin and to give wettability property to the fabrics. The printed fabrics were dipped into the coating solution for 3 min and then were dried in an oven (70ºC, 10 min) in order to evaporate the MEK. Then the coating layer was cured on the fabric surface by using 300 W Osram Ultra-Vitalux UV-lamp.

The obtained printed, EA coated fabric samples were washed twice by using ECE non-ionic detergent (4 g/L) solution in water at 40ºC for ½ h [14]. The quality of the printing process was evaluated both before and after the washing step. Furthermore, the uncoated/coated fabric samples before and after washing steps were characterized by light microscopy (Olympus B×51) in order to observe the surface properties in details.

Evaluation of the Printability Properties

CIE *L**, *a**, and *b** values of the printed uncoated samples and the printed samples coated with EA oligomer were measured by the D50 illuminant/2° observer values using X-Rite eXact Densitometer [15, 16]. BYK Portable glossmeter (BYK-Gardner Gmbh, Geretsried, Germany) was used based on ISO 2813 (2014) to determine the gloss values of the printed uncoated samples and the printed samples coated with EA oligomer [15, 16]. Both CIE *L**, *a**, and *b** color values and gloss values of the printed samples were measured immediately after printing and after each washing.

RESULTS AND DISCUSSION

Print Lightness

The lightness value shows the saturation of the color and ranges from 0 to 100. If it is close to 0, it means the print is darker whilst close to 100 means the print becomes lighter [17].

In Figs. 1 and 2, the L* values of the printed uncoated and EA coated CO, PA and PES textile fabrics, before and after double washing steps are given depending on various temperatures. Accordingly, the print lightness values slightly decreased with EA coating layer. After double washing, no significant change in print lightness values was recorded in uncoated and EA coated PES textile fabric,whereas in CO and PA fabrics, the print lightness values decreased, especially at 140 ºC after double washing (Fig. 2).

Print Chroma

High color saturation is an important property for good quality prints. High chroma indicates high color saturation. The print chroma value (C_{ab}) was calculated by Eq. 1 [18].

$$C_{ab} = \sqrt{a^{*2} + b^{*2}} \quad (1)$$

For a*, negative values indicate green, while positive values indicate magenta. For b*, negative values indicate blue, and positive values indicate yellow.

The chroma values of uncoated and EA coated CO, PA, and PES printed samples before and after double washings are given in Figs. 3 and 4 depending on the temperature change. According to

Fig. 3, a noticeable decrease in print chroma values for all samples after EA coated was recorded. This decrease proved that color gamut of EA coated samples is smaller than color gamut of uncoated samples. After a double washing process (Fig. 4), the print chroma values of uncoated samples decreased whereas in EA coated printed samples the print chroma values were all enhanced especially for CO and PES textile fabrics.

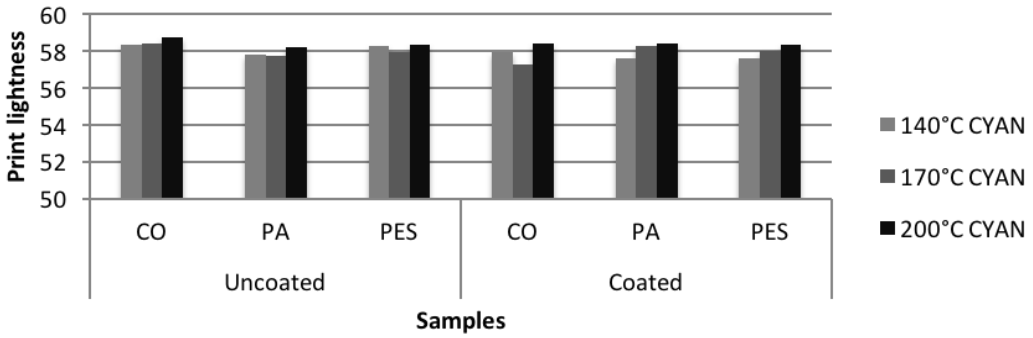

Fig. 1. Print lightness of uncoated and EA coated samples before washing

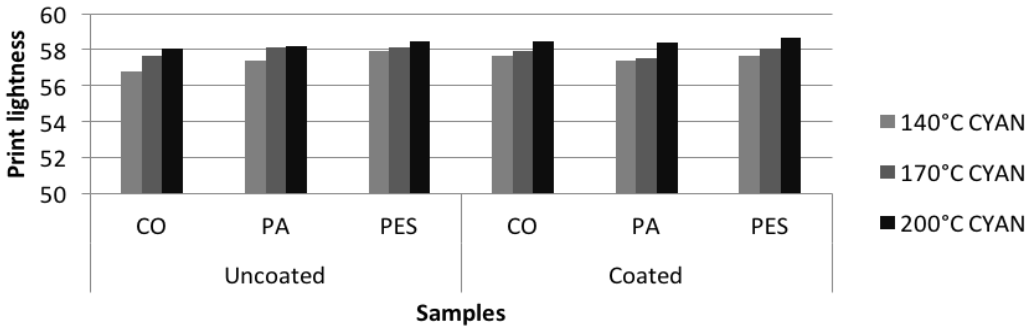

Fig. 2. Print lightness of uncoated and EA coated samples after double washing.

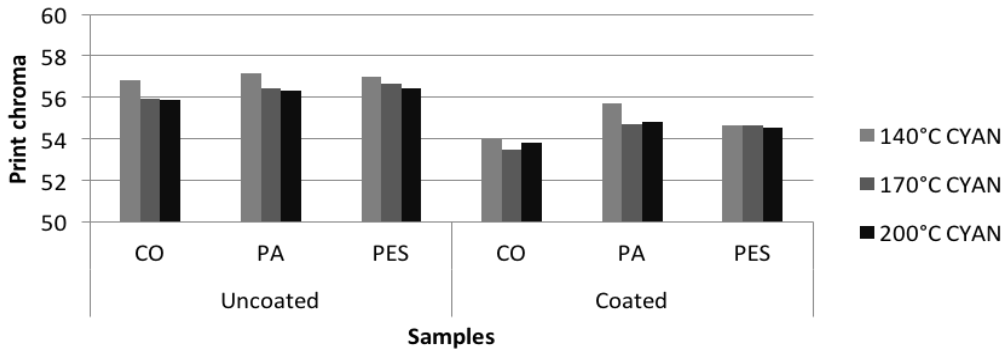

Fig. 3. Print chroma of uncoated and EA coated samples before washing.

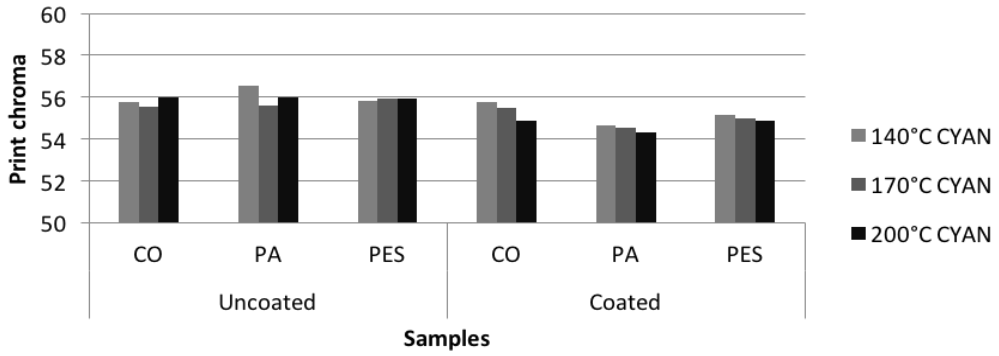

Fig. 4. Print chroma of uncoated and EA coated samples after double washing.

Print Gloss

Although surface properties of materials have an important effect on gloss value, the ink properties and its ingredients are effective to determine the final gloss value [19].

The gloss values of the printed samples of uncoated and EA coated CO, PA and PES textile fabrics at 60° before and after double washing depending on the temperature change are illustrated in Figures 5 and 6. Results showed that the print gloss values of the uncoated samples were all almost at the same levels. After EA coating, the print gloss values of PA textile fabric increased at 140°C, whilst decreased at 170°C and 200°C. The print gloss values of CO and PES textile fabrics all increased with EA coating step at all temperatures (Fig. 5). An increase in the print gloss value is an important property of the printability parameters, as the visual quality is enhanced by the print gloss value. After double washing process (Fig. 6), the print gloss values of uncoated and EA coated samples all decreased. The decrease in EA coated samples was greater than in uncoated samples.

Light Microscopy Images of Printed Samples

Fig. 7 shows the light microscopy images of printed-uncoated, printed-EA coated fabrics, and fabrics after abrasion resistance test. Accordingly, EA coating process caused a rough surface for all samples. The least roughness was observed in PA fabric samples. The roughness may be formed due to the shrinkage of EA layer after the UV-curing stage resulting in puckering of the textile fabric. After 50,000 cycle-abrasion test, the fabric images retained almost the same look in printed-EA coated samples.

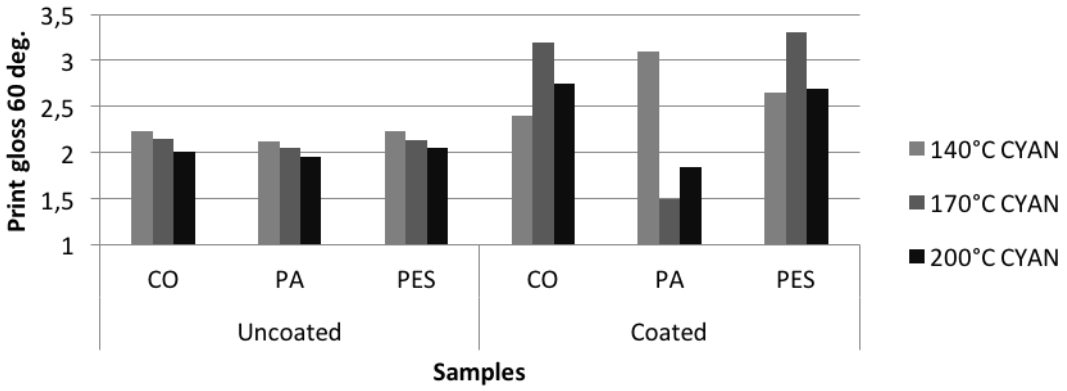

Fig. 5. Print gloss of uncoated and EA coated samples before washing.

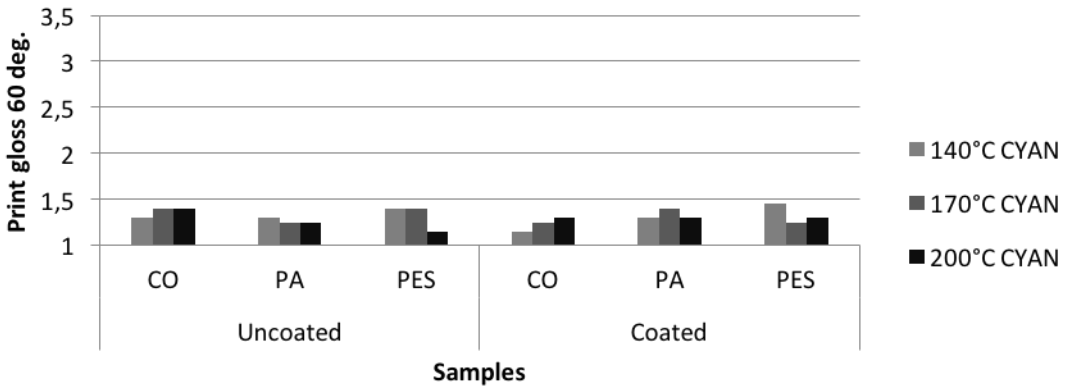

Fig. 6. Print gloss of uncoated and EA coated samples after double washing.

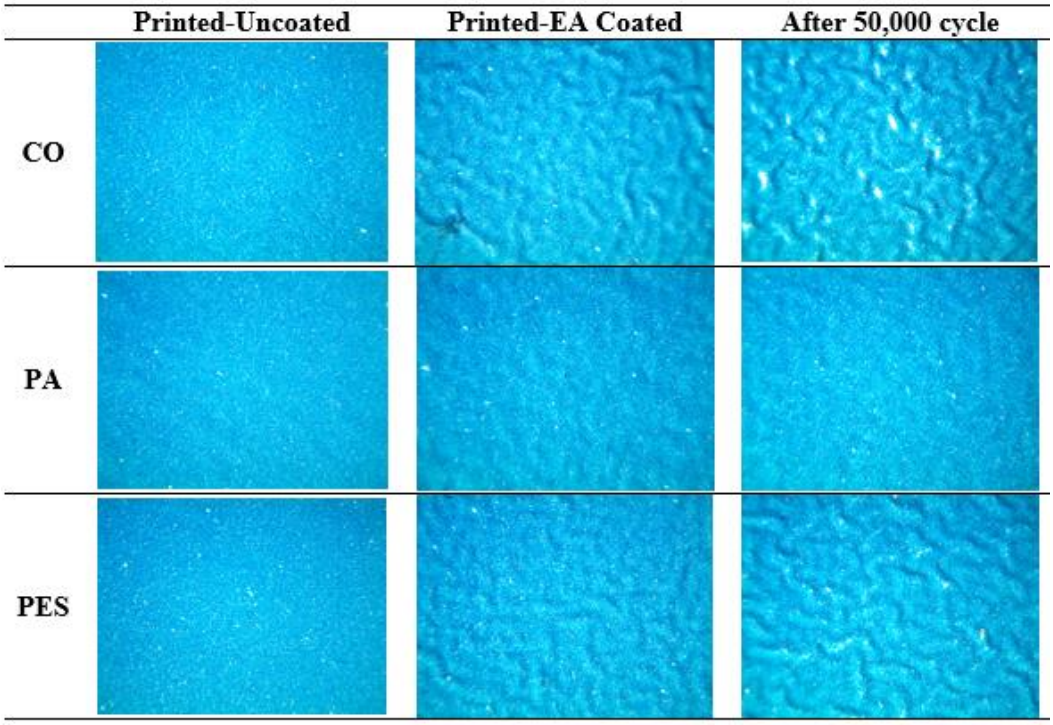

Fig. 7. Light microscopy images of printed, EA coated fabric samples after 50,000 cycles.

CONCLUSIONS

This study aimed to enhance the printing quality of the thermal transfer printing process in various textile fabrics. For this purpose the printing process was performed at three different temperatures. In order to enhance the printing quality an EA oligomer was synthesized and applied on the printed fabrics *via* dip-coating following the UV-curing step. Results proved that the EA coating layer enhanced the gloss values of printed fabrics.

1. The print lightness values of printed CO, PA, and PES textile fabrics decreased after the EA coating process. Considering the printing temperatures, the print lightness value of PES fabric was not affected after double washing, whilst the print lightness values of uncoated and EA coated CO and PA textile fabrics decreased, especially at 140 °C.

2. The print chroma value of printed CO, PA, and PES fabrics decreased after the EA coating process. After double washing process, the print chroma values of printed, EA coated CO and PES textile fabrics increased, whereas the print chroma values of uncoated printed fabrics decreased after double washing. Temperature changes during the printing process did not affect the print chroma values.

3. Before the washing process, the print gloss values of printed-EA coated CO, PA, and PES textile fabrics were higher than of printed-uncoated CO, PA and PES textile fabrics. However, after double washing process, the print gloss values of printed-EA coated CO, PA, and PES textile fabrics decreased and were at the same level as uncoated.

REFERENCES

1. M. G. Sari, B. Ramezanzadeh, M. Shahbazi, A. S. Pakdel, *Corrosion Sci.*, **92**, 162 (2015).
2. S. Jiang, Y. Shi, X. Qian, K. Zhou, X. Haiyan, S. Lo, Z. Gui, Y. Hu, *Ind. Eng. Chem. Research*, **52**, 17442 (2013).
3. F. Khelifa, M. E. Druart, Y. Habibi, F. Bénard, P. Leclère, O. Philippe, M. Olivier, P. Dubois, *Progress Org. Coatings*, **76**, 900-911(2013).
4. M. Liu, X. Mao, H. Zhu, A. Lin, D. Wang, *Corrosion Sci.*, **75**, 106 (2013).
5. S. K. Olsson, M. Johansson, M. Westin, E. Östmark, *Polymer Degradation and Stability*, **110**, 405 (2014).
6. O. Rahman, M. Kashif, S. Ahmad, *Progress Org. Coatings*, **80**, 77 (2015).
7. L. Shen, Y. Li, J. Zheng, M. Lu, K. Wu *Progress Org. Coatings*, **89**, 17 (2015).
8. Y. Huang, B. Cao, C. Xu, Q. Fan, J. Shao, *Textile Research J.*, **85**(7), 759 (2014).
9. M. Stančić, N. Kašiković, D. Novaković, R. Milošević, D. Grujić, *J. Graphic Eng. Design*, **4**, 27 (2013).
10. S. Sonmez, S. Akgul, Z. Yildiz, Investigation of Effect on The Image Quality and Durability on Different Textile Fabrics of The Change of The Temperature in Thermal Transfer Printing System, Paper presented at the Ist International Print Technologies Symposium, Istanbul, Turkey, 2015, p. 205.
11. S. Sonmez, *BioResources*, **12**, 760 (2016).

12. Y. Su, L. Cheng, K. Cheng, T. Don, *Materials Chem. Phy.*, **132**, 540 (2012).
13. Z. Yildiz, A. Gungor, A. Onen, I. Usta, *J. Ind. Textiles*, **46**, 596 (2016).
14. TS EN ISO 105-C06:Textiles - Tests for colour fastness - Part C06: Colour Fastness to Domestic and Commercial Laundering, 2012.
15. O. Simseker, B. Kurt, E. Arman, *Asian J. Chem.*, **24**, 5253 (2012).
16. S. Sonmez, *Asian J. Chem.*, **23**, 2609 (2011).
17. R. A. Viscarra-Rossel, B. Minasny, P. Roudier, A. B. McBratney, *Geoderma*, **133**, 320 (2006).
18. M. Fairchild, Color Appearance Models: CIECAM02 and Beyond, Paper presented at the tutorial notes, IS&T/SID 12th Color Imaging Conference, Scottsdale, USA, 2004.
19. M. C. Béland, S. Lindberg, P. A. Johansson, *J. Pulp Paper Sci.*, **26**, 120 (2000).
20. M. Juuti, T. Prykäri, E. Alarousu, H. Koivula, M. Myllys, A. Lähteelä, M. Toivakka, J. Timonen, R. Myllylä, K. E. Peiponen, *Colloids and Surfaces A: Physicochemical and Engineering Aspects*, **299**, 101 (2007).

Bulgarian Chemical Communications, Volume 51, Issue 1, (pp. 54 – 59) 2019

Hydrogen evolution reaction on electroless Ni-P coatings deposited at different pH values

V. Chakarova, M. Monev

Rostislaw Kaischew Institute of Physical Chemistry, Bulgarian Academy of Sciences, Acad. G. Bonchev Str., Bl. 11, 1113 Sofia, Bulgaria

Received August 7, 2018; Accepted September 12, 2018

Electroless Ni-P coatings are deposited on a steel substrate at pH of the solution from 2.8 to 5.3. Under these conditions, the P content of the Ni-P coatings varies from 10.5 to 18.1 mass %. It is found by electrochemical methods that the electrochemical activity of the amorphous Ni-P alloys in regard to the hydrogen evolution reaction in 1M KOH is comparable to that of electrodeposited Ni at current density close to the real values for hydrogen production. The structure, morphology and elemental composition of Ni-P coatings are characterized by XRD, SEM and EDS.

Key words: Electroless deposition, Ni-P coatings, Hydrogen evolution reaction, SEM, XRD

INTRODUCTION

Ni-based electrodes are usually employed in industrial electrolytic cells for electrochemical production of hydrogen from KOH solution. Their application is a result of the specific properties of Ni, as good corrosion resistance and high electrocatalytic activity in respect to hydrogen evolution reaction (HER) [1].

Ni-P_x alloys have been considered as potential candidates for HER electrocatalysis [2]. Articles, devoted to the regularities of HER on electroless Ni-P_x coatings, are significantly less than those referring to electrodeposited coatings and moreover, there is a contradiction between the experimental results. The activity of the electrodes depends on the experimental conditions of their preparation, as well as on the P content. According to [3, 4], the catalytic activity of electroless Ni-P coatings decreases with the increase of the P content in the alloy. However, it is reported in [5] that the catalytic activity is high at a high content of P upon annealing. Some authors point out an optimal value of P content of 3.8 mass % P [6], while other authors claim that this value is 10 mass % P [7]. The P content into the coating can be controlled by the deposition conditions, for example the acidity of the solution and the concentration of the reducing agent (NaH_2PO_2). The increase of pH leads to a decrease of the P content in the coating [8, 9], while the increase of NaH_2PO_2 concentration increases the P content [5, 7]. However, the conditions which cause changes in the P content of the alloys also change other properties of the coatings, for example structure [10], real surface [11] and corrosion resistance [12].

The aim of the present study was to obtain Ni-P coatings with different content of P by alteration of the acidity (pH) of the solution for electroless Ni deposition, as well as to investigate their activity with respect to HER in alkaline solution by electrochemical methods.

EXPERIMENTAL

The composition of the Ni-P bath is presented in Table 1.

Table 1. Composition and operating conditions of the Ni-P plating bath.

Components of the solution	Concentration
$NiSO_4.7H_2O$, g L^{-1}	25
$NaH_2PO_2.2H_2O$, g L^{-1}	22
CH_3COONa, g L^{-1}	20
Lactic acid /80 %/, g L^{-1}	20
Operating conditions	
pH	2.8 – 5.3
Temperature, ^oC	82
Deposition time, min	30

The coatings were deposited onto mild steel substrates with dimensions 50 × 35 mm. For further analyses, samples of appropriate size were cut out. To determine the elemental chemical composition of the coatings, energy dispersive spectroscopy (EDS) was used (JEOL JSM 733, Japan). The thickness of the coatings was measured on-line with a cross-section by X-ray microanalysis with the help of a combined scanning electron microscope (focused ion beam system LYRA I XMU (Tescan) equipped with EDX microanalyzer (Quantax, Bruker) (Fig. 1). Before preparing the cross-section,

* To whom all correspondence should be sent:
E-mail: vchakarova@ipc.bas.bg

the samples were covered with a protective layer of Cu by electroplating.

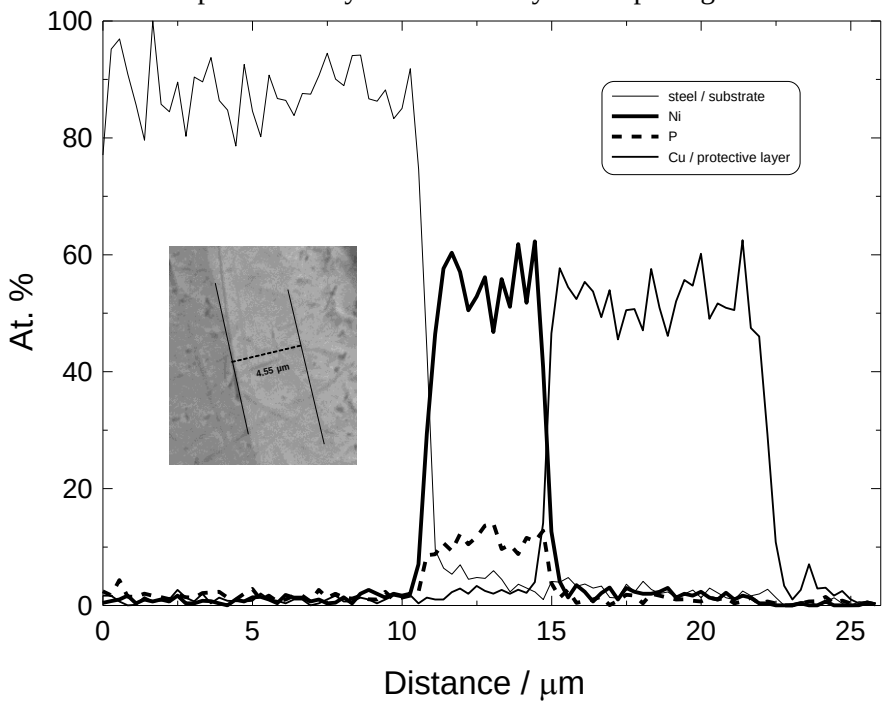

Fig. 1. EDX line-scan over the coating thickness. Inset: SEM of the measuring area with markers outlining the Ni-P layer.

The electrochemical investigations were performed in 1 M aqueous KOH solution (analytical reagent grade) at 20 °C. A three-electrode cell, supplied with a Pt-counter electrode, Hg/HgO reference electrode and working electrode with surface area of 0.2 cm^2 was used. The measurements were fulfilled by using a potentiostat/galvanosat model 263A (EG&G Princeton Applied Research, USA). The voltammetric dependences were obtained by scanning the potential from the open circuit potential to the vertex potential in the cathodic direction and *vice versa* at a scan rate of 25 mV s^{-1}. The electrokinetic properties of the Ni-P coatings in respect to HER were compared with those of electroplated Ni coatings deposited in Watt's electrolyte. For greater clarity, in some figures only the dependences of Ni-P coatings obtained at two pH values are presented.

X-ray powder diffraction patterns were recorded in the angle interval of 10-90° (2θ), on a Philips PW 1050 diffractometer, equipped with CuKα tube and scintillation detector.

The morphology of the coatings was examined by scanning electron microscopy (SEM) (JEOL JSM 733, Japan).

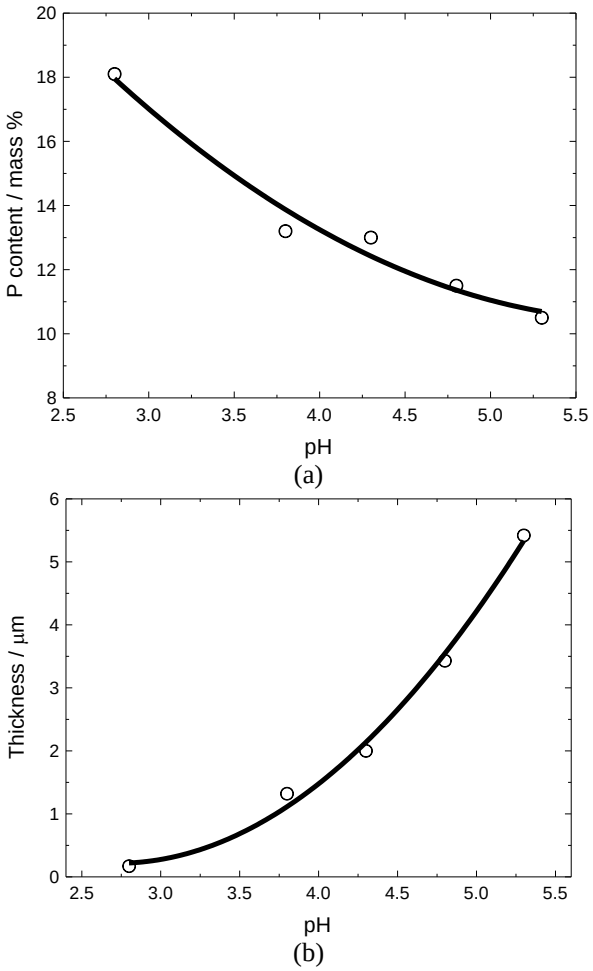

Fig. 2. Influence of pH of the solution on the content of P in the coating (a) and on the thickness of the Ni-P coating (b).

RESULTS

Influence of pH of the solution on the thickness and P content of the coatings

The decrease in pH of the solution leads to a decrease in the reduction activity of NaH_2PO_2 and at pH lower than 3, the reaction slows down [8]. The deposition rate of Ni increases with increase of pH, however, at pH higher than 5.5 the stability of the solution decreases. For that reason, the deposition rate and the elemental composition of the Ni-P coatings were determined at five selected values of pH in the range of pH 2.8-5.3. The dependences of the deposition rate and the content of P in the coating on pH of the solution are shown in Fig. 2. As seen, the increase of pH leads to an increase of the thickness of the N-P coating, while the content of P in the coating decreases. This conclusion is in agreement with the literature data [8, 9], as well as with our previous studies [13]. Generally, the values of the P content in the coating at the selected experimental conditions are in the range of high-P coatings [14]. This feature determines the amorphous structure of the coatings (Fig. 3).

Figure 4 presents the alteration of the surface morphology of the Ni-P coatings. For comparison, a picture showing the surface morphology of electrodeposited Ni coating is also given (Fig. 4a). As the Ni-P coating deposited at pH 2.8 for 30 min is very thin (an average thickness < 0.5 μm), it is possible to draw some conclusions for the initial stages of crystallization of the electroless coating (Fig. 4b). The iron has no catalytic properties, but as it is more negative than Ni, crystalline nuclei of Ni are formed through exchange onto the iron surface during its immersion into the solution for electroless deposition. The Ni nuclei initiate the subsequent process of deposition [8]. After formation of a thin Ni-P layer which covers the steel surface, the process of growing is followed by formation of spherical aggregates. With increase of pH, the deposition rate also increases and at one and the same time of deposition, thicker coatings are formed with a spherical nodular structure (Fig. 4c-e). With increase of pH, the size of the formations also increases and at pH 5.3, new nanosized spherical formations are observed on them (Fig. 4f). According to the X-ray microanalysis, the new formations are characterized by about 3 % higher content of P as compared with the remaining surface. The cited value is approximate, as the method can not exclude the contribution of the remaining surface.

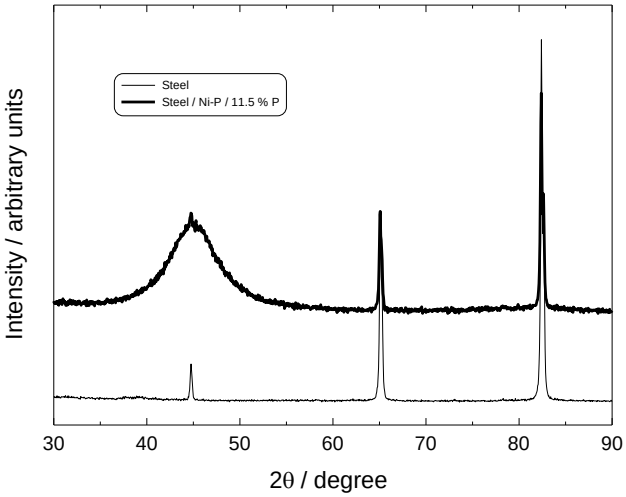

Fig. 3. XRD spectra of samples of steel and Ni-P coating containing 11.5 mass % P.

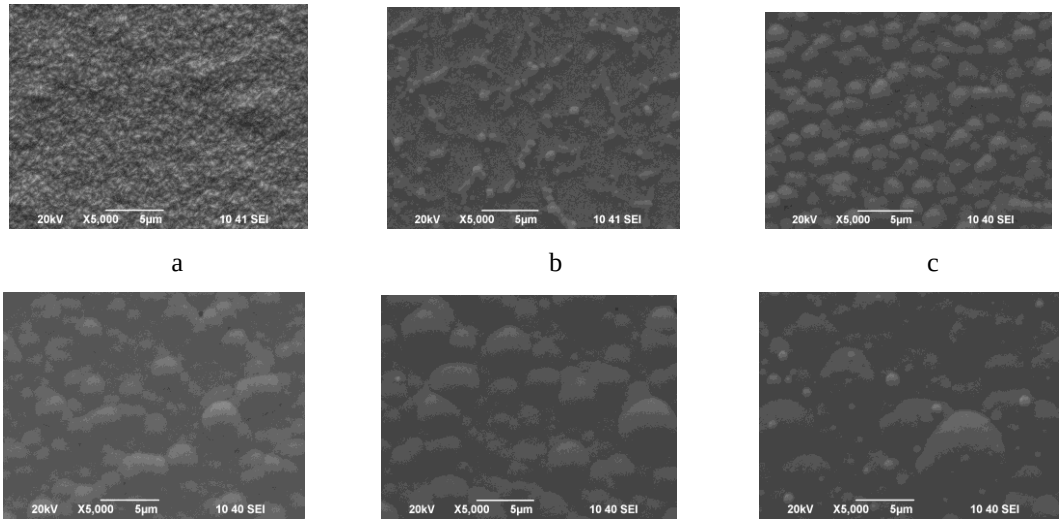

Fig. 4. Surface morphology of electrodeposited Ni (a) and alteration of the morphology of electroless Ni-P coatings *vs* pH of the solution: (b) pH 2.8, (c) pH 3.8, (d) pH 4.3, (e) pH 4.8, (f) pH 5.3.

Open circuit potential/time (OCP) measurements

Two types of Ni-P coatings with different content of P (Ni-11.5 mass % P and Ni-18.1 mass % P), as well as electrodeposited Ni coating were subjected to potential/time measurements at OCP in a solution of 1 M KOH (Fig. 5). Both samples of electroless Ni-P coatings show more negative potential as compared to that of electrodeposited Ni. The Ni-P coating with the lower P content of 11.5 mass % is more positive. This behavior could be explained not only by the lower P content, but also with the contribution of the smaller thickness of the coating.

Cyclic voltammetry

The activity of the electroless Ni-P coatings in respect to HER was investigated by cyclic voltammetry (Fig. 6). For comparison, samples of steel and electrodeposited Ni coating were also tested. In the investigated potential range, both types of electroless Ni-P coatings show lower activity in respect to HER as compared to electrodeposited Ni. The Ni-P coating with 11.5 mass % P shows higher activity and HER starts at a more positive potential as compared to the Ni-P coating with 18.1 mass % P.

The curve of the steel sample displays a cathodic maximum at about -1.2 V which can be explained by the reduction of the oxide layer. Similar maxima (but significantly smaller) are also registered on the corresponding curves of the Ni-P samples at a more positive potential. The maxima of the steel and Ni-P coating containing 18.1 mass % P are compared in the inset of Fig. 6.

Polarization measurements

At low polarization, the rate of HER is different for the different samples (Fig. 6). However, with increase of the current density to values of 10-20 A dm^{-2}, close to the real values for hydrogen production [1], the potentials of the Ni and Ni-P coatings overlap. Figure 7 presents the alteration of the polarization with time at 10 A dm^{-2}.

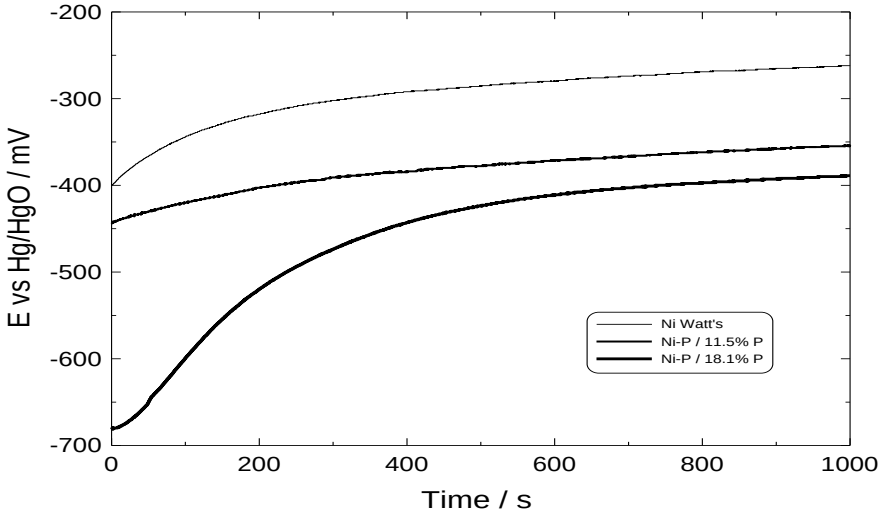

Fig. 5. OCP *vs*. time relations for samples of Ni, Ni-11.5 mass % P and Ni-18.1 mass % P in 1 M KOH.

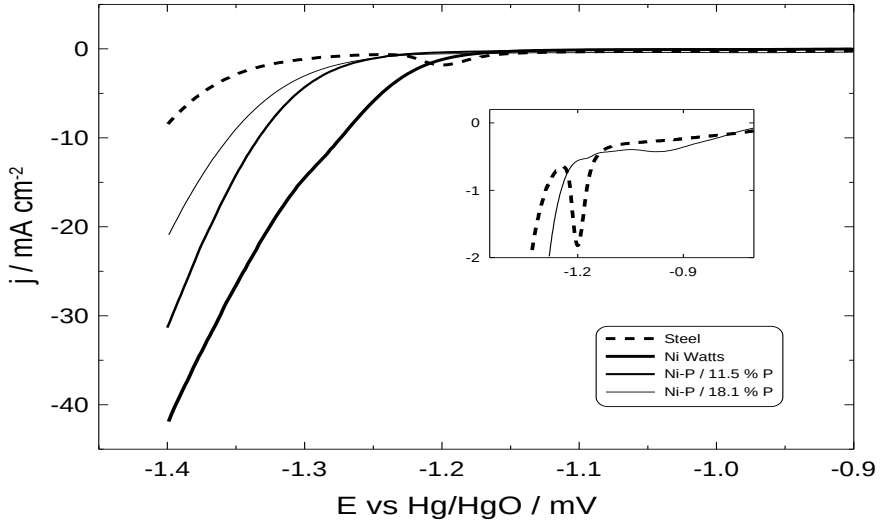

Fig. 6. Voltammograms of samples of steel, Ni, Ni-11.5 mass % P and Ni-18.1 mass % P in 1M KOH.

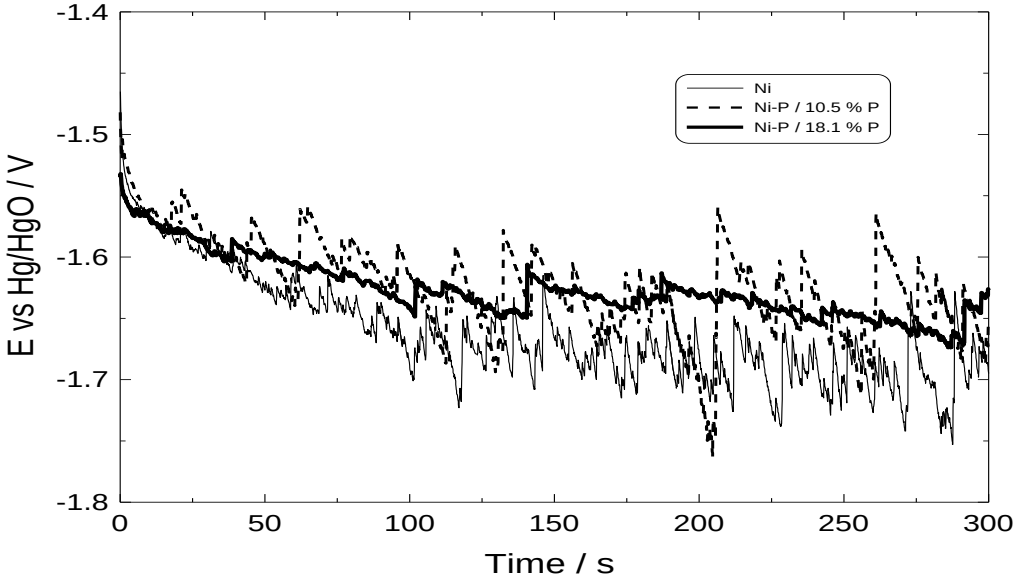

Fig. 7. Galvanostatic potential *vs*. time curves obtained with samples of Ni, Ni-10.5 mass % P and Ni-18.1 mass % P at 10 A dm^{-2} in 1M KOH.

CONCLUSIONS

Electroless Ni-P coatings with P content in the range from 10.5 to 18.1 mass % are deposited by alteration of pH of the solution from 2.8 to 5.3. The corresponding coatings display an amorphous structure. At sufficiently high current density (10-20 A dm^{-2}), the overpotential of HER on the Ni and Ni-P coatings is approximately the same. This feature of the Ni-P coatings allows the advantages of the electroless deposition as deposit uniformity and physical and chemical stability to be used, if necessary.

At lower polarization, different rates of HER are observed during the measurements with electrodeposited Ni and electroless Ni-P coatings. In addition to the content of P, the thickness of the coatings may also be a factor. Therefore, the next investigations should be directed to deposition of coatings with lower P content, probably by controlling the concentration of the reducing agent (NaH_2PO_2). It is also important to perform a more comprehensive study of HER on electroless Ni-P coatings obtained in the initial stages of the deposition.

Acknowledgement: *These investigations were performed with the financial support of the Project DFNP-17-127. The authors would like to thank Material Science Laboratory of the Faculty of Physics for performing surface measurements of Ni-P coatings.*

REFERENCES

1. K. Zeng, D. Zhang, Recent progress in alkaline water electrolysis for hydrogen production and applications, *Prog. Energy Combust. Sci*., **36**, 307 (2010).
2. A. Eftekhari, Electrocatalysts for hydrogen evolution reaction, *Int. J. Hydrogen Energy*, **42**, 11053 (2017).
3. J. J. Podesta, R. C. V. Piatti, A. J. Arvia, P. Ekdunge, K. Jüttner, G. Kreysa, The behaviour of Ni-Co-P base amorphous alloys for water electrolysis in strongly alkaline solutions prepared through electroless deposition, *Int. J. Hydrogen Energy*, **17**, 9 (1992).
4. G. Lu, P. Evans, G. Zangari, Electrolytic properties of Ni-based alloys toward hydrogen evolution reaction in acidic media, *J. Electrochem. Soc.*, **150**, A551 (2003).
5. A. M. Fundo, L. M. Abrantes, The electrocatalytic behavior of electroless Ni-P alloys, *J. Electroanalyt. Chem*., **600**, 63 (2007).
6. W. Wang, T. Nakamura, Hydrogen evolution behavior on electroless nickel deposit in an acidic solution, *J. Surf. Finish. Soc*., **46**, 278 (1995).
7. S. M. A. Shibli, V. S. Dilimon, Effect of phosphorous content and TiO_2-reinforcement on Ni-P electroless plates for hydrogen evolution reaction, *Int. J. Hydrogen Energy*, **32**, 1694 (2007).
8. G. Gavrilov, Z. Nikolov, Electroless deposition of nickel and composite coatings, Technika, Sofia, 1985.
9. M. Schlesinger, Electroless deposition of nickel, in: Modern electroplating, Fourth ed., M. Schlesinger, M. Paunovic (eds.), JohnWiley&Sons, Inc., 2000, p. 667.
10. J. Sudagar, J. Lian, W. Sha, Electroless nickel alloy, composite and nano coatings – A critical review, *J. Alloys Compd*., **571**, 183 (2013).
11. M. Islam, M. Rizwan Azhar, N. Fredj, T. David Burleigh, Electrochemical impedance spectroscopy and indentation studies of pure and composite

electroless Ni-P coatings, *Surf. Coat. Technol*., **236**, 262 (2013).

12. K. Hari Krishanan, S. John, K. N. Srinivasan, J. Praveen, An overall aspect of electroless Ni-P depositions - A review article, *Metall. Mater. Trans. A*, **37A,** 1917 (2006).
13. M. Georgieva, M. Petrova, V. Chakarova, Obtaining of electroless Ni-P/ZrO_2 composite coatings on flexible substrates of polyethylene terephthalate, *Bulg. Chem. Commun.*, **45**, 116 (2013).
14. M. M. Mirza, E. Rasu, A. Desilva, Surface coatings on steel pipes used in oil and gas industries – A review, *ACSJ*, **13**, 1 (2016).

Bulgarian Chemical Communications, Volume 51, Issue 1, (pp. 60 – 65) 2019

In silico investigation of the relation between calcium channel blockers' molecular descriptors and oral bioavailability data

J. V. Odović*

Department of Analytical Chemistry, Faculty of Pharmacy, University of Belgrade, Vojvode Stepe 450, Belgrade, Serbia

Received November 2, 2017; Accepted November 11, 2018

Calcium channel blockers are commonly prescribed antihypertensive drugs. In this study, nine calcium channel blockers (amlodipine, felodipine, isradipine, nicardipine, nifedipine, nimodipine, nisoldipine, verapamil and diltiazem) were investigated to evaluate the relationship between their molecular properties and oral bioavailability data collected from relevant literature. Several molecular descriptors of calcium channel blockers: lipophilicity descriptors, different log*P* values (Alog*Ps*, AClog*P*, AB/log*P*, milog*P*, Alog*P*, Mlog*P*, KOWWINlog*P*, XLOG*P*2, XLOG*P*3), aqueous solubility data (log*S*), electronic descriptor - polar surface area (PSA), constitutional parameter - molecular weight (Mw), geometric descriptor - volume value (Vol), acidity descriptor (pKa) were calculated using different software packages. The relationships between computed molecular descriptors and literature-obtained oral bioavailability data were firstly investigated using simple linear regression analysis showing relatively poor correlations with $R^2 < 0.6$. In continuation, multiple linear regression was applied to achieve higher correlation between calcium channel blockers' oral bioavailability and their molecular properties, on the first place lipophilicity and one additional, molecular descriptor. The best correlations were established between calcium channel blockers' oral bioavailability and their lipophilicity data (milog*P* or KOWWINlog*P*) with application of acidity descriptor as additional independent variable (R^2 = 0.783 and R^2 = 0.826). Application of computed molecular descriptors in evaluating drugs bioavailability was checked on three additional, fourth generation CCBs, cilnidipine, lacidipine, lercandipine.

Keywords: Calcium channel blockers, oral bioavailability, lipophilicity, acidity.

INTRODUCTION

High blood pressure, hypertension, is a world widespread disease. Typically, hypertension has no symptoms but it may have deadly consequences if not treated. Calcium channel blockers (CCBs) are among the most widely applied drugs in cardiovascular medicine. They can be applied not only in hypertension but also in angina pectoris, post-myocardial infarction, supraventricular dysrhythmias, hypertrophic cardiomyopathy [1-3].

According to their structural and functional distinctions CCBs can be subdivided in: dihydropyridine derivatives: amlodipine, felodipine, isradipine, lacidipine, lercanidipine, nicardipine, nifedipine, nisoldipine; phenylalkylamine: verapamil and benzothiazepine derivatives: diltiazem [1].

Drugs' clinical success mostly depends on their absorption, distribution, metabolism or route of elimination (ADME) [4]. A number of molecular physicochemical properties such as lipophilicity, acidity (pKa), molecular weight (Mw), molecular volume (Vol), polar surface area (PSA) or solubility data (logS), play important role in drugs absorption, penetration into tissues, degree of distribution, degree of plasma protein binding, activity and route of elimination [5-10].

Lipophilicity is one of the most significant physicochemical properties of biologically active molecules. Its importance in drug research is a consequence of hydrophobic interactions of the drugs with their biological targets, penetration across biological membranes during drug transport, as well as toxic aspects of drug action [4]. The lipophilicity influences drugs' absorption, distribution, binding to plasma proteins and elimination [7]. It can be characterized by the *n*-octanol/water partition coefficient (log$P_{O/W}$). The traditional technique for determination of selected molecule's lipophilicity, its log*P* value, is the so-called *shake flask* method [7]. Besides, different chromatographic techniques, high-performance liquid chromatography or thin-layer chromatography, are well known as methods that can yield significant amounts of retention data which can be correlated with physicochemical and biological properties, on the first place lipophilicity, for large sets of structurally different compounds. However, today, *in silico* obtained hydrophobicity parameters, calculated log*P* values, are generally accepted as a measure of drug's lipophilicity. Also numbers of other calculated molecular descriptors are applied in evaluation of different drugs' ADME properties [6 -10].

* To whom all correspondence should be sent:
E-mail: jodovic@pharmacy.bg.ac.rs

According to the available literature, a number of authors investigated antihypertensive drugs including those belonging to CCBs group, their design and synthesis [11,12] as well as pharmacokinetics, pharmacodynamics and efficacy [13-16].

In recently published papers acidity, lipophilicity, solubility or absorption were evaluated for a large group of antihypertensive drugs [17], as well as for selected ACE imhibitors [18] based on their molecular structure with application of computer programs. Also, in our previous papers the correlation between ACE inhibitors' lipophilicity, investigated using ultra-high performance liquid chromatography–tandem mass spectrometry and reversed-phase thin-layer chromatography, and oral absorption [19] as well as the effect of calcium channel blockers' molecular properties on their route of elimination [20] were studied. In continuation to these researches, the aim of this study was to investigate the correlation between oral bioavailability data of nine calcium channel blockers and their different molecular properties calculated using three different software packages [21-23]. The most suitable molecular descriptor should be established.

THEORETICAL

Investigated drugs

In this study nine most often prescribed calcium channel blockers were investigated:

1. Amlodipine - (3-ethyl 5-methyl2-[(2-aminoethoxy)methyl]-4-(2-chlorophenyl)-6-methyl-1,4-dihydro-3,5-pyridinedicarboxylate);
2. Felodipine - (ethyl methyl 4-(2,3-dichlorophenyl)-2,6-dimethyl-1,4-dihydro-3,5-pyridinedicarboxylate);
3. Isradipine - (isopropyl methyl 4-(2,1,3-benzoxadiazol-4-yl)-2,6-dimethyl-1,4-dihydro-3,5-pyridinedicarboxylate);
4. Nicardipine - (2-[benzyl(methyl)amino] ethylmethyl2,6-dimethyl-4-(3-nitrophenyl)-1,4-dihydro-3,5-pyridinedicarboxylate);
5. Nifedipine = (dimethyl 2,6-dimethyl-4-(2-nitrophenyl)-1,4-dihydro-3,5-pyridinedicarboxylate);
6. Nimodipine - (isopropyl 2-methoxyethyl 2,6-dimethyl-4-(3-nitrophenyl)-1,4-dihydro-3,5-pyridinedicarboxylate);
7. Nisoldipine - (isobutyl methyl 2,6-dimethyl-4-(2-nitrophenyl)-1,4-dihydro-3,5-pyridinedicarboxylate);
8. Verapamil - (2-(3,4-dimethoxyphenyl)-5-{[2-(3,4-dimethoxyphenyl)ethyl](methyl)amino}-2-isopropylpentanenitrile) and
9. Diltiazem - ((2S,3S)-5-[2-(dimethylamino) ethyl]-2-(4-methoxyphenyl)-4-oxo-2,3,4,5-tetrahydro-1,5-benzothiazepin-3-yl acetate).

Additionally, three CCBs of fourth generation: cilnidipine, lacidipine, lercandipine, were selected for testing the applicability of the correlation established in the first part of the study.

Calculations

The CCBs lipophilicity descriptors, nine different log*P* values (Alog*P*s, AClog*P*, AB/log*P*, milog*P*, Alog*P*, Mlog*P*, KOWWINlog*P*, XLOG*P*2, XLOG*P*3), as well as their aqueous solubility data (log*S*) were calculated using the software package, Virtual Computational Chemistry Laboratory [21]. The software package Molinspiration Depiction Software (Molinspiration Cheminfirmatics) [22] was used for the calculation of several molecular descriptors, electronic descriptor - polar surface area (PSA); constitutional parameter - molecular weight (Mw) and geometric descriptor - volume value (Vol) while software package DrugBank [23] was used for the calculation of CCBs acidity descriptors pK_a values. The values of CCBs molecular descriptors, Mw, Vol and PSA were presented in our previous paper where the effect of calcium channel blockers' molecular properties on their route of elimination [20] was investigated, while selected lipophilicity descriptors (milog*P* and KOWWINlog*P*), as well as acidity descriptors, pKa values are presented in Table 1. The oral bioavailability data of the investigated CCBs (Table 2) were obtained from the relevant literature [1]. The statistical analysis of the regressions was performed using Microsoft Excel 2003 and Origin 7.0 PRO (Origin Lab Corporation, USA).

RESULTS AND DISCUSSION

The bioavailability is one of the most important pharmacologic properties in drug design and development. It is a subcategory of absorption and represents the fraction of drugs' administered dose that reaches the systemic circulation. High bioavailability reduces the amount of the administered drug necessary to achieve a desired pharmacological effect and consequently can reduce the risk of side-effects and toxicity. On the contrary, poor oral bioavailability can result in low efficacy and lead to unpredictable response to a drug.

Bioavailability for intravenously administered drugs is 100%. However, for orally administered drugs, bioavailability usually decreases due to incomplete absorption and first-pass metabolism, as well as due to high degree of plasma protein binding. Furthermore, drugs administration with or

without food also affects absorption. Concurrent intake of other drugs may alter absorption and first-pass metabolism, while intestinal motility alters the dissolution and may affect the degree of chemical degradation of the drug by intestinal microflora.

Drugs physical properties such as hydrophobicity, acidity, solubility, molecular mass, volume and polar surface area, as well as drugs formulation, age and gender of the patients or dosing scheme also exert important influence on drugs' BA. Drug's oral absorption and bioavailability, as well as duration of action or efficiency of its elimination is highly affected by its lipophilicity, acidity, solubility, molecular size and other molecular properties. The molecules with high lipophilicity show higher degree of oral absorption and bioavailability, better penetration into tissues and distribution compared to less lipophilic ones with similar properties [1-3,24,25].

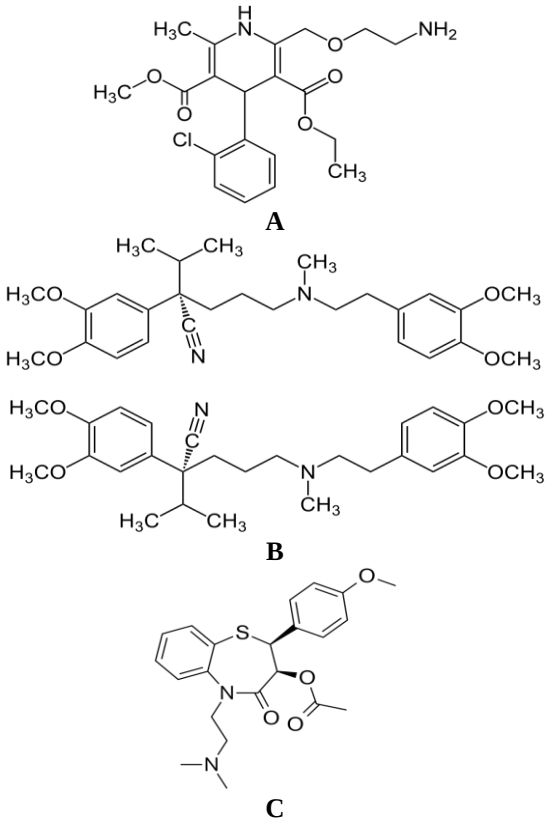

Figure 1. The structures of the CCBs representatives: **A)** Amlodipine; **B)** Verapamil; **C)** Diltiazem

According to the available literature, CCBs pharmacokinetics, pharmacodynamics and efficacy were investigated by a number of authors [13-16]. Still, most of these methods have certain limitations and a new approach for fast, reliable and cost-effective evaluation of CCBs oral bioavailability should be developed. Since drugs oral bioavailability importantly affects drugs activity, the application of computed molecular descriptors in prediction of drugs oral bioavailability is of great importance, especially for the newly synthesized drugs.

In this research nine CCBs (amlodipine, felodipine, isradipine, nicardipine, nifedipine, nimodipine, nisoldipine, verapamil and diltiazem) were studied in order to evaluate the correlation between their oral bioavailability data obtained from relevant literature and calculated molecular descriptors. The structures of the CCBs representatives: A) Amlodipine, dihydropyridine derivative; B) Verapamil, phenylalkylamine; and C) Diltiazem, benzothiazepine derivative are presented in Fig. 1.The main goal was to establish a high-throughput approach using simple or multiple linear regression analysis capable of predicting oral bioavailability data of selected CCBs. Several CCBs molecular descriptors (electronic descriptor – PSA, constitutional parameter – Mw, geometric descriptor – Vol, values, aqueous solubility data – logS and acidity descriptor – pKa), as well as a number of lipophilicity descriptors (Alog*P*s, AClog*P*, AB/log*P*, milog*P*, Alog*P*, Mlog*P*, KOWWINlog*P*, XLOG*P*2, XLOG*P*3) were calculated using different software packages.

According to the data available from the literature, most of CCBs, with exception of amlodipine and nifedipine, have relatively low oral bioavailability because of extensive first-pass metabolism. Their oral bioavailability varies from 5% for nisoldipine, through 58% (45% to 70%) for nifedipine, to around 80% for amlodipine [1-3]. The CCBs selected molecular descriptors are presented in Table 1.

Table 1. Calculated molecular descriptors of investigated CCBs.

CCBs	milog*P*	KOWWINlog*P*	pKa
1.	2.58	2.07	8.79
2.	4.80	4.46	16.04
3.	3.81	3.49	16.14
4.	5.00	3.90	7.99
5.	3.07	2.50	15.92
6.	4.10	3.13	15.85
7.	4.19	3.90	15.93
8.	4.55	4.80	9.60
9.	3.34	2.79	8.37

The numbers denote CCBs.

The correlations between CCBs oral bioavailability data obtained from relevant literature and the calculated descriptors (PSA, Mw, Vol, pKa, log*P*, log*S*) were firstly investigated using simple linear regression. The relationships between CCBs oral bioavailability and the majority of their molecular descriptors, PSA, Mw, Vol, pKa,

log*P*, log*S*, provided correlations with coefficient R^2 lower than 0.40. Only for lipophilicity descriptors milog*P* and KOWWINlog*P* correlations with R^2=0.570 and R^2=0.542, respectively, were established.

Following, in the next stage of the study, the relationships between CCBs oral bioavailability data and two different CCBs molecular descriptors were investigated using multiple linear regression (MLR). The lipophilicity descriptors milog*P* or KOWWINlog*P* values were chosen as the first independent variable since they showed best correlations with CCBs oral bioavailability, while values of Mw, Vol, pKa and PSA were chosen as possible second independent variable. Values of aqueous solubility data, log*S* values, were not applicable as the second independent variable, since their relationships with milog*P* and KOWWINlog*P* values provide correlations with R^2 = 0.413 and R^2 = 0.385, respectively.

The MLR analyses with application of lipophilicity descriptor, KOWWINlog*P* and one additional calculated molecular descriptor, Mw, Vol or PSA, as independent variable provided correlations with coefficients (R^2) from 0.607 to 0.660 (R^2 = 0.607; R^2 = 0.618; R^2 = 0.660, respectively). Similar correlation with slightly lower coefficient, R^2 = 0.590 was obtained in MLR with application of milog*P* and PSA as independent variables while better correlations were achieved with application of milog*P* and Mw or Vol values as independent variables (R^2 = 0.725 and R^2 = 0.671, respectively).

However, the best correlations between CCBs bioavailability and calculated molecular descriptors, with acceptable correlation coefficients (R^2), as well as probability value ($P < 0.05$) were established using MLR analysis with application of lipophilicity descriptors, milog*P* or KOWWINlog*P* values and acidity descriptor, pKa as independent variables ((Eq. 1.) and (Eq. 2.)):

$$BA_{pred}(\%) = -20.972(\pm5.065)\text{milog}P - 3.112(\pm1,067)pK_a + 155.575(\pm23.544) \quad \text{Eq. 1.}$$

with n = 9; R^2 = 0.822; S.D. = 11.629; F = 13.881

$$BA_{pred}(\%) = -18.068(\pm5.051)\text{KOWWINlog}P - 3.036(\pm1.186)pK_a + 134.319(\pm22.292) \quad \text{Eq. 2.}$$

with n = 9; R^2 = 0.781; S.D. = 12.904; F = 10.711

The CCBs bioavailability data collected from relevant literature, as well as those predicted using MLR with application of computed lipophilicity descriptor, milog*P* or KOWWINlog*P* and acidity descriptor, pKa as independent variables are presented in Table 2 and in Figure 2.

The interrelationships between obtained BA data of calcium channel blockers investigated, those collected from relevant literature, predicted from milog*P* and pKa values and those predicted from KOWWINlog*P* and pKa values were studied. Obtained coefficients are presented in Table 3 and it can be seen that very good agreements were obtained between all three BA values.

Table 2. CCBs BA data collected from relevant literature (1); predicted from milog*P* and pKa values (2) and KOWWINlog*P* and pKa values (3).

CCBs	BA (1)	BA (2)	BA (3)
1.	77	74	70
2.	15	5	5
3.	20	25	22
4.	35	26	40
5.	58	42	41
6.	13	20	30
7.	5	18	15
8.	27	30	18
9.	50	60	58

(1) BA (%) data obtained from literature [1]. The numbers denote CCBs.

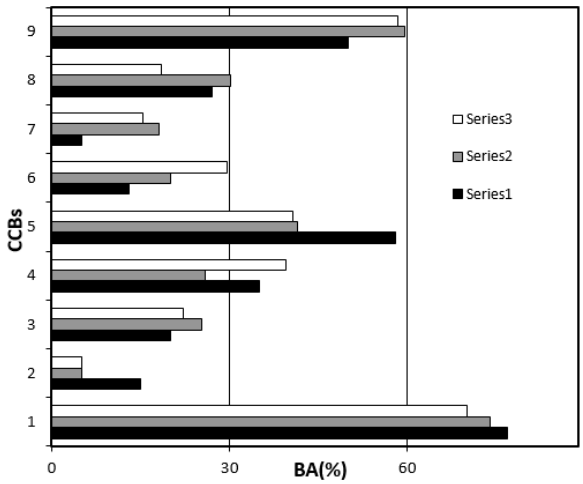

Figure 2. Relationship between CCBs bioavailability data collected from relevant literature and [1] *(Series 1)*; predicted using MLR with application of milog*P* and pKa values *(Series 2)* and KOWWINlog*P* and pKa values *(Series 3)*. The numbers denote CCBs.

Table 3. Interrelations between different BA data of calcium channel blockers investigated: those collected from relevant literature (1); predicted from milog*P* and pKa values (2) and KOWWINlog*P* and pKa values (3).

	BA (1)	BA (2)	BA (3)
BA (1)	1		
BA (2)	0.908	1	
BA (3)	0.884	0.935	1

Following, in the final stage of the study, the best established correlation obtained in MLR with application of milogP and pKa as independent

variables, was used to calculate the values of oral bioavailability for additional CCBs – nitrendipine, as well as three fourth-generation drugs: cilnidipine, lacidipine and lercandipine.

There are limited data available in the literature for these CCBs, showing relatively low values of their oral BA: for nitrendipine 10-23% and for lacidipine and lercandipine: 18.5% (range 4 to 52) and around 10%, respectively. The calculated pKa values for nitrendipine, cilnidipine, lacidipine and lercandipine were 15.88, 15.61; 16.12 and 8.64, respectively [23]. The values of their lipophilicity parameters, milogP, which provided best correlation, Eq.1, were 3.94, 5.72, 5.46 and 7.87, respectively [22] indicating large differences between nitrendipine (with milogP 3.94) and the very lipophilic CCBs of fourth generation.

Considering computed molecular descriptors and using MLR (Eq. 1) for nitrendipine as additional checking CCB, a value of 23% for oral BA was obtained, showing very good agreement between literature available and predicted oral BA data.

However, for selected CCBs of fourth generation, BA values around zero were calculated, indicating their low oral BA, but also their incompatibility with the established model (Eq 1). These results could be explained with their molecular properties. Namely, lercandipine is one of the CCBs with highest molecular weight (Mw = 612), volume value (575), lipophilicity (milogP = 7.87) and the lowest solubility (logS = -6.00). Cilnidipine and lacidipine also have very high lipophilicity (with milog P 5.72 and 5.46) and very low solubility, log*S* values (-4.99 and -4.67 respectively). Considering these values it can be seen that these three drugs, CCBs of fourth generation, are not in accordance with "Lipinski's rule of five" and they should not be considered in relationship between CCBs lipophilicity and oral BA data established for CCBs which belong to drugs of first to third generation.

The acceptable correlations that were found using MLR analyses between oral bioavailability of drugs belonging to first to third generation of CCBs data with application of their *in silico* obtained molecular descriptors – lipophilicity parameter (milog*P* and KOWWINlog*P*) and in the first place acidity descriptor (pK_a) and in addition constitutional descriptor - molecular weight (Mw) and geometric descriptor - volume value (Vol) confirmed descriptors calculations as a useful screening technique which is, however, not always capable of exact evaluation of oral bioavailability of compounds with some deviation in structure.

CONCLUSION

This study included nine often prescribed calcium channel blockers. The correlation between calcium channel blockers oral bioavailability data and different molecular descriptors was investigated. Relatively poor correlation was obtained between oral bioavailability data and calculated molecular descriptors using simple linear regression analysis (R^2 < 0.4). However, the application of two molecular descriptors milogP or KOWWINlog*P* values and Mw, Vol or pKa as independent variables in MLR analysis provided better correlations. The best correlations were established using MLR analysis with application of lipophilicity (milog*P* or KOWWINlog*P*) and acidity descriptor (pKa) as independent variable (R^2 = 0.783 and R^2 = 0.826, respectively). As a result, applicability of calculated molecular descriptors especially lipophilicity descriptors, milog*P* and KOWWINlog*P* and acidity descriptor, pKa, in CCBs oral bioavailability evaluation was established.

The proposed methodology and correlations that were found in the presented study confirmed that molecular properties, especially lipophilicity and acidity but also molecular weight and volume are essential for drugs oral bioavailability. Obtained correlations could be regarded as a new, additional, *in vitro* approach appropriate for evaluating oral bioavailability of the investigated group of calcium channel blockers. The application of computed molecular descriptors can be highly useful in drug research.

Acknowledgment: *This work was partly supported by the Ministry of Education, Science and Technological Development of the Republic of Serbia as a part of Project TR34031.*

REFERENCES

1. T. L. Lemke, D.A. Williams (eds.), The Foye's Principles of Medicinal Chemistry, 7th edn., Lippincott Williams & Wilkins, Philadelphia, 2013.
2. H. P. Rang, J. M. Ritter, R. J. Flower, G. Henderson, Rang and Dale's Farmacology, 8th edn., Elsevier, Churchill Livingstone, 2012.
3. A. C. Moffat, M. D. Osselton, B. Widdop (eds.), Clarke's Analysis of Drugs and Poisons 4th edn., Pharmaceutical Press, London, 2011.
4. L. Di, E. H. Kernsy, *Curr. Opin. Chem. Biol.*, **7,** 402 (2003).
5. M. Remko, A. Remková, R. Broer, *Molecules*, **21** (185), 1 (2016).
6. Z. Mandić, **(**ed.) Physico-Chemical Methods in Drug Discovery and Development, IAPC Publishing, Zagreb, Croatia, 2012.

7. T. Hartmann, J. Schmitt, *Drug Discov. Today Techn*. **1**(4) 431 (2004)
8. A. T. Florence, D. Attwood, Physicochemical Principles of Pharmacy, 6th ed., Pharmaceutical Press, London, 2016.
9. Y. H. Zhao, J. Le, M. H. Abraham, A. Hersey, P. J. Eddershaw, C. N. Luscombe, D. Boutina, G. Beck, B. Sherbone, I. Cooper, J. A. Platts, *J. Pharm. Sci.*, **90**, 749 (2001).
10. Y. H. Zhao, M. H. Abraham, J. Le, A. Hersey, C. N. Luscombe, G. Beck, B. Sherborne, I. Cooper, *Pharmac. Res.*, **19,** 1446 (2002).
11. J. A. M. Christiaans, A. D. Windhorst, P. M. Groenenberg, H. Van der Goot, H. Timmerman, *Eur. J. Med. Chem.*, **28**, 859 (1993).
12. P. K. Kalavagunta, P. K. Bagul, A. Jallapally, S. Kantevari, S. K. Banerjee, N. Ravirala, *Eur. J. Med. Chem.*, **83,** 344 (2014).
13. E. D. Pozo, J.M. Baeyens, *Eur. J. Pharmacol*. **128**(1–2), 49 (1986).
14. L. Sepehr-Ara, S. A. Seyed Ahmad Mohajeri, M. Mahmoudian, *Pathophysiology*, **18(**3),175 (2011).
15. I. Whyte, N. Buckley, A. Dawson, *Medicine*, **40**, 112 (2012).
16. C. Mayama, *Eur. J. Pharmacol.* **739,** 96 (2014).
17. M. Remko, M. Swart, M. F. Bickelhaupt, *Bioorg. Med. Chem.* **14,** 1715 (2006).
18. M. Remko, *Chem. Papers*, **61**(2), 133 (2007).
19. J. V. Odovic, B. D. Markovic, R. D. Injac, S. M. Vladimirov, K. D. Karljikovic-Rajic, *J. Chromatogr. A.*, **1258**, 94 (2012).
20. J. Trbojević-Stanković, J. Odović, R. Jelić, D. Nešić, B.Stojimirović, *Arch. Biol. Sci.*, **67**(3), 801 (2015).
21. Tetko IV. Virtual Computational Chemistry Laboratory. Available from URL: http://vcclab.org (accessed on September 2017).
22. Molinspiration software or free molecular property calculation services. Available from URL: http://molinspiration.com (accessed on September 2017).
23. Program available online: http://drugbank.ca (accessed on September 2017).
24. C. A. Lipinski, *J. Pharmacol. Toxicol. Met.*, **44**, 235 (2000).
25. A. K. Ghose, V. N. Viswanadhan, J. J Wendoloski, *J. Combin. Chem.*, **1**, 55 (1999).
26. A. G. Asuero, A. Sayago, A. G. Gonzalez, *Crit. Rev. Anal. Chem.*, **36,** 41 (2006).

Bulgarian Chemical Communications, Volume 51, Number 1 (pp. 66 – 72) 2019

Improvement of the electrochemical properties of Ni-Zn rechargeable batteries by adding B(Pb)SrCaCuO conducting ceramics

G. Ivanova[1], A. Stoyanova-Ivanova[2], D. Kovacheva[3], A. Stoyanova[1*]

[1] *Institute of Electrochemistry and Energy Systems, Bulgarian Academy of Sciences, Acad. G. Bonchev Str, 10, 1113 Sofia, Bulgaria.*

[2] *Georgi Nadjakov Institute of Solid State Physics, Bulgarian Academy of Sciences, 72, Tzarigradsko Chaussee Blvd., 1784 Sofia, Bulgaria*

[3] *Institute of General and Inorganic Chemistry, Bulgarian Academy of Sciences, Acad. G. Bonchev Str. 11, 1113, Sofia, Bulgaria*

Received November 22, 2018; Revised December 12, 2018

The improvement of the electrochemical properties of Zn-electrode in the Ni-Zn battery cell by adding two types of B(Pb)SrCaCuO conducting ceramics (($Bi_{1.7}Pb_{0.3}Sr_2CuO_x$ (B(Pb)SCCO 2201) and $Bi_{1,7}Pb_{0,3}Sr_2CaCu_2O_x$ (B(Pb)SCO 2212)) is confirmed. Their presence in the zinc electrode mass increases the discharge capacity of the battery, forming a strong conducting network between the zinc oxide particles. No significant difference in their effect is observed. The shorter thermal treatment synthesis mode of the system (B(Pb)SCCO 2201 must also be taken into account, which determines it to be a more suitable additive in the battery cells under consideration.

Keywords: B(Pb)SrCaCuO conducting ceramics, Zn-electrode, Ni-Zn rechargeable batteries, electrochemical properties

INTRODUCTION

Enhanced interest in rechargeable alkaline nickel-zinc (Ni-Zn) batteries is driven by the wide range of practical applications. These types of batteries possess high energy density (55 – 85 Wh kg^{-1}), high power density (140 -200 W kg^{-1}), high voltage (1,73 V), ability to operate at high current densities, low cost of materials used and low content of potentially environment polluting substances. They do not contain any heavy metals (Hg, Pb, Cd), or flammable active materials and electrolytes and offer a simple recycling process of the metal recovering. Besides, the electrochemical Ni-Zn system is similar as battery technology to the Ni-Cd system widely used in the practice but it is advantageously environmentally friendly by replacing the toxic cadmium with common zinc [1-4]. Nickel-zinc batteries are the ideal choices when there is a need for a small, lightweight power source at a cost significantly lower than that of lithium-ion battery[1,4,5].

Along with the listed advantages, the main disadvantage of this type of rechargeable batteries is the rather poor electrical conductivity of the ZnO electrode, and the limited lifetime expressed in cycles, which is mainly due to the zinc electrode transformation during cycling. The reason for this is the solubility of zinc in the alkaline electrolyte, leading to the formation of dendrites in the cycling process, accompanied by the formation of short-circuits, which leads to shorter battery lifetime [6,7].

One way to ensure a longer battery lifetime is to add different carbon materials as conductive agents (graphite, carbon foam, acetylene carbon black) into the active mass of the Zn electrode [8]. This, however, induces strong hydrogen evolution during the charging process, which decreases the charge/discharge effectiveness, as well it as may cause mechanical destruction of the electrode mass and reduces the battery life [7].

In order to avoid this disadvantage the application of different conductive oxides and hydroxides as additives to the anode mass attracts the attention of researchers [9]. It is found out that the additions of $Ca(OH)_2$ and $Ba(OH)_2$ lead to increasing the battery capacity [9]. $Ca(OH)_2$ reacts with ZnO to form $Ca(OH)_2.2Zn(OH)_2.2H_2O$ and the resulting complex compound has a low solubility in the electrolyte, which hinders the dissolution of zinc and the formation of dendrites and thus extends the battery lifetime [10,11]. The use of $Ba(OH)_2$ as an additive to the active mass of the zinc electrode leads to an increase in both the discharge capacity and the cyclability of the electrode. The comparison of the electrochemical behavior of commercial ZnO and zinc oxide doped with $Ba(OH)_2$ revealed that the capacity of the pure

* To whom all correspondence should be sent:
E-mail: antonia.stoyanova@iees.bas.bg

zinc electrode decreased very steeply compared to that with $Ba(OH)_2$ additive. In the latter case, mixed barium-zinc hydroxide ($BaZn(OH)_4.xH_2O$) is obtained, which has an effect analogous to that mentioned above with $Ca(OH)_2$ additive [12].

In order to improve the properties of the nickel-zinc battery and to study the effects of the additives on the performance of zinc electrode, three content levels of four additives (acetylene black, Bi_2O_3, PbO, Ca $[Zn(OH)_3]_2 \cdot 2H_2O$ coated by $La(OH)_3$) that affect the zinc electrode performance were tested with orthogonal design experiments. The experimental evidences indicate that the optimal ratio of electrode additive is as follows: 0.02 g acetylene black, 0.5 g Bi_2O_3, 0.3 g PbO and 0.2 g $Ca[Zn(OH)_3]_2 \cdot 2H_2O$ coated with $La(OH)_3$in a 5 g sample [13].

A modern approach to remove the mentioned disadvantages of the zinc electrode is the use of conductive ceramic powders that not only improve the battery lifetime but they also increase its performance.

Ceramics obtained from various oxides $(ZnO)_{0.92}$ $(Bi_2O_3)_{0.054}$ $(ZnO)_{0.92}$ $(Bi_2O_3)_{0.054}$ $(Co_2O_3)_{0.025}$ $(Nb_2O_5)_{0.00075}$ $(Y_2O_3)_{0.00025}$ were tested as additives to the Zn electrode. It has been found out that Zn electrode with addition of conductive ceramic demonstrates improved electrochemical properties, such as higher discharge capacity, cycling stability and efficiency compared to the zinc electrode with pure nanosized ZnO. The observed positive effect is explained by the formation of a highly conductive network of metals Bi, Co and Y during cycling, which helps to improve the electrical contact between ZnO particles and increases their active surface area [14,15].

The high-temperature superconductors are discovered in 1986 by Georg Bednorz and K. Alex Müller [16] and since then the technological research has been focused on producing high-temperature superconductor (HTS) materials in sufficient quantities to optimize their properties in relation to a wide range of advanced applications. The superconductors of the cuprate ceramic systems Y-Ba-Cu-O (YBCO) [17,18] are a representative of the most advanced HTS materials with potential large-scale engineering applications. Their chemical stability is one of the most important factors for their practical application. In our previous paper the possibility of using YBCO and BSCCO [19,20] powders of superconducting materials as additives to the zinc electrode mass of nickel-zinc alkaline rechargeable batteries was studied. The high chemical resistance of the ceramics to the battery electrolyte has been confirmed by structural and surface morphology observations, as well as by magnetic measurements of ceramic samples after prolonged exposure to the alkaline electrolyte. The electrochemical tests have shown that the zinc electrode with YBCO ceramic additive (7 wt.%) exhibits good cycling ability and capacity stability, and higher (by 30%) specific discharge capacity than the zinc electrode with a "classic" conductive carbon additive [21,22].

The results of the electrochemical studies show that the nickel-zinc battery cell with zinc electrode with active mass containing superconducting BSCCO (2212) and BSCO (2201) ceramic additive also exhibits good cycling ability and performance stability during prolonged charge-discharge cycling. The measurements of the electric resistance of the composite electrode masses have shown that the resistance of the zinc electrode mass with addition of $Bi_{1.7}Pb_{0.3}Sr_2Ca_2Cu_3O_x$ ceramic (230 ohm.cm) is by about 30% lower than the resistance of the electrode mass with carbon additive (330 ohm.cm). It is supposed that the superconducting powder forms a highly conductive network between the particles of the zinc oxide in the electrode mass, thus improving the electric contact in the power generation material of the zinc electrode. The addition of BSCCO ceramics improves not only the conductivity and electrochemical homogeneity of the electrode mass and reduces the gas evolution (because of the absence of carbon materials with a low-overpotential of hydrogen evolution) but it also stabilizes its porosity structure [23-25].

The aim the present paper was to compare two types of cuprate ceramics (B(Pb)SCO 2212 and B(Pb)SCCO 2201) as additives to the zinc electrode mass in the rechargeable alkaline Ni-Zn batteries. For this purpose, they are structurally characterized and subjected to charge-discharge electrochemical cycling tests in alkaline electrolyte according to preliminary-developed test methodology. The possible mechanism of their action is discussed.

EXPERIMENTAL

Synthesis of B(Pb)SCO 2212 and B(Pb)SCCO 2201

Powder samples of two modifications $Bi_{1,7}Pb_{0,3}Sr_2CaCu_2O_x$ (B(Pb)SCO 2212) and $Bi_{1.7}Pb_{0.3}Sr_2CuO_x$ (B(Pb)SCCO 2201) were prepared by the standard solid state reaction from high-purity oxides of Bi_2O_3, PbO, CuO, $SrCO_3$ and $CaCO_3$. After mixing, grinding and initial heat treatment at 780°C for 24 hours in air atmosphere the powder obtained was ground and pressed into pellets (5-6 MPa). In air atmosphere the B(Pb)SCCO 2201 was sintered at 830°C for 24 hours and B(Pb)SCO 2212 at 830°C for 48 hours.

The pellets of sintered ceramic samples (10 mm diameter, 2 mm thick) were first soaked in 50 ml of 7M solution of KOH and then exposed to the alkaline solution for 24, 48, 72 or 96 hours. Then they were removed from the solution and dried at room temperature. Since the changes of all samples towards the exposure period (time) were practically negligible, further in the paper only results for the longest soaking time (96 hours) are presented.

Preparation of the zinc electrode and battery assembling

Preparation of the zinc paste. The electrochemically active nanosized powdered ZnO was produced by a solution combustion method using as initial compound $Zn(NO_3)_2.6H_2O$ and sucrose. The amorphous powder oxide material produced after evaporation of the water was subjected to thermal treatment at 600 ^oC in order to obtain the appropriate size of the crystallites.

The electrode mass is composed of powdered ZnO (88 wt.%), conducting additives – cuprate ceramic powder B(Pb)SCO 2212 and B(Pb)SCCO 2201, and carbon (acetylene black) (7 wt.%) and binding agents – polytetrafluorethylene (PTFE, 4 wt.%) and carboxymethylcellulose (CMC, 1 wt.%). The electrode mass was thoroughly mixed with a certain amount of distilled water to form mushy paste according to a procedure developed previously and described in detail [26,27].

Pasted electrode and battery assembling. Zinc electrode prepared by inserting the zinc paste into the matrix of copper foam (successively covered with tin and zinc) with dimensions 5.0 × 3.0 cm (thickness 0.15 cm) was used as current collector and carrier of the zinc mass. The pasted electrode was dried at 70^0C for 2 hours, pressed under 30 MPa for 2 min and then mounted into a separator pocket made of a polypropylene type of microporous separator (Celgard C3501, Celgard, USA). A solution of 7M KOH was used as a battery electrolyte. The electrode-separator package was soaked under vacuum with battery electrolyte for 10 min before mounting it in the prismatic nickel-zinc battery cell. Sintered type of nickel electrodes (CLAIO, Poznan, Poland) with dimensions 5.0 × 3.0 cm and thickness 0.12 cm, and a nominal capacity about two times higher than that of the zinc electrodes, were used for cathodes in the nickel-zinc battery cell. The electrodes were directly wetted with the electrolyte before mounting in the cell using the same evacuation procedure. The container of the prismatic battery cell was made of a transparent plastic material and the cell was assembled with two nickel cathodes and one zinc anode [27].

Physicochemical and electrochemical characterization. The X-ray diffraction patterns of the ceramic powdered samples were obtained within the range of 5.3 to 80^o 2θ at a constant step of 0.02° 2θ on a Bruker D8 Advance diffractometer with Cu Kα_radiation and a LynxEye detector. The phase identification was performed by a Diffrac plus EVA v. 15 program using the ICDD-PDF2 data base. The mean crystallite size and the unit cell parameters were determined by the Topas v.4.2 software package using the fundamental parameters peak shape description including appropriate corrections for the instrumental line broadening and difractometer geometry [28].

The electrochemical investigations of the nickel-zinc battery cells were carried out under galvanostatic conditions using an automatic battery testing apparatus CDT10. The apparatus gives a possibility for complex control and monitoring of the main cell parameters during charge/discharge cycling - cell voltage and current, capacity and temperature. The zinc electrodes were characterized by the developed test methodology comprising the several steps already described in [29].

The efficiency of the electrodes was determined by the equation:

$$\theta = Q_{disch} / Q_{ch} .100\% \quad (1),$$

where Q_{disch} is the discharge capacity, and Q_{ch} - the charge capacity of the electrode.

RESULTS AND DISCUSSION

Our previous investigations show that no phase changes in the semiconducting B(Pb)SrCaCuO ceramics have occurred after prolonged contact of the samples with a strong alkaline solution (7 M KOH). After treatment in the alkaline solution no essential changes in the bulk morphology of the BSCCO samples were observed too [23].

X-ray diffraction patterns of the cuprate ceramics B(Pb)SCCO 2201 and B(Pb)SCO 2212 are given in Figures 1 and 2, respectively.

Based on XRD analysis a single phase in a well crystallized form of both investigated ceramics is observed. Secondary phases are not detected.

The refined unit cell parameters for B(Pb)SCCO 2201 are a =5.3920 Å; b = 24.6030 Å; c = 5.3000 Å with orthorhombic unit cell volume V_m(B(Pb)SCCO 2201) = 703.09Å^3 (Fig.1a) and those for B(Pb)SCO 2212 are $a = b$ = 5.395 Å; c = 30.714 Å, with tetragonal unit cell volume V_m (B(Pb)SCO 2212) = 893.962 Å^3 (Fig. 1b).

It is noticeable that the structure of the obtained ceramics differs from that of the ceramic additives used so far [14, 15]. Under certain conditions these

ceramics can exhibit superconducting properties [16-18].

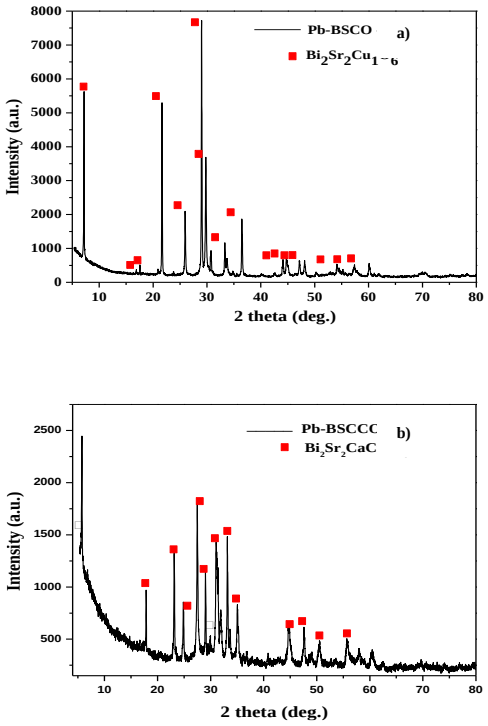

Figure 1. Powder X-ray diffraction pattern of B(Pb)SCCO 2201 (a) and B(Pb)SCO 2212 (b) ceramics.

The electrochemical tests of the zinc electrodes with additives of B(Pb)SCCO 2201 and B(Pb)SCO 2212 ceramics were conducted according to the developed methodology, which includes several charge/discharge current modes up to the critical maximum 9C [29]. For comparison, the same tests were carried out with conventional carbon additive (acetylene black). In Figs. 2 and 3 the voltage-time curves are shown (the 8thcycle) of the zinc electrode with B(Pb)SCCO 2201, B(Pb)SCO 2212 and carbon conductive additives at 1C and 9C, respectively.

As it is seen in Fig. 2, the electrochemical processes under this current mode proceed without the occurrence of any side effects. The main difference in the voltage profiles is the higher value of perceived charge at DC current in the cells with BSCCO additive compared to that of a cell with a carbon additive. This can be explained with the better conductivity of the cuprate ceramics used over that of carbon.

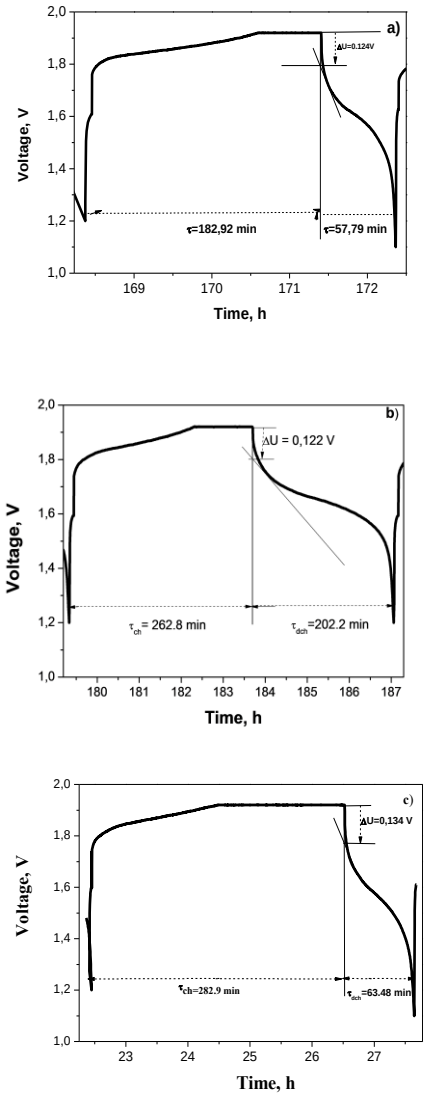

Figure 2. Charge/discharge curves of the Ni/Zn cells with B(Pb)SCCO 2201 **(a),** B(Pb)SCO 2212 **(b)** and carbon (c) additives to the active mass of the zinc electrode at current loads 30 mAg^{-1} (mode 1C).

The data in Table 1 show that the initial voltage drop at the beginning of the discharge process is lower for Zn electrodes with ceramic additives ($\Delta U_{B(Pb)SCCO\ 2201}$ = 0,124V, $\Delta U_{B(Pb)SCO\ 2212}$ = 0.122V, ΔU_C = 0.134V), respectively their lower resistance is ($R_{B(Pb)SCCO\ 2201}$ = 4.13, $R_{B(Pb)SCO\ 2212}$ = 4,27, R_C = 4.47). No significant difference is observed comparing both electrodes with B(Pb)SrCaCuO additive.

Another important advantage of the ceramics-modified zinc electrodes is the higher efficiency of their operation (93.80% and 96.82%, respectively), which exceeds by 16-18% that of the carbon-doped electrode (78.90%). The role of the additive is reflected in its contribution to reducing hydrogen releases during the charging of the electrode.

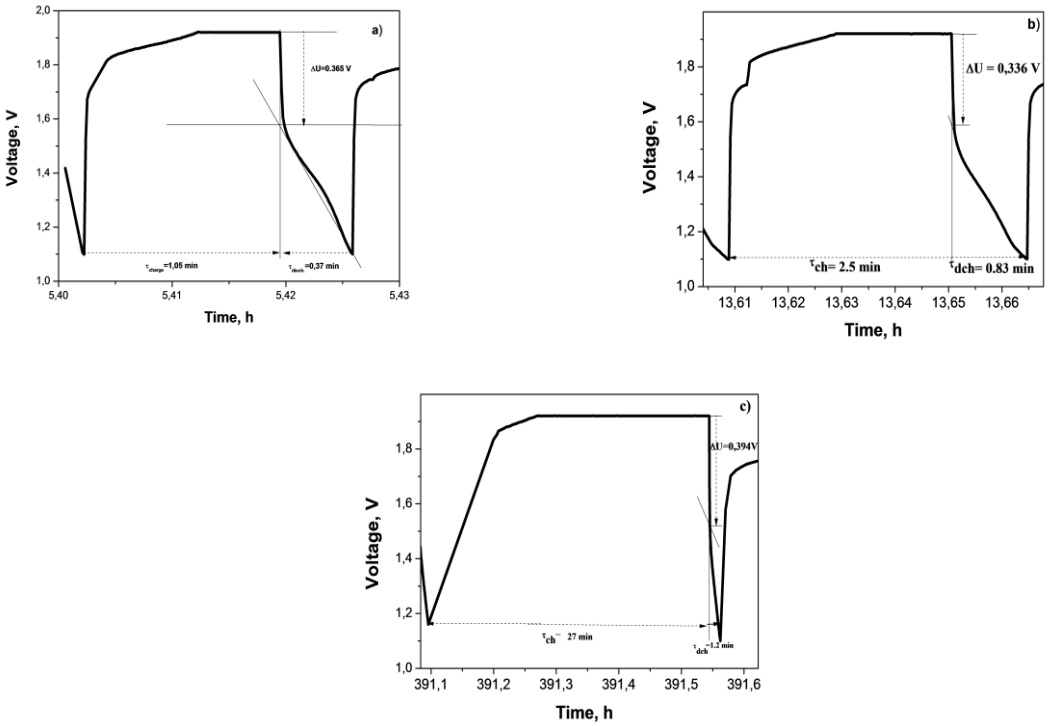

Figure 3. Charge/discharge curves of the Ni/Zn cells with B(Pb)SCCO 2201 **(a),** B(Pb)SCO 2212 **(b)** and carbon (c) to the active mass of the zinc electrode at current loads of 270 mA g^{-1} (mode 9C)

Table 1. Calculated values based on charge/discharge curves for Zn electodes with different additives (current mode 1C and 9C): ΔU- voltage drop, Q_{ch}/ Q_{disch} - charge/discharge capacitance, Θ – efficiency

Additive	ΔU,V		Q_{ch}, mAh		Q_{disch}, mAh		Θ, %	
	1C	9C	1C	9C	1C	9C	1C	9C
B(Pb)SCCO 2201	0.124	0.365	1.662	0.223	1.562	0.213	93.80	95.52
B(Pb)SCO 2212	0.122	0.336	1.386	0.288	1.342	0.260	96.82	90.27
Carbon	0.134	0.394	1.341	0.226	1.058	0.180	78.90	79.60

The voltage-time curves of Ni/Zn cells with B(Pb)SrCaCuO and carbon modified electrodes performed at extreme current mode (9C, 270 mAg^{-1}) are shown in Fig. 3.

Fig. 3 shows that the voltage profile does not change significantly and even under these extreme conditions the B(Pb)SrCaCuO-modified conductive ceramic electrodes perceive more than 50% of the DC charge. The initial voltage drop is low ($\Delta U_{B(Pb)SCCO\ 2201}$ = 0.365 V, $\Delta U_{B(Pb)SCO\ 2212}$=0.336 V), and in this case the voltage profile has a plateau character at a high average voltage of 1.615 V. The efficiency of these electrodes is also high (90 - 95%).

The Zn electrode with carbon additive is strongly polarized (ΔU_C= 0.394 V) and it shows significantly lower average discharge voltage (1.409 V) and much lower capacitive values and efficiency (79.60%), compared to the ceramic-modified electrodes.The dependences of the specific capacity for the electrodes on the number of charge-discharge cycles during prolonged cycling are shown in Figure 4.

Comparing the capacity of the cells with zinc electrodes containing carbon and ceramic additives show that the presence of two modifications B(Pb)SCCO 2201 and B(Pb)SCO 2212 of a ceramic additive to the negative active mass of a Ni-Zn battery results in higher and more stable specific discharge capacity in comparison to the zinc electrode with classic carbon additive, especially under high current (0.5 A) [25, 26, 29]. At the begnning the discharge capacity of the carbon-containing electrode exceeds by about 11% that of the electrodes with B(Pb)SrCaCuO ceramics, but this electrode is unstable and it drops steeply with the increase in the cycle numbers. The discharge capacity of the cells with B(Pb)SrCaCuO conductive additives is by more than 30% higher than that of the conventional zinc electrode and is stable over 500 cycles. This result can be explained by the formation of a highly conducting network between the zinc oxide particles in the electrode mass in the presence of cuprate ceramics.

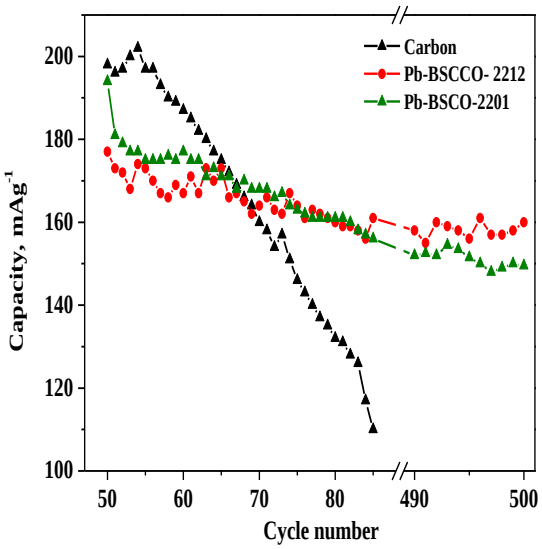

Figure 4. Dependence of the specific discharge capacity of the zinc electrode with carbon, B(Pb)SCCO 2201 (a) and B(Pb)SCO 2212 (b) ceramic additives on the cycle number, at current load C/5 (0.2 A)

CONCLUSION

The electrochemical characteristics of the Ni-Zn battery cell were enhanced by adding two types of Bi(Pb)SrCaCuO conducting ceramics ($Bi_{1.7}Pb_{0.3}Sr_2CuO_x$ (B(Pb)SCCO 2201) and $Bi_{1,7}Pb_{0,3}Sr_2\,CaCu_2O_x$ (B(Pb)SCO 2212)) to the zinc electrode mass. The conducted electrochemical tests confirmed the positive effect of both ceramics on the battery electrochemical properties at prolonged cycling, as no substantial difference in their effect was established. The results obtained can be explained again by an increase in the conductivity and homogeneity of the electrode mass in the presence of the additives used, on the one hand, and the formation of a highly conducting network between the zinc oxide particles, on the other. The shorter thermal treatment synthesis mode of B(Pb)SCCO 2201 ceramic determines it to be a more suitable additive in the battery cells under consideration.

Acknowledgements: *The experiments were performed with equipment included in the National Infrastructure NI SEVE supported by the Ministry of Education and Science under grant agreement № DO1-160/28.08.18.*

The authors express their sincere thanks to Prof. R. Raicheff, Assoc. Prof. Ml. Mladenov and Eng. Lozan Stoyanov for their invaluable help in the preparation of this work.

REFERENCES

1 M. Geng, D. Northwood, *Int. J. Hydrogen. Energ*., **28**, 633 (2003).
2 H. Mcgraw (ed.) Handbook of batteries (New York, 2004).
3 S. Philips, S. Mohanta, M. Geng, J. Bartom, Mc Kinney, J.Wu, *ECS Trans.*, **16,** 11 (2009).
4 G. Zhang, *ECS Trans.*, **16**, 47 (2009).
5 R. Raicheff, M. Mladenov, L. Stoyanov, N. Boshkov, V. Bachvarov, *Bulg. Chem. Commun.*, **48,** 61 (2016).
6 M. Ma, J. Tu, Y. Yuan, X. Wang, K. Li, F. Mao, Z. Zeng, *J. Power Sources*, **179,** 395 (2008).
7 W. Long, Z. Yang, X. Fan, B. Yang, Z. Zhao, J. Jing, *Electrochim. Acta*, **12,** 40 (2013).
8 H. Tao, X. Tong, X. Gan, S. Zhang, X. Liu, *J. Alloys Compd.*, **658,** 119 (2016).
9 Y. Zheng, J. Wang, H. Chen, J. Zhang, C. Cao, *Mater. Chem. Phys*., **84,** 99 (2004).
10 Y. Yuan, J. Tu, H. Wu, Z. Zhang, X. Huang, X. Zhao, *Electrochem. Commun.*, **8,** 653 (2006).
11 R. Shivkumar, S. Umamaheswari, G. Kalaignan, T. Vasudevan, *Indian J. Chem.Technol.*, **8,** 95 (2001).
12 J. Wang, C. Zhang, L. Zhang, J. Zhang, C. Cao, *Mater. Chem. Phys.*, **70,** 254 (2001).
13 G. Cheng, Y. Zhang, W. Zhao, W. Yu, H. Hou, *Met. Soc. China***, 2,** 3551 (2014).
14 H. Huang, L. Zhang, W. Zhang, Y. Gan, G. Shao, *J. Power Sources*, **184,** 663 (2008).
15 L. Zhang, H. Huang, W. Zhang, Y. Gan, C.Wang, *Electrochim. Acta*, **53,** 5386 (2008).
16 J. Bednorz, K. Müller, *Z. Phys. B.*, **64,** 189 (1986).
17 M. Wu, J. Ashburn, C. Torng, P. Hor, R. Meng, L. Gao, Z. Huang, Y. Wang, C. Chu, *Phys. Rev. Lett.*, **58,** 908 (1987).
18 V. Kovachev, E. Vlachov, K. Nenkov, V. Lovchinov, M. Gospodinov, A. Stoyanova, D. Dimitrov, M. Czyczek, *Intern. J. Modern Phys. B*, **1,** 479 (1987).
19 C. Michel, M. Hervieu, M. Borel, A. Grandin, F. Deslandes, J. Provost, B. Raveau, *Phys. B-Condensed. Matter.*, **68**, 421 (1987).
20 H. Maeda, Y. Tanaka, M. Fukotomi, T. Asano, *Jpn. J. Appl. Phys. Lett.*, **27**, 209 (1988).
21 G. Ivanova, A. Stoyanova-Ivanova, S. Terzieva, D. Kovacheva, M. Mladenov, B. Blagoev, D. Dimitrov, Proceedings of the 12th Cryogenics International Conference, **11** (2012).
22 A. Stoyanova–Ivanova, S. Terzieva, G. Ivanova, M. Mladenov, D. Kovacheva, R. Raicheff, S. Georgieva, B. Blagoev, A. Zaleski, V. Mikli, *Bulg. Chem. Commun.*, **47,** 221 (2014).
23 G. Ivanova, L. Stoyanov, S. Terzieva, A. Stoyanova-Ivanova, M. Mladenov, D. Kovacheva, R. Raicheff, *Nanoscience&Nanotechnology*, **14,** 33 (2014).
24 L. Stoyanov, S. Terzieva, A. Stoyanova, A. Stoyanova- Ivanova, M. Mladenov, D. Kovacheva, R. Raicheff, *JPRC*, **2,** 83 (2016).
25 G. Ivanova, L. Stoyanov, A. Stoyanova, M. Mladenov, R. Raicheff, *Nanoscience & Nanotechnology*, **16,** 27 (2016).
26 M. Mladenov, R. Raicheff, L. Stoyanov, A. Stoyanova-Ivanova, S. Terzieva, D. Kovacheva, *BG Patent Reg. # 111 646 (*in Bulgarian) (2013).

27 M. Mladenov, R. Raicheff, L. Stoyanov, D. Kovacheva, *BG Patent Reg. # 111 775 (*in Bulgarian) (2014).

28 PAS V4: General profile and structure analysis software for powder diffraction data, User's Manual, Bruker AXS, Karlsruhe, Germany, Bruker AXS (2008).

29 G. Mitrova, PhD Thesis (IEES-BAS Bulgaria) (2015).

Bulgarian Chemical Communications, Volume 51, Issue 1, (pp. 73 – 79) 2019

Synthesis and biological activity of 2-alkylthio-5-(4-N-acetyl(N-chloroacetyl)aminophenyl)-1,3,4-oxadiazoles

D. S. Ismailova, A. A. Ziyaev*, S. A. Sasmakov, U. S. Makhmudov, Sh. Sh. Khasanov, Sh. S. Azimova, B. Zh. Elmuradov

Acad. S.Yu. Yunusov Institute of Chemistry of Plant Substances, Academy of Sciences of the Republic of Uzbekistan, 100170, Tashkent, 77, M. Ulugbek str, Republic of Uzbekistan

Received November 3, 2017; Revised November 13, 2018

New 2-alkylthio-5-(4-N-acetyl(N-chloroacetyl)aminophenyl)-1,3,4-oxadiazoles were synthesized. Optimal conditions for the synthesis were found. The physicochemical characteristics and structures of the synthesized compounds were established. On the example of compound **10** we carried out X-ray diffraction analysis (XRD). The antibacterial and antifungal activities of these compounds were investigated. The screening results showed that 2-alkylthio-5-(4-N-chloroacetylaminophenyl)-1,3,4-oxadiazoles of **17**,**18**,**21**,**22** display an appreciable antibacterial activity against Gram-positive bacteria of *Bacillus subtilis* and *Staphylococcus aureus.*

Keywords: 2-alkylthio-5-(4-N-acetyl(N-chloroacetyl)aminophenyl)-1,3,4-oxadiazoles, X-ray analysis, crystal structure, antibacterial and antifungal activity.

INTRODUCTION

One of the most interesting representatives of five-membered heterocyclic compounds - 5-substituted-1,3,4-oxadiazole-2-thiones, along with great practical significance (a number of oxadiazolethione derivatives possess pesticide, pharmacological and other biological activities) represent theoretical interest for studying the relationship "structure - biological activity", which is well described in the reviews [1-4] and partly in our earlier work [5-8]. In contrast to the other oxadiazoliones, which we studied earlier [6,9,10], 5-(4-aminophenyl)-1,3,4-oxadiazol-2-thione, in addition to the two reaction centers (sulfur and nitrogen atoms) in the thioamide group NH-C=S has another reaction center - amino group in position 4 of the aromatic ring. It is known that the good reactivity of the amino group allows for carrying out chemical transformations with the formation of compounds with different substituents possessing different properties, including biological ones. A study of the literature showed that such compounds show appreciable biological activity. However, the data on such transformations and biological activity related to 5-(4-aminophenyl)-1,3,4-oxadiazole-2-thiones turned out to be very limited [11-13].

EXPERIMENTAL

IR spectra of the synthesized compounds were recorded on a Perkin Elmer-2000 Fourier spectrometer using KBr pellets, UV spectra recorded on a Perkin Elmer Lambda-16 spectrometer in ethanol. ^{1}H NMR spectra were recorded on the Unity-400+ spectrometer (400 MHz, $CDCl_3$ solvent, HMDS internal standard) at 20-25°C. The reactions and individuality of the synthesized compounds were monitored by TLC on Merck silicagel 60F254 plates using 10:1 $CHCI_3$-EtOH solvent system; developed plates were visualised under UV lamp and iodine tank, where necessary. The melting point of all synthesized substances was determined on a "Boetius" apparatus.

The unit cell parameters of the crystals were determined and refined with CCD Xcalibur Ruby diffractometer (Oxford Diffraction) using CuKα-radiation, graphite monochromator (T=293 K).

Crystal growth. Single crystal of 2-butylthio-5-(4-N-acetylaminophenyl)-1,3,4-oxadiazole **10** was grown from solutions of acetone by slow evaporation at room temperature.

X-ray structure determination. The unit cell parameters of the crystal were determined and refined with CCD Xcalibur Ruby diffractometer (Oxford Diffraction) using CuKα-radiation, graphite monochromator (T=293 K). The three-dimensional set of reflections was obtained using the appropriate diffractometer. The amendment was introduced to the absorption by Multi-scan [14]. Table 1 shows the main parameters of the X-ray diffraction experiment and refinement calculations of the structure **10**.

* To whom all correspondence should be sent:
E-mail: aziyaev05@rambler.ru

Table 1. Basic crystallographic parameters and characteristics of the X-ray diffraction for structure **10**.

Compound	10
Molecular formula	$C_{14}H_{17}N_3O_2S$
Mr	291.36
Crystal symmetry	Orthorhombic
Space group	Pbca
Z	8
a, Å	9.8091(3)
b, Å	9.2603(4)
c, Å	32.1709(14)
α, °	90
β, °	90
γ, °	90
V, $Å^3$	2922.2(2)
ρ, g/cm^3	1.325
Crystal dimension (mm)	0.35×0.48×0.55
Range scanned, 2θ°	5.282≤θ≤ 76.248o
μexp (cm^{-1})	2.017
No. reflection collected	3026
No. reflection with I>2σ(I)	2024
R1 (I>2σ(I) and total)	0.0457 (0.0772)
wR^2	0.1061 (0.1250)
GOOF	1.028
Largest diff. peak and hole (e $Å^{-3}$)	0.180 and –0.190
CCDC	1554510

The structure was solved by direct methods using SHELXS-2014 and refined using SHELXL-2014 programs [15]. All non-hydrogen atoms were refined by anisotropic full-matrix least-squares methods (over F^2). Positions of H atoms were found geometrically and refined with fixed isotropic thermal parameters Uiso=nUeq, where n=1.5 for methyl hydrogens and 1.2 for others and Ueq is the equivalent isotropic thermal parameter of the corresponding C atoms.

Materials X-ray diffraction as a CIF file were deposited at the Cambridge center of crystal data (CCDC), from which they can be obtained free on request at the following link: www.ccdc.cam.ac.uk/data_request/cif (CCDC number is 1554510).

Antimicrobial assay. The synthetic compounds were tested for antimicrobial activity by the agar disk-diffusion method [16-18]. The antimicrobial activity was evaluated using five species of microorganisms: Gram-positive bacteria *Bacillus subtilis* (RKMUz - 5) and *Staphylococcus aureus* (ATCC 25923); Gram-negative bacteria *Escherichia coli* (RKMUz - 221) and *Pseudomonas aeruginosa* (ATCC 27879) and the fungus *Candida albicans* (RKMUz - 247). The RKMUz microorganism cultures were obtained from the strain collection of the Institute of Microbiology, Academy of Sciences of the Republic of Uzbekistan. Sterile nutrient agar (25 g agar/l distilled water) was inoculated with bacterial cells (200 μl of bacterial cell in 2 ml of 0.9% NaCl suspension and 20 ml medium) and poured into Petri dishes to give a solid medium. *Candida albicans* ($1×10^6$ colony forming units per ml) was inoculated into sterile Mueller-Hinton-agar. Forty microliters of test material (0.2 mg/per disc of the compounds) was applied on sterile paper discs (Whatman No 1, 6 mm diameter). Ampicillin, ceftriaxone and nystatin (20 μg/disc) were used as positive controls and the solvents as negative controls. The solvents were allowed to evaporate in a stream of air. The discs were deposited on the surface of the inoculated agar plates. Plates were kept for 3 h in a refrigerator to enable the diffusion of the substances into the agar. Plates with bacteria were incubated for 24 h at 37°C and plates with yeasts for 48 h at 26°C. The inhibition zone (including the disc diameter) was measured and recorded after the incubation time. An average zone of inhibition was calculated for the three replicates in independent assays.

Interaction of 2-alkylthio-5-(p-aminophenyl)-1,3,4-oxadiazoles with acetyl and chloroacetyl chlorides (general procedure). 2-Alkylthio-5-(4-aminophenyl)-1,3,4-oxadiazole [8] (0.01 mol) was dissolved in 15 mL of benzene with continuous stirring, then triethylamine (0.015 mol) was added. A solution of acetyl chloride (0.011 mol) or chloroacetylchloride in 10 mL benzene was added dropwise to the resulting mixture at room

temperature. HCI was isolated as a white haze, the reaction mixture was left overnight, and then the resulting precipitate was filtered, washed with benzene, an alkali solution and water.

2-Propylthio-5-(4-N-acetylaminophenyl)-1,3,4-oxadiazole (9). Yield 97%, mp 166-167 °C, R_f = 0.46; UV spectrum (λ_{max}, nm): 298.9; ^{1}H NMR (δ, ppm, J/Hz): 0.99 (3H, t, J = 7.3, CH_3), 1.79 (2H, m, $CH_2C\underline{H}_2CH_3$), 2.06 (3H, s, CH_3-CO), 3.24 (2H,t, J = 7.1, S-CH_2), 7.77 (2H, d, J = 8.8, H-3,5), 7.87 (2H, d, J = 8.9, H-2,6), 9.40(1H, brs, NH). IR spectrum(ν, cm^{-1}): 1694 (CH_3CO), 1523 (NH), 1179 (C-O-C, oxadiazole).

2-Butylthio-5-(4-N-acetylaminophenyl)-1,3,4-oxadiazole (10). Yield 89%, mp 162-163 °C, R_f = 0.51; UV spectrum(λ_{max}, nm): 298.7; ^{1}H NMR (δ, ppm, J/ Hz): 0.59 (3H, t, J = 7.4, CH_3), 1.15 (2H, m, $CH_2CH_2C\underline{H}_2CH_3$), 1.49 (2H, m, $CH_2C\underline{H}_2CH_2CH_3$), 1.98 (3H, CH_3-CO), 3.71 (2H, t, J = 7.3, S-CH_2) 7.45 (2H, d, J = 8.6, H-3,5), 7.68 (2H, d, J = 8.6, H-2, 6), 9.40 (1H, brs, NH). IR spectrum(ν, cm^{-1}): 1668 (CH_3CO), 1537 (NH), 1176 (C-O-C, oxadiazole).

2-Amylthio-5-(4-N-acetylaminophenyl)-1,3,4-oxadiazole (11). Yield 92%, mp 135-136 °C, R_f = 0.46; UV spectrum(λ_{max}, nm): 299.2; ^{1}H NMR (δ, ppm, J/Hz): 0.84 (3H, t, J = 7.3, CH_3), 1.36 (4H, m, $C\underline{H}_2C\underline{H}_2CH_3$), 1.78 (2H, m, $C\underline{H}_2CH_2CH_2CH_3$), 2.06 (3H, s, CH_3-CO), 3.26 (2H, t, J = 7.3, S-$C\underline{H}_2CH_2CH_2CH_2CH_3$), 7.77 (2H, d, J = 8.9, H-3, 5), 7.88 (2H, d, J = 8.9, H-2, 6), 9.42 (1H, brs, NH). IR spectrum(ν, cm^{-1}): 1674 (CH_3CO), 1536 (NH), 1173 (C-O-C, oxadiazole).

2-iso-Amylthio-5-(4-N-acetylaminophenyl)-1,3,4-oxadiazole (12). Yield 95%, mp 128-129 °C, R_f = 0.51; UV spectrum(λ_{max}, nm): 298.6; ^{1}H NMR (δ, ppm, J/Hz): 0.95 (6H, d, d, J = 7.3, J = 7.3, $2CH_3$), 1.64 (3H, m, $C\underline{H}_2C\underline{H}(CH_3)_2$), 2.08 (3H, s CH_3-CO), 3.27 (2H, t, J = 7.9, S-$C\underline{H}_2CH_2CH(CH_3)_2$), 7.77 (2H, d, J = 8.7, H-3, 5), 7.87 (2H, d, J = 8.7, H-2, 6), 9.48 (1H, brs, NH). IR spectrum(ν, cm^{-1}): 1676 (CH_3CO), 1542 (NH), 1174 (C-O-C, oxadiazole).

2-Hexylthio-5-(4-N-acetylaminophenyl)-1,3,4-oxadiazole (13). Yield 98%, mp 130-131 °C, R_f = 0.48; UV spectrum(λ_{max}, nm): 298.7; ^{1}H NMR (δ, ppm , J/Hz): 0.82 (3H, t, J = 7.1, CH_3), 1.27 (4H, m, $C\underline{H}_2CH_2CH_3$), 1.42 (2H, m, $C\underline{H}_2CH_2CH_2CH_3$), 1.77 (2H, m, $C\underline{H}_2(CH_2)_3CH_3$), 2.06 (3H, s, CH_3-CO), 3.26 (2H, t, J = 7.3, S-$C\underline{H}_2(CH_2)_4CH_3$), 7.76 (2H, d, J = 8.9, H-3, 5), 7.87 (2H, d, J = 8.8, H-2, 6), 9.40 (1H, brs, NH). IR spectrum(ν, cm^{-1}): 1707 (CH_3CO), 1532 (NH), 1174 (C-O-C, oxadiazole).

2-Heptylthio-5-(4-N-acetylaminophenyl)-1,3,4-oxadiazole (14). Yield 98%, mp 105-106 °C, R_f = 0.51; UV spectrum(λ_{max}, nm): 299.5; ^{1}H NMR (δ, ppm J/Hz): 0.81 (3H, t, J = 6.7, CH_3), 1.24 (6H, m, $C\underline{H}_2C\underline{H}_2CH_2CH_3$), 1.42 (2H, m, $C\underline{H}_2(CH_2)_3CH_3$), 1.78 2H, m, $C\underline{H}_2(CH_2)_4CH_3$), 2.06 (3H, s, CH_3-CO), 3.26 (2H, t, J = 7.3, S-$C\underline{H}_2(CH_2)_5CH_3$), 7.78 (2H, d, J = 8.8 , H-3, 5), 7.86 (2H, d, J = 8.8, H-2, 6), 9.42 (1H, brs, NH). IR spectrum(ν, cm^{-1}): 1702 (CH_3CO), 1535 (NH), 1174 (C-O-C, oxadiazole).

2-Octylthio-5-(4-N-acetylaminophenyl)-1,3,4-oxadiazole (15). Yield 97%, mp 112-113 °C, R_f = 0.53; UV spectrum(λ_{max}, nm): 300.1; 1H NMR(δ, ppm, J/Hz): 0.80 (3H, t, J = 6.6, CH_3), 1.22 (8H, m, $C\underline{H}_2(C\underline{H}_2)_3CH_3$), 1.42 (2H, $C\underline{H}_2(CH_2)_4CH_3$), 1.78 (2H, m, $C\underline{H}_2(CH_2)_5CH_3$), 2.06 (3H, s, CH_3-CO), 3.27 (2H, t, J = 7.3, S-$C\underline{H}_2(CH_2)_6CH_3$), 7.77 (2H, d, J = 8.9, H-3, 5), 7.86 (2H, d, J = 8.8, H-2, 6), 9.42 (1H, brs, NH). IR spectrum(ν, cm^{-1}): 1698 (CH_3CO), 1530 (NH), 1176 (C-O-C, oxadiazole).

2-Nonylthio-5-(4-N-acetylaminophenyl)-1,3,4-oxadiazole (16). Yield 97%, mp 151-116 °C, R_f = 0.49; UV spectrum (λ_{max}, nm): 298.9; ^{1}H NMR (δ, ppm, J/Hz): 0.80 (3H, t, J = 6.7, CH_3), 1.22 (10H, m, $C\underline{H}_2(C\underline{H}_2)_4CH_3$), 1.42 (2H, m, $C\underline{H}_2(CH_2)_5CH_3$), 1.78 (2H, m, $C\underline{H}_2(CH_2)_6CH_3$), 2.06 (3H, s, CH_3-CO), 3.27 (2H, t, J = 7.3, S-$C\underline{H}_2(CH_2)_7CH_3$), 7.77 (2H, d , J = 8.7, H-3, 5), 7.86 (2H, d, J = 8.8, H-2, 6) 9.41 (1H, brs, NH). IR spectrum(ν, cm^{-1}): 1697 (CH_3CO), 1529 (NH), 1178 (C-O-C, oxadiazole).

2-Propylthio-5-(4-N-chloroacetylaminophenyl)-1,3,4-oxadiazole (17). Yield 85%, mp 111-112 °C, R_f = 0.66; UV spectrum (λ_{max}, nm): 297.7; ^{1}H NMR (δ, ppm, J/Hz): 1.01 (3H, t, J = 7.3, CH_3), 1.81 (2H, m, $CH_2C\underline{H}_2CH_3$), 3.21 (2H, t, J = 7.1, S-CH_2) 4.16 (2H, s, CH_2-CO), 7.67 (2H, d, J = 8.7, H-3,5), 7.93 (2H, d, J = 8.8, H-2,6), 8.43 (1H, brs, NH). IR spectrum (ν, cm^{-1}): 1703 (-CH_2CO), 1537 (NH), 1177 (C-O-C, oxadiazole).

2-Butylthio-5-(4-N-chloroacetylaminophenyl)-1,3,4-oxadiazole (18). Yield 96%, mp 142-143 °C, R_f = 0.60; UV spectrum (λ_{max}, nm): 301.5; ^{1}H NMR δ, ppm J/Hz): 0.90 (3H, t, J = 7.3, CH_3), 1.43 (2H, m, $CH_2CH_2C\underline{H}_2CH_3$), 1.76 (2H, m, $CH_2C\underline{H}_2CH_2CH_3$), 3.20 (2H, t, J = 7.3, S-CH_2), 4.16 (2H, s, CH_2-CO), 7.66 (2H, d, J = 8.5, H-3, 5), 7.93 (2H, d, J = 8.9, H-2, 6), 8.41 (1H, brs, NH). IR spectrum (ν, cm^{-1}: 1675 (-CH_2CO), 1550 (NH), 1176 (C-O-C, oxadiazole).

2-Amylthio-5-(4-N-chloroacetylaminophenyl)-1,3,4-oxadiazole (19). Yield 98%, mp 165-166 °C, R_f = 0.63; UV spectrum(λ_{max}, nm): 298.8; ^{1}H NMR (δ, ppm, J/Hz): 0.84 (3H, t, J = 7.3, CH_3), 1.34 (4H, m, $C\underline{H}_2C\underline{H}_2CH_3$), 1.78 (2H, m, $C\underline{H}_2CH_2CH_2CH_3$), 3.23 (2H, t, J = 7.3, S-$C\underline{H}_2CH_2CH_2CH_2CH_3$), 4.23 (2H, s, CH_2-CO), 7.83 (2H, d, J = 8.7, H-3,5), 7.89 (2H, d, J = 8.8, H-2, 6), 9.75 (1H, brs, NH). IR spectrum (ν, cm^{-1}): 1659 (-CH_2CO), 1540 (NH), 1176 (C-O-C, oxadiazole).

2-Hexylthio-5-(4-N-chloroacetylaminophenyl)-1,3,4-oxadiazole (20). Yield 93%, mp 107-108 °C, R_f =0.57; UV spectrum(λ_{max}, nm): 298.3; 1H NMR δ, ppm, J/Hz): 0.82 (3H, t, J = 7.1, CH_3), 1.27 (4H, m, $C\underline{H}_2C\underline{H}_2CH_3$), 1.42 (2H, m, $C\underline{H}_2CH_2CH_2CH_3$), 1.78 (2H, m, $C\underline{H}_2(CH_2)_3CH_3$), 3.27 (2H, t, J = 7.3, S-$C\underline{H}_2(CH_2)_4CH_3$), 4.23 (2H, s, CH_2-CO), 7.82 (2H, d, J = 8.9, H-3, 5), 7.92 (2H, d, J = 8.8, H-2, 6), 9.69 (1H, brs, NH). IR spectrum (ν, cm^{-1}): 1681 (-CH_2CO), 1542 (NH), 1177 (C-O-C, oxadiazole).

2-Heptylthio-5-(4-N-chloroacetylaminophenyl)-1,3,4-oxadiazole (21). Yield 95%, mp 96-97 °C, R_f = 0.58; UV spectrum (λ_{max}, nm): 298.0; ^{1}H NMR (δ, ppm, J/Hz): 0.81 (3H, t, J = 6.9, CH_3), 1.24 (6H, m, $C\underline{H}_2C\underline{H}_2CH_2CH_3$), 1.41 (2H, m, $C\underline{H}_2(CH_2)_3CH_3$), 1.78 (2H, m, $CH_2(CH_2)_4CH_3$), 3.27 (2H, t, J = 7.3, S-$CH_2(CH_2)_5CH_3$), 4.23 (2H, s, CH_2-CO), 7.82 (2H, d, J = 8.9 , H-3, 5), 7.91 (2H, d, J = 8.8, H-2, 6), 9.68 (1H, brs, NH). IR spectrum (ν, cm^{-1}): 1675 (-CH_2CO), 1545 (NH), 1176 (C-O-C, oxadiazole).

2-Octylthio-5-(4-N-chloroacetylaminophenyl)-1,3,4-oxadiazole (22). Yield 98%, mp 100 - 101 °C, R_f = 0.61; UV spectrum(λmax, nm) 298.3; ^{1}H NMR (δ, ppm J/Hz): 0.81 (3H, t, J = 6.8, CH_3), 1.22 (8H, m, $C\underline{H}_2(C\underline{H}_2)_3CH_3$), 1.42 (2H, $C\underline{H}_2(CH_2)_4CH_3$), 1.78 (2H, m, $C\underline{H}_2(CH_2)_5CH_3$), 3.27 (2H, t, J = 7.3, S-$C\underline{H}_2(CH_2)_6CH_3$), 4.23 (2H, s, CH_2-CO), 7.82 (2H, d, J = 8.8, H-3, 5), 7.91 (2H, d, J = 8.9, H-2, 6), 9.68 (1H, brs, NH). IR spectrum (ν, cm^{-1}): 1684 (-CH_2CO), 1539 (NH), 1177 (C-O-C, oxadiazole).

2-Nonylthio-5-(4-N-chloroacetylaminophenyl)-1,3,4-oxadiazole (23). Yield 87%, mp 71-77 °C, R_f = 0.61; UV spectrum (λ_{max}, nm): 298.7; ^{1}H NMR (δ, ppm, J/ Hz): 0.80 (3H, t, J = 6.7, CH_3), 1.23 (10H, m, $C\underline{H}_2(CH_2)_4CH_3$), 1.43 (2H, m, $C\underline{H}_2(CH_2)_5CH_3$), 1.78 (2H, m, $C\underline{H}_2(CH_2)_6CH_3$), 3.27 (2H, t, J = 7.3, S-$C\underline{H}_2(CH_2)_7CH_3$), 4.24 (2H, s, CH_2-CO), 7.34 (2H, d , J = 8.9, H-3, 5), 7.91 (2H, d, J = 8.9, H-2,6), 9.79 (1H, brs, NH). IR spectrum (ν, cm^{-1}): 1677 (-CH_2CO), 1539 (NH), 1179 (C-O-C, oxadiazole).

RESULTS AND DISCUSSION

With the aim to synthesize new derivatives on the functional amino group of 5-(4-aminophenyl)-1,3,4-oxadiazole-2-thione and to study their physico-chemical characteristics and antimicrobial activity, acylation reactions of the previously synthesized 2-alkylthio-5-(4-aminophenyl)-1,3,4-oxadiazoles **1-8** [8] with acetyl chloride (AC) and chloroacetyl chloride (CAC) were carried out. The experiments were carried out in acetone, benzene at room temperature and at the boiling point of the solvents. Also, the influence of the ratio of chemical reagents - alkyl substituted compounds **1-8**, acylating agent and HCl acceptor triethylamine (TEA) on product yield was studied. Optimal reaction conditions were established at which the highest yields (85-98%) of the desired products were achieved.

The optimal reaction conditions were established at which the highest yields (85-98%) of the desired products of 2-alkylthio-5-(4-N-acetyl(N-chloroacetyl)aminophenyl)-1,3,4-oxadiazoles **9-23** (Scheme 1) were achieved (in benzene at room temperature, the ratio of 2-alkylthio-5-(4-aminophenyl)-1,3,4-oxadiazoles **1-8**: AC or CAC : TEA - 1: 1.1: 1.5 respectively):

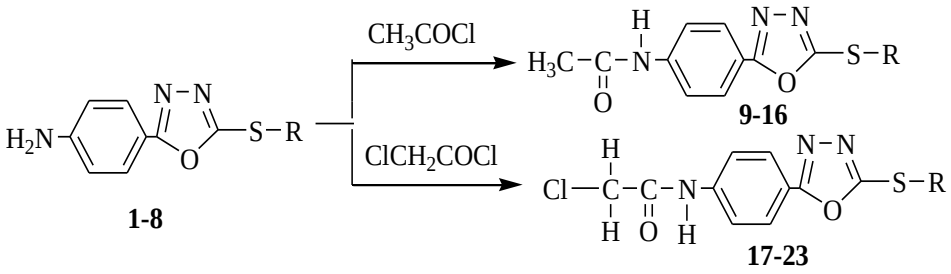

R=C_3H_7(**1**,**9**,**17**), C_4H_9(**2**,**10**,**18**), C_5H_{11}(**3**,**11**,**19**), i-C_5H_{11}(**4**,**12**), C_6H_{13}(**5**,**13**,**20**), C_7H_{15}(**6**,**14**,**21**), C_8H_{17}(**7**,**15**,**22**), C_9H_{19}(**8**,**16**,**23**)

Scheme 1. Synthesis of 2-alkylthio-5-(4-N-acetyl(N-chloroacetyl)aminophenyl)-1,3,4-oxadiazoles **9-23**

Reactions were monitored by TLC. All synthesized compounds are solids. The structure of the obtained derivatives is proved and characterized by ^{1}H NMR, IR and UV spectra. So in the ^{1}H NMR spectra, substituted amino group (NH) proton signals are seen at 9.40-9.48 ppm in 2-alkylthio-5-(4-N-acetylaminophenyl)-1,3,4-oxadiazoles **9-16** and at 8.41-9.75 ppm in 2-alkylthio-5-(4-N-chloroacetylaminophenyl)-1,3,4-oxadiazoles **17-23**. They are very different from the chemical shifts of the unchanged NH_2 group of the initial alkyl derivatives **1-8** where the signals are observed in a

stronger field of 3.72-4.11 ppm [8] that indicates that the acylation reaction proceeds through this amino group. Also the signals at 1.98-2.08 ppm are observed in spectra in the form of singlet corresponding to the protons of the acetyl group (CH_3CO-) of 2-alkylthio-5-(4-N-acetylamino-phenyl)-1,3,4-oxadiazoles **9-16** and at 4.06-4.24 ppm corresponding to the protons of $Cl\text{-}CH_2$ fragment of 2-alkylthio-5-(4-N-chloroacetylamino-phenyl)-1,3,4-oxadiazoles **17-23**. The appearance of absorption bands in the interval of 1674-1707, 1523-1542 cm^{-1} in IR spectra of compounds **9-16** and for **17-23** in the interval of 1659-1703, 1537-1550 cm^{-1}, respectively, corresponding to C=O and NH groups, confirms the production of acyl derivatives on the amino group.

The results of X-ray diffraction analysis of 2-butylthio-5-(4-N-acetylaminophenyl)-1,3,4-oxadiazole also confirm the previously established structures of the synthesized compounds. A crystal of 2-butylthio-5-(4-N-acetylaminophenyl)-1,3,4-oxadiazole **10** was grown from solutions of acetone by slow evaporation at room temperature.

The five-membered heterocyclic ring in molecular structure **10** is flat (within ± 0.002 Å) (Fig.1.). The phenyl ring is also flat (within ± 0.001 Å). The location of phenyl ring relative to the plane of the oxadiazole nucleus is characterized with a value of torsion angle O1-C5-C6-C7 of 5.15°. The location of the acetamido fragment relative to the plane of the phenyl ring is characterized with a value of torsion angle C8-C9-N12-C13 -8.94°.

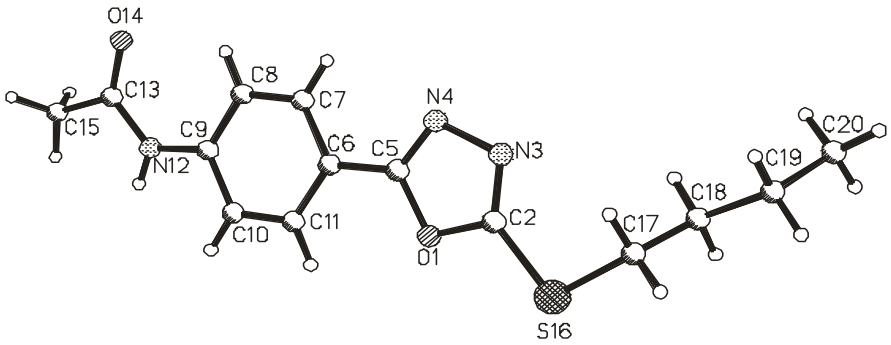

Fig. 1. Numbering of the atoms in the structure **10**.

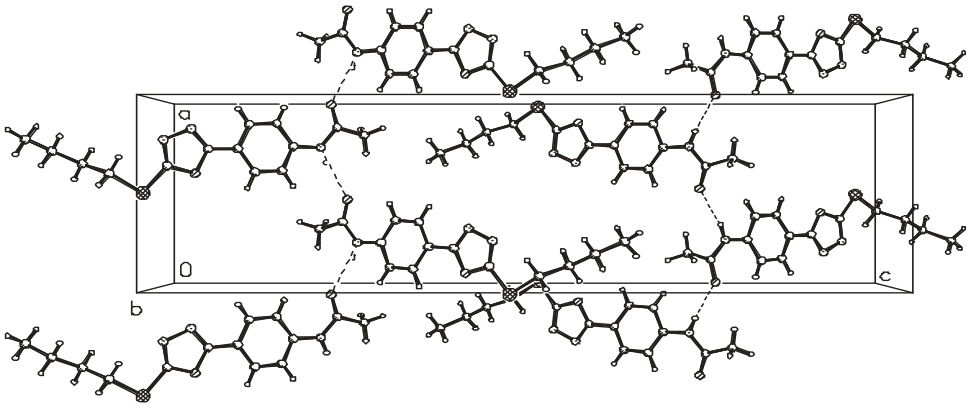

Fig. 2. Packing structure **10**.

In the crystal structure of **10** C=O group and NH group form intermolecular H-bonds. In the crystal between molecules related by glide plane are formed N-H...O type H-bonded chains along *a* axis with graph set motifs of $C_1^1(4)$ [19] (Fig. 2.). Parameters of H-bond are as follows: N-H 0.86 Å, H…O 2.12 Å, N…O 2.934(3) Å, angle N-H…O 159°, symmetry *-1/2+x,y,3/2-z*.

In the structure **10** a weak π...π interaction was observed between the five- and six-membered aromatic rings (atoms O1, C2, N3, N4, C5 and C6, C7, C8, C9, C10, C11) of molecules related by symmetry *3/2-x,-1/2+y,z* and with centroid-centroid distance of 3.6766(15) Å [20].

Herein, the antimicrobial activity of the compounds **9-23** against *Staphylococcus aureus*, *Bacillus subtilis*, *Pseudomonas aeruginosa*, *Escherichia coli* as well as the fungus *Candida albicans* was assessed using the agar disk-diffusion method [17,18]. The results of the current research are displayed in Table 2 and show that Gram-positive bacteria were susceptible to the studied compounds. *B. subtilis* and *S. aureus* are more susceptible to the antimicrobial activity of the

compounds **17**, **18**, **21** and **22** displaying inhibition zone diameters between 8-14 mm at a concentration of 200 μg/per disc. All tested compounds showed no inhibitory activity against Gram-negative bacteria and *C. albicans* fungus.

Table 2. Antimicrobial effect evaluated by diameter of inhibition zone (mm) for compounds 9-23 using agar disk-diffusion assay

Compound	Gram-positive bacteria		Gram-negative bacteria		Fungus
	B. subtilis	*S. aureus*	*P. aeruginosa*	*E. coli*	*C. albicans*
9	NA	NA	NA	NA	NA
10	NA	NA	NA	NA	NA
11	NA	NA	NA	NA	NA
12	NA	NA	NA	NA	NA
13	NA	NA	NA	NA	NA
14	NA	NA	NA	NA	NA
15	NA	NA	NA	NA	NA
16	NA	NA	NA	NA	NA
17	14	11	NA	NA	NA
18	10	8	NA	NA	NA
19	6	6	NA	NA	NA
20	6	6	NA	NA	NA
21	10	12	NA	NA	NA
22	9	11	NA	NA	NA
23	NA	NA	NA	NA	NA
Ampicillin (20μg/disc)	26	25	NT	26	NT
Ceftriaxone (20 μg/disc)	NT	NT	25	NT	NT
Nystatin (20 μg /disc)	NT	NT	NT	NT	20

NA- not active; NT – not tested

CONCLUSION

The new 2-alkylthio-5-(4-N-acetyl (N-chloroacetyl) aminophenyl)-1,3,4-oxadiazoles **9-23** were synthesized by the reaction of 2-alkylthio-5-(4-aminophenyl)-1,3,4-oxadiazoles with acetyl and chloroacetylchlorides. Optimal conditions for the synthesis were found; the physicochemical characteristics and structures of the synthesized compounds were established. X-ray diffraction analysis was carried out using compound **10** as an example, which confirmed the structures of the substances obtained. The 2-alkylthio-5-(4-N-chloroacetylaminophenyl)-1,3,4-oxadiazoles **17-22** showed appreciable antibacterial activity against Gram-positive bacteria.

Acknowledgment: *Authors are thankful to the Academy of Sciences of the Republic of Uzbekistan for supporting this study (grant VA-FA-F-7-006 and VA-FA-F-6-009).*

REFERENCES

1. R. Kharb, R. Kaur et al. *Eur. J. Biomed. and Pharm. Scienc.*, **1**, 401 (2014).
2. R. Sharma, N. Kumar, R. Yaday, *Research & Reviews: J. Chem.*, **4**, 1 (2015).
3. H. Khalilullah, M.J. Ahsan, M. Hedaitullah, S. Khan, B. Ahmed, *Mini-Reviews in Medicinal Chemistry*, **12**, 789 (2012).
4. P. Dholaria, K. Parikh, D. Joshi, *Int. J. Chemtech. Applications*, **4**, 1 (2015).
5. A.A. Ziyaev, D.S. Ismailova, *World J. Pharm. Res.*, **6**, 52 (2017).
6. A.A. Ziyaev, I.F. Tozhiev, Kh.M. Shakhidoyatov, *Chem. Heterocycl. Compd.*, **48**, 488 (2012).
7. D.S. Ismailova, A.A. Ziyaev, E.R. Kurbanova, International Congress on Heterocyclic Chemistry "KOST-2015", Moskow, Russia, 2015, p. 434.
8. D.S. Ismailova, A.A. Ziyaev, B.Z. Elmuradov, T.T. Toshmurodov, Kh.M. Bobakulov, R.P. Zakirova, *J. Basic Appl. Res.*, **2**, 476 (2016).
9. A.A. Ziyaev, D.S. Ismailova, *Uzbek Chem. J.*, **1**, 15 (2015).
10. I.F. Tozhiev, A.A. Ziyaev, Kh.M. Shakhidoyatov, *Chemistry and Chemical Technology, Tashkent*, **4**, 17 (2012).
11. H.P. Shah, B.R. Shah, J.J. Bhatt, N.C. Desai, P.B. Trivedi, N.K. Undavia, *Indian J. Chem., Sect. B.*, **37B**, 180 (1998).
12. V. Modi, P. Modi, *J. Saudi Chem. Soc.*, **16**, 327 (2012).

13. E. Ghanem, S. Al-Hariri, M. Benalia, *Australian J. Basic Appl. Sciences*, **7**, 135 (2013).
14. Oxford Diffraction, CrysAlisPro, Oxford Diffraction Ltd, Abingdon, Oxfordshire, England, 2007.
15. G.M. Sheldrick, *Acta Cryst. A.,* **64**, 112 (2008).
16. N.A. Awadh Ali, W-D. Jülich, C. Kusnick, U. Lindequist, *J. Ethnopharmacol.*, **74**, 173 (2001).
17. CLSI, Performance Standards for Antimicrobial Disk Susceptibility Tests; Approved Standard, National Committee for Clinical Laboratory Standards, Wayne, PA, USA, 11th edn., 2014.
18. DIN Taschenbuch 222, Medizinische Mikrobiologie und Immunologie, Beuth-Verlag, Berlin, 2004.
19. M.C. Etter, J.C. MacDonald, *Acta Cryst., B.*, **46**, 256 (1990).
20. C. Estarellas, D. Escudero, A. Frontera, D. Quinonero, P. Deya, *Theor. Chem Account.*, **122**, 325 (2009).

Bulgarian Chemical Communications, Volume 51, Issue 1, (pp. 80 – 87) 2019

Development and validation of a chromatographic method to identify and quantify the flavonoids extracted from *S. rebaudiana* Bertoni

A. Carrera-Lanestosa[1], M. Segura-Campos[1], T. Coral-Martinez[2], D. Ruíz-Ciau[2], J. Araujo-León[2], D. Betancur-Ancona[1], Y. Moguel-Ordóñez[3*]

[1]*Facultad de Ingeniería Química, Universidad Autónoma de Yucatán, Mérida, México (Posgrado Institucional en Ciencias Químicas y Bioquímicas)*
[2]*Facultad de Química, Universidad Autónoma de Yucatán, Mérida, México*
[3]*Campo Experimental Mocochá, CIRSE-INIFAP, Mocochá, México*

Received August 8, 2018; Revised September 5, 2018

Leaf extracts of *Stevia rebaudiana* contain a great variety of flavonoids which are potential antioxidants for the human body. In this work a high-performance liquid chromatography (HPLC)-based method to identify and quantify flavonoids (quercetin, kaempferol, luteolin and apigenin) from extracts of *S. rebaudiana* was developed and validated. A HPLC with a diode detector array at 200 nm wavelength and an Eclipse XDB-C18 column (150 mm length, 4.6 mm d.i., and 5 μm particle size) was used. The mobile phase was acidified methanol (pH 2.5) in a gradient elution system. Sample injection volume was 10 μL at 1 mL/min flow rate and 25 °C temperature. Aqueous extracts of *S. rebaudiana* were prepared and its flavonoids quantified with the developed method. The validation of the method was performed according to the ICH Q2A guideline, that is, assessing selectivity, linearity, sensitivity, precision, detection limits (DL), quantification limits (QL), and accuracy. Calibration curves showed a linear trend with a correlation and determination coefficient higher than 0.99. Precision showed relative standard deviation (RSD) values lower than 10%. DLs and QLs were 1.93 and 3.35 – 6.43 μg/mL, respectively, while accuracy showed 90 – 100% recovery of fortified samples. The implemented method fulfills the metrics of the ICH and is suitable to identify and quantify flavonoids in *S. rebaudiana* Bertoni.

Keywords: *Stevia rebaudiana*, Flavonoids, ICH, Validation, HPLC.

INTRODUCTION

Several pharmacological, clinical, toxicological and therapeutic applications of leaf extracts of *S. rebaudiana* [1, 2], as well as numerous biological activities such as antacid, anticaries [3], anti-rotavirus, antibacterial [4], antihypertensive, antifungal, anti-inflammatory, antiviral, anti-yeast, diuretic, antioxidant, anti-cancer, etc., have been found [5].

S. rebaudiana is currently grown commercially for use as a sweetener as it contains diterpene glycosides [6], stevioside and rebaudioside A being most common in the leaves (5 – 10% and 2 – 4% w/w on a dry basis, respectively). On the other hand, rebaudioside B, rebaudioside C, rebaudioside D, rebaudioside E, rebaudioside F, dulcoside A, rubusoside, and esteviolbioside are less common glycosides in *S. rebaudiana* leaves [7].

S. rebaudiana leaves also contain a complex mixture of other compounds, such as diterpenes, labdanos, triterpenes, stigmasterol, tannins, ascorbic acid, alkaloids, steroids, saponins, β-carotene, chromium, cobalt, magnesium, iron, potassium, phosphorus, riboflavin, thiamin, tin, zinc, β-sitosterol, caffeic acid, campesterol, caryophyllene, centaureidin, chlorogenic acid, chlorophyll, flavonoids, among others [8]. Flavonoids are bioactive compounds present in fruits, vegetables, grains, nuts, seeds, spices, medicinal plants, and some usual drinks such as tea, red wine, and beer [9]. Flavonoids are of scientific interest due to their antioxidant activity which makes them suitable for stabilizing and eliminating oxygen reactive species (ORS). Furthermore, flavonoids have other beneficial effects including anti-inflammatory, antimicrobial and antidiabetic, antihypertensive, and anticancer effects [8, 9]. Flavonoids have a base structure consisting of two benzene rings at the ends of the molecule joined by a 3-carbon ring. Other molecules, such as methyl, oxyhydrides, and sugars, can be added to the 3-carbon ring, making possible the generation of different types of flavonoids such as flavanones, flavonols, catechins, flavones, anthocyanins, and isoflavones [10].

Some flavonoids, such as quercetin, kaempferol, luteolin and apigenin (Fig. 1), are present in *S. rebaudiana*. However, the content of these compounds highly depends on the stress of the plant as a consequence of the type of soil, weather, agronomic conditions, or disease [8, 9].

* To whom all correspondence should be sent:
E-mail: moguel.yolanda@inifap.gob.mx

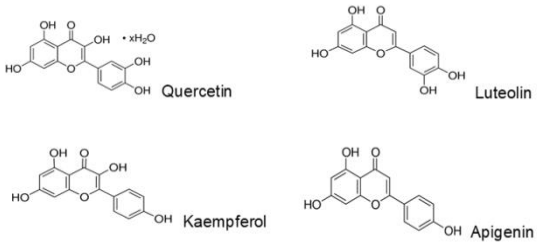

Fig 1. Chemical structure of the flavonoids in *S. rebaudiana* Bertoni [9].

There are several methods to identify and quantify flavonoids in *S. rebaudiana* including colorimetric [8, 11, 12] and spectrophotometric methods, [4, 13, 14], thin-layer chromatography (TLC) [9], high-performance liquid chromatography (HPLC) [15], and others. HPLC is frequently used to identify and quantify diverse compounds in numerous biological extracts with a high precision and reliability. Currently, there is no official method to identify and quantify flavonoids in *S. rebaudiana*. Therefore, this works aims to develop and validate a HPLC-based method to identify and quantify the flavonoids (quercetin, kaempferol, luteolin, and apigenin) from aqueous leaf extracts of *S. rebaudiana* Bertoni.

EXPERIMENTAL

Reactive and standard reference materials

Two standard reference materials were used for flavonols and flavones: the one contained quercetin (Sigma PHR1488) and kaempferol (Sigma 96353), and the second contained luteolin (Sigma 72511) and apigenin (Sigma 42251), respectively. Standard flavonoids were diluted with deionized water (Milli Q water) to prepare the mother solutions (1 mg/mL) used to generate the required calibration curves to validate the method. These solutions were filtered through a nylon membrane (0.45 μm) before injecting in the equipment.

Reactive and standard reference materials

An Agilent Technologies equipment (model: 1200 series) with a diode detector array at 200 nm wavelength, packed with an autosampler, degasser, and temperature controller was used. Chromatographic separations were performed with a packed Eclipse XDB-C18 column (150 mm length, 4.6 internal diameter, and 5 μm particle size) (Agilent Technologies) at 25°C temperature. The mobile phase was methanol (HPLC-grade, J.T. Baker Phillipsburg, NJ) and acidified water (pH 2.5) using a system of gradient elution of 30 min, starting and ending with a water-to-methanol ratio of 3/7 and 7/3, respectively. The injection volume was 10 μL during 30 min (1 mL/min) for both, the standard reference materials and the samples.

Validating the method

The developed method was validated under the metrics of the International Conference of Harmonization (ICH Q2A), which establishes the analytical parameters that must be assessed to validate a chromatographic method. The reliability of the method was determined with the parameters described below [16].

Selectivity: Selectivity refers to the capacity of the method to unequivocally assess the analyte in the presence of other components. All the standard reference materials were analyzed at 50 μg/mL according to the chromatographic conditions described earlier. The chromatographic peaks of each standard reference material were obtained, as well as their retention times (t_R) and ultraviolet-visible spectra.

Linearity and sensitivity: Linearity is the capacity of the method to obtain directly proportional responses to the content of analyte in the sample within a range. This parameter was assessed using the mother solutions under concentrations of 1 mg/mL for each flavonoid, which were diluted until reaching concentrations of 25, 50, 75, 100, 150, and 200 μg/mL to generate the calibration curves. The obtained contents were injected in triplicate and linearity was assessed by calculating the regression equation, as well as the correlation (r) and determination (R^2) coefficients. Sensibility was assessed as the slope of the equations of each analyte.

Precision: Intraday and interday precisions were assessed. The former was demonstrated by means of the analysis of a homogeneous sample under the same conditions and on the same day, obtaining a minimum grade of dispersion among the results. The second was performed by analyzing the sample under the same conditions but on different days. Both, intraday and interday precisions, must reach a relative standard deviation (RSD%) lower than 10% to consider the method precise. Intraday and interday RSD%, retention times (t_R), and areas under the curves were calculated considering the standard deviation (SD) and mean using equation 1.

$$\% RSD = SD/X \times 100 \quad (1)$$

Detection and quantification limits (DL and QL): DL is the lowest concentration of an analyte in a sample that can be detected but not necessarily quantified as an exact value. On the other hand, QL is the lowest concentration of an analyte contained in a sample that can be quantitatively determined

with an acceptable precision and accuracy. These factors were computed using equation 2.

$$DL = 3.3/SD \text{ and } QL = 10/SD, \quad (2)$$

3.3 and 10 being the standard deviation of the intercepts.

Accuracy: Accuracy refers to how close an identified value is to a predetermined value. The accuracy of the method was assessed by testing the recovery of analytes intentionally added to the aqueous extract of *S. rebaudiana* to fortify them. 100 µg/mL of each flavonoid was added to the aqueous extract of *S. rebaudiana* and each test was performed in triplicate. The recovery of analytes must range between 90% to 110%.

Aqueous extract of S. rebaudiana

Aqueous leaf extracts of *S. rebaudiana* Bertoni from Yucatan, Mexico, were obtained by the method developed by Dutta *et al.* [17]. 10 g of milled leaves were suspended in 100 mL of distilled water (10% w/v). Extraction was performed in a 250 mL beaker in a Maria bath at 40 °C temperature under constant agitation during 3 h. Extracts were then centrifugated at 2500 rpm, 10 °C temperature for 30 min, and supernatants were recovered. Extraction was performed twice discarding the residue after the last washing. Supernatants were mixed and filtered at vacuum using Whatman 2 filter papers, and were lyophilized using a Labconco FreeZone 4.5 lyophilizer.

Identification and quantification of flavonoids in the aqueous extract of S. rebaudiana Bertoni

After validating the chromatographic method, flavonoids from *S. rebaudiana* were identified by superposition of the standard reference materials with the extract. As the vegetable material has a complex chemical composition, as well as a high portion of analytes and interferent materials, the UV-visible spectral region of the peaks identified in the extract was used as comparison criterion to confirm or highlight the presence of analytes. A 10-mg aliquot of lyophilized extract was diluted in 3 mL of Milli Q water, collected in a 5 mL volumetric flask, filtered through a 0.45-µm nylon membrane, and analyzed.

Statistical analysis

Regression analysis was performed to assess the linearity by the least-square method using the Statgraphics CENTURION XV software. Microsoft Excel spreadsheets were configured to analyze the precision, DL, QL, and accuracy parameters.

RESULTS AND DISCUSSION

Validating the method

Selectivity: Chromatographic peaks were obtained during the analysis of the flavonoids and their t_R were identified. The presence of the analytes was verified with their UV-visible spectra to check the selectivity of the method (Fig 2).

The t_R of the assessed analytes were shorter than those reported by Muanda *et al*. [18], who got t_R for quercetin and apigenin of 42.87 and 44.89 min, respectively, using a mobile phase (50 mM ammonium phosphate, 80% acetonitrile, and 200 mM phosphoric acid) and a C18 intersil ODS column. Toso & Skliar, [19], got a t_R of 33.12 min for kaempferol using a mobile phase in methanol-water (15:85 – 100:0) gradient and a RP-C18 column, while Xiao-quing & Jian-bo, [20] reported a t_R of 20.1 min for luteolin using a mobile phase consisting of a mixture of methanol, acetonitrile, acetic acid, and phosphoric acid (200:100:10:10:200 v/v) and a Kromasil RP-C18 column. The polarity among the analytes and the mobile phase, along with the type of column, might explain the differences in t_Rs. A C-18 column, which can retain each component depending on its affinity, was used in all the cases (octadecyl functional group). However, this was not the case for the mobile phases which play a relevant role on t_Rs. Flavonoids are non-polar analytes and have affinity for less polar mobile phases. Muanda *et al.* [18] and Xiao-quing & Jian-bo, [20] used salts, acids, and/or acetonitrile as mobile phases, which are more polar than methanol. In this sense, the assessed analytes were retained much longer in a chromatographic column due to the affinity and difference of polarities. Toso & Skliar, [19] used a gradient mobile phase similar to that of this study but using a methanol-water gradient of (15:85) at the beginning. In minute 32 the less polar solvent reached a higher percentage (100:0) and therefore, kaempferol was eluted from the column in 33.12 min t_R, which is longer than in this study using gradient elution (water-methanol 70:30 v/v). However, since the beginning the percentage of methanol increased quickly, which allowed for eluting the analytes in a shorter time. It is important to highlight that the t_R obtained in this study under the developed method have a great advantage as they are shorter and require a lower volume of the mobile phase to determine the flavonoids from *S. rebaudiana*.

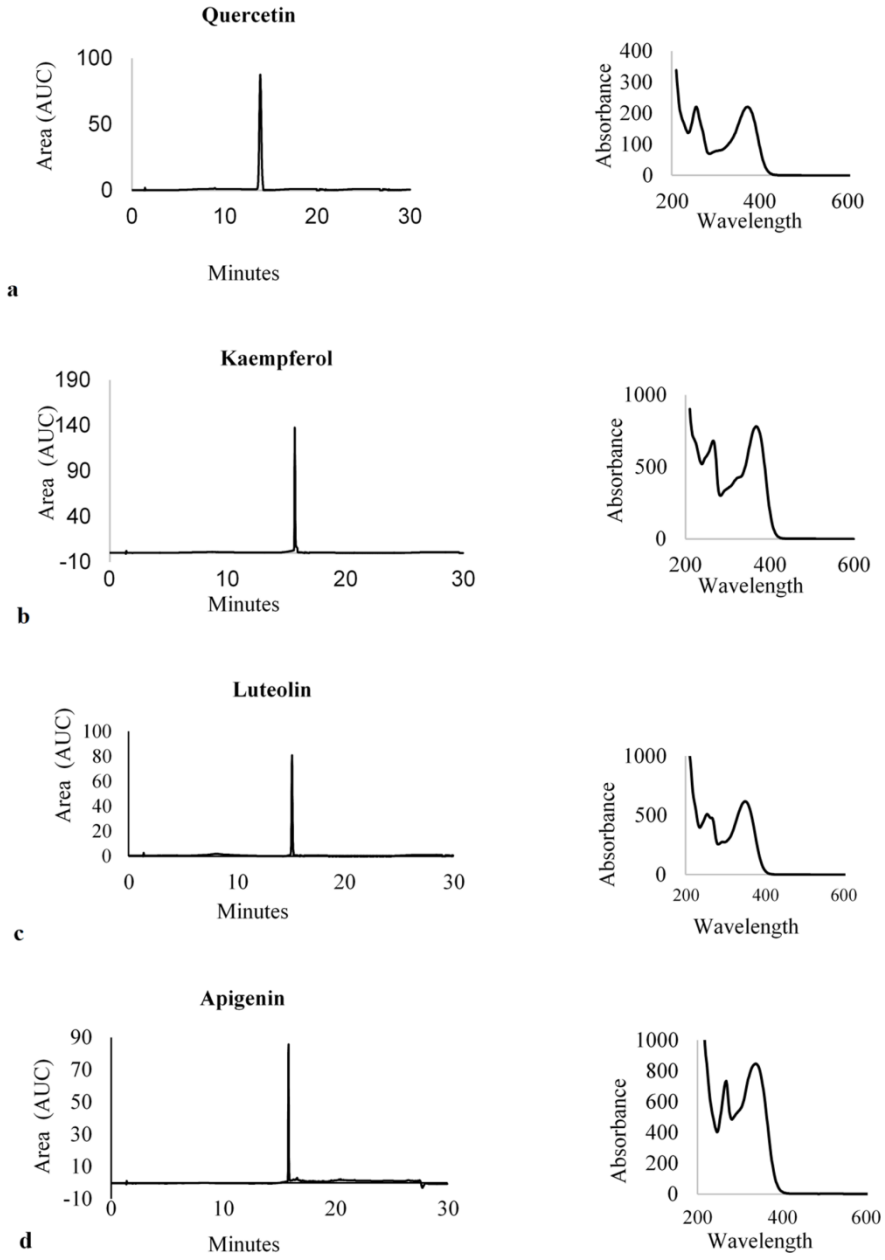

Fig. 2. Retention times (t_R) and UV spectra of the flavonoids at a concentration of 50 µg/mL. a) quercetin (t_R 13.88 min), b) kaempferol (t_R 15.62 min), c) luteolin (t_R 15.08 min), d) apigenin (t_R 15.81 min).

Linearity and sensitivity: The linearity of the developed method was appropriate to quantify flavonoids as it showed a linear regression between the concentration of the standard reference material and the area under the curve of the chromatographic analysis. The correlation coefficient (r) showed a linear trend between the two of the analyzed variables (area under the concentration curve) of 0.99. The determination coefficient (R^2) was higher than 99% in most of the cases but kaempferol, for which it was 98%. The intercepts refer to the point where two lines meet, while the values of the slopes - to the inclination of the line in the linear model (Fig 3). Luteolin slopes had a higher inclination (23.48) than apigenin (16.73), which indicates a greater sensitivity to the developed method than the slopes with a lower inclination, such as those for quercetin and kaempferol (12.69 and 12.60, respectively) (Table 1).

Table 1. Parameters of the linear regression model (y = a + b*x) of the standard reference materials of flavonoids (quercetin, kaempferol, luteolin, and apigenin).

Parameter	Quercetin	Kaempferol	Luteolin	Apigenin
r	0.999	0.993	0.999	0.998
R^2	0.999	0.987	0.999	0.997
Intercept in the Y axis	-50.52	732.95	147.81	989.66
Slope	12.69	12.60	23.48	16.73

R: correlation coefficient, R^2: determination coefficient.

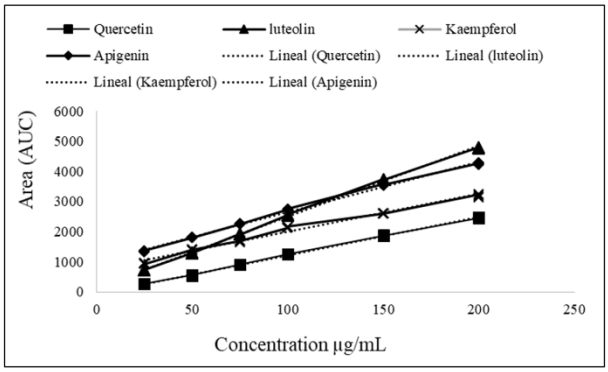

Fig. 3. Linear regression graphic (mean ± SD). Area (AUC) *vs* concentration (y = a + bx) for quercetin, kaempferol, luteolin and apigenin.

Precision: Concentrations of 50, 100, and 200 µg/mL were used to measure the intraday precision. As indicated in Table 2, the RSD% for t_R was lower for luteolin (0.04%), and higher for quercetin (0.22%) and kaempferol (1.55%). The concentrations used to measure interday precision were the same. In this case, the RSD% for t_R was lower for kaemperfol (0.01%) and higher for quercetin (0.45%). The RSD% values of the area under the curve were lower than 9%, obtaining a lower value for apigenin (0.56%) and a higher value for kaempferol (8.68%).

Table 2. Intraday precision of the standard reference materials of flavonoids.

Flavonoid	Conc. (µg/mL)	t_R (Mean ± SD)	RSD% Time	Area (Mean ± SD)	RSD% Area
Quercetin	50	13.86±0.03	0.22	547.63±6.57	1.20
	100	13.84±0.01	0.08	1247.37±2.74	0.22
	200	13.80±0.01	0.07	2469.9±16.11	0.65
Kaempferol	50	15.62±0.02	0.09	1388.47±9.8	0.71
	100	15.61±0.005	0.04	2149.27±24.3	1.13
	200	15.60±0.005	0.04	3191.6±49.5	1.55
Luteolin	50	15.07± 0.01	0.04	1282.13±10.7	0.84
	100	15.07±0.01	0.04	2546.5±16.2	0.64
	200	15.07±0.01	0.04	4788.47±15.6	0.33
Apigenin	50	15.81±0.01	0.04	1804.07±6.70	0.37
	100	15.80±0.005	0.06	2739.43±6.48	0.24
	200	15.80±0.005	0.04	4257.07±34.9	0.82

Table 3. Interday precision of the standard reference materials of flavonoids.

Flavonoid	Conc. (µg/mL)	t_R (Mean ± SD)	RSD% Time	Area (Mean ± SD)	RSD% Area
Quercetin	50	13.88±0.06	0.22	545.48±6.4	1.20
	100	13.85±0.04	0.08	1243.49±7.0	0.22
	200	13.83±0.05	0.07	2468.63±15.6	0.65
Kaempferol	50	15.62±0.01	0.09	1416.74±38.8	0.71
	100	15.61±0.007	0.04	2072.27±179.8	1.13
	200	15.55±0.17	0.04	3116.11±136.8	1.55
Luteolin	50	15.07±0.02	0.04	1254.13±22.6	0.84
	100	15.07±0.01	0.04	2525.08±22.5	0.64
	200	15.07±0.01	0.04	4758.32±28.8	0.33
Apigenin	50	15.81±0.007	0.04	1812.38±20.5	0.37
	100	15.80±0.007	0.06	2742.77±12.2	0.24
	200	15.81±0.007	0.04	4260.12±28.6	0.82

In both cases the RSD% was lower than 10%, indicating a minimum grade of dispersion in the results (Table 3). This demonstrates that the method is precise as it is under the predetermined acceptance criteria.

Table 4. Detection limits (DL) and quantification limits (QL) of the standard reference materials of flavonoids.

Flavonoid	Detection Limit (DL) (µg/mL)	Quantification Limit (QL) (µg/mL)
Quercetin	1.00	3.35
Kaempferol	1.76	5.85
Luteolin	1.93	6.46
Apigenin	1.19	3.99

Detection and quantification limits: The DL of the flavonoids ranged between 1.00 and 1.93 µg/mL, quercetin and luteolin being detected at 1.00 and 1.93 µg/mL, respectively. The concentrations of flavonoids that could be quantified with an acceptable precision (QL) ranged between 3.35 and 6.46 µg/mL. In this case, quercetin displayed a lower value of the quantification limit (3.35 µg/mL), while for luteolin the concentration was higher (6.46 µg/mL). Quercetin can be detected and quantified under lower concentration as it contains a higher number of fluorescent groups which provide a higher molecular sensitivity (Table 4).

Accuracy: Accuracy was measured using the extract of *S. rebaudiana* fortified with the 4 flavonoids recovering 94.28 – 100.86% of the added analytes (Table 5), luteolin being the most recovered (100.86%) analyte, followed by quercetin (100.73%). On the other hand, kaempferol and apigenin were the least recovered analytes (94.28 and 96.70%, respectively). A higher content of luteolin and quercetin in the extract of S. *rebaudiana* explains these differences. These results indicate that the developed method is accurate and does not lead to losses in the assessed analytes as it is within the predetermined acceptable criteria.

Table 5. Accuracy of the analytical method expressed as the recovery percentage of the samples fortified with the standard reference materials of flavonoids

Flavonoid	Accuracy (%) Mean ± SD
Quercetin	100.73±1.10
Kaempferol	94.28±2.08
Luteolin	100.86±0.58
Apigenin	96.70±0.64

Samples were fortified with 100 µg/mL of each standard reference material.

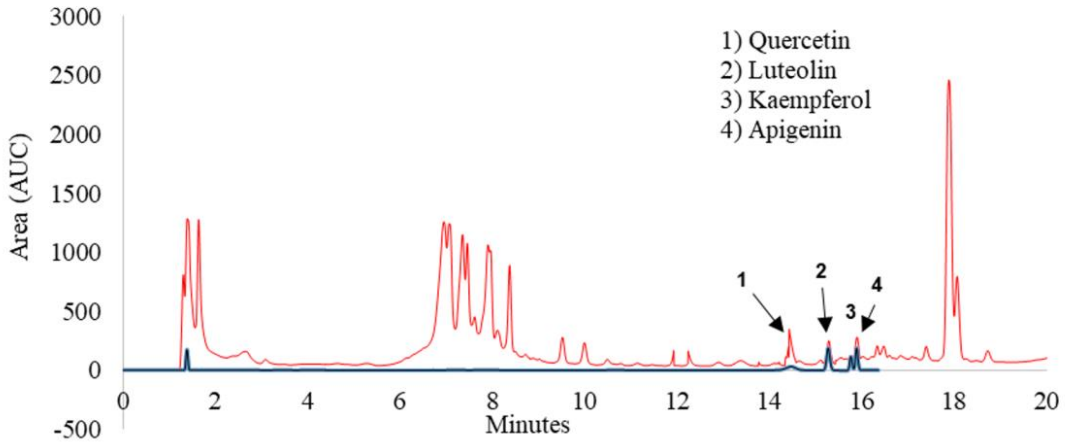

Fig. 4. Chromatogram of the extract of *S. rebaudiana* Bertoni.

Identification and quantification of the flavonoids from the aqueous extracts of S. rebaudiana Bertoni

Fig. 4 shows the chromatographic analysis to identify and quantify the flavonoids from the extract of *S. rebaudiana*. Both the chromatographic peaks and the superposition of the 4 flavonoids have the same t_R.

Table 6 shows the quantification of the flavonoids through the calibration curves performed during the validation process. Quercetin, luteolin, and apigenin contents identified in this work were higher than those reported by Periche *et al.* (2016), who assessed the hydro alcoholic extracts of *S. rebaudiana* leaves by HPLC and found a high

content of quercetin and apigenin of 0.039 g/100g of dried leaves for both analytes. This may be due to the fact that the presently analysed sample of *S. rebaudiana* was from a new genetic material that has been selected considering its agronomic conditions which were adapted to the conditions in the southeastern zone of Mexico. Thus, *S. rebaudiana* grew under pretty particular conditions including a leptosol soil (not very deep soils, dark color limited by rock, retains up to 80% water, and has a high salt content which means high electric conductivity). This created stressful conditions for Stevia, which could cause a higher phytochemical content.

Table 6. Flavonoid content expressed as g/100g of leaves of *S. rebaudiana*.

Flavonoid	*S. rebaudiana* Mean ± SD
Quercetin	0.062 ± 0.5^{b}
Kaempferol	ND[a]
Luteolin	0.084 ± 0.2^{d}
Apigenin	0.079 ± 0.06^{c}

ND: not detected. [a-d] Different letters indicate statistical difference ($P < 0.05$).

Regarding the luteolin and kaempferol contents in *S. rebaudiana*, no reports about their quantification by HPLC were found. Mehenni *et al.* [21] found luteolin (0.061g/100 g dried leaves) in ethanolic extracts of *P. lentiscus* leaves. Ghanta *et al.* [9] characterized kaempferol-3-O-ramnoside in a derivate of kaempferol containing a rest of rhamnose in the C-3 position of the original compound. The presence of kaempferol was not detected in the assessed extracts possibly because its content is below the detection and quantification limits reported in the validation stage. Furthermore, the kaempferol used in this study was the original compound and not the characterized glycosylate used by Ghanta *et al.* [9].

López-Corona [22] reported an 8.64 µg/mL content of kaempferol in the hydrolyzed methanolic extract of *C. graciliar* leaves using low concentrations in the standard curve. The extract could be detected and therefore, the differences with this work might rely on the type of vegetable species used, as well as on the geo-climatic and agronomic conditions of the crop.

CONCLUSIONS

The developed method was validated and was found selective, linear, sensitive, precise, and accurate within the ranges predetermined by the ICH. Therefore, this method can be applied to identify and quantify flavonoids extracted from *S. rebaudiana* Bertoni cultivated in southeastern Mexico.

Acknowledgement: *This work was supported by the Fiscal Funds Program-INIFAP through the "Development of based food products based on Stevia rebaudiana Bertoni leaves" project. We also want to thank to the Program for Improvement of Professor [Programa de Mejoramiento al Profesorado (PROMEP)] by the given scholarship.*

REFERENCES

1. K. Das, R. Dang, N. Gupta, *Int. J. Nat. Eng. Sci.*, **3**, 65 (2009).
2. D. Preethi, T.M. Sridhar, P. Josthna, C.V. Naidu,. *J. Ecobiotech.*, **3**, 05 (2011).
3. S. A. González-Moralejo, An approach to understand a potential natural sweetener, *S. rebaudiana* Bertoni: production, consumption, and potential demand. [In Spanish]. *Agro.*, **17**, 57 (2011).
4. S. Singh, V. Garg, D. Yadav, M. N. Beg, N. Sharma, In vitro antioxidative and antibacterial activities of various parts of S. rebaudiana (Bertoni). *Intern. J Pharmacy Pharmaceutical Sci..*, **4**, 468 (2012).
5. J. R. Ramirez, O. Y. Moguel, *Stevia rebaudiana* Bertoni, a crop with a productive, sweetener and medicinal potential in México, in: D. Betancur-Ancona (ed.) *S. rebaudiana*, Chemical composition, uses and health promoting aspects, Yucatán, México: Nova, 2015, p. 1.
6. K. Y. Ashok, D. Singh, P. S. Ahuj, *Can. J. Plant Sci.*, **91**, 1 (2011).
7. M. C. Carakostas, A. C. Curry, D. J. Brusick, *Food Chem. Toxicol.*, **46**, S1 (2008).
8. S. Bakkar, M. M. R. Rahman, M. A. Hossain, M. A. Rashid, *J. Trop. Asian Pac. Dis.*, **4**, 275 (2014).
9. S. Ghanta, A. P. Banerjee, S. Chattopadhyay, *J. Agric. Food Chem.*, **55**, 10962 (2007).
10. J. C. I. Escamilla, M. E. Y. Cuevas, F. J. Guevara, *J. Rev. Fac. Med.*, **52**, 73 (2009).
11. K. Il-Suk, Y. Mira, L. Ok-Hwan, *Food Science Technology*, **44**, 1328 (2011).
12. S. Sutradhar, U. Preeti, A. Humera, A. M. Muneem, *Res. J. Pharm, Biol. Chem. Sci.*, **14**, 674 (2013).
13. A. E. Abou-Arab, A. A. Abou-Arab, M. F. Abu-Salem., *Afric. J. Food Sci.*, **4**, 269 (2010).
14. E. Zayova, I. Stancheva, M. Geneva, M. Petrova, L. Dimitrova, *Turk J. Biol.*, **37**, 106 (2013).
15. A. Periche, M. L. Castelló, A. Heredia, I. Escriche, Effect of different drying methods on the phenolic, *J. Flavour Fragr.*, **31**, 173 (2016).
16. ICH. Harmonized tripartite guideline validation on analytical procedures: text and methodology. International Conference on Harmonization Q2A(R1) (2005).
17. P. K. Dutta, M. M. Razu, M. K. Alam, M. A. Awal, M. Mostofa, *Int. J. of Biol. Res.*, **2**, 17 (2010).

18. F. N. Muanda, R. Soulimani, B. Diop, A. Dicko, *Food Sci. Technol.*, **44**, 1865 (2011).
19. R. E. Toso, M. I. Skliar, Aislamiento, identificación y cuantificación de compuestos con actividad gastroprotectora presentes en Centaurea solstitialis. Ciencia Veterinaria. Facultad de Ciencias Veterinaria sp U.N.L. Pam, **17** (2002).
20. C. Xiao-qing, X. Jian-bo, RP-HPLC-DAD. *Iranian J. Pharm. Res.*, **3**, 175 (2005).
21. C. Mehenni, D. Kilani-Atmani, S. Dumarcay, D. Perrin, P. Gerardin, D. Atmani, *J. Food Drug Analysis*, **1** (2016).
22. M. G. López-Corona, Identificación y cuantificación del ácido clorogénico y de flavonoides presentes en hojas y frutos de *Crataegus gracilior* PHIPPS. Tesis de Licenciatura. Universidad Autónoma de Querétaro, Facultad de Química, 2013.

Bulgarian Chemical Communications, Volume 51, Issue 1, (pp. 88 – 95) 2019

Application of vibrational spectroscopy and XRD analysis for investigation of calcium oxalate kidney stones

D. Petrova[1], K.Petkova[1], I. Saltirov[1], Ts. Kolev[2*]

[1]Department of Urology and Nephrology, Military Medical Academy, 3, G. Sofiiski str., 1606, Sofia, Bulgaria
Acad. Roumen Tsanev Institute of Molecular Biology, Bulgarian Academy of Sciences, Acad. G. Bonchev str., build. 21, 1113, Sofia, Bulgaria

Received October 16, 2018; Revised November 20, 2018

We performed FTIR and XRD analysis to study 78 consecutive urinary stones from 78 patients (58 men and 20 women; age range 18÷66). We have found the highest percentage of stones of calcium oxalate monohydrate - 41%. Half of the stones of calcium oxalate dihydrate are less - 19.2%, and the mixed composition of the studied stones was found in 39.7% of patients: COM + COD - 3.8%; COM + Calcium hydrogen phosphate (CHP) (apatite) - 7.7%; COD + CHP - 2.6%; COD + Uric acid (UA) - 5.1%; COM + UA - 3.8%; COM + COD + CHP - 10.3%; COM + COD + UA - 6.4%. The identification of the components of urinary stones provides useful information in order to understand the cause of their formation and to prevent their recurrence.

Keywords: FTIR, XRD, Kidney stones, Vibrational assignment

INTRODUCTION AND OBJECTIVE

Kidney stones are the products of a pathological bio mineralization process in the urinary system [1,2] and are mostly mixtures of two, three or more components. This disorder is multifactorial in origin and is influenced by the physical–chemical conditions of the urinary system [3]. Determination of the stone type (at both elemental and molecular levels) can help to identify the pathogenesis of kidney stones and to formulate future strategies for the treatment and prevention of this disease in stone-forming patients.

The wet chemical technique is one of the most widely used approaches for stone analysis. However, it can only determine the presence of individual ions and radicals and not differentiate mixtures [4].

A major part of the assessment of the risk of recurrence of urolithiasis in stone-forming patients is the analysis of each eliminated stone, the aim of which is the qualitative differentiation of all stone components and their semi-quantitative and quantitative determination. The wet chemical methods used in our country are sensitive but they can only identify the components of the kidney stone as chemical elements. As a result, the various polymorphs of calcium oxalate, apatite and uric acid salts cannot be separately distinguished. Some authors reported error rate for chemical analysis from 6.5% to 94%, which highlights the extreme inaccuracy of these methods [5].

Until now, only wet chemical methods have been used in Bulgaria for kidney stones analysis. The European Urological Association (EAU) Urolithiasis Guidelines (2017) highlight the aging of the chemical analysis and recommend the use of FT-IR and XRD for kidney stones analysis [6].

Silva *et al.* compared chemical and morphological analyses of kidney stones and reported that unlike the morphological analysis, chemical analysis can detect only Ca and oxalate separately and not differentiate crystalline types. Identifying the crystalline form is very useful for planning therapy, for example, calcium oxalate dihydrate is associated with hypercalciuria, while calcium oxalate monohydrate is more closely related to hyperoxaluria. Thus, these authors suggested using both types of routine analysis for a better understanding of the mechanisms involved in lithogenesis [7]. The use of infrared spectroscopy and / or X-ray diffraction allowed us to find out the crystalline and molecular composition of each eliminated stone, as well as to determine the semi-quantitative and quantitative content of all stone components.

The combined application of IR and Raman spectroscopy technique to the analysis of urinary calculi was reviewed by Carmona *et al.*[8].

The authors documented that some of the characteristic bands are very useful for analytical purposes, further suggesting the adaptability of spectroscopy methods to the routine analysis of renal stones. Paluszkiewicz *et al.* linked the structural composition of renal stones, as determined by FT-IR and FT-Raman spectroscopy, with the elemental composition of the stones determined using protoninduced X-ray emission

* To whom all correspondence should be sent:
E-mail: tskolev@bio21.bas.bg

and atomic emission spectroscopy [9]. Based on this study and other published studies, it can be concluded that IR and Raman spectroscopy are the best spectroscopic methods for the identification and quantitative analysis of kidney stones [10]. Both techniques are fast and simple to use, and they only require a small quantity of matter for testing. Raman spectroscopy is used alone or as complementary to IR spectroscopy to achieve the same objective. Both XRD and IR spectroscopy have also been employed as reference techniques for stone analysis, and many studies were subsequently designed to compare the quality of these methods [11,12].

It is also well documented that the analytical results obtained with both the XRD and IR spectroscopy methods are comparable and highly acceptable, consequently, these two techniques can be considered to be reference methods for the analysis of urinary calculi [13]

X-Ray powder diffraction (XRD)

X-ray powder diffraction uses monochromatic X-rays for identifying the constituents of a renal stone based on the unique diffraction pattern produced by a crystalline material. Crystal moieties of structure diffract or reflect penetrated X- rays in particular patterns [4].

Since the 1970s, thermogravimetric analysis (TG or TGA) has been extensively applied for the analysis of kidney stones [14].

This technique is based on the continuous recording of both the temperature and weight loss of the material sampled during a progressive temperature increase to 1,000 °C in an oxygen atmosphere. As each substance has its own specific transformation properties, the starting and ending temperature of the transformation, the amount of the weight change, enthalpy, the nature of the substance and the magnitude of this change indicates the proportion of the elements present [4].

There are different forms in which the same chemical component may crystallize: for example, calcium oxalate may be present in the form of calcium oxalate monohydrate (COM), calcium oxalate dihydrate (COD) or very rarely as calcium oxalate trihydrate (COT). Often, these appear with their mineralogical denominations: whewellite for calcium oxalate monohydrate (Wh); whedellite for calcium oxalate dihydrate (Wd). Uric acid is found in two types of crystallisation: anhydrate (UA) and uric acid dihydrate (UA2). Calcium phosphate is found in multiple forms. In urinary calculi phosphate has many forms: calcium phosphate, calcium hydrogen phosphate dihydrate (brushite), calcium hydrogen phosphate, apatite like carbonate apatite (CAP) and hydroxyapatite (HAP), octacalcium phosphate, a.o. From all the forms in which calcium phosphate can be found, the one which mostly occurs is carbapatite (a carbonate calcium phosphate crystallized in the hexagonal system). Different biochemical conditions can cause several crystallization forms [15]. Consequently, accurate stone analysis must determine not only the molecular species of the calculus, but also the crystalline forms of the chemical constituents.

The aim of our study was to analyze 78 urinary stones with both infrared spectroscopy and XRD and to emphasize the possibility, through these methods, to establish the crystalline and molecular composition of each eliminated stone, as well as to determine semi-quantitatively and quantitatively all stone components.

Materials and methods

We analyzed 78 consecutive urinary stones, from 78 patients (58 men and 20 women; age range 18÷66) hospitalized in the Clinic of Endourology of the Military Medical Academy in Sofia. We used IR-spectroscopy and XRD. FT-IR spectra of all urinary calculi were recorded as potassium bromide (KBr) pellets using a Tensor 37 (Bruker) spectrometer at the Institute of Mineralogy and Crystallography of the Bulgarian Academy of Sciences and the Institute of General and Inorganic Chemistry of the Bulgarian Academy of Sciences. This method requires a small sample of 1-2 mg. In the first stage, the calculi were repeatedly washed with distilled water, and then dried at room temperature for 24 h. Afterwards, a little piece of each calculus was cut with the help of a fine saw; it was examined with a magnifying glass and looked at under a microscope. When the examined section showed a nucleus or other distinctive areas, its parts were studied separately. From the homogeneous stones a piece of approximately 10-20 mg weight was broken and it was powdered in an agate mortar. From it, we weighed a sample of about 2 mg which was mixed with about 200 mg of KBr (Merck-pure for infrared spectroscopy). The mixture was powdered again to obtain practically complete homogenization. This mixture was transferred into an appropriate die and pressed at 10 t/cm^2 to form a transparent pellet, 13 mm in diameter. The pellet, assembled in a holder, was placed in the infrared (IR) beam of the spectrometer. Under this pressure, the potassium bromide mixture is practically vitrified. The spectral region investigated was from 4000 to 400 cm^{-1}; We can measure the spectrum in transmittance or absorbance. The spectrum was printed on a sheet of paper A4 and recorded as an

(ASCI) file. The spectra were measured at a resolution of 2 cm^{-1} and a standard 32 scans. In some of the more complicated cases, up to 100 scans have been used, to improve the signal-noise ratio. The number, position and intensity of absorption bands depend on the molecular composition and crystal structure of the test substance (crystal). The band intensity in the IR spectrum depends on the change in the dipole moment of the connection in the normal vibration process. As much as this change is significant, the band is more intense, if the change is zero, there is no band in the spectrum, i.e it is forbidden for symmetric reasons. In the Raman spectrum band intensity is determined by the change of polarizability over normal coordinate during the normal vibration ðα/ðQ> 0.

In a preliminary stage of our research, in order to find out the type of urolithiasis, we proceeded to the recording of standard IR spectra of the chemically pure compounds found in calculi: organic (oxalic acid and uric acid) and inorganic (phosphates: carbonate apatite, calcium hydrogen phosphate dihydrate, tricalcium phosphate, and carbonates: calcite- calcium carbonates). We used Merck (Germany) and Fluka (Switzerland) compounds. Carbonate apatite (CAP) is a calculus which was chosen out of a multitude of calculi analyzed by FT-IR, by comparing the obtained IR spectra with the one belonging to CAP registered in literature (in the IR atlases) [10,16].

Wide angle X-ray diffraction (WAXD) scans were recorded on a Bruker D8 Advance ECO diffractometer in reflection mode with Ni-filtered Cu Kα radiation over the 2θ range of 1-80 θ with a step of 0.02 θ.

RESULTS AND DISCUSSION

Analysis of the composition of stones eliminated from our patients was performed by using infrared spectroscopy. This made it possible to differentiate between all crystal components in the composition of the stones. For calcium oxalate lithiasis, it is of utmost importance to distinguish the two crystalline forms - calcium oxalate monohydrate and calcium oxalate dihydrate which cannot be achieved with the wet chemical analysis used in our country. We have found the highest percentage of stones of calcium oxalate monohydrate - 41%. Half of the stones of calcium oxalate dihydrate are less - 19.2%, and the mixed composition of the studied stones was found in 39.7% of patients: COM + COD - 3.8%; COM + Calcium hydrogen phosphate (CHP) (apatite) - 7.7%; COD + CHP - 2.6%; COD + uric acid(UA) - 5.1%; COM + UA - 3.8%; COM + COD + CHP - 10.3%; COM + COD + UA - 6.4%.

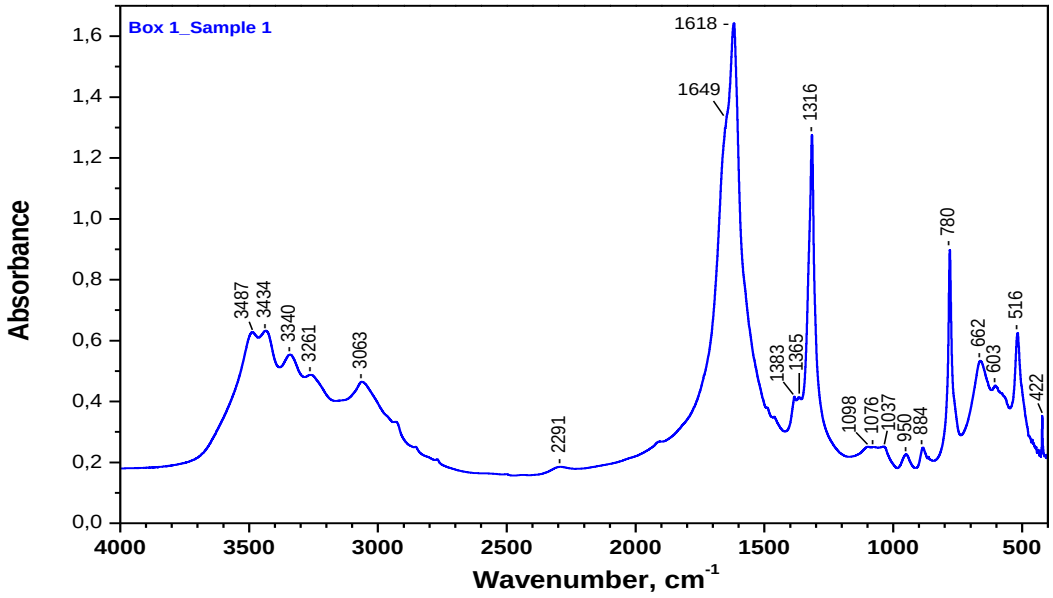

Figure 1. FTIR spectra of calcium oxalate monohydrate

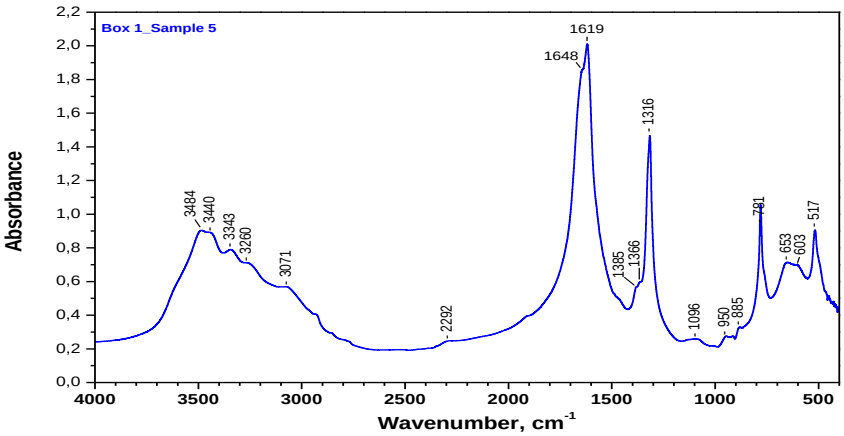

Figure 2. FTIR spectra of calcium oxalate monohydrate and dihydrate

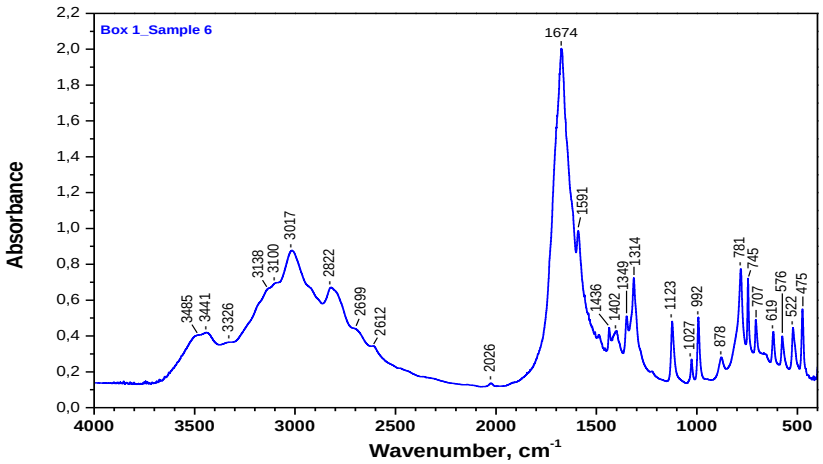

Figure 3. FTIR spectra of calcium oxalate monohydrate and uric acid

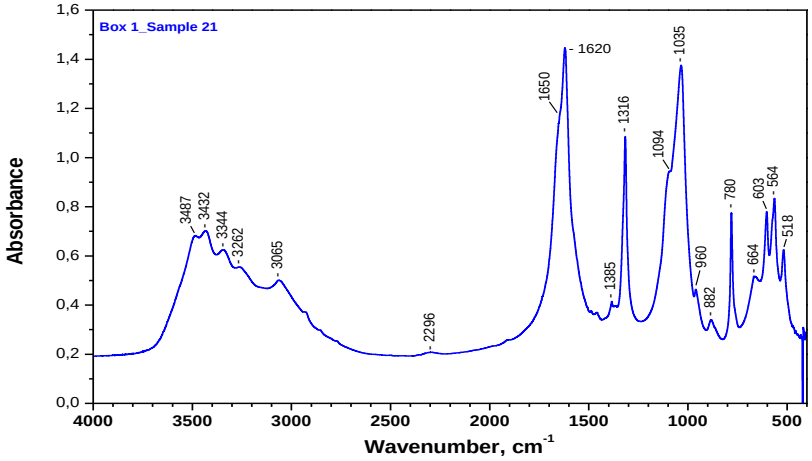

Figure 4. FTIR spectra of calcium oxalate monohydrate and $Ca_5(PO4)_3$ OH

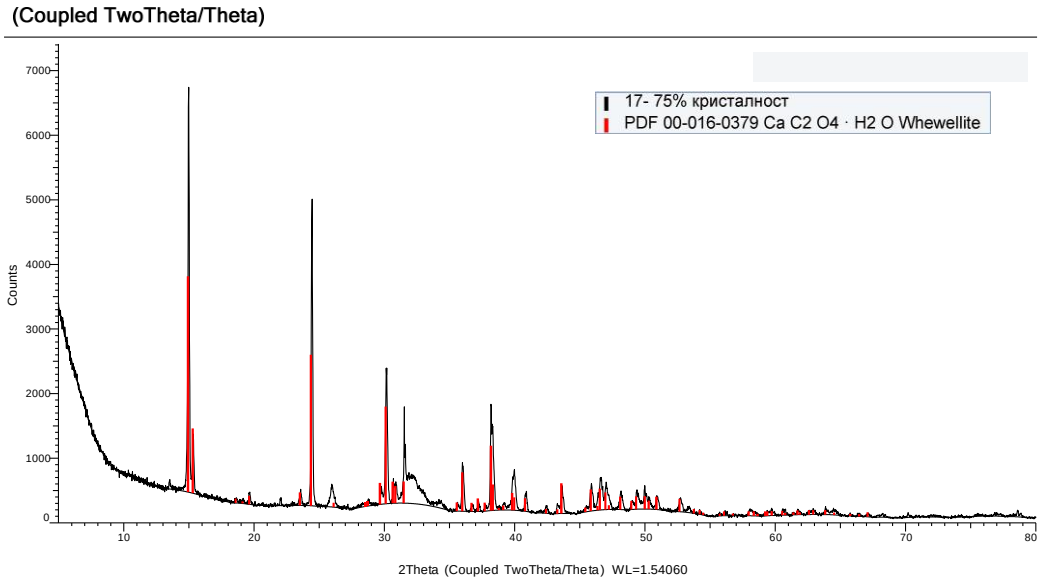

Figure 5. XRD pattern of calcium oxalate monohydrate

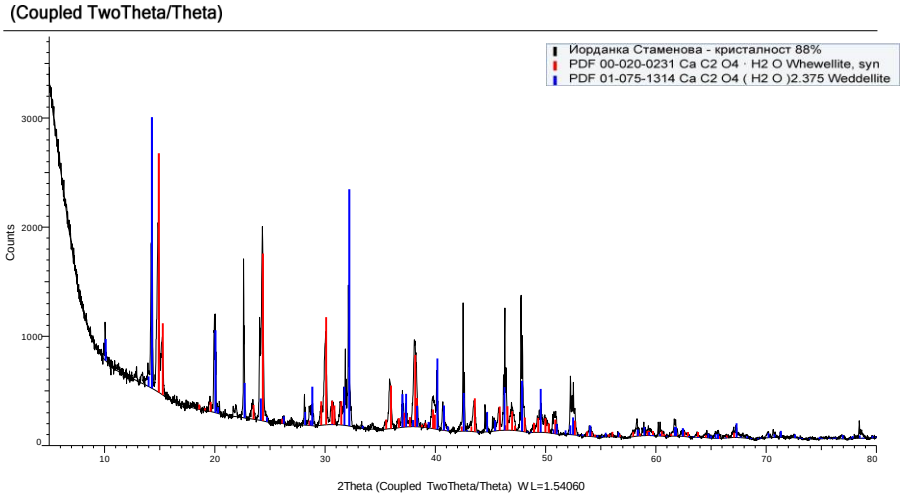

Figure 6. XRD pattern of calcium oxalate monohydrate and dihydrate

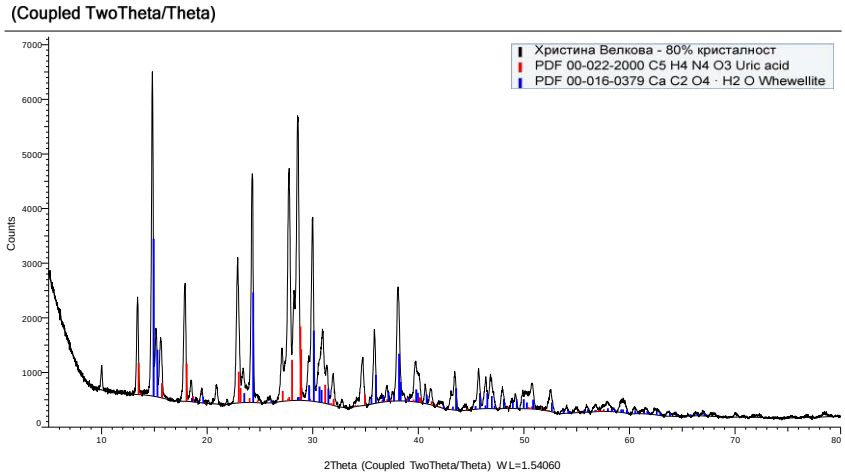

Figure 7. XRD pattern of calcium oxalate monohydrate and uric acid

The spectra of the chemically pure substances were considered as "standard" spectra. By comparing and superposing the calculi spectra with "standard" spectra, we have determined the qualitative and semi-qualitative composition of urinary stones. The intensity of IR bands displays (semi-quantitative) information regarding the degree to which a component's content is found in the calculus (if the compound concentration in the calculus is low, the result will be a specific band of low intensity). The IR absorption of the studied sample has shown the presence of oxalate, uric acid and/or hydroxyapatite groups in the urinary calculi. The reproducibility of the wavenumbers of the peaks may vary in the order of 1-3 cm^{-1}. In some cases, the $\nu^{as}C=O$) has a shoulder at about 1650 cm^{-1}, or the shoulder varies from 1645 to 1650 cm^{-1} in another case [17-19].

The IR band at 1620 cm^{-1} and that at 1316 cm^{-1} (Fig. 1), 1314 cm^{-1} (Fig. 3) of calcium oxalate monohydrate correspond to the symmetric and asymmetric C=O stretching vibrations of coordinated oxalate groups. The IR band at 1618 cm^{-1} and that at 1315 cm^{-1} (Fig. 3), monohydrate calcium oxalate correspond to the symmetric and asymmetric C=O stretchings of coordinated oxalate groups. The strong band at 1620 cm^{-1} appears in a narrow frequency range (1618-1622) cm^{-1}. So this mode is very characteristic. The band at 1316 cm^{-1} is also characteristic – it appears at 1314-1319 cm^{-1} and the band is also very characteristic. For other calculi, the stretching frequencies characteristic to the calcium oxalate were found at 1621 cm^{-1} and 1319 cm^{-1} and were assigned to $\nu^{as}C=O$) and $\nu^{s}C=O$). The degree of hydration of different substances can be given by the presence or absence of some bands from the IR spectrum; therefore, for COM (calcium oxalate monohydrate), this degree is indicated by the two peaks between 850 and 950 cm^{-1} (for COD these two peaks do not appear). In the 3500-3000 cm^{-1} region a broad spectrum appears for COD (calcium oxalate dihydrate), by contrast with the one for COM, which contains four weak but good resolved peaks (Fig. 2). The difference in ν(C=O) of oxalic acid and calcium oxalate is *ca*. 130 cm^{-1}. In literature, the question of the presence of four (O-H) bands is not discussed but only reported as a fact. We conceive that in this case there is a Fermi resonance of both ν^{as}(OH) and ν^{s}(OH) due to the crystal field. Similar phenomena of functional groups of organics, inorganic and complex compounds are described in detail by Kolev and Ivanova [20]. The presence of Fermi resonance and Davydov splitting [21,22] was established by means of polarization infrared spectroscopy in nematic liquid crystals. The band at 3062 cm^{-1} cannot be unambiguously attributed to a certain normal vibration for now. In the literature this band is not commented. For now we cannot adequately assign this band. For the mixed calculi types, these differences cannot be very clearly observed and can be mistaken because of the overlapping of the bands characteristic of different constituents, and for this reason the second derivative has been used [23]. The strong peaks around 1620 cm^{-1} and the weak band at 661 cm^{-1}

could be assigned to the bending and wagging modes of the water molecules.

The bands at 1622 for (COM)/or 1645 (for COD), 1319, 780 and 517 cm^{-1} are due to ν^{a}(C=O), ν^{s}(C=O), δ(O–C=O) and ν(Ca–O), frequencies of the oxalate part [20]. In the literature, the band at 517 cm^{-1} is referred to ν(Ca-O), but this attribution is questionable because this bond has more electro-valent than covalent character, because this is a typical coordination compound like all calcium oxalates. We consider by analyzing the crystalline structure of COM and COD that ν(Ca-O) should be searched at lower wavenumbers, i.e. < 400 cm^{-1} [20]. In previous studies of infrared spectra of carbonyl-containing compounds, the deformation vibrations of the carbonyl groups are in most cases below 400 cm^{-1}, detected with O^{18} labelled carbonyl compounds [24].

IR spectrum of the uric acid is characterized by many bands indicated by the purinic ring absorption bands at 3138, 3020 and 2836 cm^{-1}. The bands are due to N-H stretching vibrations, and also, there are additional bands at 1351, 1124, 1029 and 786 cm^{-1} wave numbers. In the case of urinary calculi, the N-H stretching vibrations appear at 3142, 3026, 2857 cm^{-1} values and there are also IR absorptions at 1353, 1126, 1031 and 788 cm^{-1}, confirming the presence of uric acid in the calculi. Deformation vibrations having frequencies of 567, 603, and 985 cm^{-1}, and stretching vibrations at 1038 cm^{-1} with a shoulder at 1105 cm^{-1} correspond to the apatite mineralogical form of the calcium phosphate. The phosphate ion from CAP/ HAP yields a strong and broad absorption between 1100 and 1000 cm^{-1}. In the best cases there are three well-separated peaks at 1150, 1100 and 1000 cm^{-1}. In some cases, the band at 1150 cm^{-1} is very weak and the only bands remaining are the two bands at 1100 and 1000 cm^{-1}. We can attribute $\nu_3(PO_4)$ and $\nu_4(PO_4)$ to the 3 major peaks of the phosphate anion at 1038, 603 and 567 cm^{-1}. In the work of Popescu *et al*. [23], the band at 567 cm^{-1} is supposedly referred to the vibration lattice mode without giving any explanation for this reference. We think that this referral is too high for lattice vibration, but this assumption has to be confirmed by isotope labelling with O^{18}. For the determination of calcium carbonate we have taken into account absorption values specific to it, at 1415 and 875 cm^{-1}. Carbonate apatite is approximately characterized by the 1422 and 1652 cm^{-1} IR bands. Also, the X-ray diffraction study confirmed the presence of HAP/CAP.

Powder X-ray diffraction, Debye-Scherrer method provides rich information on the structure of the crystallinity grade of many materials from which no suitable sizeable single cristals can be obtained for X-ray determination. The method is widely used today to characterize various materials in modern organic and inorganic material science and also organometallics. The kidney stones, which we studied, are an almost ideal subject for X-ray powder diffraction studies due to their isotropicity. This method gives us information about the formation of crystals in the process of their formation. The magnitude of the crystallites, the degree of crystallinity of the sample, can give in many cases guidance on the different phases of the stone formation process. From this analysis, direct and indirect data on stone formation can be derived. For several years, the Rietveld method has been attempted to obtain the elementary cell parameters. Rietveld refinement is a technique described by Hugo Rietveld for use in the characterisation of crystalline materials. The neutron and X-ray diffraction of powder samples results in a pattern characterised by reflections (peaks in intensity) at certain positions. The height, width and position of these reflections can be used to determine many aspects of the material's structure.

The Rietveld method uses a least squares approach to refine a theoretical line profile until it matches the measured profile. The introduction of this technique was a significant step forward in the diffraction analysis of powder samples as, unlike other techniques at that time, it was able to deal reliably with strongly overlapping reflections.

The method was first implemented in 1967 [25], and reported in 1969 [26] for the diffraction of monochromatic neutrons where the reflection position is reported in terms of the Bragg angle 2θ. In view of the above, we have decided to use the data from this method as a complement to our research. In the case of monocomponent crystals, the match between the results of the two methods is almost perfect, in the case of mixed stones the main components can be identified. If the components are more than three, their determination is of a qualitative nature.

CONCLUSION

The identification of the components of urinary stones provides useful information in order to understand the cause of their formation and to prevent their recurrence. These data are of interest for the clinical guideline in the prophylaxis, therapy and metaphylaxis of urolithiasis. FTIR is also effective in the identification of both the crystalline and amorphous nature of a stone, even when analyzing a small amount of sample. A combination of at least two complementary techniques (in our case FTIR and XRD) would be necessary to obtain enough information on the

morphology, as well as on the molecular and crystalline composition of stones. The data from the XRD method in most cases complement the FTIR spectra, and in some cases the XRD information has its own value.

REFERENCES

1. D. Bazin, M. Daudon, M. C. Combes, C. Rey, *Chem. Rev.*, **112,** 5092 (2012).
2. D. Bazin, M. Daudon, *J. Phys. D: Appl. Phys.*, **45** (2012).
3. M. Daudon, C.A. Bader, *Scan. Microsc.,* **7,** 1081 (1993).
4. G.P. Kasidas, C.T. Samuell, T.B. Weir, *Ann. Clin. Biochem.*, **41,** 91 (2004).
5. I. Singh, *International Urology and Nephrology*, **40**, 595 (2008).
6. C. Türk, EAU Guidelines, ISBN 978-94-92671-01-1.
7. S. F. R. Silva, *Acta Cir. Bras.*, **25**, 444 (2010).
8. P. Carmona, J. Bellanato, E. Escolar, A review, *Biospectroscopy*, **3,** 331 (1997).
9. C. Paluszkiewicz, M. Galka, W. Kwiatek, A. Parczewski, *Biospectroscopy*, **3,** 403 (1997).
10. D. Nguyen Quy, M. Daudon, Infrared and Raman spectra of calculi, Elsevier, Paris, 1997.
11. A. Hesse, H.J. Schneider, E. Hienzsch, *Dtsch. Med. Wochenschr.*, **97,** 1694 (1972).
12. H. J. Schneider, M. Berenyi, A. Hesse, J. Tscharnke, *Int. Urol. Nephrol.*, **5,** 9 (1973).
13. G. Rebentisch, *Scand. J. Clin. Lab. Invest. Suppl.*, **212** (1993).
14. H.P. Lee, D. Leong, C.T. Heng, *Urol. Res.*, **40,** 197 (2012).
15. J. Bellanato, J.E.A. Wickham, A. Colinbuck, Churchill Livingstone (ed.), New York, 1990, p. 45.
16. A. Hesse, G. Sanders, Atlas of infrared spectra for analysis of urinary concrements, Georg Time Verlag, Stuttgart, 1988.
17. C. Bouropoulos, N. Vagenas, P. Klepetsanis, N. Stavropoulos, N Bouropoulologes, *Cryst. Res. Technol.*, **39,** 699 (2004).
18. A.P. Bhatt, P. Paul, *J. Chem. Sci.*, **120(2),** 267 (2008).
19. K. Nakamoto, Infrared and Raman spectra of inorganic and coordination compounds, John Willey and Sons, New York, 1997.
20. B. Ivanova, T. Kolev. Linearly polarized IR spectroscopy. Theory and Aplications for Structural analysis. 2011, CRC Press, Taylor & Francis Group, Boca Raton, US, 2011.
21. A.S. Davydov, Theory of Molecular Excitons, MC-Graw Hill, New York, 1962.
22. A.S. Davydov, Theory of Molecular Excitons, Nauka, Moscow, 1968.
23. S.G. Popescu, I. Ionescu, R. Grecu, A. Preda, *Revista Română de Medicină de Laborator*, **18**, 4, (2010).
24. T. Kolev, *J. Mol. Struct*., **349**, 381 (1995).
25. A. Heat, O.F. William, E. David, L. van Eijck, *J. Appl. Cryst*., **49**, 1394 (2016).
26. H.M. Rietveld, *J. Appl. Cryst.*, **2**, 65 (1969).

Experimental study on coalbed methane (CBM) displacement by mixed carbon dioxide and nitrogen

Wenxu She[1,2,3], Junbin Chen[2], Hai Huang[2], Haoping Zhu[3], Jianyong Lei[3], Dazhong Ren[2*], Yunyun Bai[4], Fengjuan Dong[2], Fu Yang[5]

[1]*State Key Laboratory for Continental Dynamics, Department of Geology in Northwest University, Xi'an, Shannxi, China*

[2]*Engineering Research Center of Western Low & Ultra-low Permeability Oilfield Development & Management in Xi'an Shiyou University, Xi'an, Shannxi, China*

[3]*Gas Production Plant 2 of PetroChina Changqing Oilfield Company, Xi'an, Shannxi, China*

[4]*College of Chemistry and Chemical Engineering, Yulin College, Yulin, Shannxi, China*

[5]*Key Laboratory of Coal Resources Exploration and Comprehensive Utilization, Ministry of Land and Resources, Xi'an, Shannxi, China*

Received, July 30, 2018; Accepted November 11, 2018

In order to describe the displacement effect on coalbed methane (CBM) by CO_2 and N_2, the paper takes displacement and replacement efficiency as evaluation parameters. There are 5 gases being taken for indoor displacement experiment on coal samples adsorbed CH_4, i.e. CO_2, N_2 and three mixed gases with different ratio (CO_2:N_2=1:1, CO_2:N_2=1:4 and CO_2:N_2=1:9) under 1.5 MPa, 2.5 MPa, 3.5 MPa, 4.5 MPa and 5.5 Mpa controlled gas injection pressure. Following rules are obtained from the experiments: (1) In terms of displacement efficiency, as the injection pressure increases, displacement efficiency of different gases will increase first and then decrease. (2) In terms of replacement efficiency, replacement efficiency of N_2 shows slow decrease as injection pressure increases, while replacement efficiency of CO_2 shows first increase and then decrease as injection pressure increases. (3) Taking coal samples saturated with CH_4 under 2.5 MPa pressure as an example, the best displacement pressure shall be 2.5-3.5 Mpa. (4) When gas injection pressure is relatively low (lower than 2.0 MPa), the displacement and replacement efficiency of N_2 is higher than that of CO_2, however, under relatively high pressure (higher than 2.0 MPa), the displacement and replacement efficiency of N_2 is lower than that of CO_2. (5) For a mixed gas with a certain mix ratio, for example (CO_2: N_2=1:1), replacement of CO_2 and displacement of N_2 will produce synergistic effect in a certain pressure range (2.5-3.5MPa). Its average displacement efficiency is 86.14%, average replacement is 30.61%, which is higher than the average CO_2 displacement efficiency (83.06%) and average N_2 displacement efficiency (83.39%) but it is lower than the average CO_2 replacement efficiency (34.92%) and higher than the average N_2 replacement efficiency (20.78%).

Key words: Coalbed methane (CBM); Displacement experiment; Carbon dioxide; Nitrogen; Synergistic effect

INTRODUCTION

Coalbed methane (CBM) yields high-quality clean energy. At the same time, under certain conditions, it is also a potential safety hazard for coal mines. The technology of stable and increased production of coalbed methane (CBM) has always been a difficult point restricting the development of coalbed methane (CBM). With successful application of improved coalbed methane (CBM) recovery by CO_2 displacement in the United States [1], this technology has provided new ideas for CO_2 gas storage and coalbed methane (CBM) development. Many scholars have conducted extensive researches on coalbed methane (CBM) production increased technologies by CO_2 and N_2 displacement, with many successful field tests in Poland, Japan, Canada, Netherlands and China **Error! Reference source not found.**. Based on a large number of laboratory experiments and field test data, it is generally believed that the mechanism of coalbed methane (CBM) production increase by gas injection mainly includes two aspects, namely displacement and replacement. Since adsorption capacity of coal to CH_4, CO_2 and N_2 is different, and CO_2 is with the strongest adsorption ability, CH_4 could be displaced by CO_2 due to competitive adsorption effect. At the same time, gas absorption increase in coal will produce expansion effect, resulting decrease of coal permeability and affecting production of coalbed methane (CBM) [8-13]. Therefore, how injected CO_2 and N_2 mixed gas will affect the increased production of coalbed methane (CBM) has become the focus of researches. After the mixed gas is injected, the partial pressure of CH_4 is reduced and desorption begins. In order to avoid CH_4 absorbed back in coalbed after desorption, as well as coalbed permeability decrease caused by a large CO_2 injection, continuous injection of mixed gas is

* To whom all correspondence should be sent:

E-mail: petrogas999@163.com

needed to make the displacement mechanism work. In view of the above process, an indoor laboratory evaluation of the effect of coalbed methane (CBM) displacement by CO_2 and N_2 gas mixture was carried out to determine the optimal gas-displacing coalbed methane (CBM) option.

EXPERIMENTAL COAL SAMPLES, METHOD AND DEVICE

Coal samples preparation

Dafosi coalbed of Jurassic Yan'an formation in western Binxian county, Xianyang city, Shaanxi province was taken as source of experimental coalbed samples. The following are detailed data of the coal samples: average formation pressure is 2.5MPa, average formation temperature is 33°C, gas content of the sampling coalbed is relatively high, between 6.89～16.69 m^3/t, average 11.55 m^3/t. Gas composition in the coalbed is mainly CH_4, gas density is 55.31～89.8%, average 75.76%; N_2 density is 9.79～41.39%, average 22.41%; CO_2 density is 0.32～4.65%, average 1.83%.

Porosity of the coal samples measured by the vacuum pressurized saturated formation water method is generally distributed in the range of 6.05%~10.24%, average porosity is 8.18%. Permeability of the coal samples is between 0.23~0.65 mD, average permeability is 0.45 mD. Porosity and permeability of the coal is relatively low, indicating that the samples belong to compacted coal.

Pulverize the coal samples by a pulverizer, and sieve them with different meshes. Screen 10~120 mesh coal particles and mix them in a certain proportion (Table 1). Put the well-mixed samples into a sand-filling pipe of 100.0 cm length, 4.0 cm diameter, load with 30 MPa overburden pressure until the samples are compacted. Then inject low-pressure non-adsorption helium gas and test. According to the test result, permeability of the sand-filling pipe is 0.55 mD, which is close to the permeability of the original coal sample and meets the experimental requirements.

Table 1. Proportion of coal particles

Mesh	10～20	20～40	40～60	60～80	80～100	100～120	120～160
Proportion	10%	10%	25%	25%	20%	5%	5%

Scheme of experiment

Take 5 gases separately for displacement experiment on coal sample adsorbed CH_4, i.e. CO_2, N_2 and three mixed gases with different mix ratio (CO_2:N_2=1:1, CO_2:N_2=1:4 and CO_2:N_2=1:9) under 1.5 MPa, 2.5 MPa, 3.5 MPa, 4.5 MPa and 5.5 Mpa controlled gas injection pressure. Two indices - displacement efficiency and replacement efficiency - are taken as evaluation parameters. Displacement and replacement efficiency are defined as follows:

Displacement efficiency:

$$\eta = \frac{V_{out}}{V_{add}} \times 100\% \quad (1)$$

where: η: displacement efficiency; V_{add}: CH_4 volume adsorbed in coal samples, mL; V_{out}: volume of CH_4 displaced from coal samples, mL.

Replacement efficiency:

$$\theta = \frac{V_{out}}{V_{in}} \times 100\% \quad (2)$$

where: θ: replacement efficiency; V_{in}: volume of gas injected into coal samples, mL; V_{out}: volume of CH_4 displaced from coal samples, mL.

Device of experiment

Displacement experiment device consists of a gas injection system, a sand-filling pipe sample chamber system, an intermediate container gas distribution system, a vacuum pumping system, a temperature control system, a drainage gas collection system, and a gas concentration system with gas chromatography analysis.

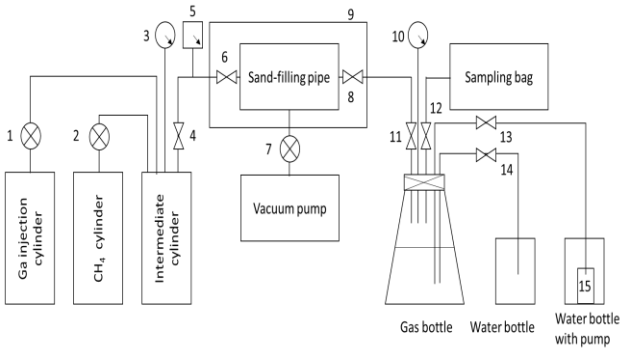

1，2，4，6，7，11，12，13，14 - Control valves；3，10 - Pressure sensors；5 - Pressure sensor and flowmeter；8 - Backpressure valve；9 - Thermostat box；15 - Submersible pump

Fig. 1. Schematic diagram of the displacement experimental device

Fig. 2. Physical map of the displacement experimental device

Procedure of experiment and calculation method

(1) Procedure of experiment

- Open the three interfaces of the sand-filling pipe, connect vacuum pump, set temperature of thermostat box to 80°C, and evacuate for 24 h;
- Switch thermostat box temperature control system off, open the thermostat box to let sand-filling tube cool off to room temperature for 3 h; Then set temperature of thermostat box to 33°C, close it and stand still at constant temperature for 2 h, turn vacuum pump off;
- Inject CH_4 into intermediate container from the CH_4 cylinder. Open the valve between intermediate container and sand-filling pipe after pressure is constant to make CH_4 enter sand-filling pipe with coal samples. Make it saturated for 12 h. During this operation, the control pressure shall be stabilized around 2.5MPa basically (which is average reservoir pressure);
- Discharge free gas in sand-filling pipe by the drainage gas recovery method. Collect gas by a bottle filled with water and measure volume of water discharged;
- Displace CH_4 gas in coal samples by gas in the gas injection cylinder. Check flow meter No. 5 for volume of injected gas. Collect gas by drainage gas recovery method. Press gas into gas sampling bag by submersible pump and fill water into the gas bottle.
- Measure volumetric concentration of CH_4 gas in sampling bag by a portable gas chromatograph. When displacement starts, measure every 10 min. When concentration of CH_4 is found below 100%, measure every 1 min. In case that three successive numerical changes show less than 5%, it is known that equilibrium state is reached, and the displacement of CH_4 volume could be calculated.
- Change type of gas and way of displacement, repeat the experiment.

(2) Calculation method

According to experimental data, displacement and replacement efficiency could be calculated as follows:

- Intermediate container CH_4 gas balance formula:

$$P_1V_1 = z_1nRT \tag{3}$$

Intermediate container gas balance formula after coal samples in sand-filling pipe are saturated with CH_4:

$$P_2(V_1+V_2) = z_2nRT \tag{4}$$

The following equation can be obtained from formula 3 and formula 4:

$$V_2 = \frac{(z_2P_1 - z_1P_2)V_1}{z_1P_2} \tag{5}$$

where: P_1: initial CH_4 pressure in the intermediate container, MPa; V_1: volume of intermediate container; z_1: initial CH_4 compression factor in the intermediate container; n: amount of CH_4 in the initial intermediate container, mol; R: thermodynamic parameter, 8.31441J/(mol·K); T: absolute temperature, K; P_2: pressure in intermediate container and sand-filling pipe when coal samples are saturated with CH_4, MPa; V_2: pore volume in sand-filling pipe, mL; z_2: CH_4 compression factor when coal samples are saturated with CH_4 in the intermediate container and sand-filling pipe.

- Convert volume of CH_4 in the sand-filling pipe into volume under standard conditions:

$$P_2V_2 = z_2n_1RT \tag{6}$$

$$P_3V_3 = z_3n_1RT \tag{7}$$

$$V_3 = \frac{z_3P_2V_2}{z_2P_3} \tag{8}$$

where: n_1: amount of CH_4 in sand-filling pipe, mol; P_3: gas pressure under standard conditions, 0.1 MPa; V_3: CH_4 gas volume under standard conditions, mL; z_3: CH_4 gas compression factor under standard conditions, 1.

- Residual CH_4 volume in sand-filling pipe after free gas is discharged:

$$V_4 = V_3 - V_5 = V_3 - \frac{m_1}{\rho_1} \tag{9}$$

where: V_4: residual CH_4 volume in sand-filling pipe after free gas is discharged , mL; V_5: volume of free CH_4 gas, mL; m_1: weight of water discharged by free CH_4 gas, g; ρ_1: density of water, g/cm^3.

- Volume of displaced CH_4:

$$V_6 = V_7 \cdot \alpha \tag{10}$$

where: V_6: volume of displaced CH_4, mL; V_7: total gas volume in gas sampling bag, mL; α: volume concentration of CH_4 in the gas sampling bag, %.

- Calculation of displacement efficiency η:

$$\eta = \frac{V_6}{V_4} \times 100\% \quad (11)$$

- Calculation of replacement efficiency θ:

$$\theta = \frac{V_4}{V_8} \times 100\% \quad (12)$$

where: V_8: volume of injected gas under standard conditions, mL.

EXPERIMENTAL RESULTS AND ANALYSIS

Carry out displacement experiments on 5 coal samples saturated with CH_4, by 5 different gases. Set a different injection pressure during the experiments, i.e. 1.5 MPa, 2.5 MPa, 3.5 MPa, 4.5 MPa and 5.5 MPa. Experimental parameters are shown in Table 2 and experimental results are shown in Figure 3.

It can be seen from Figure 3(a) that:

(1) Changing trend of displacement efficiency on CH_4 adsorbed in coal samples by different gases is the same, i.e. displacement efficiency will increase and then decrease along with increasing displacement pressure. The highest displacement efficiency appears when displacement pressure is in the range of 2.5-3.5 MPa.

When displacement pressure increases, it will improve the flow of displacement gas, resulting in an increase of displacement efficiency at the beginning. However, the continuous increase of pressure also makes CH_4 desorption more difficult from the pores of coal samples. The higher the pressure, the less desorption of CH_4 will be, so the displacement efficiency gradually decreases with increasing pressure.

(2) When pressure is relatively low (lower than 2.0 MPa), N_2 has the highest displacement efficiency and CO_2 - the lowest displacement efficiency under the same pressure. When displacement pressure is 1.5 MPa, displacement efficiency of N_2 is 76.01%, and displacement efficiency of CO_2 is only 68.19%. When pressure is gradually increased, displacement efficiency of CO_2 is with the fastest growth, reaching a peak of 83.96% at 2.5 Mpa, while displacement efficiency of N_2 is relatively slow, reaching a peak of 85.03% at 3.5 Mpa.

Table 2. Experimental parameters of gas injection

Gas number	G1 CO_2	G2 N_2	G3 (CO_2：N_2=1：1)	G4 (CO_2：N_2=1：4)	G5 (CO_2：N_2=1：9)
Injection pressure 1.5MPa					
Coal sample number	M1-1.5	M2-1.5	M3-1.5	M4-1.5	M5-1.5
Injection pressure 2.5MPa					
Coal sample number	M1-2.5	M2-2.5	M3-2.5	M4-2.5	M5-2.5
Injection pressure 3.5 MPa					
Coal sample number	M1-3.5	M2-3.5	M3-3.5	M4-3.5	M5-3.5
Injection pressure 4.5MPa					
Coal sample number	M1-4.5	M2-4.5	M3-4.5	M4-4.5	M5-4.5
Injection pressure 5.5MPa					
Coal sample number	M1-5.5	M2-5.5	M3-5.5	M4-5.5	M5-5.5

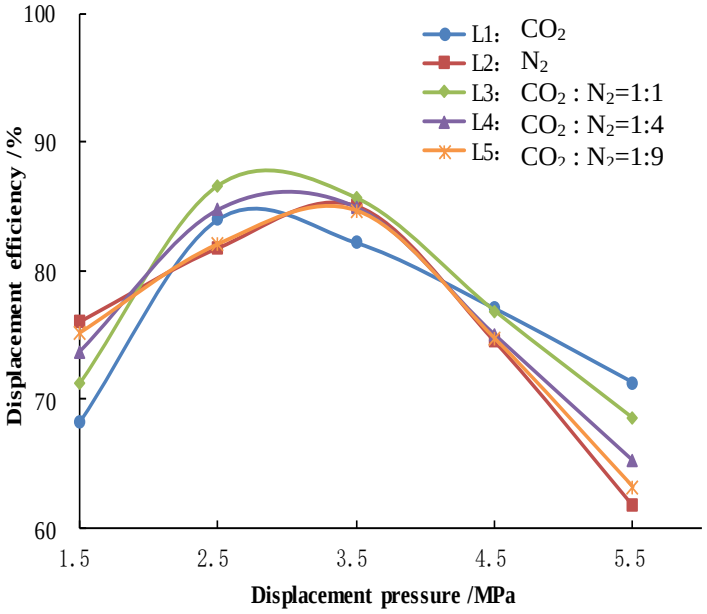

(a) Curve of displacement efficiency

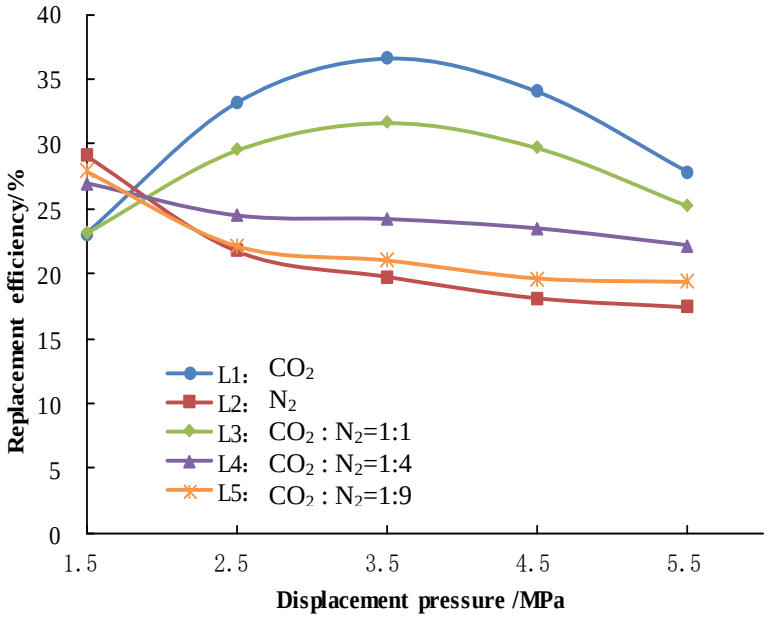

(b) Curve of replacement efficiency

Fig. 3. Parameter curves of gas injection displacement experiment

As the pressure further increases, displacement efficiency of N_2 rapidly decreases, but the decrease rate of CO_2 displacement efficiency is relatively slow. At 5.5 MPa, the displacement efficiency of CO_2 is reduced to 71.31%, while displacement efficiency of N_2 is only 61.71%.

When pressure is relatively low, CH_4 desorption is mainly controlled by pressure, and competitive adsorption of CO_2 to CH_4 does not affect displacement much. Since displacement pressure is not sufficient to allow gas entering smaller pores, the strong adsorption capacity of CO_2 makes pores in the matrix of coal samples plugged and permeability decreases, the resulting displacement efficiency being smaller than that of N_2. As pressure increases, desorption of CH_4 is suppressed to a certain extent, and the displacement effect caused by competitive adsorption of CO_2 is gradually seen. The higher the CO_2 content, the more obvious the displacement efficiency is driven by replacement effect. Therefore, as pressure increases, CO_2 displacement efficiency is with fastest growth. Under higher pressure, CO_2 displacement efficiency is higher than that of N_2.

(3) In the range from 2.0 to 4.5 MPa, the mixed gas displacement efficiency curve is higher than those of single CO_2 or N_2 indicating that displacement efficiency of the mixed gas is higher than that of single gases in the same pressure range. Among all curves, the curve of L3 and L4 with CO_2: N_2 mixing ratio of 1:1 and 1:4 are the most obvious. Displacement efficiency of L3 reaches 86.61% at 2.5 MPa, which obviously exceeds the displacement efficiency of single CO_2 or N_2 under the same conditions.

Gas injected into the coal sample displaced and replaced CH_4 adsorbed on the pore walls of the coal sample, which is the main mechanism of increasing coalbed methane (CBM) production by gas injection. As the adsorption capacity of CO_2, CH_4 and N_2 gradually decreased in coal samples, replacement of CO_2 is more obvious under the same pressure and temperature, while displacement is the main effect of N_2. Under medium pressure conditions (2.0-4.5 MPa), on the one hand, comparing to the amount of free CH_4 desorption under low-pressure conditions, the amount of free CH_4 desorption is suppressed to a certain extent. In order to displace CH_4, competitive adsorption of CO_2 is required. The higher the CO_2 content, the greater the contribution of displacement will be. On the other hand, in order to avoid desorbed CH_4 absorbed back to coal samples, it is necessary to displace CH_4 by N_2 since N_2 has weaker adsorption capacity than CH_4. The higher the N_2 content, the more contribution of displacement will be. Mixed gas displacement efficiency by synergistic effect from displacement and replacement is better than displacement effect of single gas.

It can be seen from Figure 3(b) that:

(1) There are different characteristics of CH_4 replacement efficiency changing trends in coal samples according to different gases. As pressure increases, CO_2 replacement efficiency increases at first and then decreases. Curve L3 with higher CO_2 content also shows the same trend. Replacement efficiency of N_2 continually decreases as the pressure increases and gradually its trend becomes slow. Replacement efficiency curves L4 and L5 with higher N_2 content also show the same changing trend. Replacement efficiency of mixed gases is generally between displacement efficiency of CO_2 and N_2. According to different proportions of CO_2 and N_2 content, replacement gas efficiency curve of mixed gases is quite different with CO_2 or N_2 displacement efficiency curves.

(2) When pressure is relatively low (lower than 2.0 MPa), replacement efficiency of N_2 is significantly higher than that of CO_2. When displacement pressure is 1.5 MPa, replacement efficiency of N_2 is 29.17% while replacement efficiency of CO_2 is only 23.04%. As pressure increases, replacement efficiency of N_2 smoothly decreases, and replacement efficiency of CO_2 rapidly increases. Replacement efficiency of CO_2 reaches a peak of 36.64% when displacement pressure increased to 3.5 MPa. When displacement pressure reaches 5.5 MPa, displacement efficiency of CO_2 decreases to 27.82% while replacement efficiency of N_2 is 17.43%.

Analysis of curves in Figure 3(b): Mechanism of CO_2 and N_2 injection in coal samples on CH_4 production is different. Under low-pressure conditions, a large number of CH_4 gas molecules start desorption, displacement effect of N_2 plays an important role on coalbed methane (CBM) production, but contribution of CO_2 replacement is not obvious. What's more, due to strong adsorption capacity, matrix micropores plugging of coal samples were decreased, which made CO_2 replacement efficiency less than that of N_2. Although displacement pressure increase could help injecting gas into smaller pores, in order to increase the displacement pressure, it will inevitably increase injection volume. High pressure will also make the CH_4 molecule not easily desorbed; hence replacement efficiency of N_2 will gradually decrease as displacement pressure increases. However, as pressure increases, CO_2 molecules could enter more pores and spread wider. Although pressure increase could cause a decrease of the amount of free CH_4 desorption to some extent, the competitive adsorption of CO_2 could help to displace more CH_4. Thus, CO_2 displacement efficiency gradually increases at the beginning of displacement pressure increase. As pressure further rises, the increase rate of gas injection is greater than the increase rate of CH_4 produced by replacement. Therefore, CO_2 replacement efficiency gradually decreases as the pressure increases.

CONCLUSIONS

Five gases were taken separately for displacement experiment on coal samples with adsorbed CH_4, i.e. CO_2, N_2 and three mixed gases with different mix ratio (CO_2:N_2=1:1, CO_2:N_2=1:4 and CO_2:N_2=1:9) under 1.5 MPa, 2.5 MPa, 3.5 MPa, 4.5 MPa and 5.5 Mpa controlled gas injection pressure. Displacement and replacement efficiency are the key parameters for evaluating the experiment results. The following rules are obtained by comparing the change of displacement and replacement efficiency in each experiment:

(1) Injection pressure of the various gases has different effects on displacement and replacement

efficiency. In terms of displacement efficiency, as the injection pressure increases, displacement efficiency of different gases will first increase and then decrease. In terms of replacement efficiency, replacement efficiency of N_2 shows a slow decrease as injection pressure increases, while replacement efficiency of CO_2 shows first an increase and then decrease as injection pressure increase. Therefore, it is not true that the higher the displacement pressure, the more coalbed methane (CBM) will be developed. Although pressure increase will help gases spread wider to some extent, it also suppresses desorption of CH_4. Taking coal samples saturated with CH_4 under 2.5 MPa pressure as an example, considering the influence of pressure on displacement and replacement efficiency, the best displacement pressure shall be 2.5-3.5 Mpa. In this pressure range, the average displacement efficiency of the 5 injected gases is 84.16%, and the average replacement efficiency is 26.44%.

(2) Under the same injection pressure conditions, different injection gases show different displacement and replacement efficiency. When gas injection pressure is relatively low (lower than 2.0 MPa), replacement of CO_2 is not obvious, displacement and replacement efficiency of N_2 are higher than those of CO_2. As pressure of gas injection increases, the amount of free desorbed CH_4 gradually decreases, and contribution of CO_2 replacement effect to CH_4 development is showing out gradually. Under relatively high pressure (higher than 2.0 MPa), displacement and replacement efficiency of CO_2 is higher than that of N_2. In a certain pressure range (2.5-3.5 MPa), replacement effect of CO_2 and displacement effect of N_2 will generate synergistic effect with a certain proportion of mixed gas (volume ratio of CO_2 and N_2 is 1:1 or 1:4 respectively). Taking mixed gas (CO_2:N_2=1:1) as an example, the average displacement efficiency is 86.14%, average replacement efficiency is 30.61%, which is higher than the average CO_2 displacement efficiency of 83.06% and the average N_2 displacement efficiency of 83.39%. It is lower than the average CO_2 replacement efficiency of 34.92%, but higher than the average N_2 replacement efficiency of 20.78%.

Acknowledgement: *This work was financially supported by the National Natural Science Foundation of China (Grant No.5167040392, 41702146,51874242), China Postdoctoral Science Foundation (2018M643554), Open Fund of State Key Laboratory of Oil and Gas Reservoir Geology and Exploitation (Chengdu University of Technology) (PLC20190502) and Project supported by the National Science and Technology Major Project of China: Key Technology of the Tight Gas Enrichment Law and the Exploration and Development(2016ZX05047).*

REFERENCES

1. F. V. Bergen, T. Tambach, H. Pagnier, *Energy Procedia*, **4**, 3112 (2011).
2. F. van Bergen, P. Krzystolik, N. Wageningen, H. Pagnier, B. Jura, J. Skiba, P. Winthaegen, Z. Kobiela, *Int. J. Coal Geol.*, **77**, 175 (2009).
3. M. Fujioka, S. Yamaguchi, M. Nako, *Int. J. Coal Geol.*, **82**, 287 (2010).
4. T. Gentzis, *Int. J. Coal Geol.*, **43**, 287 (2000).
5. C. N. Hamelinck, A. P. C. Faaij, W. C. Turkenburg, F. Bergen, H.J.M Pagnie, O.H.M. Barzandji, K.-H.A.A. Wolf, G..J. Ruijg, *Energy*, **27**, 647 (2002).
6. S. Wong, D. Law, X. Deng, J. Robinson, B. Kadatz, W. D. Gunter, Y. Jianping, F. Sanli, F. Zhiqiang, *Int. J. Greenhouse Gas Control*, **1**, 215 (2007).
7. H. Yu, G. Zhou, W. Fan, J. Ye, *Int. J. Coal Geol*, **71**, 345 (2007).
8. X. Cui, R. M. Bustin, G. Dipple, *Fuel,* **83**, 293 (2004).
9. J. E. Fitzgerald, Z. Pan, M. Sudibandriyo, R.L. Robinson. Jr., K.A.M. Gasem, S. Reeves, *Fuel*, **84**, 2351 (2005).
10. K. Jessen, G. Q. Tang, A. R. Kovscek, *Transport in Porous Media*, **73**, 141 (2008).
11. S. Mazumder, K. Wolf, P. van Hemert, A. Busch, *Transport Porous Media*, **75**, 63 (2008).
12. Y. Tu, C. L. Xie, R. M. Li, S. X. Xie, *Adv. Materials Res.*, **616-618**, 778 (2012).
13. H. Kumar, D. Elsworth, J. Liu, D. Pone, J. P. Mathews, *J. Greenhouse Gas Control*,, **11**, 86 (2012).

Bulgarian Chemical Communications, Volume 51, Issue 1 (pp. 103 – 112) 2019

Characterization of extracts from red hot pepper (*Capsicum annuum L.*)

J. M. Simonovska[1], D. Y. Yancheva[2*], B. P. Mikhova[2], S. M. Momchilova[2], Ž. F. Knez[3], M. J. Primožić[3], Z. S. Kavrakovski[4], V. G. Rafajlovska[1]

[1] *Institute of Organic Technology, Faculty of Technology and Metallurgy, Ss. Cyril and Methodius University in Skopje, 16 Rudjer Boskovic Str., 1000 Skopje, Republic of Macedonia*

[2] *Institute of Organic Chemistry with Centre of Phytochemistry, Bulgarian Academy of Sciences, Acad. G. Bonchev Str., Bl. 9, 1113 Sofia, Bulgaria*

[3] *Laboratory of Separation Processes and Product Design, Faculty of Chemistry and Chemical Engineering, University in Maribor, 17 Smetanova Str., 2000 Maribor, Slovenia*

[4] *Institute of Applied Chemistry and Pharmaceutical Analyses, Faculty of Pharmacy, Ss. Cyril and Methodius University in Skopje, 47 Mother Theresa Str., 1000 Skopje, Republic of Macedonia*

Received November 11, 2017; Revised November 30, 2018

Samples from pericarp, placenta, seeds, and stalk of red hot pepper (*Capsicum annuum L.*), obtained by extraction with *n*-hexane and supercritical carbon dioxide were characterized using ATR-IR and NMR spectroscopy. It was shown that both NMR and IR spectroscopy provide useful information on the triacylglycerols composition, degree of unsaturation and capsaicin content of hot red pepper extracts as IR spectroscopy could serve as a fast tool for identification of capsaicinoids in the extracts, whereas NMR analysis could be successfully applied for determination of the proportion triacylglycerols : capsaicinoids.

Keywords: *Capsicum annuum L.*, red hot pepper, IR, NMR, triacylglycerols, capsaicinoids.

INTRODUCTION

Pepper is an excellent source of fibres, vitamins, minerals, proteins, lipids, phenolic compounds, aromatic substances and other biologically active compounds [1]. The importance of red hot pepper varieties and their oleoresin extracts in the food and pharmaceutical industries is due to the characteristic compounds, capsaicinoids and carotenoids [2]. Mainly, for determination of the compounds in the sweet or hot pepper varieties, chromatographic (TLC, HPLC and GC) and UV-VIS spectrometric methods were used [3, 4]. On the other hand, ^{1}H NMR spectroscopy has been extensively employed to provide information about the composition and relative content of fatty acid residues in triacylglycerols [5-7]. Moreover, NMR spectroscopy is one of the most informative methods applied for analysis of the capsaicinoids and carotenoids [8]. The degree of unsaturation of vegetable oils can be effectively studied also by IR spectroscopy based on the changes observed in the frequency data of some bands and in the ratios of absorbances of the IR spectra [9, 10]. Thus, ^{1}H NMR and ATR-IR can be used as simpler, more rapid and less expensive methods requiring no sample pretreatment compared to the chromatographic methods. In continuation of our studies on the composition of red hot pepper (*Capsicum annuum L.*) [11, 12], the aim of this study was to evaluate the possibility of applying spectroscopic techniques (NMR and IR) in the characterization of extracts obtained from red hot pepper.

MATERIALS AND METHODS

Plant material and oils

Pericarp, placenta, seed, and stalk separated were obtained from red hot pepper (*Capsicum annuum* L. ssp. *microcarpum longum conoides* convar. Horgoshka), grown in the area of Markova Česma (geographical location: +41°21'36" N latitude, +21°33'36" E longitude and 640 m altitude), Prilep, Republic of Macedonia, in the year 2015. The dried samples with 12% moisture content determined using AOAC method no. 925.10 [13] were grounded using Retsch ZM1 mill (Haan, Germany) with sieve diameter of 0.25, 0.5 mm and 1.0 mm. Rose hip oil used as a reference was bought in a drugstore in Sofia (Bulgaria). Olive, soybean, sunflower, corn, walnut and linseed oils were from the local market.

Chemicals

Analytical grade solvents: acetone, ethanol, and *n*-hexane, as well as, phosphomolybdic acid, boron trichloride (BCl_3), 2,2-dimethoxypropane (DTP), and anhydrous sodium sulfate (Na_2SO_4) were supplied from Merck (Darmstadt, Germany).

* To whom all correspondence should be sent:
E-mail: deni@orgchm.bas.bg

Carbon dioxide (CO_2, > 99.5% purity) and helium (He, > 99.9% purity) were purchased from Messer (Ruše, Slovenia). The standards of *β*-sitosterol, oleic acid, 1,3-diolein, 1-monoolein-rac-glycerol and reference standard mixture of fatty acids methyl esters (FAME Mix RM-6) were obtained from Sigma Chemicals Co. (St. Louis, MO, USA). Deuterated chloroform ($CDCl_3$, 99.8% D) with tetramethylsilane (TMS) were purchased from Deutero GmbH (Kastellaun, Germany).

Extraction of plant material

The samples of pericarp, placenta, seed and stalk from red hot pepper were extracted with *n*-hexane and supercritical CO_2 (Table 1). Soxhlet procedure no. 920.85 [13] was used for the extraction of samples of red hot pepper with *n*-hexane. Five grams of sample (0.0001 g accurately weighted) were extracted in the presence of 10 boiling glass regulators with 200 mL *n*-hexane for 5 h. The solvent was removed from the extract by using rotary vacuum evaporator type Devarot (Ljubljana, Slovenia) at 40 °C and 200 mPa, and vacuum dried in a Heraeus Vacutherm VT 6025 (Langenselbold, Germany) at 40 °C and 105 mPa, followed by cooling in a desiccator and weighing. The steps of drying, cooling and weighing were repeated until the difference between two consecutive weights was smaller than 2 mg. The extraction of plant samples with supercritical CO_2 at 40°C and 400 bar was performed on an apparatus manufactured by the company UHDE-GmbH-Hagen from Hagen (Germany), according the procedure reported by Škerget and Knez [14]. The obtained extracts were evaporated to dryness under a steam of nitrogen. The extract samples accurately weighed (± 0.0001 g) were dissolved in *n*-hexane to 20 mg/mL stock solution concentration, prior to analysis.

Table 1. Extracts of red hot pepper (*Capsicum annuum* L.) obtained with *n*-hexane (A) and supercritical carbon dioxide (B).

Sample code	Plant material		Extraction method	Yield of extract (g/100 g DM*)
	Type	Particle size (mm)		
N1	seed	0.5	A	24.37
N2	seed	0.5	B	37.43
N3	seed	1	A	19.38
N4	seed	1	B	34.91
N5	pericarp	0.5	A	7.05
N6	pericarp	0.5	B	3.05
N7	pericarp	1	B	2.06
N8	placenta	0.25	A	8.87
N9	placenta	0.25	B	6.23
N10	placenta	0.5	A	7.05
N11	stalk	1	A	3.97
N12	stalk	0.25	B	9.95

*Calculated according to the corresponding dry matter (DM).

Table 2. Degree of unsaturation (A_1 / A_2 and A_1 / A_3) of the studied *Capsicum annuum* extracts and various edible oils calculated based on the peak heights for C-H stretching of the *cis*-double bonds (A_1), asymmetric (A_2) and symmetric (A_3) C-H stretching the methylene bonds.

Sample	Peak position for ν(=C-H) (cm^{-1})	Peak height for ν(=C-H) (A_1)	Peak height for $\nu^{as}(CH_2)$ (A_2)	Peak height for $\nu^{s}(CH_2)$ (A_3)	Degree of unsaturation	
					(A_1 / A_2)	(A_1 / A_3)
Capsicum annuum seed extract						
N1	3009.2	0.022	0.130	0.089	0.169	0.247
N2	3009.5	0.012	0.066	0.046	0.182	0.261
N3	3009.1	0.027	0.159	0.108	0.170	0.250
N4	3009.3	0.027	0.159	0.108	0.170	0.250
Olive oil	3005.0	0.016	0.177	0.119	0.090	0.134
Soybean oil	3008.9	0.022	0.155	0.103	0.142	0.214
Sunflower oil	3008.3	0.023	0.157	0.104	0.146	0.221
Corn oil	3008.7	0.024	0.162	0.109	0.148	0.220
Walnut oil	3009.2	0.027	0.138	0.093	0.196	0.290
Linseed oil	3010.4	0.035	0.133	0.090	0.263	0.389

Attenuated total reflectance infrared spectroscopy

Attenuated total reflectance infrared (ATR-IR) spectroscopy was performed on a Bruker Tensor 27 FT spectrometer. The spectra were acquired in the range of 4000–600 cm^{-1} at a resolution of 2 cm^{-1} by accumulation of 64 scans. The samples were

directly deposited on diamond crystal ATR accessory.

Nuclear Magnetic Resonance

Nuclear magnetic resonance (NMR) spectra were recorded on a Bruker AVANCE II+ 600 spectrometer at ambient temperature. About 15 mg of each sample were dissolved in 0.6 mL $CDCl_3$. TMS was used as an internal standard. The spectral data were reported in ppm. A 30 degree pulse of 3.6 μs and a relaxation delay of 5 s were used in quantitative analysis. Window functions Exponential Multiplication (LB = 0.2) and manual Base Line Correction were applied in the spectra processing.

Thin layer chromatography

Thin layer chromatography (TLC) for qualitative characterization of the main neutral lipid classes in the extracts was performed on aluminum sheets with 0.25 mm thick layer of silica gel 60 (Merck, Darmstadt, Germany). Samples were applied as spots (5 μL of each stock solution) with references applied nearby. After development with *n*-hexane:acetone (100:7, v/v) mixture as a mobile phase, the plates were air dried, sprayed with 10% ethanolic phosphomolybdic acid and heated at 120°C to visualize the separated components.

Gas chromatography

Fatty acid composition of the extracts was determined by gas chromatography (GC) of methyl esters (FAME) in accordance with the AOCS Official Method Ce 1–62 [15] using a Shimadzu GC 2010-Plus (Tokyo, Japan) gas chromatograph equipped with a flame ionization detector and a ZB-FFAP column (30 m × 0.25 mm × 0.25 μm, Phenomenex, USA). Methyl esters were prepared by derivatization of 0.1 g extract in 1 mL *n*-hexane with 2 mL 12% methanolic BCl_3 and 0.5 mL DTP. After heating at 60°C for 10 min the mixture was cooled and 1 mL Milli-Q water (PURELAB classic system, 18.2 MΩ-cm, ELGA, USA) and 1 mL *n*-hexane were added. The organic layer was dried by anhydrous Na_2SO_4 and then diluted to 10 mL with *n*-hexane. Aliquots of 1.0 μL were injected into the column. The carrier gas was He at 3.0 mL min^{-1}, split ratio 1:50. The oven temperature was set at 180°C (3 min) and increased by 2°C min^{-1} to 240°C (25 min). The injector and detector temperatures were 250°C and 260°C, respectively. Identification was according to the retention times of reference FAME standards.

RESULTS AND DISCUSSION

Thin layer chromatography

Samples were subjected to qualitative thin layer chromatography for characterization of their main components (Fig. 1). The results revealed that all extracts contained triacylglycerols (R_f about 0.7) as main component and small amounts of sterols, partial acylglycerols and other concomitants as minor components. The extracts from seeds (samples **N1 – N4**, Table 1) had the profile typical for plant seed oils (rose hip oil as a reference) and contained significantly lower quantities of polar compounds than the extracts from pericarp, placenta and stalk.

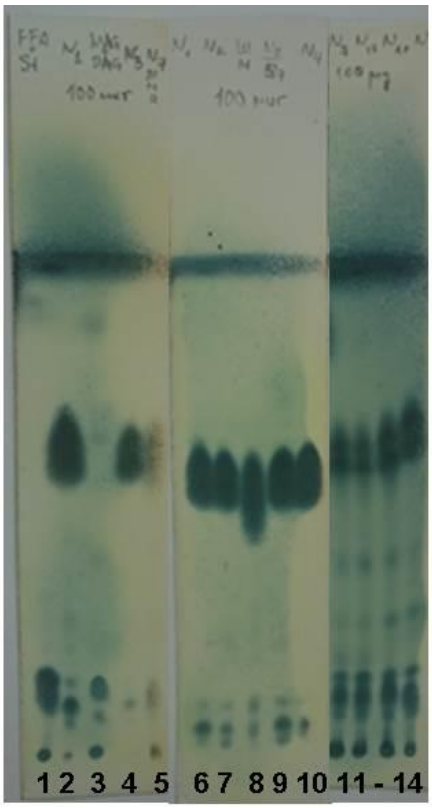

Fig. 1. TLC plates for qualitative characterization of extracts. Tracks: 1 – reference free fatty acids and sterols; 2 – sample **N1**; 3 – reference mono- and diacylglycerols; 4 - sample **N3**; 5 - sample **N7**; 6 - sample **N1**; 7 - sample **N2**; 8 – reference rose hip oil; 9 - sample **N3**; 10 - sample **N4**; 11 - sample **N9**; 12 - sample **N10**; 13 - sample **N11**; 14 - sample **N12**.

The official method for determination of the fatty acid composition of oils is by gas chromatography (GC) [15]. Predominant acyl residues in the triacylglycerols (TAG) of red hot pepper are those from saturated, oleic, linoleic and linolenic acids (Scheme 1).

IR spectroscopy

The IR spectra of the extracts obtained from seed, pericarp, placenta, and stalk, of hot fruits of *Capsicum annuum* are presented in Fig. 2. However, the differences in the extract composition resulted in variations of the positions and intensities of the main IR bands as well as in the presence of additional bands in some of the cases.

The ATR-IR spectra of the seed extracts **N1 – N4** are very similar to each other. As illustrated in Fig. 2, the most characteristic bands appeared at the following positions: 3009 ν(=C-H), 2923 $\nu^{as}(CH_2)$, 2853 $\nu^{s}(CH_2)$, 1743 ν(C=O), 1464 $\delta(CH_2)$, 1377 $\delta^{s}(CH_3)$, 1237 ν(C-O), 1160 ν(C-O), and 722 cm^{-1} $\rho(CH_2)$. All of them originate from the molecular vibrations of triacylglycerols [10, 16]. It is known that the exact position of the band for the C-H stretching of the *cis*-double bond is sensitive to the oil composition, and it is shifted to higher frequency when the oil has higher content of polyunsaturated acyl groups [9, 10]. In the ATR-IR spectra of the seed extracts **N1 – N4** the band for ν(=C-H) was found at ca 3009 cm^{-1} (Table 2). This is near to the value measured in our laboratory using the same ATR technique for walnut oil which is rich in polyunsaturated acyl groups. In the ATR-IR spectrum of linseed oil the band is shifted to 3010 cm^{-1}. Likewise, for olive oil, which contains predominantly monounsaturated acyl residues, the band was found at 3005 cm^{-1}.

Furthermore, the ratio of the absorbance of the bands responsible for *cis*-double bond and methylene groups could be used for quantitative estimation of the degree of unsaturation of the oil [9, 10]. For this purpose, either the ratio of the peak heights A_1 and A_2 [10] or the peak heights A_1 and A_3 [9] can be used as a measure. The respective bands are denoted in Fig. 2. The ratios A_1 / A_2 and A_1 / A_3 calculated for extracts **N1 – N4** are compared with the ratios obtained under the same conditions for olive, soybean, corn, walnut and linseed oils (Table 2) which degree of unsaturation has been confirmed by their fatty acid composition [17]. Both ratios represent a uniform trend – the extracts from *Capsicum annuum L.* seeds show a degree of unsaturation much higher than the olive oil. The degree of unsaturation of extracts **N1 – N4** falls in between the values obtained for soybean, sunflower and corn oil on the one hand and walnut and linseed oil on the other hand.

The IR spectra of the pericarp extracts **N5** and N6 resemble very much that of the seed extracts. They show all characteristic bands for triacylglycerols content and the respective band positions are very similar to the above-mentioned ones. The presence of a small amount of capsaicin in extract **N7** was identified by the appearance of two weak bands at 1647 and 1515 cm^{-1} (Fig. 2). The positions of these bands correspond to the frequencies of the amide ν(C=O) and δ(N-H) vibrations of capsaicin (or other capsaicinoid compounds) [18, 19]. The ATR-FTIR spectra of extracts **N8 – N10** obtained from placenta show different IR characteristics (Fig. 2). Along with the bands corresponding to the vibrations of the triacylglycerols there are several bands originating from the capsaicinoids vibrations: 3332 cm^{-1} overlapped ν(O-H) and ν(N-H), 1647 ν(C=O), 1516 δ(N-H), 1273 $\gamma(CH_2)$, 1036 cm^{-1} $\nu(O\text{-}CH_3)$.

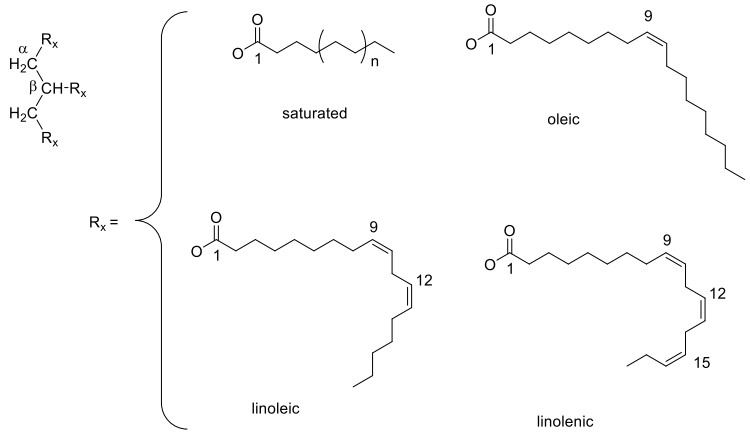

Scheme 1. Structure of the main fatty acids residues in TAG of red hot pepper.

(a)

(b)

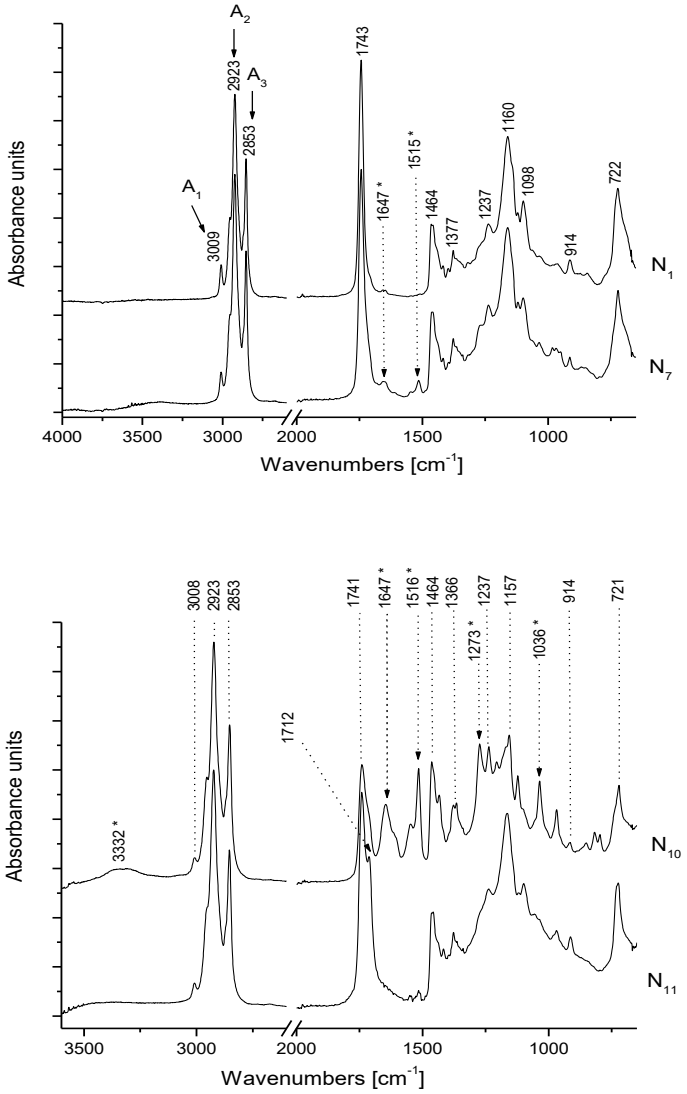

Fig. 2. ATR-IR spectra of *Capsicum annuum L.* extracts: (a) **N1** from seeds and **N7** from pericarp; peak heights A_1 – A_3 are used for quantitative estimation of the degree of unsaturation; IR bands attributed to capsaicinoids are marked with asterisk; (b) **N10** from placenta and **N11** from stalk; IR bands attributed to capsaicinoids

The band for the stretching vibration of the ester carbonyl groups of triacylglycerols is slightly shifted to lower frequencies compared to extracts **N1 – N7** and appears with an asymmetric shape on the low-frequency side. Another specific feature is the considerably increased intensity of the bands for the C-H stretching vibrations which are by far the most intensive in the spectra of **N8 – N10**. Such predominant intensity of the bands of the C-H stretching vibrations and appearance of multiple bands for carbonyl stretching is characteristic for plant waxes [20]. It could be assumed that extracts **N8 – N10** are a mixture of triacylglycerols, capsaicinoids and waxes.

The same is observed in the IR spectra of the stalk extracts **N11** and **N12** where the band for ν(C=O) of the triacylglycerols is at 1741 cm^{-1} overlapped with another one at 1712 cm^{-1} for ν(C=O) of plant waxes (Fig. 2). The amount of capsaicinoids is obviously much lower as only a weak band at 1515 cm^{-1} is present in the spectra of **N11** and **N12**.

The ratios A_1 / A_2 and A_1 / A_3 calculated from the spectra of **N5 – N7** are lower than those for the extracts from seeds. This fact might be due to different proportions of the monounsaturated and polyunsaturated fatty acid residues in the extracts obtained from different parts of *C. annuum L.* [21, 22].

The ratios A_1 / A_2 and A_1 / A_3 calculated for the placenta extracts **N8 – N10** are also lower than those for the extracts from seeds. It is in agreement

with the fact that the band for the C-H stretching of the *cis*-double bond is found at 3008 cm^{-1} in the ATR-IR spectra of **N8 – N10**. However, it should be taken into account that the intensity of the absorption A_2 and A_3 might be significantly increased by the presence of waxes, so the calculated ratio A_1 / A_2 and A_1 / A_3 would not reflect reliably the degree of unsaturation coming from the oil itself. In the ATR-IR spectra of **N11** and **N12** the band for ν(=C-H) is found at 3009 cm^{-1}, but the two extracts show much different degree of unsaturation. The degree of unsaturation of extract **N11** obtained by Soxhlet extraction of stalk with 1 mm, is similar to that of the extracts from pericarp and placenta, while the degree of unsaturation of extract **N12**, obtained by supercritical carbon dioxide extraction of stalk with 0.25 mm, is close to the values shown by the extracts of *Capsicum annuum* seeds.

The frequencies of the amide C=O stretching and amide N-H bending vibration of capsaicinoids do not overlap with the IR bands of triacylglycerols, and therefore might serve for identification of capsaicinoids even at low concentrations. However, the exact determination of the capsaicinoid content requires a calibration curve based on a series of standard mixtures with known amount of triacylglycerols and capsaicin.

NMR spectroscopy

A methodology for determination of the fatty acid composition through ^1H NMR has been proposed as a simpler, more rapid and less expensive method requiring no sample pretreatment. It can be explained briefly by the following [6, 7]:

The protons of the two αCH_2 groups of the glycerol show signals at δ 4.1 - 4.3 ppm with integral for total 4H ($2\times CH_2$), and the signals of the βCH at 5.23 ppm for 1H (Fig. 3). The proton signals at $\delta \sim 2.30$ ppm are due to $CO\text{-}CH_2$ groups. They would appear in the spectra of both saturated and unsaturated fatty acids. The same is valid for the signals of $CO\text{-}CH_2\text{-}CH_2$- groups of saturated and unsaturated fatty acids at $\delta \sim 1.6$ ppm. Each of these signals should show integral for 6H. The above mentioned signals can be used for calibration of the integral areas of the fatty acid signals in the ^1H spectrum. The proton signals of the terminal methyl groups appear at $\delta \sim$ 0.8-1.00 ppm and should be integrated for 9H.

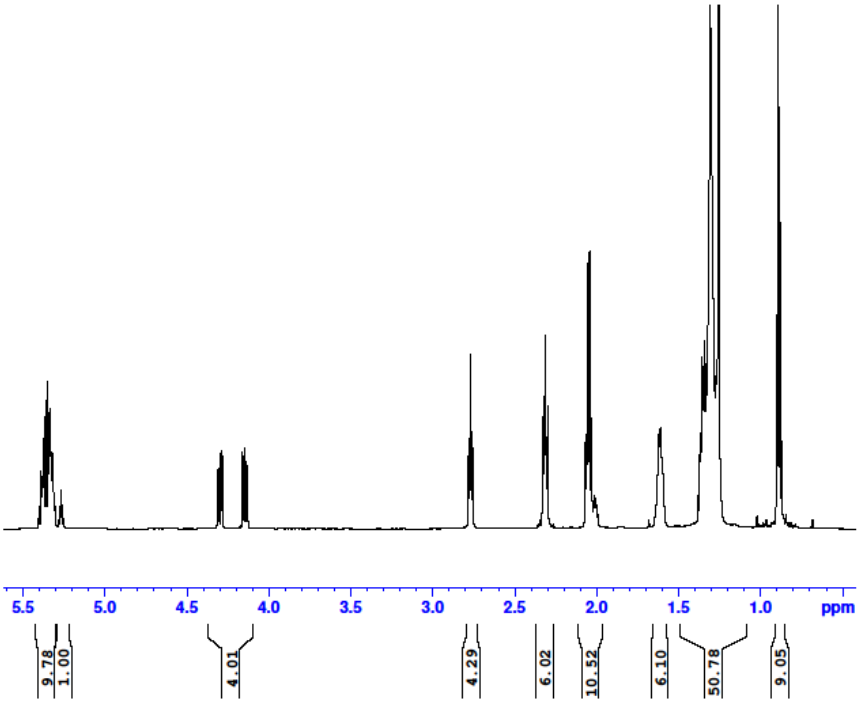

Fig. 3. ^1H NMR spectrum of the extract **N1** from seeds with supercritical carbon dioxide. On the bottom line are depicted the values of the integral areas.

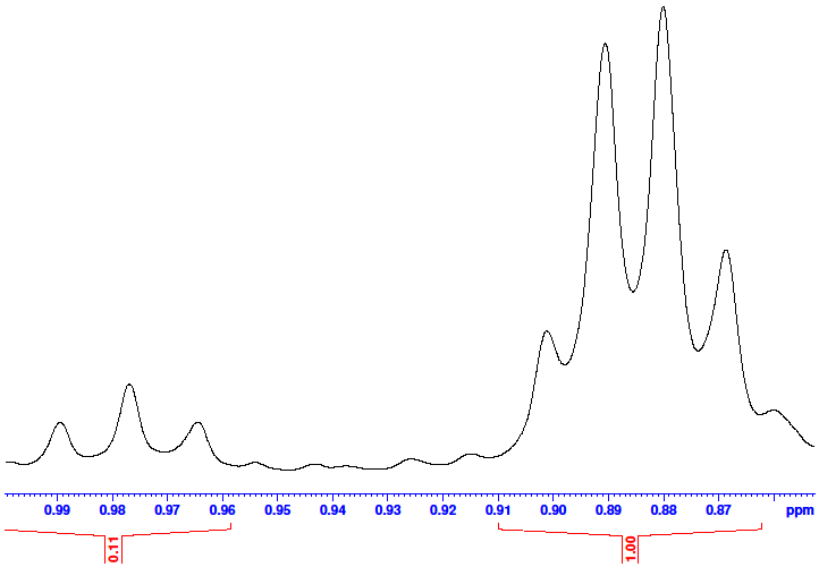

Fig. 4. ^{1}H NMR spectral region 0.86 - 1.00 ppm of extract **N6** from pericarp.

From them the triplet at δ 0.98 ppm gives the percentage of linolenic acid (Fig. 4).

The signals at δ 5.3 - 5.42 ppm correspond to the total amount of olefinic protons in unsaturated fatty acids.

Only polyunsaturated fatty acids would give signals at δ 2.78 ppm corresponding to the chemical shifts of the methylene hydrogens between two double bonds.

^{1}H NMR signals at δ 2.05 ppm are characteristic for the allylic methylene protons of all unsaturated fatty acids, including monoenoic and polyunsaturated and the molar percentage of unsaturated fatty acids could be obtained from the area of this peak.

For triacylglycerols containing virtually no saturated fatty acids residues the ratio of the peak areas at δ 2.05 ppm (allylic methylene protons) and terminal methyl protons $\delta \sim 0.8$ - 1.00 ppm should be 12:9.

The signals in the region 1.2 - 1.4 ppm belong to saturated CH_2 chains.

It should be noted that NMR spectra do not give information about the fatty acid distribution in α and β positions of glycerol units rather their proportion in the sample.

NMR spectroscopy is one of the most informative methods applied for analysis of the capsaicinoids. A large amount of NMR data of capsaicinoids has been published [8]. In capsaicin and all types of capsaicinoids the aromatic signals characteristic for a 1,2,4-substituted phenyl at δ 6.7 - 6.9 ppm are observed (d, $J \sim 8$ Hz; dd $J \sim 8$, 2 Hz and d, $J \sim 2$ Hz.

The protons at the double bonds of carotenoids resonate in the region of δ 5.7 – 6.5 ppm [23].

*Extracts from seeds - samples **N1 – N4***

The samples **N1** (Fig. 3) – **N4** showed similar spectra and fatty acids compositions. The signal at δ 0.98 ppm characteristic for linolenic acid was not observed. The fatty acids composition of N1 determined with GC and NMR analysis is given in Table 3. From the integrals of the peaks at 0.9 ppm and 2.05 ppm approximately 87% of unsaturated acid and 13% saturated, respectively could be calculated. The signal at δ 2.78 which corresponds to the chemical shifts of the double-allylic protons and is characteristic for polyunsaturated fatty acids. It was obviously due to the presence of linoleic acid because linolenic acid could be practically excluded. The results of the NMR analysis of samples **N1 – N4** vary in the range of a few percents (7% - 13%, 8% - 11% and 76%-82% for saturated, oleic and linoleic acids, respectively).

The results of the NMR spectra are in agreement with the results of GC analysis (Table 3) and with previous studies of *C. annuum* [21, 24].

Traces of capsaicinoids were detected. Quantitative determination was not possible.

In this way the composition of triacylglycerols in the seeds was shown to be similar to sunflower and soybean oil [6, 7, 24].

Table 3. Fatty acid composition of extract **N1** from seed obtained with GC and NMR analyses.

Fatty acid		GC	NMR
Saturated		*12.7*	13
Palmitic	C16:0	10.203	
Stearic	C18:0	2.494	
Monounsaturated		*8.7*	8
Palmitoleic	C16:1	0.167	
Oleic	C18:1	8.537	
Polyunsaturated		*78.3*	79
Linoleic	C18:2	78.183	
Linolenic	C18:3	0.145	

*Extracts from pericarp- samples **N5 – N7***

The spectra of the samples **N5 – N7** (Fig. 5) indicated more complex mixtures which made difficult the determination of the triglyceride composition. The main difference between the spectra of **N1 – N4** and the spectra of the samples **N5 – N7** is the signal at δ 0.98 ppm characteristic for the methyl groups of linolenic acid (Fig. 4). This finding is in accordance with the results of Perez-Calvez *et al.* [21] about the composition of fatty acids of the pericarp and seeds of some varieties of *C. annuum L.*

In addition, **N5** and **N6** showed intense signals in the region *of* δ 1.5 - 1.7 where protons from saturated long chains resonate (Fig. 5). In the spectrum of **N7** these signals did not appear. In the spectrum of **N7** a small amount of capsaicin (about 10%) was detected (Fig. 6).

*Extracts from placenta- samples **N8 – N10***

The samples **N8**, **N9** and **N10** from placenta (Fig. 7) showed similar spectra. In the region *of* $\delta \sim$ 1.2 - 1.4 ppm intense signals appeared for long CH_2 chains, probably waxes. The proportion of different types of fatty acids could not be estimated because of the overlap with the signals of capsaicinoids.

In the samples from the placenta a substantial amount of capsaicinoids was presented, approximately:

N8 - Capsaicinoids : TAG ~ 5 : 1.
N9 - Capsaicinoids : TAG ~ 2 : 1.
N10 - Capsaicinoids : TAG ~ 3 : 1.

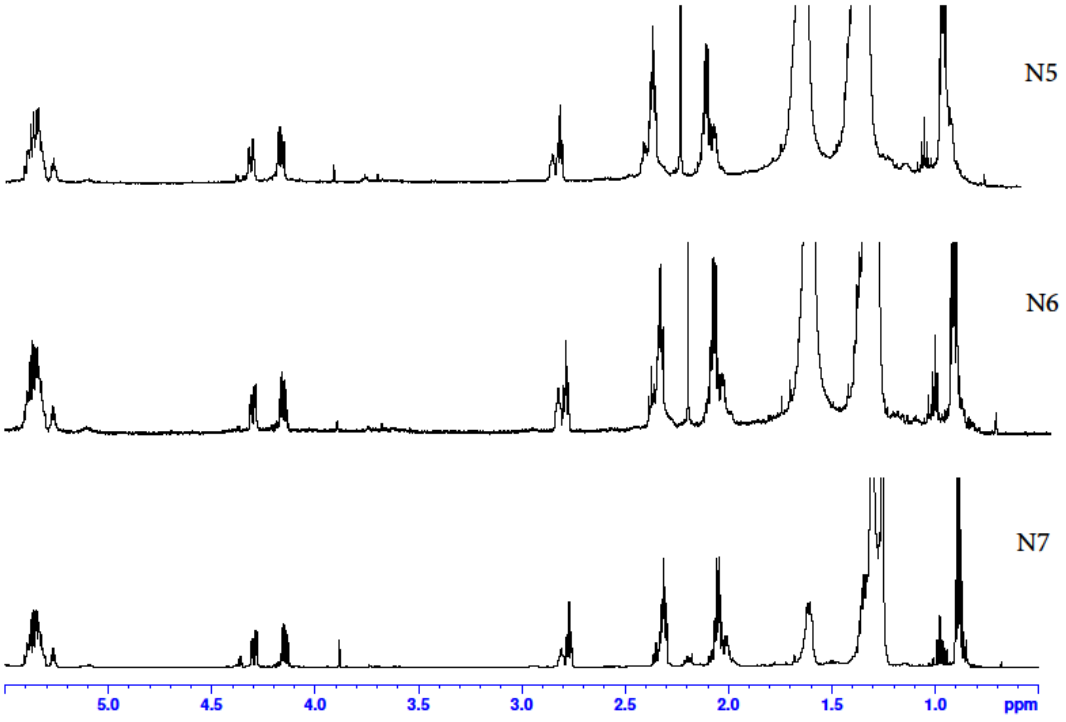

Fig. 5. ^{1}H NMR spectra of extracts from pericarp (**N5 – N7**) in the region 0 – 5.5 ppm.

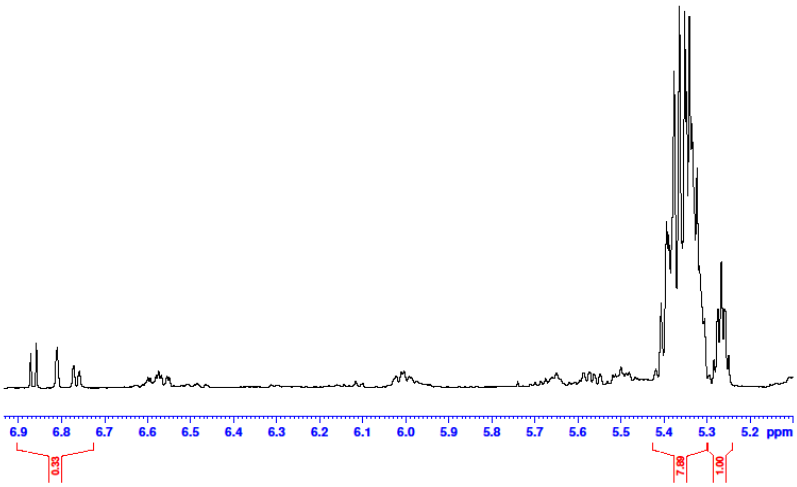

Fig. 6. ^{1}H NMR spectra of extract from pericarp (**N7**). ^{1}H NMR spectral region 5.1 - 7.0 ppm

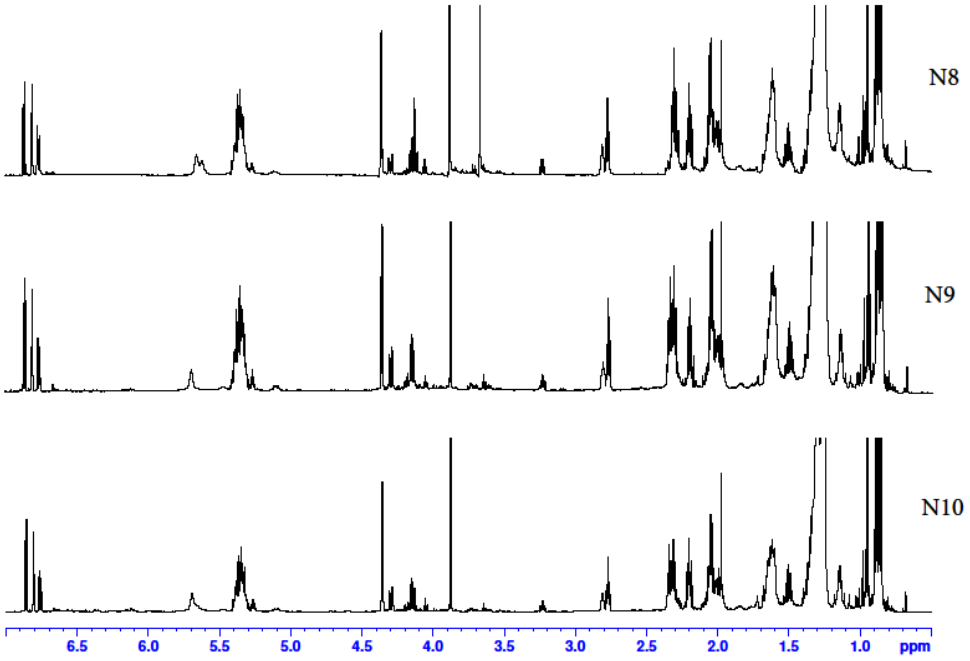

Fig. 7. ^{1}H NMR spectra of extracts from placenta (**N8** – **N10**).

*Extracts from placenta- samples **N8 - N10***

The samples **N8**, **N9** and **N10** from placenta (Fig. 7) showed similar spectra. In the region $\delta \sim$ 1.2 - 1.4 ppm intense signals appeared for long CH_2 chains, probably waxes. The proportion of different types of fatty acids could not be estimated because of the overlap with the signals of capsaicinoids.

In the samples from the placenta a substantial amount of capsaicinoids was presented, approximately:

N8 - Capsaicinoids : TAG ~ 5 : 1.

N9 - Capsaicinoids : TAG ~ 2 : 1.

N10 - Capsaicinoids : TAG ~ 3 : 1.

*Extracts from stalk - samples **N11**, **N12***

The samples **N11** and **N12** showed similar spectra and quantitative proportions. In the region $\delta \sim$ 1.2 - 1.4 ppm intensive signals were obtained probably due to presence of waxes. The proportion of different types of fatty acids could not be estimated because of the overlap with the signals of capsicinoids. The correlation capsaicinoids: TAG was estimated to be ~ 0.15 : 1.

Despite of the characteristic color of the samples carotenoids were not detected in the NMR and ATR-IR spectra.

It should be noted that NMR is less sensitive than the traditional chromatographic methods. The merit of the method is in its simplicity and swiftness but the quantitative measurements depend to some extent on the manually calibration of the integral area. For a more exact quantitative analysis the information from the NMR spectra should be supported with other analysis (GC, HPLC).

CONCLUSIONS

Extracts from the seeds, pericarp, placenta and stalk of hot red pepper (*Capsicum annuum* L., ssp. *microcarpum longum conoides*, convar. Horgoshka) were studied by NMR and IR spectroscopy. It was shown that both spectral techniques can be used to follow the extraction effectiveness in simple, rapid and inexpensive way without sample pretreatment and that both spectral techniques provide useful information on the triacylglycerol content and degree of unsaturation of the hot red pepper extracts. The IR spectroscopy could serve as a fast tool for identification of capsaicinoids in the extracts, while the NMR analysis could be successfully applied for determination of the proportion triacylglycerols : capsaicinoids.

In summary, the obtained spectral results showed that the seed extracts **N1 – N4** have similar triacylglycerol content with approximate ratio of saturated (7% - 13%), oleic (8% - 11%) and linoleic acids (76% - 82%) and only traces of capsaicinoids. The pericarp extracts **N5 – N7** encompassed more complex triacylglycerol mixtures including linolenic acid, saturated long chain hydrocarbons – presumably plant waxes, and a small amount of capsaicinoids in the case of N7. On the other hand, the placenta extracts **N8 – N10** had predominant capsaicinoid content with capsaicinoids : TAG ratio from 5:1 to 2:1. The stalk extracts **N11** and **N12** contained triglycerols, plant waxes and smaller amount of capsaicinoids. The ratio capsaicinoids : TAG was estimated to be ~ 0.15 : 1.

REFERENCES

1. M. R. S. Campos, K. R. Gómez, Y. M. Ordoñez, D. B. Ancona, *Food Nutr. Sci.*, **4**, 47 (2013).
2. I. Guzman, P. W. Bosland, M. A. O'Connell in: The Biological Activity of Phytochemicals. Recent Advances in Phytochemistry, D. R. Gang (ed.), vol. 41, Springer Science+Business Media, Springer, New York, Dordrecht, Heidelberg, London, 2011, p. 109.
3. C. B. Davis, C. E. Markey, M. A. Busch, K. W. Bush, *J. Agric. Food Chem.*, **55**, 5925 (2007).
4. Z. A. A. Othman, Y. B. H. Ahmed, M. A. Habila, A. A. Ghafar, *Molecules*, **16**, 8919 (2011).
5. G. Vlahov, *Prog. Nucl. Mag. Res. Sp.*, **35**, 341 (1999).
6. A. Barison, C. W. P. da Silva, F. R. Campos, F. Simonelli, C. A. Lenz, A. G. Ferreira, *Magn. Reson. Chem*., **48**, 642 (2010).
7. T.-Y. Shiao, M.-S. Shiao, *Bot. Bull. Acad. Sinica*, **30**, 191 (1989).
8. V. Gómez-Calvario, M. L. Garduño-Ramírez, I. León-Rivera, M. Y. Rios, M.Y, *Magn. Reson. Chem.*, **54**, 268 (2016).
9. M. D. Guillen, A. Ruiz, N. Cabo, G. Pascual, *J. Am. Oil Chem. Soc*., **80**, 755 (2003).
10. N. Vlachos, Y. Skopelitis, M. Psaroudaki, V. Konstantinidou, A. Chatzilazarou, E. Tegou, *Anal. Chim. Acta*, **573-574,** 459 (2006).
11. J. Simonovska, M. Škerget, Z. Knez, M. Srbinoska, Z. Kavrakovski, A. Grozdanov, V. Rafajlovska, *Maced. J. Chem. En.*, **35**, 199 (2016).
12. J. Simonovska, V. Rafajlovska, Z. Kavrakovski, M. Srbinoska, *Maced. J. Chem. Eng.*, **33**, 97 (2014).
13. AOAC. Official Methods of Analysis. Association of Official Analytical Chemists International, 18th ed., Gaintersburg, MD, USA, 2006.
14. M. Škerget, Ž. Knez, *Comp. Chem. Eng*., **25**, 879 (2001).
15. A.O.C.S. Official Methods Ce 1-62, American Oil Chemists' Society, IL, USA.
16. M. D. Guillen, N. Cabo, *J. Sci. Food Agric.*, **75**, 1 (1997).
17. F. D. Gunstone, J. L. Harwood in: The Lipid Handbook, F. D. Gunstone, J. L. Harwood, A. J. Dijkstra (eds.), CRC Press, Boca Raton, USA, 2007, p. 37.
18. A. Alberti, V. Galasso, B. Kovac, A. Modelli, F. Pichierri, *J. Phys. Chem. A*,**112,** 5700 (2008).
19. J. S. P. P. Leela, R. Hemamalini, S. Muthu, A. A. Al-Saadi, *Spectrochim. Acta A*, **146**, 177 (2015).
20. B. R. da Luz, *New Phytol.*, **172**, 305 (2006**)**.
21. A. Perez-Galvez, J. Garrido-Fernandez, M. I. Minguez-Mosquera, M. Lozano-Ruiz, V. Montero-de-Espinosa, *J. Am. Oil Chem. Soc.*, **76**, 205 (1999).
22. G. T. de Souza Sora, A. H. P. Souza, A. A. F. Zielinski, C. W. I. Haminiuk, M. Matsushita, R. M. Peralta, *Ciênc. Agrotec. Lavras*, **39**, 372 (2015**)**.
23. G. Englert, *Pure &Appl. Chem.*, **57**, 801 (1985).
24. R. L. Jarret, I. J. Levy, T. L. Potter, S. C. Cermak, *J. Food Comp. Anal.*, **30**, 102 (2003).

Bulgarian Chemical Communications, Volume 51, Issue 1, (pp. 113 – 116) 2019

Polyphenols content and antioxidant activity of various pomegranate juices

S. I. Papanov[1]*, Ek. G. Petkova[2], I. G. Ivanov[3]

[1]*Medical University Plovdiv, Faculty of Pharmacy, 15A, V. Aprilov Blvd., 4000 Plovdiv, Bulgaria*
[2]*Medical University Plovdiv, Medical College, 120, Br. Bakston Str., 4004 Plovdiv, Bulgaria*
[3]*University of Food Technologies, Technological Faculty, 26, Maritza Blvd., 4002 Plovdiv, Bulgaria*

Received July 16, 2018; Revised October 29, 2018

The aim of the study was the determination and analysis of pH, content of common phenols, antioxidant activity (radical trapping activity), common anthocyanins and acidity of pomegranate (*Punica granatum*) and their relation to the soil composition and altitude. Methods for systematic approach and critical analysis of the available scientific periodicals were applied. Spectrophotometric method was used for determination of adsorption with gallic acid standard; DPPH method was used for determining the antioxidant activity (radical trapping activity). It was found that the value of pH index ranges from 3.05 to 4.29. The lowest level of common phenols 67.71 ± 0.12 mg GAE/100 ml was observed in the Red Filk variety. Total anthocyanins were within the range of 0.60 ± 0.01 mg/100 ml (Red Filk) to 35.80 ± 0.65 mg/100 ml (Pink Satin). Antioxidant activity (DPPH) was: 966.13 ± 37.67 mmol TE/100 ml (Red Filk) to 2271.72 ± 26.91 mmol TE/100 ml. Titratable acidity was within the range: 0.47 ± 0.10 g/100 mL for Red Filk and up to 1.64 ± 0.10 g/100 mL for Pink Satin. It was concluded that there is a direct correlation between the antioxidant activity and the altitude at which the pomegranate is growing. There is a direct correlation between the common phenols and the antioxidant activity, excluding variety Wonderful.

Keywords: Pomegranate, Antioxidant activity, Phenols, Anthocyanins.

INTRODUCTION

The pomegranate is a type of deciduous tree or a bush of the genus *Punica*. The plant is dry and "comes" from Asia, Africa, Europe and Middle East. Pomegranate fruits are mainly consumed fresh but they are also used in the preparation of fresh juices, canned beverages, jellies, jams, etc. In recent years there has been increasing interest in pomegranate (number of published materials grew 7 times) as medical and food industry product. The pomegranate tree especially its fruit, has a long history and a bunch of healing properties. Depending on the characteristics and composition, pomegranates may be intended for fresh consumption, industrial processing or medical purposes. It is therefore important to know the characteristics of different pomegranate varieties in order to gain more knowledge about their application [1-3]. Pomegranate juice has powerful antioxidant properties. They may be associated with anti-inflammatory effects on a plant-based basis. Phytochemistry and pharmacological actions of all components of *Punica granatum* suggest a wide range of clinical applications for cancer treatment and prophylaxis [2, 4-10]. As a result of the increased attention given to pomegranate, the number of countries producing pomegranate has increased and new varieties appeared [3-8, 11]. The synergistic effect of pomegranate ingredients is better than that of the individual components. Over the last decade, numerous studies have been published on the antioxidant, anticancer and anti-inflammatory properties of pomegranate ingredients for the treatment and prevention of cancer, cardiovascular disease, diabetes, dental conditions, erectile dysfunction, bacterial infections, antibiotic resistance and skin damage [4, 11-13].

Pomegranate juice has been proven to be extremely effective in the prevention of atherosclerosis [14, 15]. Gil *et al*. determined the antioxidant activity of pomegranate juice by 4 different methods and found that it is 3 times higher than that of red wine and green tea [16]. Hmid *et al*. investigated the pomegranate varieties grown in Morocco and found high concentration of phenolic compounds, antocyanins and organic acids [17].

The aim of this study was the determination and analysis of pH, total polyphenols, antioxidant activity (radical trapping activity) total anthocyanins and acidity of pomegranate (*Punica granatum*) and their dependence on the altitude.

METHODS AND MATERIALS

Fruit sample

The antioxidant characteristics of pomegranates from different varieties grown in Bulgaria (Garnet Sash and Wonderful), Greece (Red Filk), Macedonia (Garnet Sash) and Turkey (Pink Satin) were studied. Pomegranate varieties from Bulgaria

* To whom all correspondence should be sent:
E-mail: stoyan.papanov@abv.bg

Delchev. The altitude of the town of Petrich is 168 m, and of Gotse Delchev 540 m. The Red Filk variety from Greece was grown in the Kavala area at an altitude of 53 m. Rosso Gigante from Macedonia is from the town of Doiran (148 m above sea level). At an altitude of 200 m above sea level near the town of Bursa is the variety Pink Satin.

Juice extraction, pH and titratable acidity analysis

To obtain the juice, pomegranate fruits were peeled by hand and the seeds were liquefied using a Philips food processor. The obtained juice was pre-filtered and then centrifuged at 3000 rpm for 15 min. pH was measured potentiometrically with a pH meter (WTWinoLab pH 7110, Germany). Titratable acidity, expressed as percentage of malic acid, was performed by titrating 10 mL of pomegranate juice with a 0.1 M NaOH to a pH point of 8.1. The results were expressed in g malic acid per 100 g juice.

Total phenolics content (TPC)

The total phenolic contents were meas-ured using a Folin-Ciocalteu assay. Folin- Ciocalteu reagent (1 mL) (Sigma) diluted five times was mixed with 0.2 mL sample and 0.8 mL 7.5% Na2CO3. The reaction was performed for 20 min at room temperature in darkness. Then the absorbance of the sample was measured at 765 nm against blank sam-ple, developed by the same way but without extract. The results were expressed in mg equivalent of gallic acid (GAE) per 100 g juice, according to calibration curve, build in range of 0.02 - 0.10 mg gallic acid (Sigma) used as a standard.

Total monomeric anthocyanins analysis

The total monomeric anthocyanins content was determined using the pH differential method described by [17]. 2 g juice were extracted with 8 mL ethanol at ultrasound bath for 15 min. The pH of juice samples was brought to 1.0 with potassium chloride and 4.5 with sodium acetate buffers. The dilutions were then allowed to equilibrate for 5 min at room temperature. The absorbance of equilibrated solutions at 520 nm for anthocyans content and 700 nm for haze correction was measured on a VIS spectrophotometer (Camspec M107, UK) with 1-cm path-length disposable cuvettes. All absorbance measurements were carried out at room temperature against distilled water as a blank. Pigment content was calculated as cyanidin-3-glucoside (cyanidin-3-glucoside) equivalents with a molecular weight of 449.2 and an extinction coefficient of 26 900 L/(cm.mol).

Antioxidant activity (DPPH assay)

Each analyzed extract (0.15 mL) was mixed with 2.85 mL of freshly prepared 0.1 m mol solution of 1,1-diphenyl-2- picrylhydrazyl radical (DPPH, Sigma) in methanol (Merck). The reaction was performed at 37 °C in darkness and the absorption at 517 nm was recorded after 15 min against methanol. The antioxidant activity was expressed as m mol Trolox equivalents (TE) per 100 g juice by using a calibration curve built with 0.05, 0.1, 0.2, 0.3, 0.4 and 0.5 mmol 6-hydroxy-2,5,7,8-tetramethylchroman-2-carboxylic acid (Trolox®, Fluka) dissolved in methanol (Sigma).

RESULTS AND DISCUSSIONS

Pomegranate (*Punica granatum* L.) is one of the oldest edible fruits. It is widely grown in different parts of Asia, North Africa, the Mediterranean areas and in the Middle East. The pomegranate fruit is pressed to prepare commercial juices. A large number of bioactive compounds would be expected to be extracted from juices and would have high antioxidant properties. The values obtained for pH, common phenols, total anthocyanins, antioxidant activity and titratable acidity during the test are presented in Tables 1 and 2. The results for juice titrable acidity (TA), and pH for the different cultivars are presented in Table 1. Significant differences were revealed among the pomegranate cultivars for all parameters. The pH values ranged between 3.0 and 4.2. The pH values obtained in the current study are in agreement with pomegranate cultivars grown in Morocco, Tunisia and Turkey [17-19]. The titrable acidity content varied from 0.47 to 1.60 g/100 mL. Similar results were also reported by Hmid *et al.* [17], whereas the values reported by Hasnaoui *et al.* were different [19]. According to the results, cultivar type plays an important role in terms of pH and titrable acidity of the pomegranate juice [17-19]. Phenolic compounds of pomegranates juice were presented as ellagic acid, gallic acid, chlorogenic acid, caffeic acid and ferulic acid [17]. It is evident from Table 2 that the highest content of total phenols has the variety Pink Satin (193.16 ± 1.12 mg GAE/ 100 mL), followed by Wonderful, Garnet Sash, Rosso Gigante and Red Filk. Additionally, many investigators reported that pomegranate juice has a high free radical scavenger capacity. Our results revealed that pomegranate juice of the Wonderful variety has the highest antioxidant activity (2271.72 ± 26.91 m mol TE/ 100 mL). In accordance, it was established that the total polyphenol content of 18 cultivars varied from 138 to 947 mg GAE/ 100 mL of pomegranate juice [17]. In addition, six

anthocyanins - 3-glucosides and 3,5-diglucoside of delphinidin, cyanidin and pelargonidin has been identified in the pomegranate juice [18, 19].

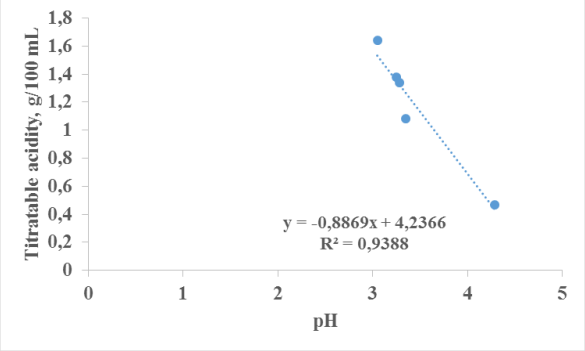

Figure 1. Correlation between pH and titratable acidity.

Turkyılmaz [18] established significant differences between total anthocyanins contents (2–44 mg/100 mL juice) in different varieties of pomegranate. Similar result were obtained in our study (Table 2). This indicator is the lowest for the Red Filk variety. The Pink Satin, Garnet Sash and Rosso Gigante varieties are approximately evenly distributed. As shown in Table 2, the total anthocyanins in different juices could be arranged in the following order: Pink Satin>> Rosso Gigante > Garnet Sash > Wonderful > Red Filk. The highest content of polyphenols coincides with the highest anthocyanins content in Pink satin variety.

The major organic acid reported in pomegranate juice is citric acid (66–74%), followed by malic acid (6–12%) [18, 19]. The relationship between pH and titratable acidity is decreasing, which corresponds to the theoretical descriptions of the scientific periodicals and the practical expectations of the study. The linear dependence between pH and antioxidant activity (Figure 1) is disturbed by the Wonderful variety - 2271.72 ± 26.91 m mol TE / 100 ml.

Table 1. pH and titratable acidity of different pomegranate juices

Variety	pH	Titratable acidity (g malic acid /100 mL)
Rosso gigante	3.25 ± 0.04	1.38 ± 0.10
Wonderful	3.35 ± 0.05	1.08 ± 0.10
Red filk	4.29 ± 0.03	0.47 ± 0.10
Garnet sash	3.28 ± 0.04	1.34 ± 0.10
Pink satin	3.05 ± 0.05	1.64 ± 0.10

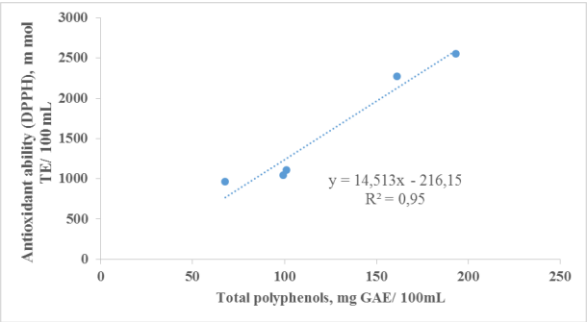

Figure 2. Correlation relation between total polyphenols and antioxidant ability.

CONCLUSIONS

The results provide important information of the polyphenols content and antioxidant capacity of pomegranate juice, which can be useful for developing fruit processing industries for commercial available pomegranate varieties. The pomegranate juice was determined as a very valuable food for people with chronic illnesses, because of its high antioxidant activity. In addition, a positive correlation between antioxidant activity and altitude of pomegranate varieties, as well as between total polyphenols and antioxidant activity was found. This study enriched the information about pomegranate fruits and demonstrated the potential beneficial health effect of this plant.

Table 2. Total phenols, total anthocyanins and antioxidant activity of different pomegranate juices

Variety	Total phenols (mg GAE/100 ml)	Total anthocyanins (mg/100 ml)	Antioxidant activity (DPPH) (m mol TE/100 ml)
Rosso gigante	99.40 ± 0.52	7.81 ± 0.10	1047.00 ± 33.63
Wonderful	161.04 ± 0.51	2.40 ± 0.03	2271.72 ± 26.91
Red filk	67.71 ± 0.12	0.60 ± 0.01	966.13 ± 37.67
Garnet sash	101.15 ± 0.91	5.10 ± 0.05	1109.77 ± 48.37
Pink satin	193.16 ± 1.12	35.80 ± 0.65	1558.09 ± 83.93

REFERENCES

1. F. Alcaraz-Mármol, N. Nuncio-Jáuregui, F. García-Sánchez, J. Martínez-Nicolás, F. Hernández, *Scientia Horticulturae*, **219**, 155 (2017)
2. A..Kulkarni, S. Aradhya, *Food Chemistry*, **93**, 2, 319 (2005).
3. O.Fawole, U. Opara, *Scientia Horticulturae*, **150**, 39 (2013).
4. E. Lanskya, R. Newman, *J. of Ethnopharmacology*, **109**, 2, 180 (2007).
5. R. Mphahlele, O. Fawole, L. Mokwena, U. Opara, *South African Journal of Botany*, **103**, 138 (2016).
6. F. Tezcan, M. Gültekin-Özgüven, T. Dikena, B. Özçelik, F. Erim, *Food Chemistry*, **115**, 3, 873 (2009).
7. S. Akhtar, T. Ismail, D. Fraternale, P. Sestili, *Food Chemistry*, **174**, 419 (2015).
8. Z. Kalaycıoğlu, F. Erim, *Food Chemistry*, **221**, 498 (2017).
9. B. Gullon, M..Pintado, J. Pérez-Álvarez, M. Viuda-Martos, *Food Control*, **59**, 94 (2016).
10. A. Tehranifara, M. Zareia, Z. Nematia, B. Esfandiyaria, M. Vazifeshenas, *Scientia Horticulturae*, **126**(2), 180 (2010).
11. J. Jurenka, *Biomed search*.com, **13**, 2 (2008).
12. H. Hayrapetyan, W. Hazeleger, R. Beumer, *Food Control*, **23**(1), 68 (2012)
13. M. Ozgen, C. Durgab, S. Serçe, C.Kaya, *Food Chemistry*, **111(**3), 703 (2008).
14. Y. Li, C. Guo, J. Yang, J. Wei, J. Xu, S. Cheng, *Food Chemistry*, **96**(2), 254 (2006).
15. G. Mousavinejad, Z. Emam-Djomeh, K. Rezaei, M. Khodaparast, *Food Chemistry*, **115**, 4(15), 1276 (2009).
16. M. Gil, F. Tomás-Barberán, B. Hess-Pierce, D. Holcroft, A. Kader, *J. Agric. Food Chem.,* **48**(10), 4583 (2000).
17. I. Hmid, D. Elothmani, H. Hanine, A. Oukabli, E. Mehinagi, *Arabian Journal of Chemistry*, **10**(2), S2678 (2017).
18. M. Turkyılmaz, *International Journal of Food Science and Technology*, **48**, 2086 (2013).
19. N. Hasnaoui, R. Jbir, M. Mars, M. Trifi, A. Kamal-Eldin, P. Melgarejo, F. Hernandez, *International Journal of Food Properties*, **14(**4), 741 (2011).

Bulgarian Chemical Communications, Volume 51, Issue 1, (pp. 117 – 124) 2019

Hydrophilic gel containing coenzyme Q_{10}-loaded liposomes: preparation, characterization and stress stability tests

N. Dragicevic [1*], D. Krajisnik [2], J. Milic [2], D. Pecarski [3], Z. Jugović [4]

[1] *Apoteka "Beograd", Bojanska 16/IV, 11000 Belgrade, Serbia, Present address: Bulevar Oslobodjenja 163, 11000 Belgrade, Serbia*

[2] *Department of* Pharmaceutical Technology *and Cosmetology, Faculty of Pharmacy, University Belgrade, Vojvode Stepe 450, 11000 Belgrade, Serbia*

[3] *College of of Professional Health Studies, Dusanova 254, Zemun, 11000 Belgrade, Serbia*

[4] *College of Profesional Health Studies" Visan", Tošin bunar 7a, 11070 Zemun, Serbia*

Received April 18, 2018; Accepted July 10, 2018

The aim of this study was to develop a semisolid formulation containing liposomes loaded with coenzyme Q_{10} (Q_{10}). Q_{10}-loaded liposome dispersion prepared from non-hydrogenated lecithin and characterized for particle size, polydispersity index (PDI), pH value and Q_{10}-content was incorporated into carbomer gel, and a liposome gel was obtained. Liposome gel and liposome-free gel were analyzed for flow properties by continuous rheology measurements, pH values and Q_{10}-content, 48 h after preparation and after a temperature stress test (1 cycle: 24 h at 4ºC, 24 h at 20±2ºC and 24 h at 40ºC), in order to predict their long-term stability. Liposomes were identified in liposome dispersion and liposome gel by freeze fracture electron microscopy (FFEM), while their particle size, PDI and zeta potential were determined by photon correlation spectroscopy (PCS). Q_{10}-loaded liposomes were of small particle size (125 nm), homogeneous (PDI=0.2) and negatively charged, and their incorporation into the gel did not significantly change ($p>0.05$) their particle size and PDI. FFEM confirmed liposomes presence in the liposome gel. Liposome and liposome-free gel revealed non-Newtonian, shear-thinning plastic flow behavior. The temperature stress test revealed that temperature changes did not significantly influence ($p>0.05$) the pH value, while they significantly decreased ($p<0.05$) Q_{10}-content in gels. Q_{10} was significantly more stable ($p<0.05$) in liposome gel than in liposome-free gel. Rheological parameters of liposome-free gel significantly changed, in contrast to the liposome gel. In conclusion, Q_{10}-loaded liposome gel suitable for dermal use was developed, exhibiting high stability even after subjecting to the temperature stress test.

Keywords*:* Liposome, Coenzyme Q_{10}, Carbomer gel, Stability, Rheology

INTRODUCTION

The application of coenzyme Q_{10} (Q_{10}) in pharmaceutical industry has grown significantly in the past decade, i.e., it has been successfully applied in medicine, cosmetics and nutraceuticals [1]. Coenzyme Q_{10} is a highly effective liposoluble non-enzymatic antioxidant which represents the first line of antioxidant defense [2]. Q_{10} has been known since 1950, but became commercially available since its isolation from tobacco plants. Biotechnological or synthetic production is nowadays possible [2].

Q_{10} has radical scavenger and bioenergetical properties. It is already known for its efficacy in the area of neurodermatitis, psoriasis, periodontitis, external substitution under stress, adiposity, immune support and has many other benefits [3]. Q_{10} is highly effective in protecting keratinocytes from DNA damage induced by UVA radiation and also in preventing photoageing *in vivo* with a reduction in wrinkle depth [4]. Because of its beneficial effects, i.e. its antioxidant activities against environmental aggressions and photoageing, Q_{10} has recently made its way into many pharmaceutical and cosmetic products. However, Q_{10} can be easily oxidized, especially under aerobic conditions and light exposure. In order to enhance the photostability of Q_{10}, it may be incorporated into different nanocarriers. Incorporation of Q_{10} into nanostructured lipid carriers (NLC) significantly improved the photo-stability of Q_{10} [5]. In addition, since Q_{10} is liposoluble and hence complicated to incorporate into cosmetic formulations, its incorporation into nanocarriers, like liposomes, nanoemulsions, nanoparticles, would facilitate its use in formulating cosmetic products. Generally, Q_{10} can be incorporated into various novel drug delivery carriers, which include liposomes, polymeric nanoparticles, polymeric micelles, solid lipid nanoparticles, nanostructured lipid carriers, self-emulsifying drug delivery systems, nanoemulsions, solid and aqueous dispersions [1]. Moreover, the incorporation of Q_{10} into nanocarriers would enhance its penetration into the skin, as it has been

* To whom all correspondence should be sent:
E-mail: ninadragicevic@hotmail.com

shown for Q_{10} encapsulated in solid lipid nanoparticles (SLN) being further incorporated in a carbomer gel [6]. The skin delivery of Q_{10} was doubled with gels containing Q_{10}-loaded SLN in comparison with gels prepared with only Q_{10}. For cosmetic purposes most cosmetic actives should be delivered into the skin in order to exhibit their effect. Hence, the use of nanocarriers loaded with cosmetic actives has proven to be adequate as they deliver the actives into the skin, i.e. even into the dermis. Nanostructured lipid carriers (NLC) with a size of about 230 nm have shown to be beneficial for the dermal delivery of Q_{10} and they increased Q_{10} skin penetration when compared to an equally sized nanoemulsion [7], which was in accordance with results reported by Chen *et al.* [8], who showed an epidermal uptake of Q_{10} from Q_{10}-NLC being 10-11 times higher compared to that achieved by the Q_{10}-emulsion, proving that NLC are a promising carrier for the topical delivery of Q_{10}. Furthermore, dependent on the drug delivery system, also transdermal delivery of Q_{10} was reported. Namely, a tocopheryl phosphate mixture which self-assembles to form vesicular structures in hydroethanolic solutions (mean size between 101-162 nm) increased the permeation of carnosine, vitamin D3, caffeine and coenzyme Q_{10} into or through the skin [9]. As to the penetration enhancing ability, liposomes have been widely used to enhance dermal and transdermal drug delivery [10-17]. In brief, liposomes are small, spherical vesicles consisting of amphiphilic lipids, enclosing an aqueous core that are still highly appreciated due to some advantages over other encapsulation technologies [18]. A variety of drugs can be entrapped within liposomes. Topical delivery of liposomally encapsulated actives may offer advantages over conventional formulations since liposomes have the potential to: (a) reduce serious side-effects and incompatibilities that may arise from undesirably high systemic absorption of drugs, (b) act as a local depot for sustained release of dermally active components, (c) serve as penetration enhancers and (d) serve as a rate-limiting membrane barrier for the modulation of systemic absorption of drugs [19]. Several independent studies have shown a higher stability against UV radiation of vitamins encapsulated in liposomes compared to conventional formulations [20-22]. An improved stability was also found in the case of retinol and ascorbyl palmitate encapsulated in liposomes stored at room temperature compared to traditional formulations [23-24].

The purpose of this study was the development, characterization and stability evaluation of a semisolid formulation containing Q_{10}-loaded liposomes. Liposome dispersions are not used in their pure form in cosmetic formulations because of their liquid nature and are therefore incorporated in semisolids. In this study, as it presents our first study on semisolids containing Q_{10}-loaded liposomes, we used a hydrophilic gel as a base (vehicle) for the incorporation of liposomes. The gel (Ultrez® 10 polymer gel) was chosen as liposomes exhibit highest stability in gels, i.e. in creams containing emulsifiers they could be degraded. Thus, at first obtained liposomes, after their preparation (24 h after preparation) were characterized for their particle size, polydispersity index (PDI), pH value and Q_{10}-content. The obtained liposome gel and the liposome-free gel were analyzed for flow properties, pH value and Q_{10}-content, 48 h after their preparation and after five cycles of temperature stress. The liposome gel was also analyzed for the presence of liposomes and their particle size and homogeneity.

MATERIALS AND METHODS

Materials

The following substances were used: non-hydrogenated soybean lecithin (Phospholipon® 80, Lipoid GmbH, Germany), ubichinon (coenzyme Q_{10}, Gfn-Selco, Germany), carbomer (Ultrez 10 ® Polymer, Lubrizol, USA), phenoxyethanol (and) methylparaben (and) ethylparaben (and) propylparaben (and) butylparaben (Phenonip™, Clariant, Switzerland), diazolidinyl urea (Germall™II, Ashland, USA), propylene glycol (BASF, Germany), potassium dihydrogenphosphate (Sigma-Aldrich, USA), sodium hydroxide (Sigma-Aldrich, USA), triethanolamine (TEA) (Sigma, USA), edetate disodium (Titriplex III, Merck Millipore, USA). The water used was double distilled.

Preparation and characterization of Q_{10}-loaded liposomes

Preparation of liposomes. Liposomes composed of Phospholipon® 80 (PL 80) were prepared by the following method: Q_{10} (0.5 % w/w) was dissolved in a mixture of ethanol (16 % w/w) and Phospholipon® 80 (10 % w/w) at 50°C and the obtained solution was added at room temperature to a phosphate buffer solution (PBS) pH 6.5 under vigorous stirring (10 000 rpm, 15 min) using the Ultra-Turrax® T 25 mixer (Ika, Labortechnik, Germany). The spontaneously formed multilamellar vesicles (MLV) were pressed through 200 nm size pore polycarbonate membrane to obtain unilamellar liposomes with the help of a Mini Extruder®

Lipofast extrusion device (Avestin Ottawa, Canada).

Characterization of liposomes in liposome dispersion and liposome gel. The diameter of vesicles, polydispersity index and zeta potential were determined by photon correlation spectroscopy using the Zetamaster S (Malvern Instruments, UK). The particle size was calculated from the autocorrelation function of the intensity of light scattered from particles, assuming spherical form of particles, medium viscosity of 0.89 mPa.s, and refractory index of 1.33. Liposome dispersions were diluted with PBS (pH 7.4) prior to the measurements, that is, 5 μL of the vesicle dispersions were diluted with 495 μL of PBS (pH 7.4). To obtain the zeta potential values of vesicles, 10 μl of vesicle dispersions were diluted with 990 μl of PBS pH 7.4.

To obtain the particle size and the polydispersity index (PDI) of liposomes incorporated in the hydrogel, 0.2 g of the hydrogel was diluted (1:10 w/w) with PBS (pH 7.4), mixed until a clear dispersion was obtained, and, afterward, the dispersion was centrifuged at 3000 rpm. Then, 50 μL of the supernatant were further diluted with 450 μL of PBS (pH 7.4) and analyzed. PDI was used as a value of a unimodal size distribution, which ranges from 0 (homogenous dispersion) to 1 (high heterogeneity). Each sample was measured three times and the mean value was determined.

Determination of pH value in the liposome dispersion. The pH value of the liposome dispersion was measured using a pH meter (HI 8417, Hanna Instruments, USA).

Preparation of Q_{10} gels

As a vehicle for the incorporation of the liposome dispersion Ultrez® 10 polymer was used since the compatibility of liposomes with carbomer gels was previously demonstrated [25, 26]. The gel was prepared by the following procedure: carbomer resin (0.8% w/w) was dispersed in distilled water in which propylene glycol (5% w/w), disodium edetate (0.1% w/w) and the preservatives (Phenonip® 0.2% w/w and Germal® II 0.3 % w/w) were previously added and left to wet for 30 min. The mixture was then neutralized by addition of 10% (w/w) triethanolamine under stirring (300 rpm, 5 min) using the Ultra-Turrax® T 25 mixer (Ika, Labortechnik, Germany), until a transparent gel appeared.

Incorporation of liposomes into the carbomer gel

The liposome dispersion was mixed into the gel by an electrical mixer (200 rpm, 5 min, Heidolph RZR 2020, Germany) and a liposome gel (G1) was obtained. The concentration of the liposomes in the gel was 10% (w/w, liposome dispersion/total), while the concentration of pure Q_{10} in the gel was 0.05% (w/w). The control gel (gel with free Q_{10}, G2) was prepared by first solubilizing Q_{10} (0.05% w/w) in water using Tween® 80 (0.25% w/w) as a solubilizer and then adding all other components, as described above.

pH determination of gels

The pH values were determined directly in gels at room temperature (HI 8417, Hanna Instruments, USA) and served to evaluate the chemical stability. Three measurements were performed for each sample and the mean value was calculated.

Rheological evaluation of gels containing liposomes

The rheometer (Rheolab MC 120, Paar Physica, Stuttgart, Germany) was used to determine flow properties of fresh (48 h old) gels with incorporated liposomes (G1) and without liposomes (G2). In order to predict their physical stability, the flow properties of these gels were also determined after subjecting them to five cycles of temperature stress (1 cycle: 24 h at 4°C, 24 h at 20±2°C and 24 h at 40°C). Measurements were performed at 20 ± 0.1°C by using the cone/plate MK 22 (radius of measuring cone 25 mm, angle of measuring cone 1°) measuring system. Continuous flow tests were carried out by increasing the shear rate from 0 to 200 s^{-1} and decreasing it back to 0 s^{-1}, each stage lasting 200 s. Under the same conditions the flow properties of the liposome gel and the control gel with free Q_{10} were examined. Three measurements were performed for each sample and the mean value was determined.

Determination of Q_{10} content in the samples by HPLC assay

The amount of non-degraded Q_{10} was determined quantitatively in the samples by HPLC analysis, 24 h after preparation. The HPLC apparatus consisted of HPLC pump Waters M600E (isocratically delivered mobile phase) and sample injector Rheodyne 7125i (injection volume: 10 μl). The investigation was performed at room temperature. The analytical column: Chromolith Performance RP-18e, 100 mm × 4.6 mm, 5 μm (Merck, Germany) and the detector: Spectral UV/VIS, PDA SPD - M10 A_{VP} (Shimadzu, Japan) were used. The flow rate was 2.1 ml/min and the UV detection was at λ = 275 nm. The used mobile phase was isopropanol : methanol (25 : 75). Three measurements were performed for each sample and the mean value was determined.

Visualization of liposomes in the liposome dispersion and liposome gel

Freeze fracture electron microscopy (FFEM) was used for the visualization of the liposomes in the liposome dispersion and liposome gel G1. Small amounts of the dispersion or gel were mounted on a gold specimen holder, which was placed between two copper preparation holders. The samples were then quickly frozen by plunge/freezing (Jet Freeze Device BAL/TEC, JFD 030, Liechtenstein) into liquid propane at -180ºC. The frozen specimens were kept in liquid nitrogen until mounting onto the sample holder. The latter was then placed into a freeze fracture device (Freeze Etching System, BAL-TEC, BAF 060, Liechtenstein). Samples were fractured and the fracture plane was replicated by evaporation of 2 nm platinum at an angle of 45º followed by 20 nm carbon at an angle of 90º. Replicas were removed from the freeze fracture device and cleaned in chloroform/methanol (1:1) mixture. Then, they were mounted onto copper grids and visualized using a transmission electron microscope (Zeiss EM 900, Zeiss, Germany).

Statistical analysis

Statistical analysis was carried out using One-Way Analysis of Variance. Significant differences were determined at $p < 0.05$.

RESULTS AND DISCUSSION

Characterization of the Q_{10}-loaded liposome dispersion

FFEM confirmed the presence of spherical liposomes in the liposome dispersion (Fig. 1). Liposomes containing Q_{10}, composed of unsaturated phospholipids (vesicles in fluid thermodynamic state) were characterized (Table 1) and the results of the particle size analysis showed that the mean size of the liposomes was 125.5 nm. Regarding the homogeneity, the low values of the polydispersity index 0.20 indicated homogeneous population of liposomes. Thus, the obtained liposomes were of small particle size and satisfactory homogeneity.

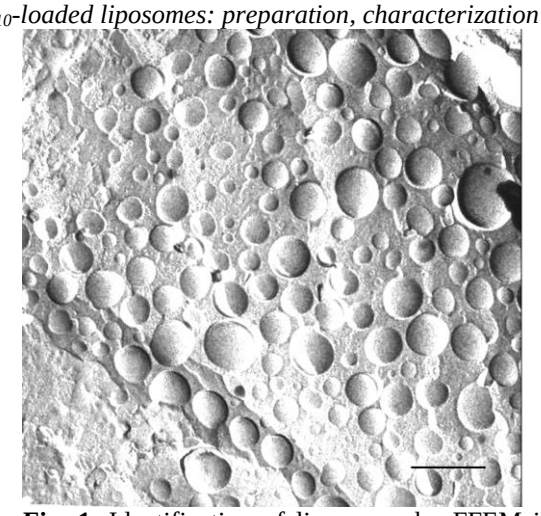

Fig. 1. Identification of liposomes by FFEM in the liposome dispersion after its preparation (scale bar = 100 nm).

As to the pH value, the results indicated that the liposome dispersion due to the use of buffer had a mild acidic pH value of 6.47, being desirable for liposomes for topical application and also because they show high chemical stability around this pH value. Namely, chemical hydrolysis of liposomal lipids at pH 6.5 occurs at the slowest rate. The pH value should always be above pH 4.5 as the pH value of 4.5 represents the critical lower limit when the degradation process of the vesicles may occur [27]. The stability of liposomes can also be predicted on the basis of the zeta potential value. As the liposome dispersion possessed a very high zeta potential of -63.9 mV (Table 1), the obtained Q_{10}-loaded liposome dispersion was classified according to the Riddick′s classification [28] into dispersions of high physical stability which do not show a potential to aggregate. Hence, the liposome dispersion containing Q_{10} could be considered as a physically and chemically stable dispersion. As to the Q_{10}-content, it was not significantly different from the declared Q_{10}-content of a 0.5% w/w dispersion (Table 1). In order to confirm the liposomes integrity in the liposome gel G1, the gel was analyzed by FFEM. As seen in the FFEM micrograph shown in Fig. 2, the liposomes were identified in the gel structure, indicating their compatibility with carbomer gel.

Table 1. Characteristic parameters of the liposome dispersion (LD), 24 h after preparation.

Sample	Mean size (nm)	PDI	Zeta potential (mV)	pH	Q_{10} content (%, w/w)
LD	125.5±0.2	0.20±0.001	-63.9±0.1	6.47±0.03	0.498±0.003

Characterization of the Q_{10}-loaded liposome gel and liposome-free gel

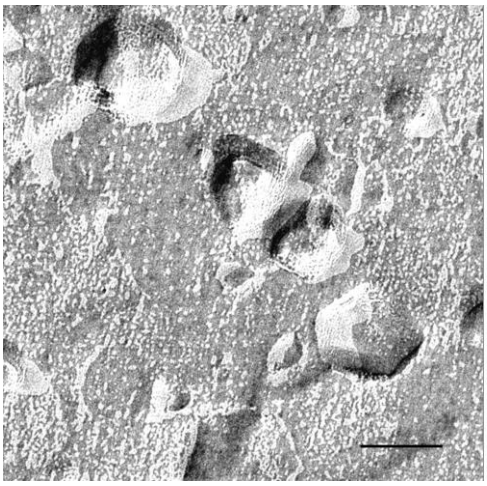

Fig. 2. Identification of liposomes by FFEM in the liposome gel G1 after its preparation (scale bar = 100 nm).

As to the characteristic parameters of the liposome gel (pH value, mean particle size and PDI of liposomes), they increased after the liposome incorporation into the gel (Table 2). As to the particle size and PDI value of liposomes in the gel, they increased compared to values in the liposome dispersion, but not remarkably, indicating compatibility of the liposomes with the carbomer gel. Regarding the pH value, its value of 6.12 for the liposome gel revealed that the gel was suitable for topical application. The same was observed for the liposome-free gel having a pH value of 6.0. The Q_{10}-content in the liposome gel and the liposome-free gel did not vary significantly from the declared Q_{10}-content of a 0.05 % w/w dispersion (Table 2).

Stability evaluation of the Q_{10}-loaded liposome gel and liposome-free gel

Rheological characterization of the gels. The rheological behavior of the gels was studied since it plays an important role in the mixing and flow characteristics of materials, their packaging into containers, physical stability and consumers' acceptability. The flow curves and the rheological parameters of the two examined gels obtained 48 h after their preparation are shown in Figs. 3 and 4 and in Table 3. Both samples showed a non-Newtonian behavior, since their viscosities were not constant, but changed as a function of the shear rate. Both gel formulations showed a shear-thinning behavior according to the Herschel-Bulkley model (excellent fitting $R > 0.999$) with continuously decreasing viscosity, thus indicating successive loss of polymer entanglement upon increasing shear stress [29]. Shear-thinning is a desirable property of semisolid dosage forms, since they should be "thin" during application and "thick" otherwise [30, 31]. The flow curves also showed a plastic behavior of the samples, since they displayed yield values, indicating that the gel network exhibited resistance to an external force before it started flowing [32]. The gel samples showed marginal thixotropy, since most carbomer polymer gels exhibit little or no thixotropy. As to rheological parameters (yield stress, minimal and maximal apparent viscosities), their values for gels examined 48 h after preparation are represented in Table 3. The yield stress can be used to evaluate the quality of a formulation and according to some authors it is the most reliable parameter for describing the stability [33, 34].

Table 2. Characteristic parameters of gel samples G1and G2 (mean size and PDI of liposomes, pH of gels), 48 h after their preparation and after the temperature stress test.

Sample labels	pH value of gels		Mean size of liposomes		PDI of liposomes		Q_{10}-content (%, w/w)	
	48 h	Stress test	48 h	Stress test	48 h	Stress test	48 h	Stress test
G1[a]	6.12±0.00	6.16±0.01	124.8±0.4	128.5±0.2	0.20±0.002	0.24±0.004	0.0496±0.002	0.0471±0.003
G2[b]	6.00±0.03	6.05±0.01	-	-	-	-	0.0499±0.002	0.0444±0.002

[a] G1 gel containing Q_{10}-liposome dispersion; [b]G2 gel containing free Q_{10}

Table 3. Yield stress values, maximal apparent and minimal apparent viscosities of gel samples G1 and G2 (mean, n = 3).

Sample labels	Yield stress value (Pa)		Maximal apparent viscosity (Pa) at 4.08 s^{-1}		Minimal apparent viscosity (Pa) at 200 s^{-1}	
	48 h	Stress test	48 h	Stress test	48 h	Stress test
G1[a]	61±0.8	75±5.8	50.8±1.3	50.3±1.7	2.93±0.08	2.96±0.08
G2[b]	51±5.8	74±4.5	33.6±0.8	36.3±0.3	2.26±0.01	2.38±0.02

[a] G1 gel containing Q_{10}-liposome dispersion; [b]G2 gel containing free Q_{10}

For topical preparations it is desirable to possess the yield stress not only in terms of good stability but also because it describes the flow behavior at small shear rates, i.e. before and after the application. The yield value of the fresh liposome gel G1 was 61 Pa, while for the liposome-free G2 gel it was 51 Pa (Table 3), indicating high stability of both gels, higher for gel G1. As to the minimal and maximal apparent viscosities, they describe different conditions of a structure, i.e. maximal apparent viscosity describes the system structure at rest, while the minimal apparent viscosity represents a measure of destruction of the gel structure. The values of these two parameters for gels G1 and G2 are represented in Table 3. Both gels possessed minimal and maximal apparent viscosities appropriate for semisolids aimed for topical application onto the skin.

Besides performing rheological measurements of the gels after their preparation, also analysis of the gels exposed to a temperature stress test was performed in order to determine the range of conditions under which the product will perform well, i.e. will remain physically stable. On the basis of the flow curves of the gels subjected to the temperature stress tests, which are shown in Figs. 3 and 4, it was concluded that the gels maintained plastic behavior after the temperature stress test, which is appropriate for topical use. In the case of gel G1, the flow curve did not change significantly, while the flow curve of the gel G2 changed when the gel was subjected to the temperature stress test. As to rheological parameters (Table 3), variations were observed in both gels exposed to the temperature stress test. It was evident that the yield stress values of both gels, significantly increased ($p<0.05$) during the temperature stress test. This can be explained by an increasing number of bonds in the polymer network which yields a higher physical stability. Thus, their stability did not decrease due to the temperature changes and based on the data on yield stress obtained by this test a high stability of gels was assumed. Further, the minimal and maximal apparent viscosities of the gel G1 did not change significantly ($p>0.05$) after the temperature stress test compared to their initial values (Table 3). In contrast, in the case of gel G2, the temperature stress test led to a significant increase ($p<0.05$) of the minimal and maximal apparent viscosities. However, the value of minimal apparent viscosity was higher only for 5 %, and the value of maximal apparent viscosity was higher for 8%, compared to their initial values. This increase in viscosity values of gel G2 could be explained by changing, e.g. by strengthening the gel structure due to forming new bonds. However, liposome gel G1 exhibited less extensive changes in rheological parameters and hence in the structure compared to gel G1, when subjected to the stress test. Further, liposome gel G1 possesses higher yield stress after preparation, indicating higher physical stability than the gel G2.

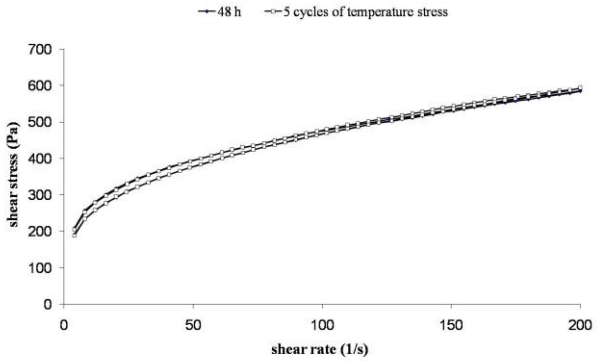

Fig. 3. Flow curves of the gel G1, 48 h after preparation and after the temperature stress test.

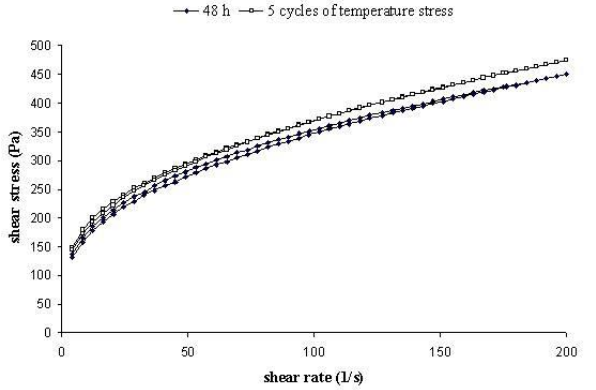

Fig. 4. Flow curves of the gel G2, 48 h after preparation and after the temperature stress test.

On the basis of these results it was concluded that both gel samples remained physically stable after the temperature stress test and that they did not exhibit relevant changes in their rheological properties which could make them unsuitable for topical use onto the skin. As to the liposome gel, the obtained results from rheology measurements revealed that the addition of liposomes into the gel neither decreased the stability of the carbomer gel, nor the stability of liposomes, as shown by PCS (see next section), indicating compatibility of liposomes and carbomer gel.

pH value of gels and mean particle size and PDI of liposomes in liposome gel

The temperature stress test did not lead to a significant ($p>0.05$) change in the pH values of the liposome gel and liposome-free gel (Table 2) and the obtained pH values were appropriate for the application onto the skin. Insignificant pH changes in the samples indicated that total neutralization of

carboxylic groups of polyacrylic acid occurred by the addition of TEA during the preparation of gels, as well as that no chemical changes took place in the samples during the temperature stress test. As to the particle size and PDI of liposomes in the gel after subjecting it to the temperature stress, no significant change ($p>0.05$) was measured. Hence, no aggregation of liposomes in the liposome gel occurred.

Stability of Q_{10} in Q_{10}-loaded liposome gel and liposome-free gel

The Q_{10}–content values of gels obtained after the temperature stress test are shown in Table 2. The statistical analysis revealed that the Q_{10}-content significantly decreased ($p<0.05$) in the gels. The Q_{10}–content in the liposome gel after the temperature stress test was 95% of the initial content, this being a satisfactory result. As to the liposome-free gel, the Q_{10}–content was found to be 89% of the initial content. The higher stability of Q_{10} in the G1 gel in comparison to the G2 could be explained by the greater ability of the liposome gel to protect Q_{10} from degradation, as Q_{10} is incorporated in the liposomes, i.e. in phospholipid bilayers, compared to plain gel without liposomes. Q_{10} showed a significantly higher ($p<0.05$) stability in the liposome gel G1 than in the liposome-free gel G2.

CONCLUSION

This study demonstrated the feasibility of preparing a Q_{10}-loaded liposome dispersion from non-hydrogenated soybean lecithin and a Q_{10}-loaded liposome gel. The incorporation of the Q_{10}-loaded liposome dispersion into the liposome gel did not lead to instability or degradation of liposomes. The obtained liposome gel, being a semisolid formulation, was in contrast to the liquid liposome dispersion, suitable for topical application onto the skin and its rheological properties were appropriate for this kind of application. In order to predict its long-term stability, the liposome gel was subjected to a temperature stress test. The liposome gel maintained a non-Newtonian plastic flow behavior without significant thixotropy after the temperature stress test, and the rheological parameters did not significantly change, indicating its physical stability. In addition, neither the liposome size nor PDI of liposomes changed dramatically in the liposome gel upon subjecting it to extreme storage conditions, confirming the vesicle stability (i.e., no agglomeration or aggregation of liposomes occurred). Furthermore, the Q_{10}-content in the liposome gel changed, but to an acceptable level, keeping in mind the extreme test conditions being used. This result clarified that extreme storage conditions should be avoided. Coenzyme Q_{10} was more stable in the liposome gel than in the liposome-free gel. Thus, the Q_{10}-loaded liposome gel could be considered, according to the results obtained after the temperature stress test, as a physically and chemically stable gel appropriate for topical use.

This liposome gel is aimed to be used as it is or as an enriched formulation with additional cosmetic actives (emollients, moisturizing agents, etc.), which should be investigated in future studies, as a cosmetic anti-ageing preparation. Not only Q_{10}, but also liposomal constituents (phospholipids) are beneficial for skin care. This study showed the feasibility of preparing a Q_{10}-loaded liposome gel serving as a delivery system of Q_{10} to the skin. The next step will be the evaluation of the penetration enhancing ability of this liposome gel, as well as an *in vivo* investigation of its anti-ageing effect.

REFERENCES

1. S. Kumar, R. Rao, A. Kumar, S. Mahant, S. Nanda, *Curr. Drug Deliv.*, **13**, 1184 (2016).
2. S. S. Shapiro, C. Saliou, *Nutrition*, **17**, 839 (2001).
3. R. A. Brunke, *Euro Cosmetics*, **4**, 43 (2002).
4. U. Hoppe, J. Bergemann, W. Diembeck, J. Ennen, S. Gohla, I. Harris, J. Jacob, J. Kielholz, W. Mei, D. Pollet, D. Schachtschabel, G. Sauermann, V. Schreiner, F. Stäb, F. Steckel, *BioFactors*, **9**, 371 (1999).
5. J. Wang, H. Wang, X. Zhou, Z. Tang, G. Liu, Q. Xia, *J. Nanosci. Nanotechnol.*, **12**, 2136 (2012).
6. E. Korkm, E. H. Gokce, O. Ozer, *Acta Pharm*., **63**, 517 (2013).
7. J. C. Schwarz, N. Baisaeng, M. Hoppel, M. Löw, C. M. Keck, C. Valenta, *Int. J. Pharm.*, **447**, 213 (2013).
8. S. Chen, W. Liu, J. Wan, X. Cheng, C. Gu, H. Zhou, S. Chen, X. Zhao, Y. Tang, X. Yang, *Drug Dev. Ind. Pharm.*, **39**, 20 (2013).
9. P. D. Gavin, M. El-Tamimy, H. H. Keah, B. J. Boyd, *Drug Deliv. Transl. Res*., **7**, 53 (2017).
10. G. Cevc, G. Blume, *Biochim. Biophys. Acta*, **1663**, 61 (2004).
11. N. Dragicevic-Curic, D. Scheglmann, V. Albrecht, A. Fahr, *J. Control. Release*, **127**, 59 (2008).
12. T. A. Ahmed, *J. Liposome Res*., **25**, 1 (2015).
13. M. A. Khan, J. Pandit, Y. Sultana, S. Sultana, A. Ali, M. Aqil, M. Chauhan, *Drug Deliv.*, **22**, 795 (2015).
14. A. H. Al Shuwaili, B. K. Rasool, A. A. Abdulrasool, *Eur. J. Pharm. Biopharm*., **102**, 101 (2016).
15. M. Kamran, A. Ahad, M. Aqil, S. S. Imam, Y. Sultana, A. Ali, *Int. J. Pharm*., **505**, 147 (2016).
16. M. Pleguezuelos-Villa, S. Mir-Palomo, O. Díez-Sales, M. A. O. V. Buso, A. R. Sauri, A. Nácher, *Colloids Surf. B Biointerfaces*, **162**, 265 (2017).

17. S. Franzé, A. Marengo, B. Stella, P. Minghetti, S. Arpicco, F. Cilurzo, *Int. J. Pharm.*, **535**, 333 (2018).
18. T. Raschke, J. Eckert, H.-J. Düsing, V. Kallmayer, K.-P. Wittern, *SÖFW-Journal*, **10**, 62 (2003).
19. H.Schreier, J. Bouwstra, *J. Control. Release*, **30**, 1 (1994).
20. K. Thoma, U. E. Jocham, in: Liposome Dermatics, O. Braun-Falco, H. C. Korting, H. I. Maibach (eds.), Springer-Verlag, Berlin, 1992, p. 150.
21. I. Arsic, S. Vidovic, in: Conference Proceedings, Int. Conference of IFSCC, Budapest, 1997, p. 452.
22. G. Blume, in: Conference Proceedings of Cosmetic and Household Ingredients, Warsaw, 1999, p. 34.
23. G. Blume, E. Teichmüller, D. D. Verma, A. Fahr, *Euro Cosmetics*, **11/12**, 28 (2000).
24. J. Kristl, B. Volk, M. Gašperlin, M.Šentjurc, P. Jurkovič, *Eur. J. Pharm. Sci*., **19**, 181 (2003).
25. N. Dragicevic-Curic, S. Winter, D. Krajisnik, M. Stupar, J. Milic, S. Graefe, A. Fahr, *J. Liposome Res.*, **20,** 38 (2010).
26. N. Dragicevic-Curic, S. Winter, M. Stupar, J. Milic, D. Krajisnik, B. Gitter, A. Fahr, *Int. J. Pharm.*, **373**, 77 (2009).
27. S. Frokjaer, E. L. Hjorth, O. Worts, in: Liposome Technology, G. Gregoriadis (ed.), Vol. 1, CRC Press Inc., Boca Raton, Florida, 1984, p. 235.
28. R. H. Müller, in: Zetapotential und Partikelladung in der Laberpraxis, R. H. Müller (ed.), Wissenschaftliche Verlagsgesellschaft mbH, Stuttgart, 1996, p. 19.
29. C. Marriott, in: Aulton's Pharmaceutics: The Design and Manufacture of Medicines, M. E. Aulton, K. M. G. Taylor (eds.), 4th ed., Elsevier Ltd., 2013, p. 94.
30. L. E. Pena, B. L. Lee, J. F. Sterns, *Pharm. Research*, **11**, 875 (1994).
31. A. T. Florence, D. Attwood, Physicochemical principles of pharmacy: in manufacture, formulation, and clinical use, Pharmaceutical Press, London, 2016, p. 313.
32. M. I. Briceno, in: Pharmaceutical Emulsions and Suspensions, F. Nielloud, G. Marti-Mestres (eds.), Marcel Dekker Inc., New York, 2000, p. 557.
33. R. Brummer, Rheology Essentials of Cosmetics and Food Emulsions, Springer-Verlag, Berlin-Heidelberg, 2006.
34. S. Tamburić, D. Q. M. Craig, *Pharm. Sci.*, **1**, 107 (1995).

Bulgarian Chemical Communications, Volume 51, Issue 1, (pp. 125 – 133) 2019

Electrocatalytic oxidation of moxifloxacin hydrochloride on modified glassy carbon surface and determination in Avelox tablets

M. Sadikoglu[1*], U. I. Soylu[2], S. Yilmaz[3], B. Selvi[4], H.Yildiz Seckin[5], A. Nosal-Wiercinska[6]

[1]*Gaziosmanpasa University, Faculty of Education, Department of Science Education, 60240, Tokat, Turkey*
[2]*Gaziosmanpasa University, Faculty of Science and Arts, Department of Chemistry, 60240, Tokat, Turkey*
[3]*Canakkale Onsekiz Mart University, Faculty of Science and Arts, Department of Chemistry, 17020, Canakkale, Turkey*
[4]*Gaziosmanpasa University, Faculty of Science and Arts, Department of Biology, 60240, Tokat, Turkey*
[5]*Gaziosmanpasa University, Faculty of Medicine, Department of Dermatology, 60240, Tokat, Turkey*
[6]*M. Curie-Skłodowska University, Faculty of Chemistry, Department of Analytical Chemistry and Instrumental Analysis, M. Curie-Skłodowska Sq. 3, 20-031 Lublin, Poland*

Received September 12, 2018; Revised January 15, 2019

This work presents an electroanalytical method for the determination of moxifloxacin hydrochloride (MOX) in tablets. The surface of the glassy carbon electrode (GCE) was modified by electrochemical polymerization of 4-aminobenzene sulfonic acid in phosphate buffer solution (pH 7.0).The oxidative behavior of MOX was studied at glassy carbon and modified glassy carbon electrodes in different buffer systems using the cyclic voltammetry technique. The modified glassy carbon electrode (poly(4-ABSA/GCE) has very high catalytic ability for electrooxidation of MOX. Acetate buffer (pH 5.0) was selected as the optimum medium for the oxidation of MOX at poly(4-ABSA/GCE) due to the highest electronic signal increase obtained. Differential pulse voltammetry (DPV) and chronoamperometry (CA) techniques were used for voltammetric determination of MOX. The values of limit of detection (LOD) and limit of quantification (LOQ) were determined to be 3.19×10^{-7}M and 1.06×10^{-6}M for DPV; and 5.50×10^{-7}M and 1.83×10^{-6}M for CA, respectively. A highly sensitive electroanalytical method for the determination of MOX in Avelox tablets by DPV was described.

Keywords: 4-Aminobenzene sulfonic acid, Modified glassy carbon electrode, Electropolymerization, Electrocatalytic ability, Moxifloxacin hydrochloride, Voltammetry

INTRODUCTION

Moxifloxacin hydrochloride {1-cyclopropyl-6-fluoro-1,4-dihydro-8-methoxy-7-[(4aS,7aS)-octahydro-6H-pyrrolo[3,4-b]pyridin-6-yl]-4-oxo-3-quinolinecarboxylic acid, monohydrochloride} (Fig. 1) is a new 8-methoxyquinolone derivative of fluoroquinolones with enhanced activity *in vitro* against gram-positive bacteria and maintenance of activity against gram-negative bacteria [1-3]. MOX has various beneficial effects on human health. The drug, which is used to treat acute bacterial sinusitis, acute bacterial exacerbation of chronic bronchitis and community-acquired pneumonia [3-6], is rapidly absorbed and reaches the maximum concentration values in plasma between 1 and 6 h after oral administration [7].

Several techniques such as HPLC [8], LC-MS/MS [9], sensitive kinetic spectrophotometry [10], liquid chromatography with column switching [11], capillary electrophoresis with laser-induced fluorescence [12] and spectrofluorimetry [13] have been used for the determination of MOX. Furthermore, several electrochemical techniques involving economic, sensitive and rapid methodologies were reported for determination of MOX [13-17].

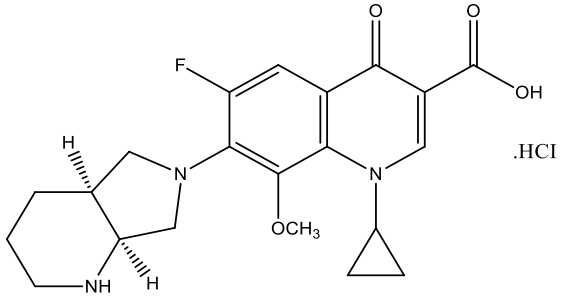

Fig. 1. Structure of moxifloxacin hydrochloride

However, the electrooxidation of MOX at carbon electrodes is kinetically slow. Therefore, the use of modified electrodes is preferred for the oxidation of MOX. Until today, the modified electrodes such as chloranil modified carbon paste electrode [18], molecularly imprinted polymer modified carbon paste electrode [19], and carbon paste modified with silver nanoparticles [20] were used to determine MOX. Furthermore, it is known that poly(4-ABSA/GCE) was used to determine samples such as phenylephrine and chlorprothixene [21], hydroquinone in the presence of catechol and resorcinol [22], uric acid [23], acyclovir [24],

* To whom all correspondence should be sent:
E-mail: murat.sadikoglu@yahoo.com

phenazopyridine hydrocloride [25] and ornidazole [26].

In this work, the surface of the glassy carbon electrode modified by electrochemical polymerization of 4-aminobenzene sulfonic acid (4-ABSA) in PBS buffer solution (pH 7.0) was investigated for determination of MOX by using different voltammetric techniques. Poly(4-ABSA/GCE) shows a high electrocatalytic ability for the oxidation of MOX in the pH range from 2 to 10. The acetate buffer (pH 5.0) was selected as the optimum medium for determination of MOX. Moreover, MOX in Avelox tablets was successfully determined with the modified glassy carbon electrode using a simple, sensitive and rapid method.

EXPERIMENTAL

Instrumentation

A potentiostat meter (VersaSTAT^3, Princeton Applied Research, USA) was used for the voltammetric measurements. All experiments were carried out with a three-electrode system. Glassy carbon electrodes (GCE) (3.0 mm diameter) were purchased from BAS and used as a working electrode. A platinum wire auxiliary electrode and an Ag/AgCl (NaCl 3 M, BAS) reference electrode were used.

All pH measurements were made using an EZDO 5011 model digital pH-meter. The deionized water was obtained from water purified with an aqua MAX^{TM}-Ultra water purification system (young Lin Inst.) 18.2 MΩ cm.

Reagents and materials

MOX and Avelox were supplied from Basel Kimyevi Maddeler ve Ilac. San. Tic. A.S. Istanbul-Turkey. A stock solution of 1.0×10^{-3}M MOX was prepared by dissolving an accurate mass in methanol and was used to prepare the diluted solutions. The working solutions were obtained by dilution of the stock solution with acetate buffer solution (pH 5.0). All solutions were protected from light and were used within 24 h to avoid decomposition. 0.2M acetate buffer (pH 5.0) was selected as the supporting electrolyte solution to investigate the voltammetric behavior of MOX. All other chemical substances were reagent-grade commercial products.

PROCEDURES

Polishing and cleaning of glassy carbon electrode

The GCE was polished successively in 1 μm, 0.3 μm and 0.05 μm alumina slurries on Buehler polishing microcloth. The polished GCE was sonicated in ultrapure water, in a mixture of 1:1 (v/v) nitric acid/water (HNO_3+H_2O) (Fluka) and then in ethanol (Aldrich) for 10 min each. Then, the cleaned GCE was rinsed with water and dried under a stream of argon. The polished and cleaned GCE was used for the derivatization.

Modification of glassy carbon electrode

The surface derivatization of the bare GC electrode was performed in 0.10 M PBS (pH 7.0) containing 2.0×10^{-3} M 4-ABSA. The oxygen in the 4-ABSA solution was removed with argon for at least 10 min before the derivatization. Then, the bare GCE was immersed in the 4-ABSA solution. The GC surface was modified using cyclic voltammetry for five cycles at a scan rate of 100 mV s^{-1} in the potential range from -1.5 to +2.5 V. Finally, the modified electrode was activated by cyclic voltammetry from -1.0 to +1.0 V at a scan rate of 100 mV s^{-1} for ten cycles in 0.10 M PBS (pH 7.0). Bare GC and modified GC electrodes were used as working electrodes.

Calibration graph for quantitative determination

The stock solution of 10^{-3} M MOX was prepared by dissolving an accurate amount of the substance in methanol and diluting with 0.1 M acetate buffer solution (pH 5.0) to obtain different MOX concentrations. The calibration graphs were constructed by using the data recorded under the optimum conditions described in the experimental section. The concentration ranges of the linear calibration curves for DPV and CA techniques are from 1×10^{-6} M to 9×10^{-6} M and from 5×10^{-6} M to 9×10^{-5} M, respectively. The DPV technique, which has lower limits of detection, was used to determine the amount of MOX in tablets.

Procedure for Avelox® tablets

Each Avelox® tablet contains 436.80 mg of moxifloxacin hydrochloride, equivalent to 400.00 mg of moxifloxacin drug and some inactive excipients. One Avelox® tablet, which weighs 0.7069 g, was powdered. The stock solution of 25.8 mg of the powdered drug tablet dosage form was prepared in methanol. The stock solution of 30 μL was transferred to a volumetric flask of 10 mL and then, the volume was diluted to 10 mL with 0.2 M acetate buffer (pH 5.0). The DPV and CV voltammograms of the sample were recorded. The content of the drug in the tablet was determined by using the drawn calibration graph.

RESULTS AND DISCUSSION

Electropolymerization of 4-ABSA on the GCE surface

The cyclic voltammogram of 10 cycles recorded in 0.10 M PBS (pH 7.0) containing 4-ABSA of 2.0×10^{-3} M for electrochemical polymerization of 4-ABSA on the GCE surface are given in Fig. 2. In the first cycle, a weak anodic and a cathodic peak were observed with a peak potential value at E_{pa} = 1.70 V and E_{pc} = -0.60 V, respectively. The two anodic peaks in the second cycle of the voltammogram appeared at peak potential values of +0.13 V and +1.45 V, respectively. The peak current increases in the subsequent cycles. Therefore, it is understood that the surface of GCE is modified with the polymerization film. The modified surface is a blue polymer film [23-26]. Furthermore, the modified GC electrode was activated with the CV voltammogram of 10 cycles at 100 mV s^{-1} scan rate in the potential range from -1.0 V to+1.0 V in 0.1 M phosphate buffer (pH 7.0) medium. After the activation process was completed, the prepared, modified and activated electrode was used for voltammetric studies. The poly(p-ABSA) modified electrode was thoroughly washed with double-distilled water and stored in 0.1 M PBS (pH 7.0) before use.

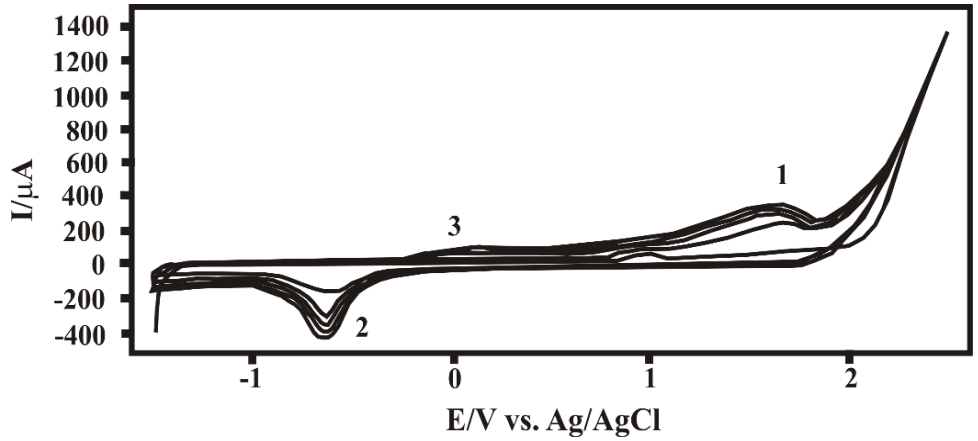

Fig. 2. The cyclic voltammogram of 10 cycles of the solution in 0.10 M PBS (pH 7.0) of 4-ABSA of 2.0×10^{-3} M in the potential range from-1.5 V to +2.4 V (scan rate 100 mV s^{-1}).

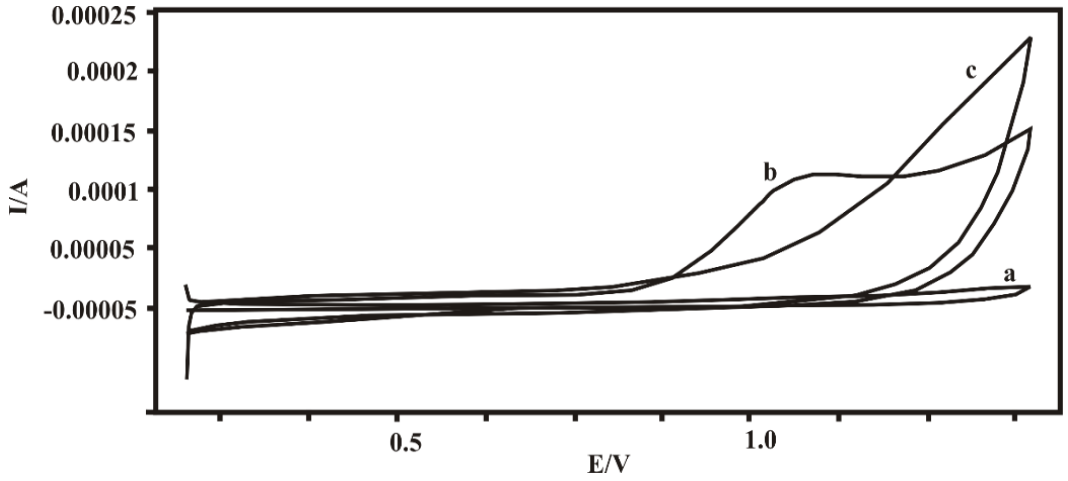

Fig. 3. Cyclic voltammograms of 1×10^{-4} M MOX recorded at the bare GC (a) and poly(4-ABSA/GC) (b) electrodes in 0.2 M acetate buffer (pH 5.0). The voltammogram of 0.2 M acetate buffer (pH 5.0) (c) is the background obtained by using the modified glassy carbon (scan rate: 50 mV s^{-1}).

Electrochemical oxidation of MOX on 4-ABSA modified glassy carbon electrode

The electrochemical responses of MOX on the bare GC and the poly(p-ABSA) modified electrodes were studied by using cyclic voltammetry. The cyclic voltammograms recorded at the GC (a) and poly(4-ABSA/GCE) (b) electrode of 1×10^{-4} M MOX in 0.2 M acetate buffer (pH 5.0) at the scan rate of 50 mV s^{-1} are given in Fig. 3.

At the bare GC electrode, MOX shows a featureless voltammogram (Fig. 3a). When the CV voltammogram of MOX is recorded at the bare GC electrode, the smaller oxidation CV peak was obtained at more negative potential values.

However, if the poly(4-ABSA/GC) electrode is used for the oxidation of MOX, an increase in the peak current was observed and the oxidation peak potential shifted to more positive values. The peak current values of CV voltammograms recorded for the oxidation of MOX at the bare GC and the poly(4-ABSA/GC) electrodes at 50 mV s^{-1} scan rate in 0.2 M acetate buffer (pH 5.0) were 9.691 µA and 112.87 µA, respectively (Figs. 3a and 3b). Consequently, an increase of eleven times in the peak current on the modified electrode surface was obtained. Furthermore, the value of peak potential of the oxidation peak of MOX at modified GC electrode was shifted to smaller positive values. These behaviors were evaluated as evidence that the modified GC electrode exhibits an electrocatalytic effect for the oxidation of MOX.

Effect of pH

The effect of pH on the oxidation of MOX was studied in the range of pH from 2 to 10 by using different buffer solutions. Britten-Robinson (B-R), phosphate and acetate buffers were used to determine the type of support electrolyte and the value of optimum pH. The peak current values of the oxidation peak obtained from the CV voltammograms of the solutions of 1×10^{-4} M MOX diluted with different support electrolytes in the range from pH 2 to 10 are shown in Fig. 4.

As seen in Fig. 4, the oxidation peak current of MOX in 0.2 M acetate buffer reached the maximum value at pH 5.0. At the same time, the anodic peak potential shifts toward less positive values with increasing pH up to 5.0. Therefore, pH 5.0 was selected for further studies.

The nature of the oxidation peak of MOX

Fig. 5 shows the cyclic voltammograms of 0.2M acetate buffer (pH 5.0) containing 1×10^{-4} M MOX on the poly(4-ABSA/GC) electrode surface at the following scan rates: 50, 60, 70, 80, 90, 100, 200, 300, 400 and 500 mV s^{-1} .

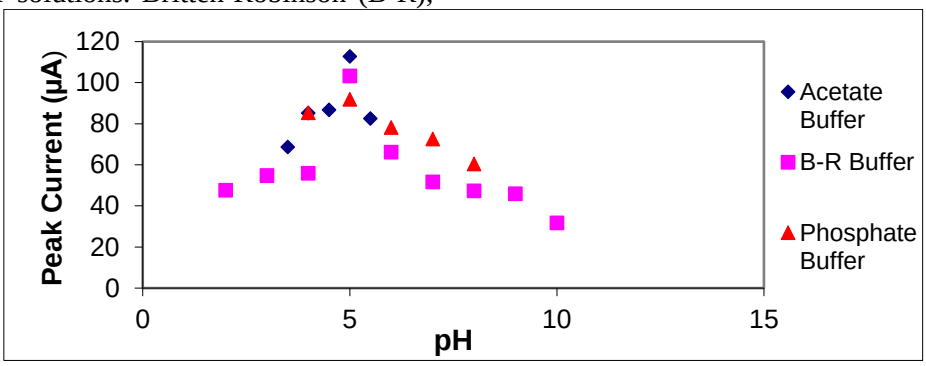

Fig. 4. The oxidation peak current values of 1×10^{-4} M MOX recorded in the range from pH 2.0 to 10.0 in 0.1 M phosphate, 0.04 M B-R and 0.2 M acetate buffers (scan rate: 50 mV s^{-1}).

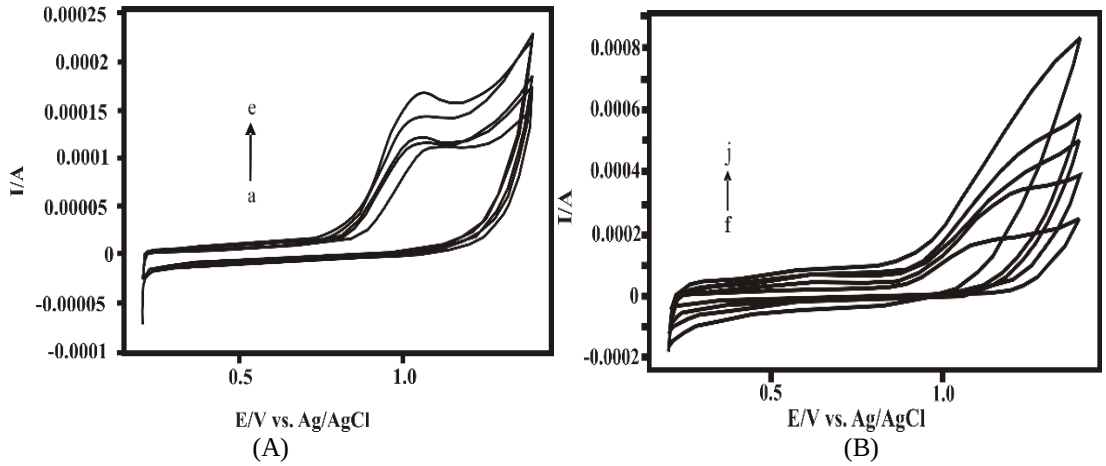

Fig. 5. Cyclic voltammograms recorded at the poly(4-ABSA/GC) electrode in 0.2 M acetate buffer (pH 5.0) containing 1×10^{-4} M MOX (scan rates: **(A)** a) 50, b) 60, c) 70, d) 80, e) 90 and **(B)** f) 100, g) 200, h) 300, i) 400, j) 500 mV s^{-1}).

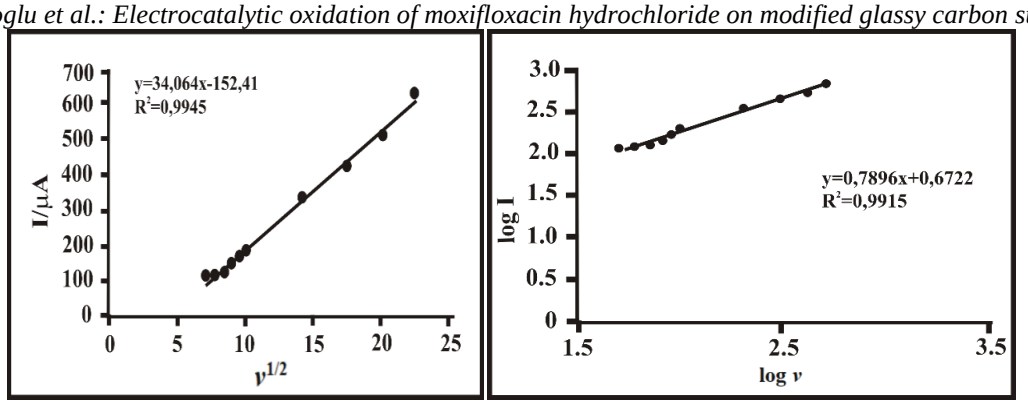

Fig. 6. (A) The peak current values plotted against $v^{1/2}$ and **(B)** the logarithm of peak current (log *I*) against the logarithm of scan rate (log *v*) of the oxidation peak obtained from the CV voltammograms recorded at the poly(4-ABSA/GC) electrode of 1×10^{-4} M MOX in 0.2 M acetate buffer (pH 5.0) (scan rates: a) 50, b) 60, c) 70, d) 80, e) 90, f) 100, g) 200, h) 300, i) 400, j) 500 mV s^{-1}).

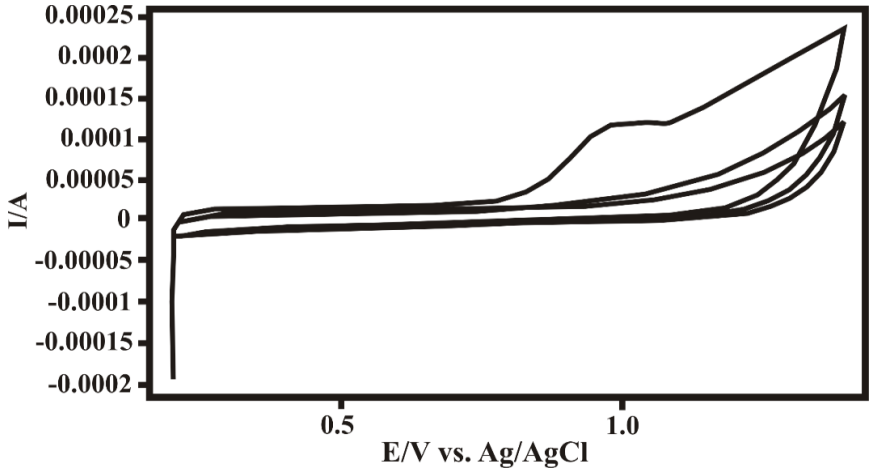

Fig. 7. The cyclic voltammogram of three cycles recorded in the potential range from 0.2 to 1.4 V of 1×10^{-4} M MOX in 0.2 M acetate buffer (pH 5.0) at the poly (4-ABSA/GC) electrode (scan rate: 50 mVs^{-1}).

A good linearity between the square root of scan rate and peak current was obtained in the range of 50-500 mV s^{-1}. The linear regression equation was Ip (μA) = 34.06 $\upsilon^{1/2}$ - 152.4 with correlation coefficient (r) = 0.994. The correlation coefficient is very close to 1.0. Consequently, it is understood that the oxidation process is diffusion-controlled [27].The plot of logarithm of peak current (log *I*) *versus* logarithm of scan rate (log *v*) has a slope of 0.789 which is greater than the theoretical value of 0.75. Since the slope is at about 0.789, it can be considered that the electrochemical oxidation reaction of MOX is diffusion-controlled but adsorption is also effective. Also, the CV voltammogram of three cycles of 1×10^{-4} M MOX in 0.2 M acetate buffer at the poly(4-ABSA/GC) electrode was recorded to evaluate the nature of the oxidation peak of MOX (Fig. 7).

As seen in Fig. 7, the oxidation peak of MOX appeared in the first cycle. However, this peak completely disappeared in the second and third cycles. It is estimated that the oxidation peak disappeared in the second and third cycles due to adsorption on the surface of the modified glassy carbon electrode of the MOX molecules or the ones of the oxidation products. This observation can be considered as another piece of evidence that the electrochemical oxidation reaction of MOX is diffusion-controlled but adsorption is also effective. Therefore, the modified glassy carbon electrodes were only used for one measurement. Consequently, the glassy carbon electrode surface was again cleaned and modified before each new experiment.

Selection of the electroanalytical technique to determine MOX

The DPV and CA techniques were used for the voltammetric determination of MOX. Fig. 8 displays the DPV voltammograms of various concentrations of MOX at the poly(4-ABSA/GC) electrode in 0.2 M acetate buffer (pH 5.0).

A plot of the peak current values as a function of the concentration was drawn. The plot was linear in

the concentration range from 1×10^{-6} to 9×10^{-6} M MOX. For the regression plot of the peak current *versus* MOX concentration, the slope was 1×10^{7} μAM^{-1}, the intercept was 159.6 μA and the correlation coefficient was $R^2 = 0.993$ (Fig. 9). Limit of detection (LOD) and limit of quantification (LOQ) values were calculated using the following equation [27]:

$$LOD = 3\ s/m,\ LOQ = 10\ s/m$$

where, s is the standard deviation of the peak current (for five runs) and m is the slope of the calibration curve. To determine LOD and LOQ values, the standard deviation of peak currents for five measurements recorded at 3×10^{-6} M, which is the concentration above the lowest concentration in the calibration graph, was determined to be 1.063. The LOD and LOQ were 3.189×10^{-7} M and 1.063×10^{-6} M, respectively, achieved at the poly(4-ABSA/GC) electrode.

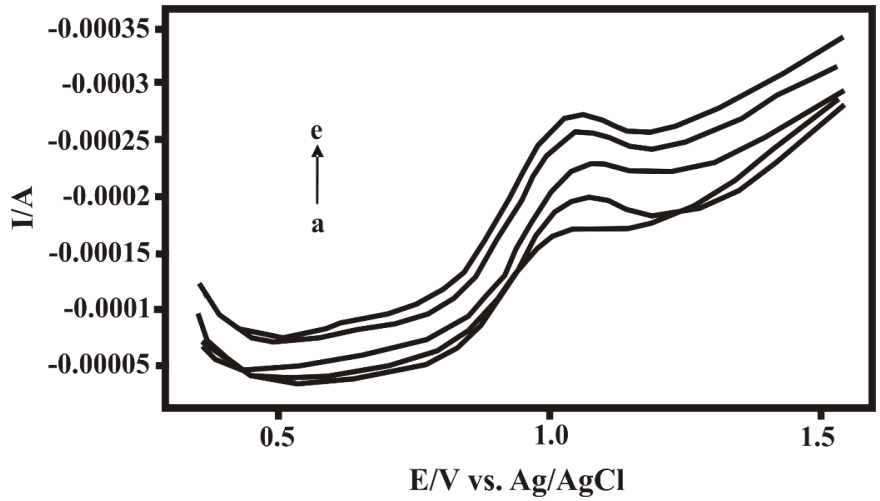

Fig. 8. DPV voltammograms for increasing concentrations of MOX: a) 1×10^{-6}, b) 3×10^{-6}, c) 5×10^{-6}, d) 7×10^{-6} and e) 9×10^{-6} M in the potential range from 0.2 V to 1.4 Vin 0.2 M acetate buffer (pH 5.0) on the poly(4-ABSA/GC) electrode surface.

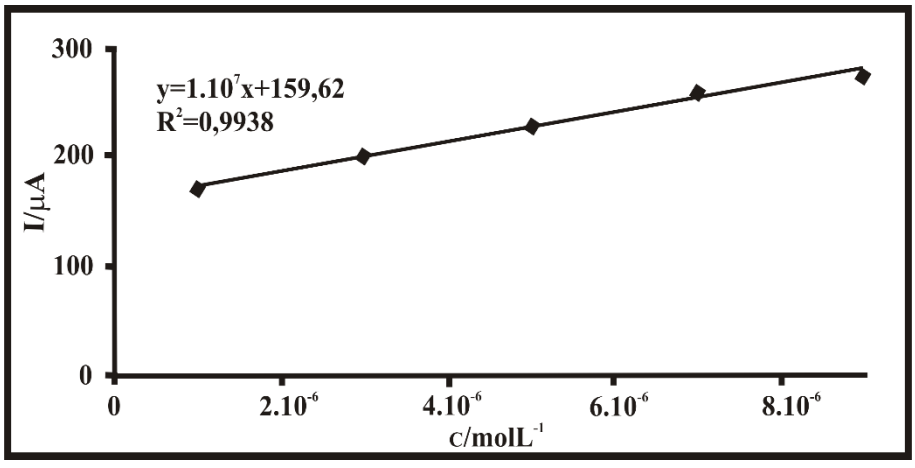

Fig. 9. Calibration plot for increasing concentrations of MOX obtained from DPV voltammograms.

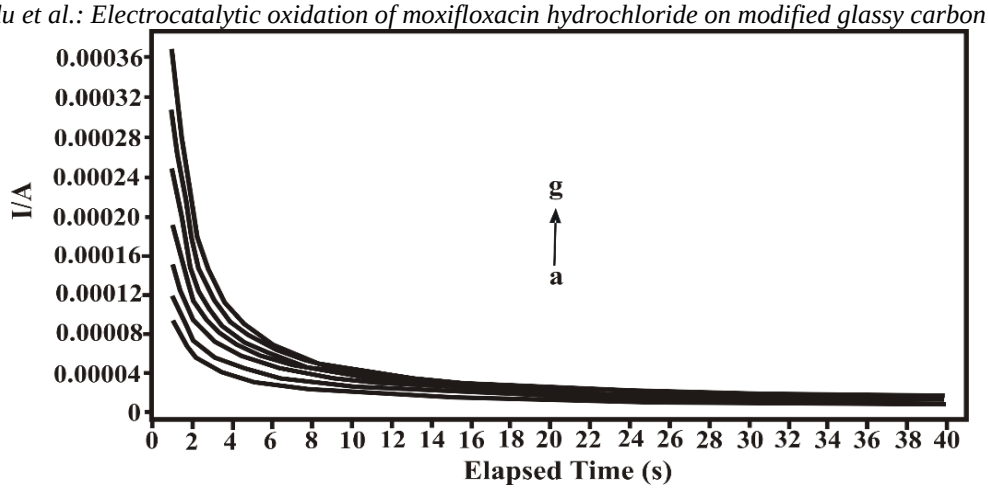

Fig. 10. Chronoamperometric response of the poly(4-ABSA/GC) electrode for increasing concentrations of MOX solutions of: a) 5×10^{-6} M, b) 9×10^{-6} M, c) 1×10^{-5} M, d) 3×10^{-5} M, e) 5×10^{-5} M, f) 7×10^{-5} M, g) 9×10^{-5} M in 0.2 M acetate buffer (pH 5.0) containing different concentrations of MOX for a potential step of 1.15 V *vs*. reference electrode. Variation of chronoamperometric currents at t= 40 s *vs*. concentration of MOX.

Also, the electrocatalytic oxidation of MOX at the poly(4-ABSA/GC) electrode was studied with the CA technique. The chronoamperograms obtained for a series of MOX solutions with various concentrations are illustrated in Fig. 10. An increase in concentration of MOX was accompanied by an increase in anodic currents obtained for a potential step of 1.15 V *versus* reference electrode.

The current values recorded from the chronoamperograms obtained for a series of MOX solutions were used to draw the calibration plot (Fig. 11).

The plot drawn with current values obtained from chronoamperometric response was linear in the concentration range from 5×10^{-6} to 9×10^{-5} M MOX. The LOD and LOQ values obtained from this calibration plot are 5.50×10^{-7} and 1.83×10^{-6} M, respectively.

When compared with the DPV and CA techniques used to determine the amount of MOX, it is understood that the detection limits obtained using the DPV technique have smaller values. Therefore, the DPV technique is preferred for determination of MOX.

Determination of MOX in pharmaceutical preparations

To determine the amount of MOX in the 400 mg Avelox tablets, a drug tablet of 0.7069 g was taken and powdered. A solution of 10 mL of 25.8 mg of the drug in powdered form was prepared in methanol. A volume of 30 μL of the stock solution was diluted to 10 mL with 0.2 M acetate buffer (pH 5.0). The DPV voltammogram of the drug tablet dosage form containing MOX is shown in Fig. 12.

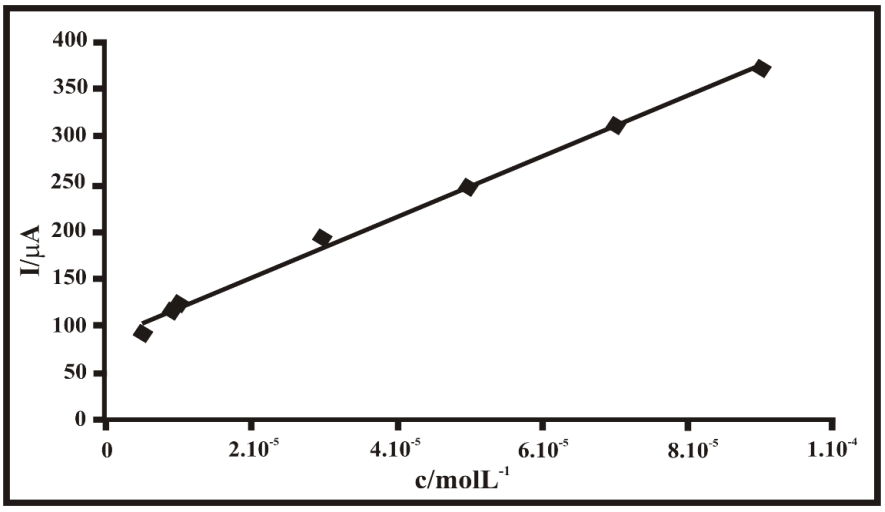

Fig. 11. Calibration plot obtained from chronoamperograms of MOX in 0.2 M acetate buffer (pH 5.0).

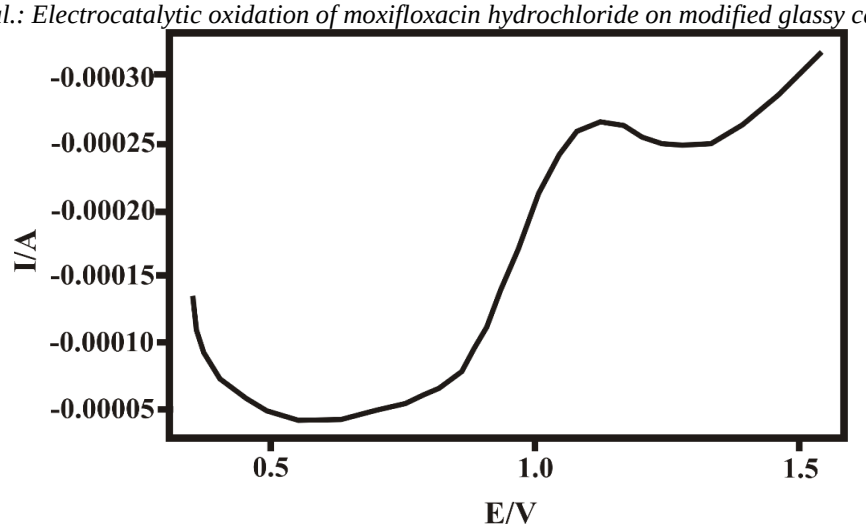

Fig. 12. The DPV voltammogram of the drug tablet sample containing MOX in 0.2 M acetate buffer in the potential range from 0.2 V to 1.4 V at poly(4-ABSA/GC) electrode.

Table 1. Application of the DPV technique for the assay of MOX in pharmaceutical preparations

Parameters	Results
Labeled MOX, mg	436.8
Amount found, mg	428.2
Number of measurements, N	5
Relative standard deviation (*RSD*), %)	0.280
Bias, %	1.96

As seen in Fig. 12, when the DPV voltammogram of the drug tablet sample containing MOX is examined, its characteristic oxidation peak is found to be at about 1.12 V and the peak current is 266.71 μA. Consequently, it is understood that there is no interference on the oxidation of moxifloxacin HCl in the drug tablet form at the poly (4-ABSA/ GC) electrode.

The amount of MOX in Avelox commercial tablets was calculated by reference to the appropriate calibration plots. The results obtained are given in Table 1.

The drug dosage form contains microcrystalline cellulose, sodium croscarmellose, lactose monohydrate, magnesium stearate, red iron (III) oxide, HPM cellulose 15 cp, polyethylene glycol 4000 and titanium dioxide as auxiliary substances together with MOX.

The amount of MOX in the sample was calculated by using the equation y=1×107x+159.62, obtained from the calibration graph of the DPV technique.

.

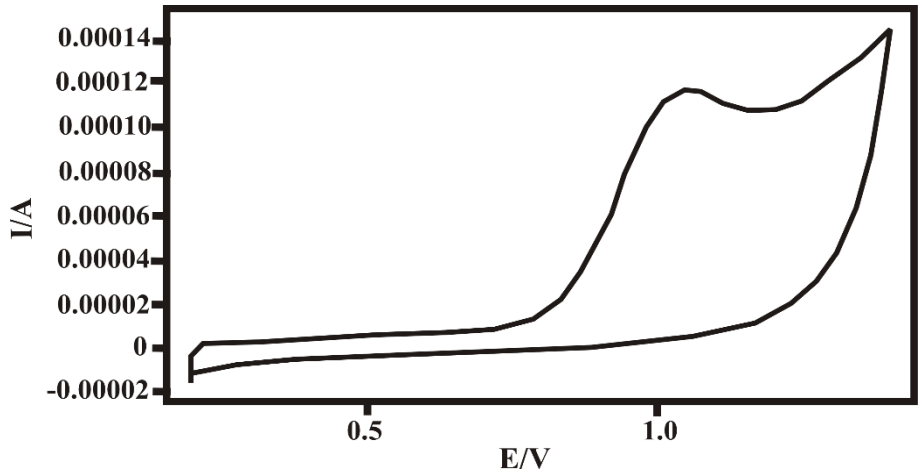

Fig. 13. The CV voltammogram of the drug tablet dosage form a sample containing MOX in 0.2 M acetate buffer in the potential range from 0.2 V to 1.4 V at poly(4-ABSA/GC) electrode.

According to the calculations made for the sample of 25.8 mg, the drug tablet contains MOX at the rate of 60.58% (w/w).

Also, the CV technique was used to reveal that there was no interference on the oxidation of MOX in the drug tablet dosage form. The CV voltammogram of the sample is shown in Fig. 13. As can be seen in Fig. 13, when the CV voltammogram of the sample is recorded, the oxidation peak of M OX is at about 1.05 V. There is no shift in the peak potential value. In addition, there is no change in the shape of the oxidation peak. Therefore, according to the CV voltammogram, it is understood that there is no interference. Consequently, the poly(4-ABSA/GC) electrode can be used for the selective and sensitive determination of the amount of MOX in tablet dosage forms.

CONCLUSIONS

Glassy carbon electrode coated with poly (4-aminobenzene sulfonic acid) film was used for electrocatalytic determination of MOX. The modified glassy carbon electrode showed good electrocatalytic activity for the oxidation of MOX. The modified electrode provides higher sensitivity and selectivity in the determination of MOX.

Differential pulse voltammetry technique can be used to the determination of MOX in the drug tablet form at the optimum conditions of GCE modified with 4-ABSA as the working electrode and 0.2 M acetate buffer (pH=5.0) as the supporting electrolyte.

***Acknowledgement**: This work was supported by Gaziosmanpasa University Scientific Research Fund with grant number 2016/76.*

REFERENCES

1. D.J. Biedenbach, M.S. Barrett, M.A.T. Croco, R.N. Jones, *Diagn. Microbiol. Infect. Dis.*, **32**, 45 (1998).
2. K. Vishwanathan, M.G. Bartlett, J.T. Stewart, *J. Pharm. Biomed. Anal.*, **30**, 961 (2002).
3. M. Donati, M.R. Fermepin, A. Olmo D'Apote, R. Cevenini, *J. Antimicrob. Chemother.*, **43**, 825 (1999).
4. T. Luxameecchanporn, C. Blair, V. Kirtsreesakul, K. Thompson, R. M. Naclerio, *Int. J. Infect. Dis.*, **10**, 401 (2006).
5. M. Miravitlles, *Int. J. Chron. Obstruct. Pulmon Dis.*, **2**, 191 (2007).
6. A.Torres, J-F.Muir, P.Corris, R.Kubin, I.Duprat-Lomon, P-P.Sagnier, G.Höffken, *Eur. Respir. J.*, **21**, 135 (2003).
7. G. Kampougeris, A. Antoniadou, E. Kavouklis, Z. Chryssouli, H. Giamarellou, *British J. Ophth.*, **89**, 628 (2005).
8. S.N. Razzaq, M. Ashfaq, I.U. Khan, I. Mariam, S. S. Razzaq, W. Azeem, *Arabian J. Chem.*, **10**, 321 (2017).
9. D.H. Vu, R.A. Koster, J.W.C. Alffenaar, J.R.B.J. Brouwers, D.R.A. Uges, *J. Chromatogr. B*, **879**, 1063 (2011).
10. S. Ashour, R. Bayram, *Spectrochim. Acta A*, **140**, 216 (2015).
11. H.A. Nguyen, J. Grellet, B.B. Ba, C. Quentin, M.-C. Saux, *J. Chromatogr. B*, **810**, 77 (2004).
12. J.-G. Möller, H. Staß, R. Heinig, G. Blaschke, *J. Chromatogr. B*, **716**, 325 (1998).
13. M. Kamruzzaman, A.-M. Alam, S.H. Lee, D. Ragupathy, Y.H. Kim, S.-R. Park, S.H. Kim, *Spectrochim. Acta* A, **86**, 375 (2012).
14. M.A.G. Trindade, G.M. Silva, V.S. Ferreira, *Microchem. Journal*, **81**, 209 (2005).
15. A-E. Radi, T. Wahdan, Z. Anwar, H. Mostafa, Drug Test, *Analysis*, **2**, 397 (2010).
16. N. Erk, *Anal. Bioanal. Chem.*, **378**, 1351 (2004).
17. M.A.G. Trindade, P.A.C. Cunha, T.A. Araújo, G.M. Silva, V. S. Ferreira, *Ecl. Quím*., **31**, 31 (2006).
18. A.K. Attia, M.A.E. Shal, *Anal. Bioanal. Electrochem.*, **4**, 213 (2012).
19. Q. Zhou, N. Long, L. Liu, H. Zhai, M. Zhu,*Int. J. Electrochem. Sci.*, **10**, 5069 (2015).
20. 20.A. M. Fekry, *Biosensors and Bioelectronics*, **87**,1065 (2017).
21. F. Huang, G. Jin, Y. Liu, J. Kong, *Talanta*, **74**, 1435 (2008).
22. Z. Yang, G. Hu, Y. Liu, J. Zhao, G. Zhao, *Canadian J. Anal. Sci. Spectrosc*., **52**,11 (2006).
23. M. Sadikoglu, G. Taskin, F. G. Demirtas, B. Selvi, M. Barut, *Int. J. Electrochem. Sci*., **7**, 11550 (2012).
24. S. Can, S. Yilmaz, G. Saglikoglu, M. Sadikoglu, N. Menek, *Electroanalysis*, **27**, 2431 (2015).
25. C. Demirtas, S. Yilmaz, G. Saglikoglu, M. Sadikoglu,*Int. J.Electrochem. Sci*.,**10**, 1883 (2015)
26. G. Saglikoglu, S. Yilmaz, *Curr. Anal.Chem*., **26**, 457 (2014).
27. M. Sadikoglu, S. Yilmaz, I. Kurt, B. Selvi, H. Sari, N. Erduran, E. Usta, G. Sağlikoglu, *Russian J. Electrochem.*, **52,** 603 (2016).

Bulgarian Chemical Communications, Volume 51, Issue 1 (pp. 134-145)

On the esterification reaction of phenacyl bromide with benzoic acids: microwave and ultrasound versus conventional heating

T. Erdogan*

Kocaeli University, Department of Chemistry and Chemical Processing Technologies, Kocaeli Vocational School, Kocaeli, Turkey

Submitted January 21, 2018; Revised February 1, 2019

In this study it was aimed to develop new experimental methods for the esterification reaction of phenacyl bromide with benzoic acids. For this purpose; ultrasound and microwave energy were used and the results showed that both sonication and microwave irradiation increase the effectiveness of the investigated esterification reaction. In the second part of the study, some DFT calculations with B3LYP method were performed and computational results were compared with the experimentally obtained data. All DFT calculations were performed at DFT B3LYP level of theory using 6-31G(d), 6-31G(d,p), 6-311G(d,p) and 6-311+G(2d,p) basis sets. NMR calculations were carried out using both CSGT and GIAO methods. MEP maps, FMOs, and Mulliken atomic charges were computationally determined with the same basis sets.

Keywords: Esterification, phenacyl benzoates, microwave chemistry, sonochemistry, computational chemistry

INTRODUCTION

Esterification reaction is one of the most fundamental reactions in organic chemistry and widely used in various areas such as pharmacology, polymer technology, flavor and fragrance industry etc. [1]. The literature contains various well-known esterification methods for the synthesis of various esters including phenacyl benzoates. Phenacyl benzoates can be synthesized via the reaction of phenacyl bromides and benzoic acids. Although, literature contains various methods for the reaction of phenacyl bromide with benzoic acid or terephthalaldehydic acid, these methods generally requires heating and/or long reaction times, so, it needs to be developed more effective and rapid methods. The extant literature contains several reports for the reaction of phenacyl bromide with benzoic acid [1-14] and for the reaction of phenacyl bromide with terephthalaldehydic acid [15] but none of these methods includes ultrasound or microwave energy. On the other hand, literature contains several reports on the microwave-assisted reaction of phenacyl bromide or substituted phenacyl bromides with substituted benzoic acids [16-19], however there is not an ultrasound-assisted method for these reactions, too.

In this study, it was postulated that the reaction between phenacyl bromide and benzoic acids could be accomplished in an efficient way by using ultrasound or microwave irradiation. In the present study, experimental studies have been focused on two different methods; one of them is ultrasound, and the other one is microwave-assisted method. To the best of our knowledge, for the reactions of phenacyl bromide with benzoic acid and terephthalaldehydic acid, there is no study in the literature in which ultrasound and/or microwave energy were used. In these methods; phenacyl bromide **(2)** was reacted with benzoic acid **(3a)** and terephthalaldehydic acid **(3b)** under sonication or under microwave irradiation in the presence of sodium carbonate. The results show that both methods allow the investigated esterification reaction in good yields. Yields for the reactions are approximately 90% for benzoic acid and 80% for terephthalaldehydic acid. The reaction pathway is given in Fig. 1.

In the microwave-assisted method, 175 W of microwave energy was applied. It was observed that increasing microwave energy increases the reaction yield but 175 W is the maximum applicable microwave energy due to a sudden increase in boiling rate of the solvent system. On the other hand, the optimum reaction time was found to be 15 minutes. The reaction yield increases by increasing reaction time gradually but over 15 minutes there is not a considerable increase in the reaction yield. In the ultrasound-assisted method, it takes 30 minutes to consume all the reactants at 70°C. In these reaction conditions, the reaction yields of both methods are identical but the microwave-assisted method is faster than the ultrasound-assisted method. The results show that both of these methods are good alternatives to conventional heating because of the dramatically decreased reaction times. The methods in which conventional heating is used, it takes minimum 2 hours of refluxing to complete the

* To whom all correspondence should be sent
E-mail: taner.erdogan@kocaeli.edu.tr:

reaction. In the synthesis of phenacyl bromide **(2)** from acetophenone **(1)**, a modified form of a literature procedure [20] was used.

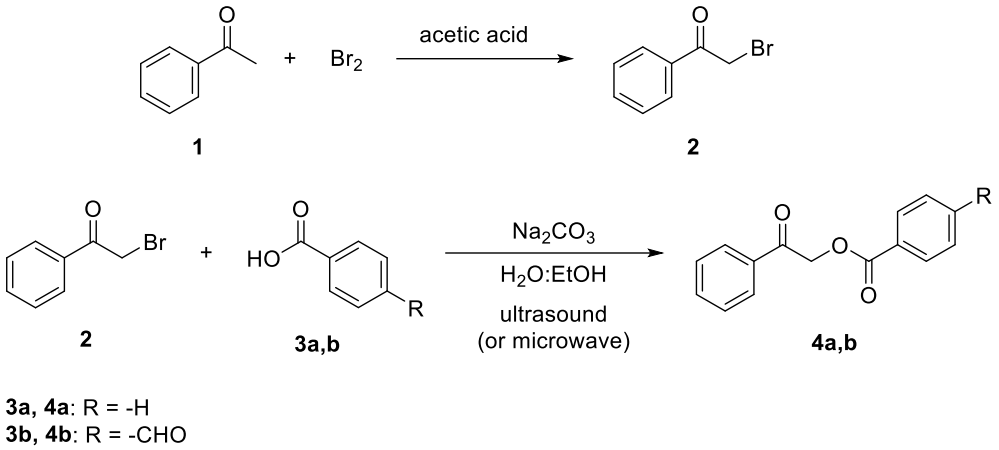

Fig. 1. Reaction pathway.

In the second part of the study, some DFT (Density Functional Theory) calculations have been performed on the investigated compounds and a comparison between experimental and computationally obtained data have been made. Geometry optimizations, frequency analysis and NMR calculations were carried out at B3LYP (Becke three-parameter hybrid functional combined with Lee-Yang-Parr correlation functional) level of theory using 6-31G(d), 6-31G(d,p), 6-311G(d,p), 6-311+G(2d,p) basis sets. In NMR calculations both GIAO (Gauge-Independent Atomic Orbital) and CSGT (Continuous Set of Gauge Transformations) methods were used. All computations have been performed using Gaussian 09. Revision D.01 [21] and Avogadro 1.1.1 [22] Program Packages, and GaussView5 [23] was used for the visualization of the computational results.

EXPERIMENTAL

Ultrasound-assisted reactions were carried out using Bandelin Sonorex ultrasonic bath. Microwave synthesis were carried out on CEM Discover SP Microwave System. NMR spectra were taken on Agilent Mercury 400. Melting points were determined using Barnstead Electrothermal 9100 melting point apparatus.

Synthesis of phenacyl bromide (2)

In the synthesis of phenacyl bromide; to an ice-cold solution of acetophenone (0.20 mol, 24 g) in acetic acid (100 mL), bromine (0.22 mol, 11.3 mL) was added dropwise in 30 minutes. The reaction mixture was stirred for additional 3 hours at room temperature then poured into crushed ice-water and formed solids were collected by filtration and recrystallized from ethanol.

Esterification reaction

Method A. Benzoic acid/terephthalaldehydic acid (5 mmol) and Na_2CO_3 (2.5 mmol, 0.265 g) were dissolved in water (5 mL), then phenacyl bromide (5 mmol, 1 g) and ethanol (10 mL) were added and the reaction mixture was placed in the ultrasonic bath and sonicated for 30 minutes at 70°C. After 30 minutes of sonication, reaction mixture was allowed to cool and formed solids were collected by filtration and recrystallized from ethanol.

Method B. Benzoic acid/terephthalaldehydic acid (5 mmol) and Na_2CO_3 (2.5 mmol, 0.265 g) were dissolved in water (5 mL), then phenacyl bromide (5 mmol, 1 g) and ethanol (10 mL) were added and the reaction mixture was placed in the microwave system and irradiated with 175 W of MW energy for 15 minutes. After 15 minutes of irradiation, reaction mixture was allowed to cool and formed solids were collected by filtration and recrystallized from ethanol.

2-oxo-2-phenylethyl benzoate (4a)

White solid, T_{mp} 113-115°C; ^{1}H NMR, δ, ppm: 5.58 s (2H, OC$\underline{H}_2$CO), 7.54-7.44 m (4H, Ar$\underline{H}$), 7.65-7.57 m (2H, Ar$\underline{H}$), 7.97 d (2H, Ar$\underline{H}$, *J* 7.6 Hz), 8.15 d (2H, Ar$\underline{H}$, *J* 7.6 Hz); [Lit. [2], ^{1}H NMR, δ, ppm: 5.61 s (2H, OC$\underline{H}_2$CO), 7.48-7.56 m (4H, Ar$\underline{H}$), 7.60-7.67 m (2H, Ar$\underline{H}$), 7.99-8.01 m (2H, Ar$\underline{H}$), 8.16-8.19 m (2H, Ar$\underline{H}$).

2-oxo-2-phenylethyl 2-phenylacetate (4b)

Light yellow solid, T_{mp} 108-110°C; ^{1}H NMR, δ, ppm: 5.62 s (2H, OC$\underline{H}_2$CO), 7.48-7.54 m (2H, Ar$\underline{H}$), 7.60-7.64 m (1H, Ar$\underline{H}$), 7.94-8.00 m (4H, Ar$\underline{H}$), 8.30 d (2H, Ar$\underline{H}$, *J* 8.4 Hz), 10.12 s (1H, C$\underline{H}$O); [Lit. [15], T_{mp} 106-109°C) ^{1}H NMR δ, ppm: 5.6 s (2H, OC$\underline{H}_2$CO), 8.05 m (9H, Ar$\underline{H}$), 10.08 s (1H, C$\underline{H}$O).

THEORETICAL CALCULATIONS

Single point energies for optimized structures

Single Point Energy (SPE) is the sum of nuclear repulsion energy and the electronic energy of the molecule at the specified nuclear configuration. A single point energy calculation is a prediction of the energy and related properties for a molecule with a specified geometric structure. [25] SPEs were determined for the optimized structures at DFT B3LYP level of theory using 6-31G(d), 6-31G(d,p), 6-311G(d,p) and 6-311+G(2d,p) basis sets. Energies for **1**, **2**, **3a**, **3b**, **4a** and **4b** are given in Table 1.

Table 1. Calculated single point energies of the compounds.

Compound	opt1[a] (eV)	opt2[b] (eV)	opt3[c] (eV)	opt4[d] (eV)
1	-10473.56	-10473.89	-10476.27	-10476.71
2	-80436.76	-80437.06	-80505.83	-80506.15
3a	-11451.16	-11451.52	-11454.35	-11454.88
3b	-14534.82	-14535.18	-14538.83	-14539.52
4a	-21891.77	-21892.28	-21897.36	-21898.28
4b	-24975.45	-24975.95	-24981.85	-24982.94

[a] B3LYP/6-31G(d) [b] B3LYP/6-31G(d,p) [c] B3LYP/6-311G(d,p) [d] B3LYP/6-311+G(2d,p)

Optimized structure analysis

Optimized structures and geometric parameters were determined computationally at DFT B3LYP level of theory using 6-31G(d), 6-31G(d,p), 6-311G(d,p) and 6-311+G(2d,p) basis sets. Optimized structures of **4a** and **4b**, calculated with 6-311+G(2d,p) basis set, are given in Fig. 2 and Fig. 3, respectively. Tables 2, 3 and 4 represent selected bond lengths and bond angles of **4a** and **4b** calculated at B3LYP/6-311+G(2d,p) level of theory and the experimental values. The experimental values have been obtained from the literature. [26] Except for some certain bonds and bond angles, it can be seen that the errors are less than 1% for bond lengths and less than 5‰ for bond angles. It was also observed that larger basis sets estimate the bond lengths and bond angles more accurately.

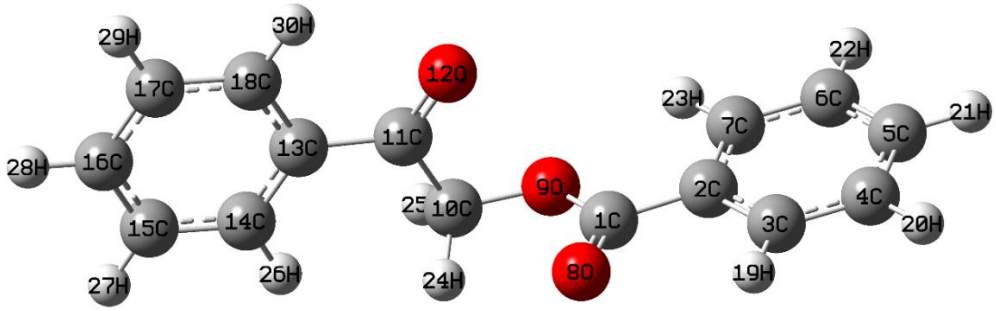

Fig. 2. Optimized structure of **4a**

Table 2. Selected experimental and calculated bond lengths for **4a**.

Atoms	Bond Length (Exp.[a]) [Å]	Bond Length (Calc.[b]) [Å]
13C-11C	1.481	1.495
11C-12O	1.205	1.210
11C-10O	1.481	1.532
10C-9O	1.441	1.420
9O-1C	1.357	1.358
1C-8O	1.197	1.207
1C-2C	1.482	1.487

[a] Lit. [26]
[b] B3LYP/6-311+G(2d,p)

Table 3. Selected experimental and calculated bond angles for **4a**.

Atoms	Bond Angle (Exp.[a]) [°]	Bond Angle (Calc.[b]) [°]
13C-11C-12O	122.2	122.0
13C-11C-10C	118.0	117.7
12O-11C-10C	119.7	120.3
11C-10C-9O	112.4	111.4
10C-9O-1C	114.6	116.0
9O-1C-8O	122.5	122.9
8O-1C-2C	124.3	124.7

[a] Lit. [26]
[b] B3LYP/6-311+G(2d,p)

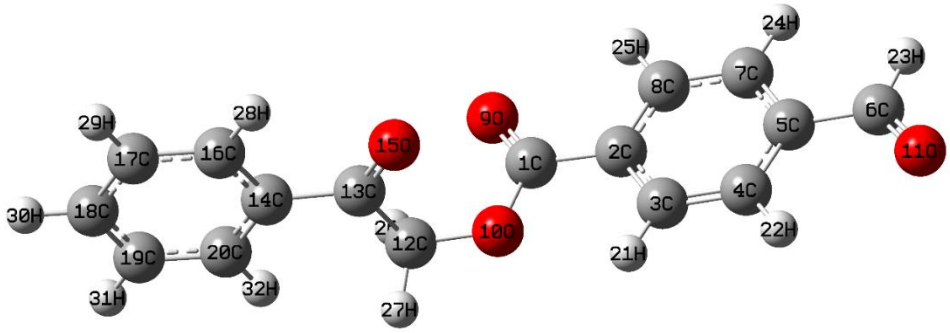

Fig. 3. Optimized structure of **4b.**

Table 4. Selected geometric parameters for **4b**.

Atoms	Bond Length [Å][a]	Atoms	Bond Angle [Å][a]
13C-15O	1.210	2C-1C-9O	124.3
13C-14C	1.493	2C-1C-10O	112.3
12C-13C	1.533	9O-1C-10O	123.3
10O-12C	1.422	1C-10O-12C	116.0
10O-1C	1.354	10O-12C-13C	111.3
1C-9O	1.207	12C-13C-15O	120.2
1C-2C	1.491	12C-13C-14C	117.7
		15O-13C-14C	122.1

[a] B3LYP/6-311+G(2d,p)

Frequency analysis

Frequency analysis were also carried out at DFT B3LYP level of theory using 6-31G(d), 6-31G(d,p), 6-311G(d,p) and 6-311+G(2d,p) basis sets. Experimental and calculated infrared spectra of **4a** and **4b** are given in Figs. 4 and 5, respectively. For the calculated infrared spectra a scale factor (0.9680) was applied. It was also observed that larger basis sets estimate IR spectra of the investigated molecules more accurately.

NMR spectral analysis

Nuclear magnetic shield tensors were computationally determined at DFT B3LYP level of theory using 6-31G(d), 6-31G(d,p), 6-311G(d,p) and 6-311+G(2d,p) basis sets with GIAO (Gauge-Independent Atomic Orbital) and CSGT (Continuous Set of Gauge Transformations) methods. Calculated and experimental ^{1}H NMR data of **4a** and **4b** are given in Tables 5, 6, 7 and 8. It can be seen that the best results were obtained at GIAO 6-31G(d,p) and CSGT 6-311+G(2d,p) levels. It was also observed that in the CSGT type NMR calculations, larger basis sets estimate the chemical

shifts more accurately, on the other hand in the GIAO type NMR calculations, larger basis sets overestimate the chemical shifts.

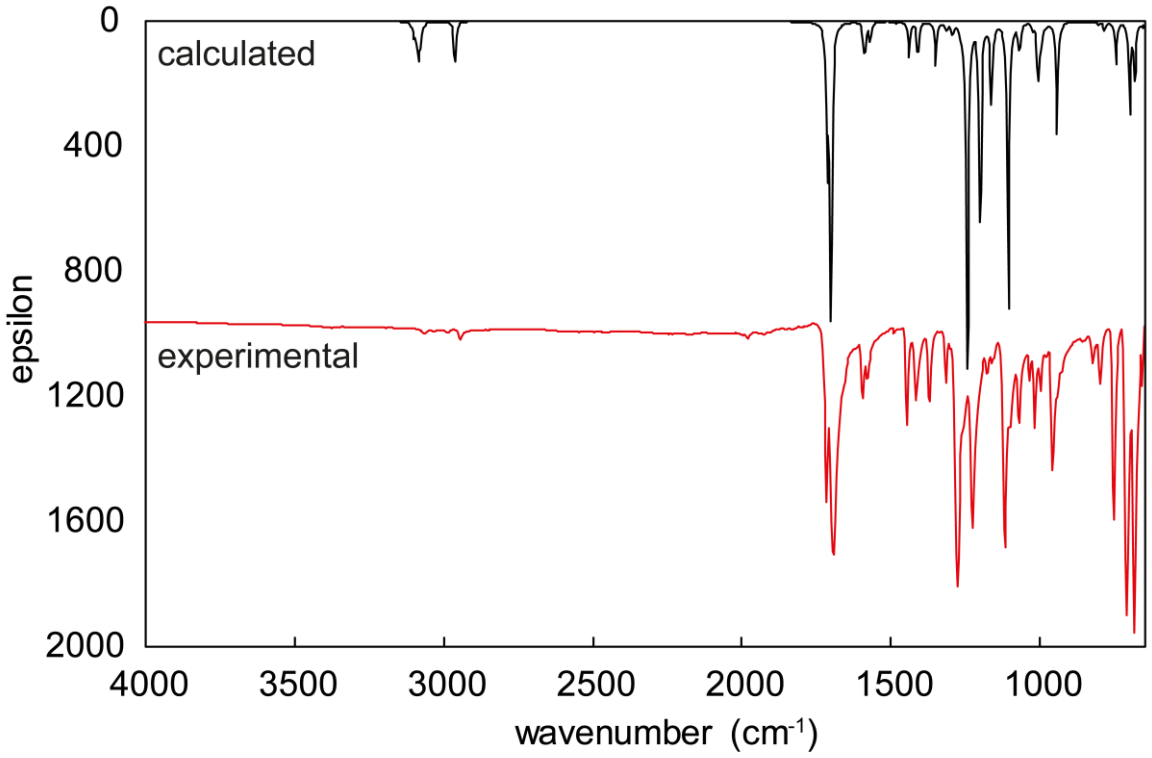

Fig. 4. Experimental and calculated infrared spectra of **4a**

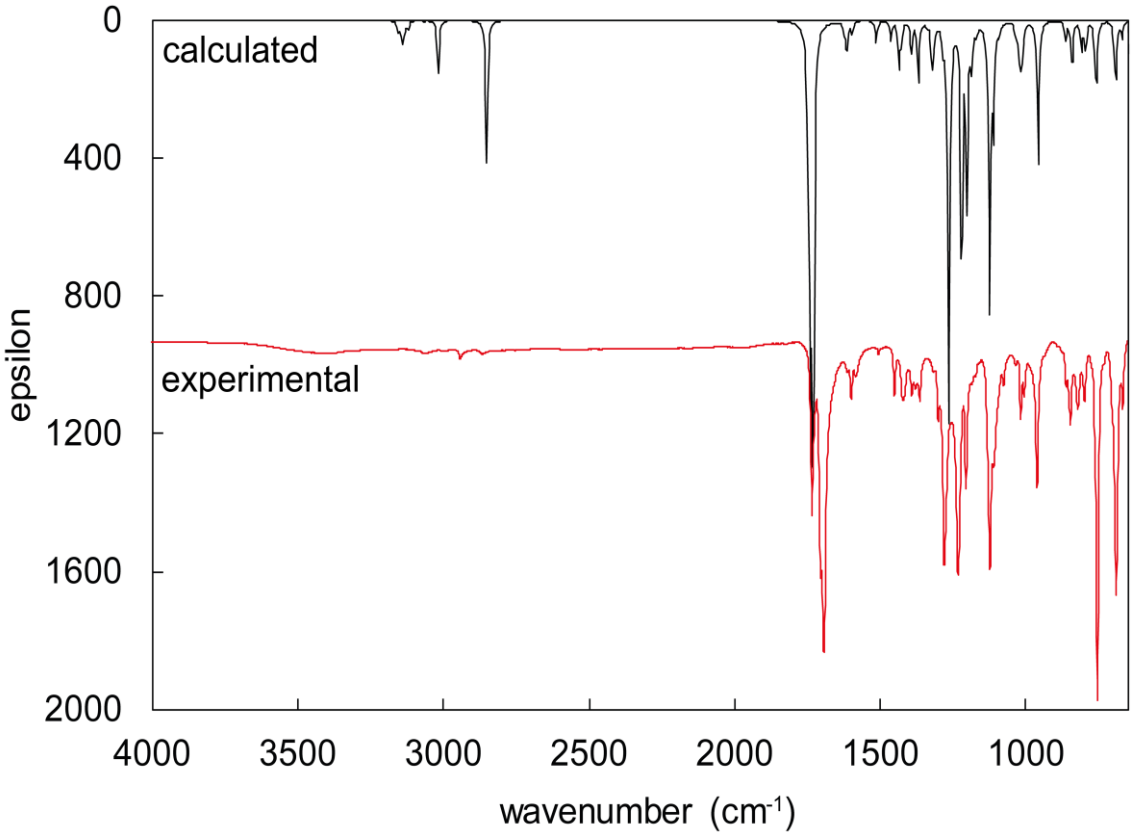

Fig. 5. Experimental and calculated infrared spectra of **4b.**

Table 5. Experimental and calculated ^{1}H NMR chemical shifts for **4a** (CSGT).

Comp.	Exp.	csgt1[a]	csgt2[b]	csgt3[c]	csgt4[d]
19H	8.15	5.22	5.80	6.98	8.23
23H	8.15	5.22	5.80	6.98	8.23
26H	7.97	4.93	5.52	6.73	8.02
30H	7.97	4.93	5.52	6.73	8.02
28H	7.65-7.57	4.82	5.38	6.51	7.50
21H	7.65-7.57	4.85	5.39	6.52	7.52
27H	7.54-7.44	4.75	5.31	6.45	7.38
29H	7.54-7.44	4.75	5.31	6.45	7.38
20H	7.54-7.44	4.77	5.32	6.47	7.42
22H	7.54-7.44	4.77	5.32	6.47	7.42
24H	5.58	2.90	3.43	4.26	5.49
25H	5.58	2.90	3.43	4.26	5.49

[a] B3LYP/6-31G(d) [b] B3LYP/6-31G(d,p) [c] B3LYP/6-311G(d,p) [d] B3LYP/6-311+G(2d,p)

Table 6. Experimental and calculated ^{1}H NMR chemical shifts for **4a** (GIAO).

Comp.	Exp.	giao1[a]	giao2[b]	giao3[c]	giao4[d]
19H	8.15	8.13	8.38	8.48	8.62
23H	8.15	8.13	8.38	8.48	8.62
26H	7.97	7.87	8.12	8.22	8.40
30H	7.97	7.87	8.12	8.22	8.40
28H	7.65-7.57	7.40	7.59	7.71	7.85
21H	7.65-7.57	7.38	7.56	7.67	7.77
27H	7.54-7.44	7.32	7.52	7.64	7.69
29H	7.54-7.44	7.32	7.52	7.64	7.69
20H	7.54-7.44	7.29	7.48	7.59	7.68
22H	7.54-7.44	7.29	7.48	7.59	7.68
24H	5.58	5.26	5.44	5.58	5.76
25H	5.58	5.26	5.44	5.58	5.76

[a] B3LYP/6-31G(d) [b] B3LYP/6-31G(d,p) [c] B3LYP/6-311G(d,p) [d] B3LYP/6-311+G(2d,p)

Table 7. Experimental and calculated ^{1}H NMR chemical shifts for **4b** (CSGT).

Comp.	Exp.	csgt1[a]	csgt2[b]	csgt3[c]	csgt4[d]
23-H	10.12	6.60	7.38	8.82	10.26
21-H	8.30	5.32	5.94	7.12	8.32
25-H	8.30	5.32	5.94	7.12	8.32
28-H	8.00-7.94	4.92	5.51	6.71	7.85
32-H	8.00-7.94	4.92	5.51	6.71	7.85
22-H	8.00-7.94	4.96	5.54	6.73	8.01
24-H	8.00-7.94	4.96	5.54	6.73	8.01
30-H	7.66-7.60	4.85	5.40	6.54	7.55
29-H	7.54-7.48	4.76	5.33	6.49	7.43
31-H	7.54-7.48	4.76	5.33	6.49	7.43
26-H	5.62	2.92	3.46	4.28	5.51
27-H	5.62	2.92	3.46	4.28	5.51

[a] B3LYP/6-31G(d) [b] B3LYP/6-31G(d,p) [c] B3LYP/6-311G(d,p) [d] B3LYP/6-311+G(2d,p)

Table 8. Experimental and calculated ^{1}H NMR chemical shifts for **4b** (GIAO).

Comp.	Exp.	giao1[a]	giao2[b]	giao3[c]	giao4[d]
23-H	10.12	9.99	10.15	10.34	10.65
21-H	8.30	8.25	8.50	8.59	8.73
25-H	8.30	8.25	8.50	8.59	8.73
28-H	8.00-7.94	7.88	8.13	8.22	8.38
32-H	8.00-7.94	7.88	8.13	8.22	8.38
22-H	8.00-7.94	7.80	8.02	8.11	8.22
24-H	8.00-7.94	7.80	8.02	8.11	8.22
30-H	7.66-7.60	7.40	7.60	7.71	7.78
29-H	7.54-7.48	7.34	7.53	7.64	7.74
31-H	7.54-7.48	7.34	7.53	7.64	7.74
26-H	5.62	5.31	5.48	5.61	5.81
27-H	5.62	5.31	5.48	5.61	5.81

[a] B3LYP/6-31G(d) [b] B3LYP/6-31G(d,p) [c] B3LYP/6-311G(d,p) [d] B3LYP/6-311+G(2d,p)

Molecular electrostatic potential maps

Molecular electrostatic potential (MEP) map gives information about the electron rich and electron deficient parts of the investigated molecule. MEP maps were calculated at DFT B3LYP/6-31G(d), B3LYP/6-311G(d,p) and B3LYP/6-311+G(2d,p) levels of theory. Calculated MEP diagrams of **3a**, **3b**, **4a** and **4b** are given in Fig. 6. For **3a** and **3b**, it can be seen that negative charge was dominantly located on the carbonyl group and partially on the hydroxyl group of carboxylic acid. For **4a** and **4b**, negative charge was located on the carbonyl and ester functional groups.

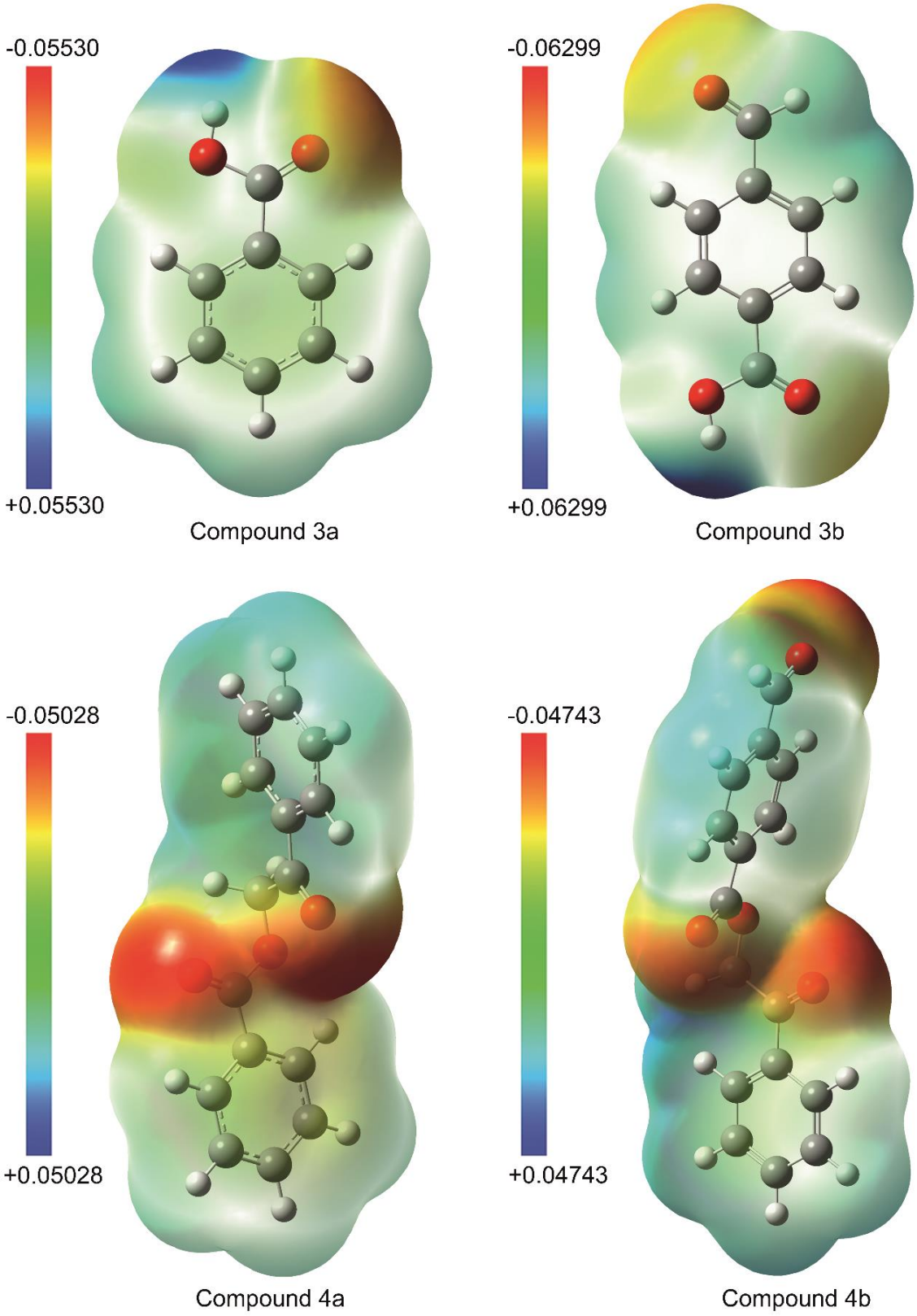

Fig. 6. MEP map diagrams of **3a**, **3b**, **4a** and **4b**.

Frontier molecular orbitals and global reactivity descriptors

Lowest unoccupied molecular orbital (LUMO) and the highest occupied molecular orbital (HOMO) energy calculations were carried out at DFT B3LYP level of theory using 6-31G(d), 6-31G(d,p), 6-311G(d,p) and 6-311+G(2d,p) basis sets.. Ionization potential (I), electron affinity (A), electronegativity (χ), chemical hardness (η), chemical softness (S),

electronic chemical potential (μ) and electrophilicity index (ω) values were determined and are given in Tables 9, 10, 11 and 12. Ionization potential can be calculated using Eqn. (1) and corresponds to a minimum energy required to remove an electron from an atom or molecule and electron affinity can be calculated using Eqn. (2). [27] and corresponds to the energy released when an electron is added to a neutral atom or molecule in the gaseous state. On the other hand, electronegativity, chemical hardness, chemical softness, electronic chemical potential and electrophilic index can be calculated using Eqns. (3-7). [28-34].

$$I = -E_{HOMO} \quad (1)$$

$$A = -E_{LUMO} \quad (2)$$

$$\chi = (I + A)/2 \quad (3)$$

$$\eta = (I - A)/2 \quad (4)$$

$$S = 1/\eta \quad (5)$$

$$\mu = -(I + A)/2 \quad (6)$$

$$\omega = \mu^2/2\eta \quad (7)$$

Table 9. Global reactivity descriptors for **3a**.

Entry	opt1[a]	opt2[b]	opt3[c]	opt4[d]
LUMO	-1.309	-1.314	-1.568	-1.783
HOMO	-7.087	-7.094	-7.336	-7.453
Gap	5.778	5.780	5.769	5.670
I	7.087	7.094	7.336	7.453
A	1.309	1.314	1.568	1.783
χ	4.198	4.204	4.452	4.618
η	2.889	2.890	2.884	2.835
S	0.346	0.346	0.347	0.353
μ	-4.198	-4.204	-4.452	-4.618
ω	3.051	3.058	3.436	3.761

[a] B3LYP/6-31G(d) [b] B3LYP/6-31G(d,p) [c] B3LYP/6-311G(d,p) [d] B3LYP/6-311+G(2d,p)

Table 10. Global reactivity descriptors for **3b.**

Entry	opt1[a]	opt2[b]	opt3[c]	opt4[d]
LUMO	-2.414	-2.417	-2.637	-2.848
HOMO	-7.230	-7.225	-7.444	-7.609
Gap	4.816	4.809	4.808	4.760
I	7.230	7.225	7.444	7.609
A	2.414	2.417	2.637	2.848
χ	4.822	4.821	5.041	5.228
η	2.408	2.404	2.404	2.380
S	0.415	0.416	0.416	0.420
μ	-4.822	-4.821	-5.041	-5.228
ω	4.828	4.833	5.284	5.742

[a] B3LYP/6-31G(d) [b] B3LYP/6-31G(d,p) [c] B3LYP/6-311G(d,p) [d] B3LYP/6-311+G(2d,p)

Chemical hardness is a measure of the resistance of a compound to change in its electronic configuration. [35] Chemical hardness values of compounds showed similar trend to the HOMO-LUMO gap values. It can be seen that chemical hardness of **3a** is bigger than **3b** and **4a** is bigger than **4b**. Electrophilicity index is considered to be a measure of electrophilic power. [27] A good electrophile is characterized by a high value of electrophilicity index, in opposite, lower values

correspond to good nucleophiles. It was found that the electrophilicity index of **3a** is lower than the electrophilicity index of **3b** and the electrophilicity index of **4a** is lower than the electrophilicity index of **4b**.

Table 11. Global reactivity descriptors for **4a.**

Entry	opt1[a]	opt2[b]	opt3[c]	opt4[d]
LUMO	-1.648	-1.657	-1.906	-2.056
HOMO	-6.880	-6.887	-7.125	-7.228
Gap	5.232	5.230	5.219	5.171
I	6.880	6.887	7.125	7.228
A	1.648	1.657	1.906	2.056
χ	4.264	4.272	4.516	4.642
η	2.616	2.615	2.609	2.586
S	0.382	0.382	0.383	0.387
μ	-4.264	-4.272	-4.516	-4.642
ω	3.476	3.489	3.908	4.167

[a] B3LYP/6-31G(d) [b] B3LYP/6-31G(d,p) [c] B3LYP/6-311G(d,p) [d] B3LYP/6-311+G(2d,p)

Table 12. Global reactivity descriptors for **4b.**

Entry	opt1[a]	opt2[b]	opt3[c]	opt4[d]
LUMO	-2.245	-2.253	-2.468	-2.642
HOMO	-7.089	-7.088	-7.304	-7.447
Gap	4.844	4.835	4.836	4.804
I	7.089	7.088	7.304	7.447
A	2.245	2.253	2.468	2.642
χ	4.667	4.670	4.886	5.045
η	2.422	2.417	2.418	2.402
S	0.413	0.414	0.414	0.416
μ	-4.667	-4.670	-4.886	-5.045
ω	4.496	4.512	4.937	5.297

[a] B3LYP/6-31G(d) [b] B3LYP/6-31G(d,p) [c] B3LYP/6-311G(d,p) [d] B3LYP/6-311+G(2d,p)

Mulliken atomic charges

The Mulliken charge distribution over the atoms affects the molecular polarizability, electronic structure, dipole moment etc. In the computational studies, the Mulliken charge distribution of the synthesized molecules were determined at DFT B3LYP/6-31G(d), B3LYP/6-31G(d,p), B3LYP/6-311G(d,p) and B3LYP/6-311+G(2d,p) levels of theory. The Mulliken atomic charges for **4a** and **4b** at B3LYP/6-311+G(2d,p) level of theory are given in Figs. 7 and 8, respectively. In **4a** and **4b**, all oxygen atoms possess negative Mulliken charges, but the charges of the carbonyl oxygens are more negative. In **4a**; all carbon atoms have negative charge except 2C, 11C, 13C and 18C. In **4b**; all carbonyl carbons (6C, 1C, 13C), ring carbons adjacent to carbonyl carbons (5C, 2C, 14C) and 16C have positive Mulliken charges.

RESULTS AND DISCUSSION

In this work, two novel methods have been proposed for the esterification reaction of phenacyl bromide with benzoic acid/terephthalaldehydic acid. The proposed methods allow investigated esterification reaction in good yields. Yields for the reactions are approximately 90% for benzoic acid and 80% for terephthalaldehydic acid.

In the esterification reaction, it was found that the yield of the reaction of phenacyl bromide with benzoic acid is higher than the yield of the reaction

of phenacyl bromide with terephthalaldehydic acid. This can be explained by the higher nucleophilic character of benzoic acid than that of terephthalaldehydic acid. Computational results also support this situation. It can be seen from Tables 9 and 10 that the electrophilicity index (ω) of the terephthalaldehydic acid is higher than that of the benzoic acid.

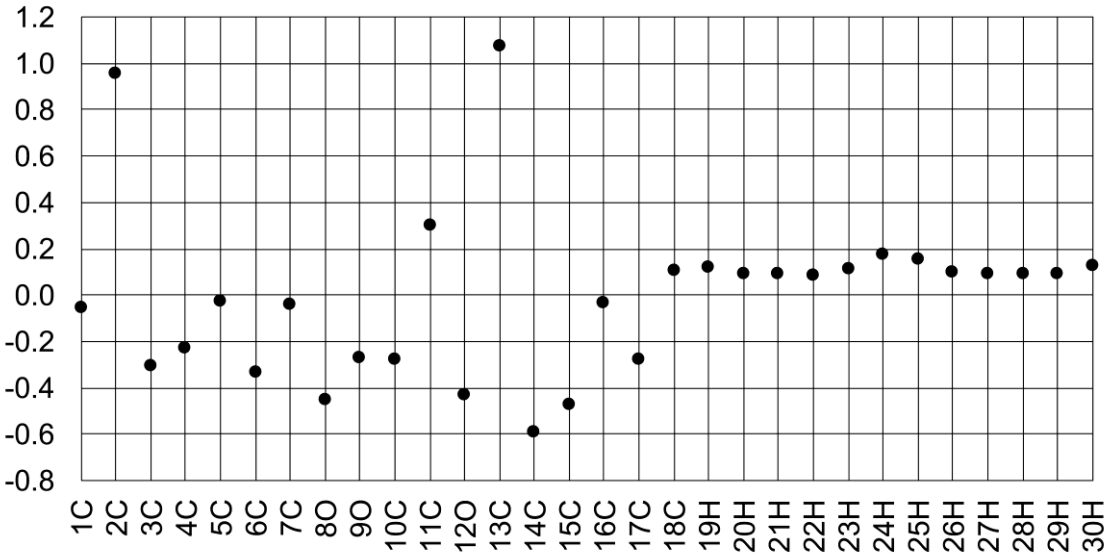

Fig. 7. Mulliken atomic charges of **4a**.

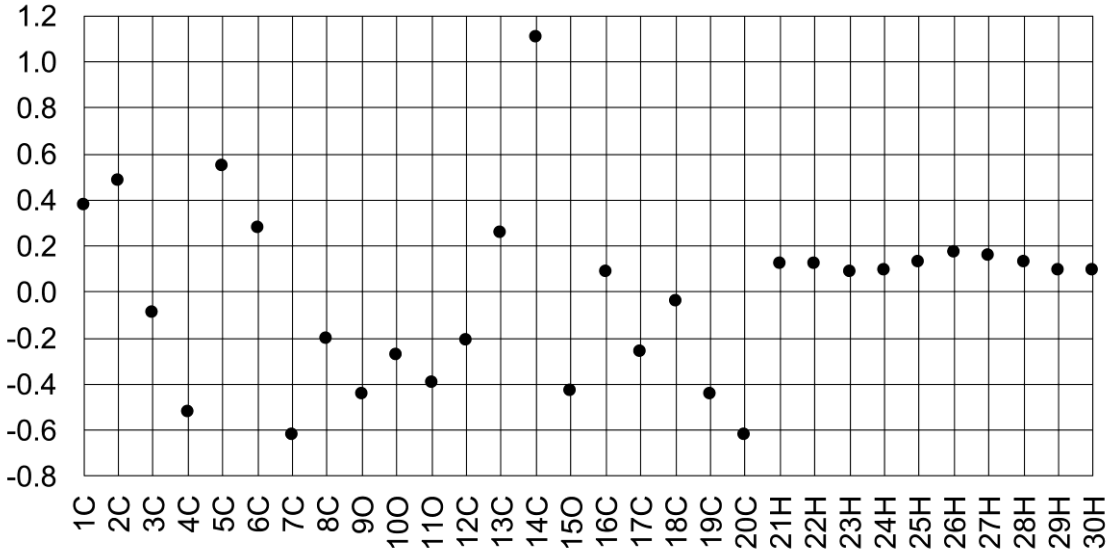

Fig. 8. Mulliken atomic charges of **4b**.

In NMR calculations, it was found that the ^{1}H NMR chemical shifts obtained from calculations at DFT B3LYP/6-31G(d,p) GIAO and at DFT B3LYP/6-311+G(2d,p) CSGT levels of theory showed good agreement with the experimental results. Similar results have been obtained in a previous study [24]. It was also observed that in general, GIAO method is more successful than CSGT method and the accuracy of the CSGT method increases with the use of larger basis sets. In our study, successful results can only be obtained with 6-311+G(2d,p) basis set for CSGT method. On the other hand, GIAO method provide acceptable results with relatively small basis sets. Relatively larger basis sets with GIAO method generally overestimates the ^{1}H NMR chemicals shifts.

In the microwave-assisted reactions, both pressure controlled closed system and atmospheric system were used. In the closed system, probably due to the increasing pressure inside the reactor, byproduct formation and as a result of this, decrease in the reaction yield was observed. It can be said that atmospheric focused microwave system is more suitable for the investigated reaction conditions.

Acknowledgements. *This work was supported by Kocaeli University Scientific Research Projects Unit. Project Numbers: 2011/062; 2017/38 HD. The*

author acknowledge Kocaeli University for the financial support.

REFERENCES

1. S.N. Dighe, R.V. Bhattad, R.R. Kulkarni, K.S. Jain, K.V. Srinivasan, *Synth. Commun.*, **40**, 3522 (2010).
2. Liu, S. Feng, C. Li, *ACS Sustainable Chem. Eng.*, **4**, 6754 (2016).
3. J. Chen, D. Liu, N. Butt, C. Li, D. Fan, Y. Liu, W. Zhang, *Angew. Chem., Int. Ed.*, **52**, 11632 (2013).
4. X. Zou, Y. Zhao, H. Cheng, Patent CN104803816A, 2015.
5. Y. Hu, J. Chen, Z.G. Le, Z.C. Chen and Q.G. Zheng, *Chin. Chem. Lett.*, **16**, 903 (2005).
6. Z. Huang, L. Xie and X. Huang, *Synth. Commun.*, **18**, 1167 (1988).
7. M. Inoue, M. Yamashita, Patent JP2008088128A, 2008.
8. M. Narender, M. Reddy, V. Kumar, K. Rao, *Synth. Commun.*, **35**, 1681 (2005).
9. J.H. Clark, J.M. Miller, *Tetrahedron Lett.*, 599 (1977).
10. R. Ruzicka, M. Zabadal, P. Klan, *Synth. Commun.*, **32**, 2581 (2002).
11. A.C. Giddens, Thesis, University of Auckland, 2008.
12. J. Chen, Z. Zhang, D. Liu and W. Zhang, *Angew. Chem., Int. Ed.*, **55**, 8444 (2016).
13. O. Noboru, Y. Takashi, S. Tadashi, T. Kazuhiko, K. Aritsune, *Bull. Chem. Soc. Japan*, **51**, 2404 (1978).
14. M. Thorat, R. Mane, M. Jagdale, M. Salunkhe, *Org. Prep. Proced. Int.*, **18**, 203 (1986).
15. J.S. Lindsey, I.C. Schreiman, H.C. Hsu, P.C. Kearney, A.M. Marguerettaz, *J. Org. Chem.*, **52**, 827 (1987).
16. Z. Li, Z.J. Quan, X.C. Wang, *Chem. Papers-Chemicke Zvesti*, **58**, 256 (2004).
17. M.M. Heravi, H.A. Oskooic, L. Bahrami, M. Ghassemzadeh, *Ind. J. Chemi., Section B-Organic Chemistry Including Medicinal Chemistry*, **45**, 779 (2006).
18. S. Tasler, M. Kraus, S. Pegoraro, A. Aschenbrenner, E. Poggesi, R. Testa, G. Motta,A. Leonardi, *Bioorg. Med. Chem. Lett.*, **15**, 2876 (2005).
19. Y.H. Zhao, M.J. Luo, H.W. Liu, L.H. Wu, *Synth. Commun.*, **45**, 857 (2015).
20. L.P. Sidorova, T.A. Tseitler, V.V. Emel'yanov, E.A. Savateeva, N.E. Maksimova, N.N. Mochul'skaya, V.A. Chereshnev, O.N. Chupakhin, *Pharm. Chem. J.*, **51**, 9 (2017).
21. M.J. Frisch, G.W. Trucks, H.B. Schlegel, G.E. Scuseria, M.A. Robb, J.R. Cheeseman, G. Scalmani, V. Barone, B. Mennucci, G.A. Petersson, H. Nakatsuji, M. Caricato, X. Li, H.P. Hratchian, A.F. Izmaylov, J. Bloino, G. Zheng, J.L. Sonnenberg, M. Hada, M. Ehara, K. Toyota, R. Fukuda, J. Hasegawa, M. Ishida, T. Nakajima, Y. Honda, O. Kitao, H. Nakai, T. Vreven, J. Montgomery, J. A. , J.E. Peralta, F. Ogliaro, M. Bearpark, J.J. Heyd, E. Brothers, K.N. Kudin, V.N. Staroverov, T. Keith, R. Kobayashi, J. Normand, K. Raghavachari, A. Rendell, J.C. Burant, S.S. Iyengar, J. Tomasi, M. Cossi, N. Rega, J.M. Millam, M. Klene, J.E. Knox, J.B. Cross, V. Bakken, C. Adamo, J. Jaramillo, R. Gomperts, R.E. Stratmann, O. Yazyev, A.J. Austin, R. Cammi, C. Pomelli, J.W. Ochterski, R.L. Martin, K. Morokuma, V.G. Zakrzewski, G.A. Voth, P. Salvador, J.J. Dannenberg, S. Dapprich, A.D. Daniels, O. Farkas, J.B. Foresman, J.V. Ortiz, J. Cioslowski and D.J. Fox, Gaussian 09, Gaussian Inc., Wallingford CT., 2013.
22. M.D. Hanwell, D.E. Curtis, D.C. Lonie, T. Vandermeersch, E. Zurek, G.R. Hutchison, *J. Cheminformatics*, **4**, 1 (2012).
23. R. Dennington, T. Keith and J. Millam, GaussView, Version 5, Semichem Inc., Shawnee Mission, KS, 2009.
24. T. Erdogan, F. Oguz Erdogan, *Lett. Org. Chem.*, **15**, 99 (2018).
25. J.B. Foresman, E. Frisch, Exploring Chemistry with Electronic Structure Methods. Second ed. Pittsburgh, PA: Gaussian, Inc., 1996.
26. H.K. Fun, S. Arshad, B. Garudachari, A.M. Isloor, M.N. Satyanarayan, *Acta Crystall., Section E-Structure Reports Online*, **67**, O1528-U1667 (2011).
27. T. Koopmans, *Physica*, **1**, 104 (1934).
28. P.K. Chattaraj, U. Sarkar D.R. Roy, *Chem. Reviews*, **106**, 2065 (2006).
29. R.S. Mulliken, *J. Chem. Phys.*, **2**, 782 (1934).
30. R.G. Parr, R.G. Pearson, *J. Amer. Chem. Soc.*, **105**, 7512 (1983).
31. R.G. Parr, L. Von Szentpaly, S.B. Liu, *Journal of the American Chemical Society*, **121**, p. 1922-1924 (1999).
32. R.G. Pearson, *J. Amer. Chem. Soc.*, **85**, 3533 (1963).
33. R.G. Pearson, *J. Chem. Educ.*, **45**, 581(1968).
34. R.G. Pearson, *J. Chem. Educ.*, **76**, 267 (1999).
35. G. Makov, *J. Phys. Chem.*, **99**, 9337 (1995).

Bulgarian Chemical Communications, Volume 51, Issue 1 (pp. 146 –151) 2019

Cadmium(II) organometallic complex with 4-chloro-N ((pyridine – 2 yl) methylene) benzene amine: synthesis, spectroscopy and antibacterial evaluation

B. Jamali Aghbash, M. Manoochehri*, M. Daghighi Asli

Department of Chemistry, Central Tehran Branch, Islamic Azad University, Tehran-Iran

Submitted March 24, 2017; Accepted August 8, 2018

In the present paper, first the ligand Schiff base was synthesized by condensing the amine with an aldehyde. Then, it was identified by ^{13}C NMR, ^{1}H NMR and IR spectrometry. Next step was coordinating it with transition metal cadmium (II) chloride. Since the produced complex was of ML type, the weighed metal should be equal to 0.001 mol. This yielded 1 to 1 molar ratio. Then, ^{13}C NMR, ^{1}H NMR and IR spectrometry was used to prove its formation. Studies on antibacterial features were performed and the obtained results showed that the metal complexes are more active than the free ligands.

Keywords: Cadmium (II) complexes, Schiff base, Antibacterial activity, Metal complexes

INTRODUCTION

Metal Schiff base molecules provide potential sites for biochemically active compounds relevant to intermolecular hydrogen bonding and proton transfer equilibria [1]. Metal complexes of Schiff base ligands can afford several applications in biological, analytical, clinical and industrial fields [2]. Considering the biological activity and highly qualified physicochemical, stereochemical, electrochemical, structural and catalytic properties of Schiff base metal complexes, their values have been considered to be highly important and this is related to their application as facilities to analyze pharmacological constituents [3]. Necessary biological reactions in life processes mostly involve transition metals; these metals usually coordinate with O- or N- terminals from protein in several modes and play a dominant role in the conformation and function of biological macromolecules [4].

Regarding the metal coordination complexes, much has been studied so far. Specially, their antimicrobial and anticancer properties have been the focus of attention through studies [5].

Recently, metal-based antioxidants have been studied to a great deal due to their capacity to protect organisms and cells from damage caused by oxidative stress or scavenging free radicals [6].

These metal complex derivatives indicating noticeable biological activity, may pave the way for a novel trend in designing new antibacterial drugs. It is of great significance to note that there have been extensive studies on the preparation of many symmetrical tetradentate bis-diamines with O-hydroxyl aldehydes/ketones [7,8].

In the present study the synthesis, characterization and antibacterial activity of complex Schiff base with transition metals, particularly with cadmium, are worked out.

EXPERIMENTAL

Ligand synthesis

To synthesis 4-chloro-N ((pyridine-2-yl) methylene) benzene amine, 0.001 mol of 4-chloro aniline was solved in 15 cm^3 of ethanol solution and 0.001 mol of pyridine 2-carbaldehyde was solved in 15 cm^3 of ethanol. Then, the two compounds were mixed at room temperature for 30 min and let to react for 30 min.

The desired ligand was formed with 88 % efficiency.

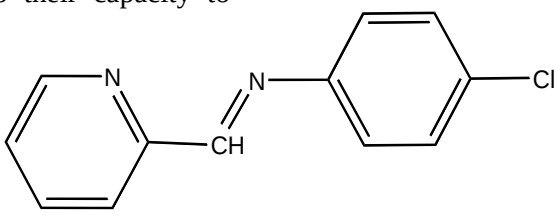

Fig. 1. Ligand structure.

* To whom all correspondence should be sent.
E-mail: *Dr.manoochehri@gmail.com*

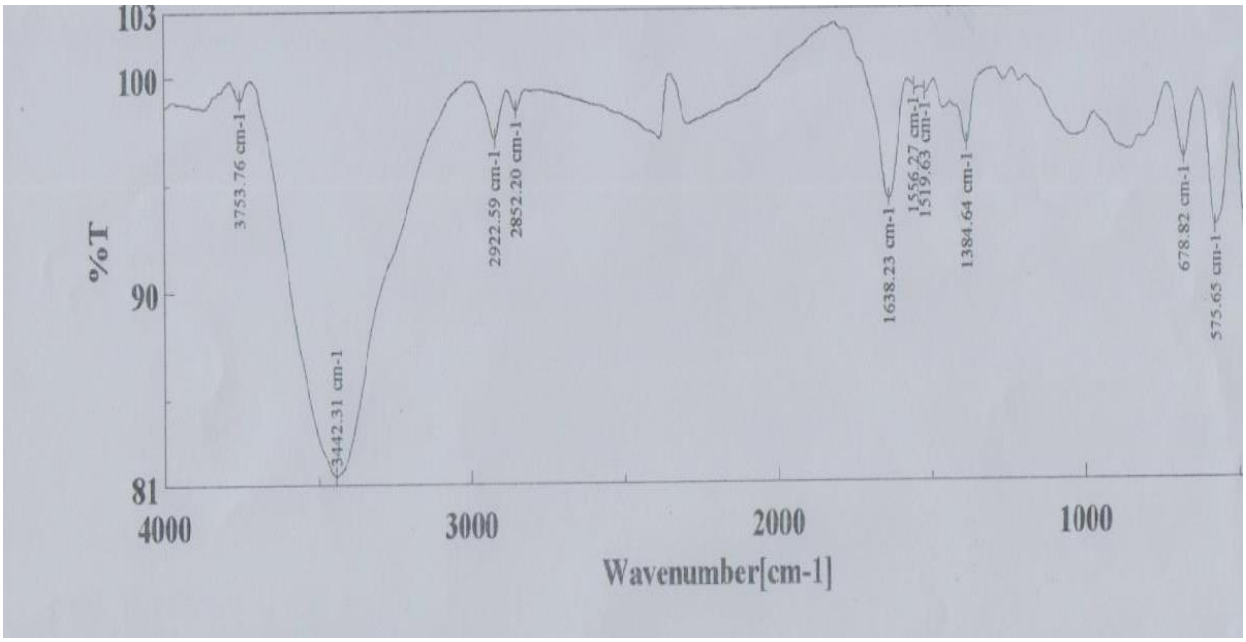

Fig. 2. IR spectrum of ligand

1- According to the graph, the strong band seen in the area of 3442 cm^{-1} is that of aromatic C-H stretching frequency.

2- The average band seen in the area of 1638 cm^{-1} is that of C=N bond. This proves the formation of the aimed product.

3- Average band between 1384 and 1533 cm^{-1} is relevant to benzene C=C bond.

4. Weak band between 870 and 1039 cm^{-1} is that of aromatic C-H bending vibration.

There are some identified signals related to various carbons. Methylene chlorides are seen at 21 ppm. Aimin carbon is seen in 148/59 ppm and aromatic carbons are seen in the range between 122 ppm and 130 ppm.

Proton aimin 7.98 ppm and aromatic protons are observed between 7.31 ppm and 7.36 ppm as multiple groups. In ligand's ^{1}H NMR spectrum appears a clear sign at 2.11 ppm representing methylene protons

.

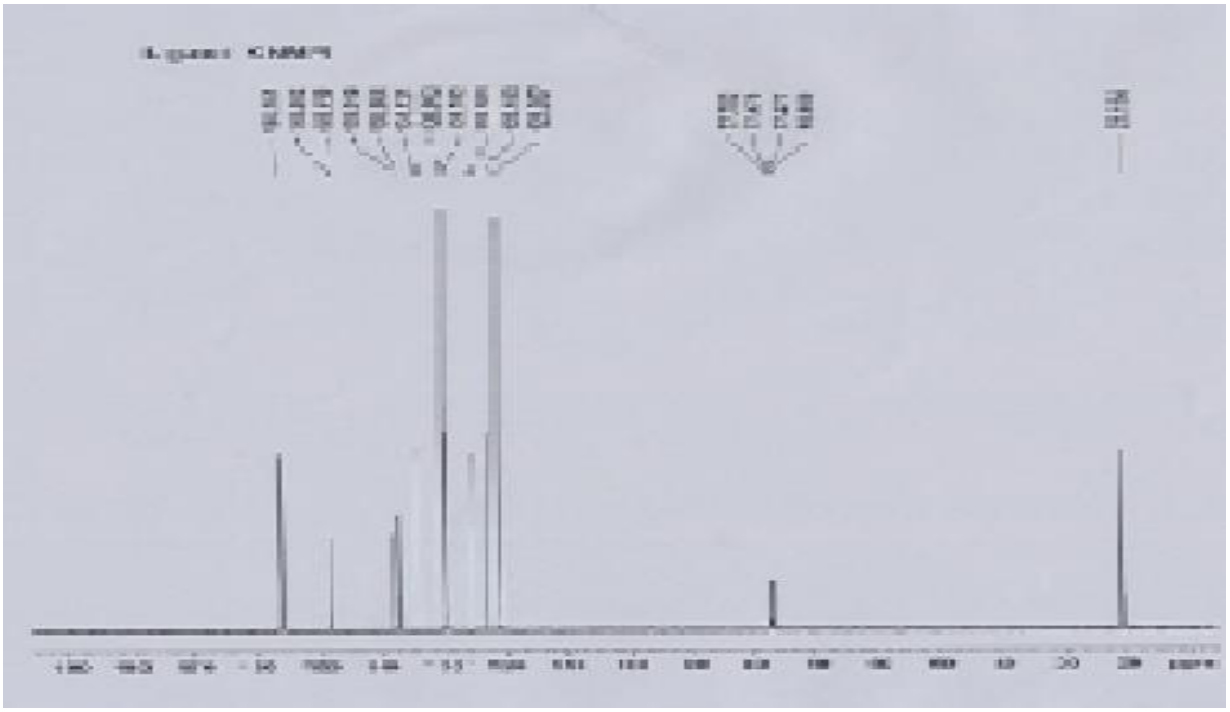

Fig. 3. ^{13}C NMR spectrum of ligand

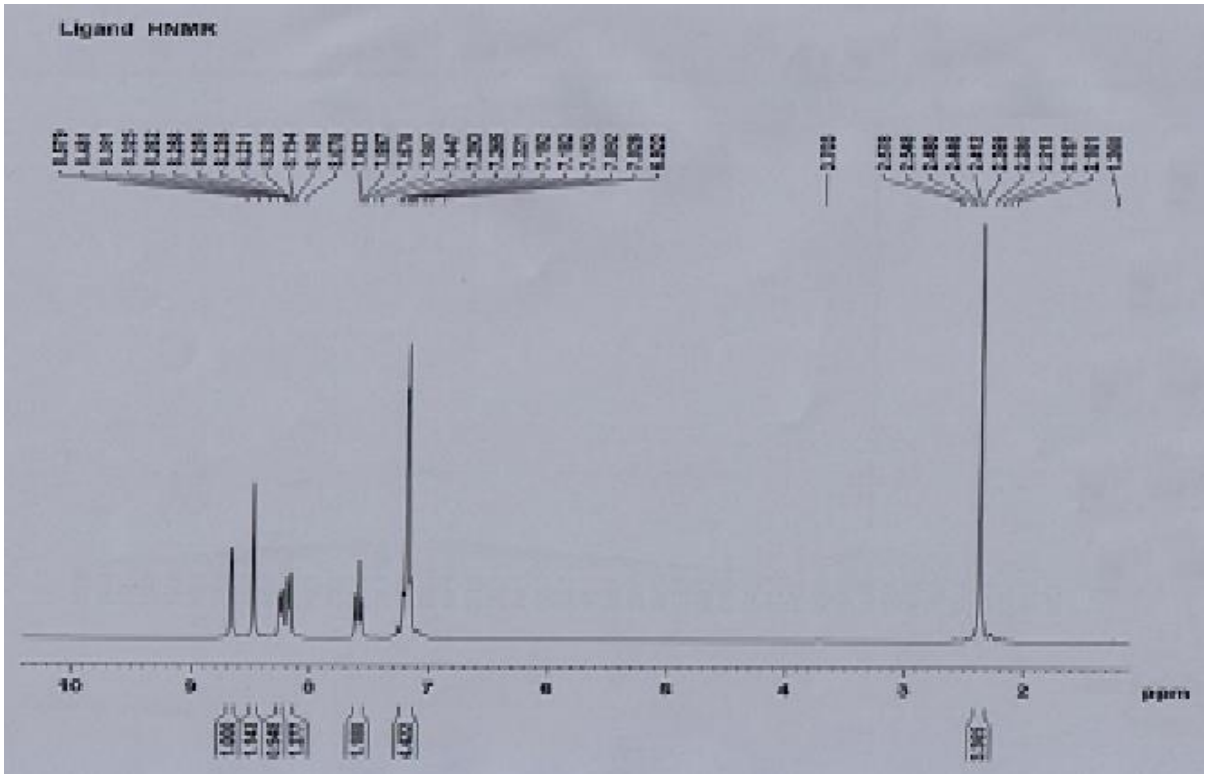

Fig. 4. ^{1}H NMR spectrum of ligand

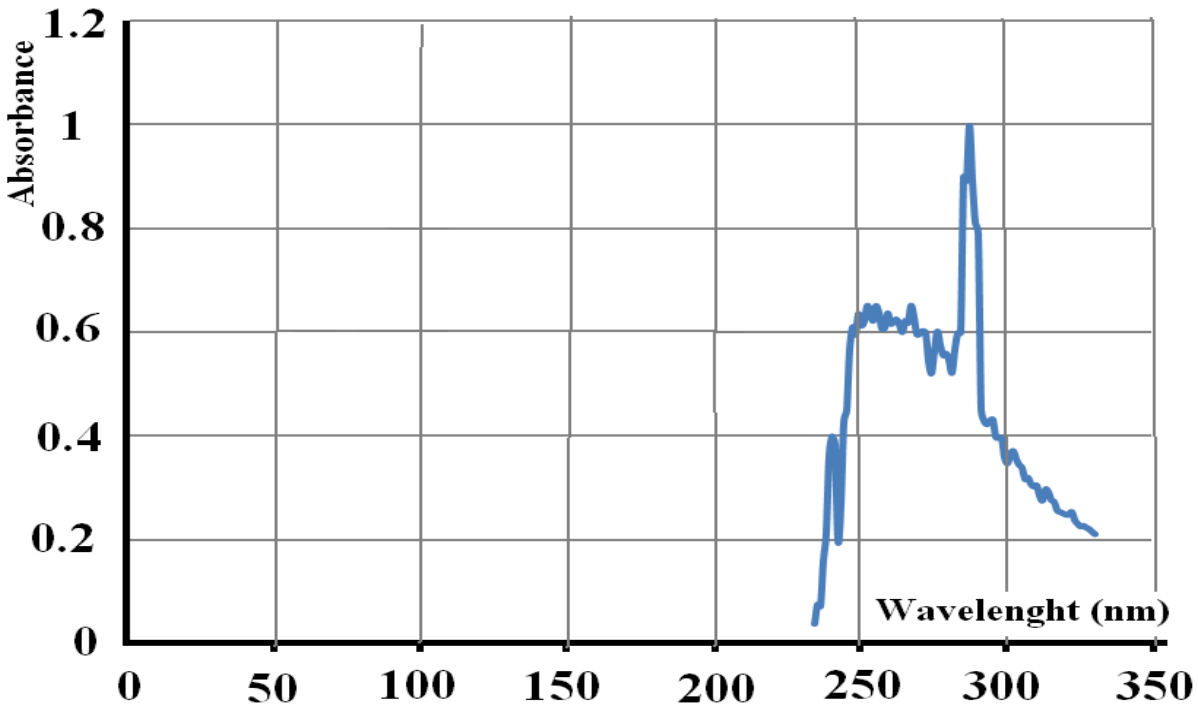

Fig. 5. UV spectrum of ligand

Two graphs are specified in the above spectrum showing electron transport: the one - transport of π to π* and the other - transport of n to π*. The first transport is of higher energy and accordingly of shorter wavelength.

Synthesis of 4-chloro-n ((pyridine-2 yl) methylene) benzene amine cadmium (ii) chloride complex

To synthesize 4-chloro-N ((pyridine-2 yl) methylene) benzene amine cadmium(II) chloride

complex, 0.001 ml of the above mentioned ligand

Then the solution was placed in a stirrer for 5 min at room temperature. Then, 0.001 ml of cadmium salt (II) was added (the least possible amount to be solvable by ethanol). This was done in 5 min like the addition of ligand. It is of great significance to consider that all stages of ligand and complex synthesis were done in absence of heat. This is because Schiff bases are sensitive to heat and decompose when exposed to heat.

In the next step, the metal was added to the ligand and the desired complex was formed. After

was solved in 10 cm^{-3} of ethanol. solvent evaporation, the produced sediment, brown in color, is separated and washed by ether. The formed complex is brown in color. The synthesis efficiency of this complex is 88 %.

The coordination number of the final product is 4 and it has *cis* isomer.

The color of the complex's points to the presence of cadmium (II) in it. Since cadmium has orbital d^{10}, it is of diamagnetic type.

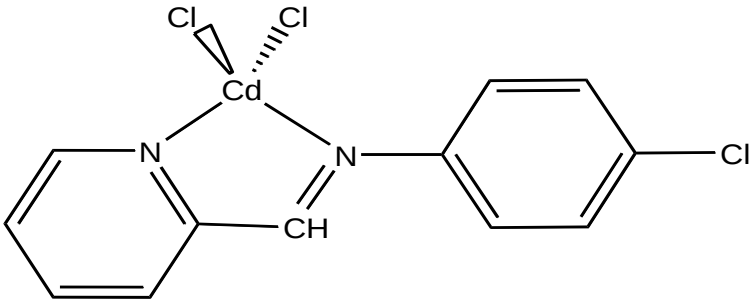

Fig. 6. Structure of the Cd(II) complex.

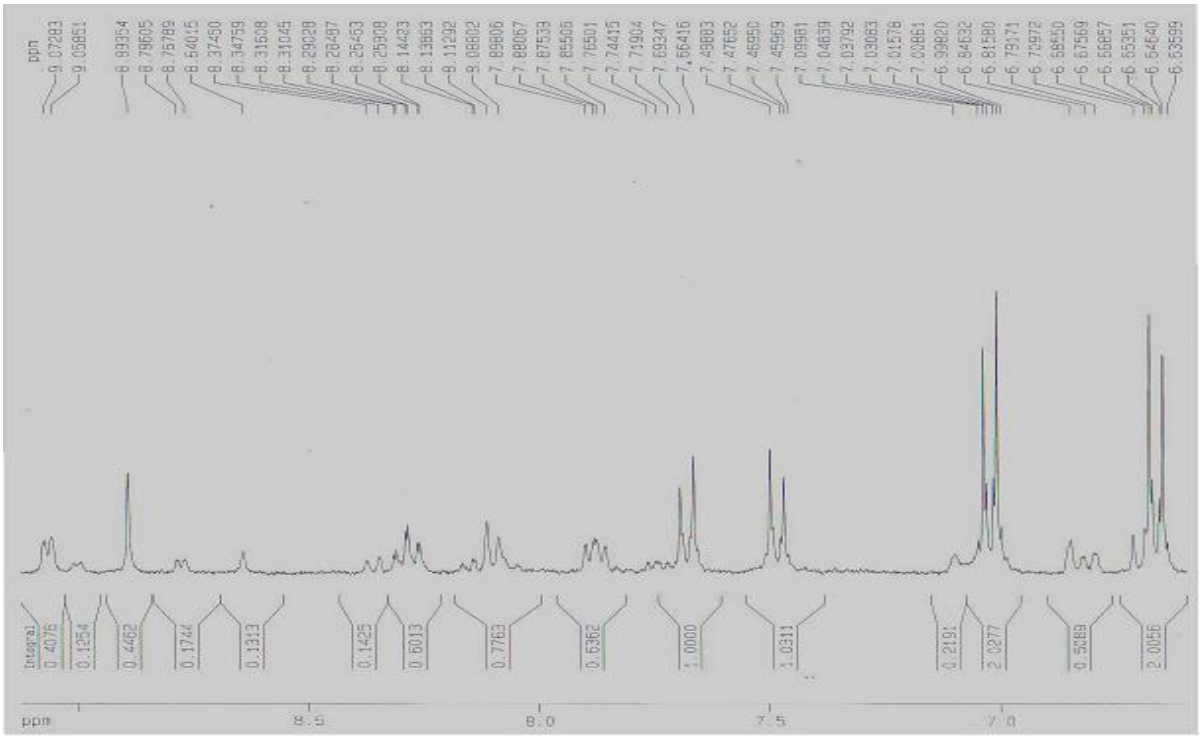

Fig. 7. ^{1}H NMR spectrum of the complex

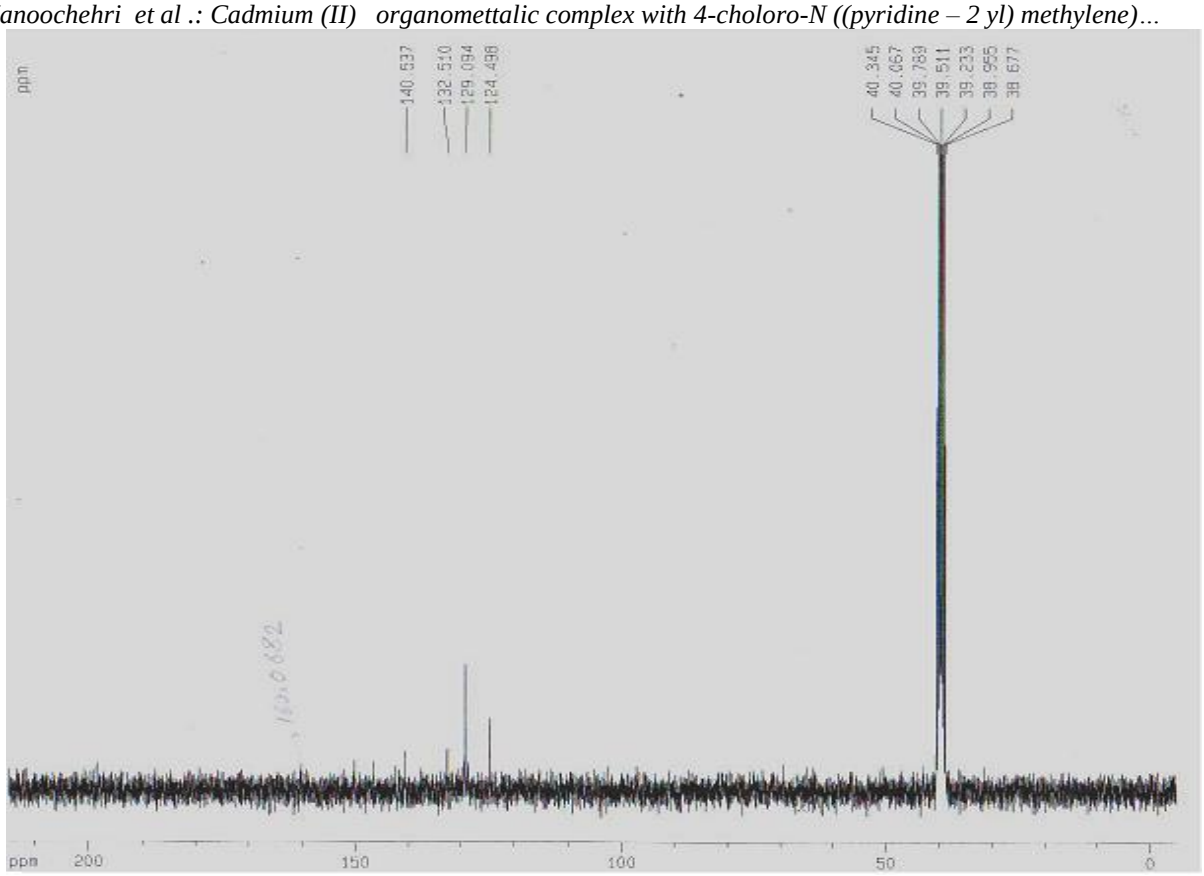

Fig. 8. ^{13}C NMR spectrum of the complex

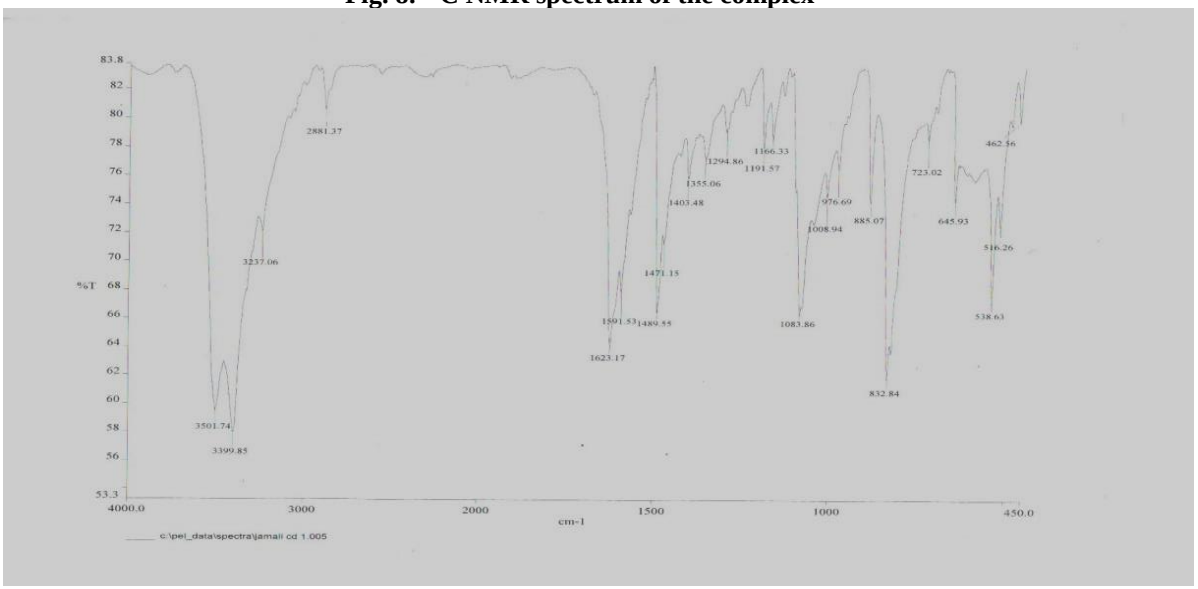

Fig. 9. IR spectrum of the complex.

Aimin proton 7.8 ppm and aromatic protons are also seen between 7.14 ppm and 7.23 ppm. In ligand's HNMR spectrum, an obvious band appears in 2.6 pmm showing methylene protons.

1. The strong band seen at 3438 cm^{-1} is due to C-H stretching frequency.
2. The average band seen at 1631 cm^{-1} is due to C=N bond which proves the formation of aimin.
3. The average bands between 1394- 1591 cm^{-1} are due to C=C benzene.
4. The weak bands between 835 and 1097are of aromatic C-H bending vibration.

Antibacterial activity

The antibacterial activity of 4-chloro-N ((pyridine-2 yl) methylene) benzene amine cadmium (II) chloride complex and 4-chloro-N ((pyridine-2-yl) methylene) benzene amine ligand were achieved by macrodilution broth susceptibility

method. For this experiment *E. coli* no: 25922 from Azad university of Karaj was used.

E. coli is an indicator of water and sewage pollution and is the cause of the most prevalent urinary tract infection. In this method MIC of the complex was determined to be 19×10^2 μg/ml, MBC 33×10^2 μg/ml, MIC for ligand 12×10^3 μg/ml and MBC was 21×10^3 μg/ml.

CONCLUSION

(C-H) 34425 cm^{-1}, (C=N)1637 $cm^{-1}$and (C=C) 1535 $cm^{-1}$are the results of ligand IR spectrum showing the formation of the desired ligand.

(C-H) 2433 $cm^{-1}$and (C=N)1632 cm^{-1} in the IR spectrum of the complex show the formation of the desired complex.

Comparison of the IR spectra shows that due to a decrease in frequency, resulted from the formation of returned π bond, it may be concluded that the complex is formed.

The shifts to lower positions in ^{1}H NMR, UV and ^{13}C NMR are an evience that the complex is formed.

Ligand, due to having two nitrogens in its structure, as a donor, incorporates well the coordinated metal and the complex. As it is clear from complex structure, the produced complex has a coordination number 4 and is a *cis* isomer. It is connected to nitrogen at two heads and to chlorine at the other two heads. The produced complex is diamagnetic due to the lack of electron-electron pairs. The obtained results for Schiff base ligand antibacterial properties are too low, but when it forms a complex, its antibacterial activity increases.

REFERENCES

1. R.S. Joseyphus, M.S. Nair, *Mycobiology*, **36,** 93 (2008).
2. S. Kumar, D.N. Dhar, P.N Saxena, P., *J. Sci. Ind. Res.*, **68,** 181 (2009).
3. S. Spange, E. Vilsmeier, S. Adolph, A. Fährmann, *J. Phys. Org. Chem.*, **12,** 547 **(**1999).
4. M. Tumer, H. Koksal, S. Serin, M. Digrak, *Transit. Met. Chem.*, **24**, 13 (1999).
5. R.A.A. Ammar, A.M.A. Alaghaz, *Int. J. Electrochem. Sci.*, **8**, 8686 (2013).
6.H.O. Omoregie, J. Woods, *Int. J. Chem.*, **3**, 207 (2011).
7. B. Halliwell, J.M.C. Gutteridge, Free Radicals in Biology and Medicine, 3rd edn., Oxford University Press, New York, NY, USA, 1999, p. 617.
8.S. Tachakittirungrod, S. Okonogi, S. Chowwanapoonpohn, *Food Chem.*, **103**, 381 (2007).

Bulgarian Chemical Communications, Volume 51, Issue 1, (pp. 152 – 157) 2019

Experimental investigation of moisture and tensile properties of shellac and chitosan films for packaging applications

U. Vrabič Brodnjak

University of Ljubljana, Faculty of Natural Sciences and Engineering, Department of Textiles, Graphic Arts and Design, Aškerčeva 12, 1000 Ljubljana, Slovenia

Received August 13, 2018; Revised September 13, 2018

Transparent films of chitosan and shellac (from *Kerria Lacca (Kerr) Lindinger (Coccideae)*) were prepared using three different amounts of plasticizers. Poly (ethylene glycol) (PEG) was used for shellac films and glycerol was a plasticizer for chitosan films. The aim of the research was to obtain improved water vapour, moisture, tensile and optic properties of films, when different amounts of plasticizers were added. The study demonstrates that the utilization of shellac films with 15% of PEG could be an alternative in the research for a sustainable packaging. The same trend was shown for chitosan films, where 15% of glycerol exhibited the best properties, compared to lower amount of plasticizer. Moreover, moisture content showed a decrease proportional to the increase in thickness and plasticizers for all treated samples. The results indicated that the addition of different amounts of glycerol and PEG affects tensile properties of the resulted films. The elongation and tensile strength were gradually increased as the plasticizer amounts in both film types increased. However, the thermal stability decreased for both films.

Key words: films, packaging, *Kerria Lacca*, tensile properties, thickness, water vapour permeability

INTRODUCTION

These days, plastics are still widely used as packaging material, due to their ability to preserve the sensory properties and nutritional values of food products [1]. On the other hand, there are high demands for the utilisation of natural polymer sources as food packaging materials [2, 3]. Natural polymers are conserved as alternatives to synthetic plastics and a lot of research has been done on the application on biopolymers in many fields [4-9]. Since food packaging materials require non-toxicity, good moisture, water, mechanical and chemical properties, many biopolymers cannot conquer to plastic materials, such as polyethylene, polypropylene, etc. Therefore good selection, production and preparation of biopolymers should be performed and implemented as food packaging. A natural polymer which is already used in many fields, including in packaging, is shellac. It is a natural polymer, obtained from purified resinous secretion, by the insects *Kerria Lacca* (Kerr) Lindinger (Coccideae). This species is the most important lac insect, being a main source of lac for the production of shellac. The insect is mostly cultivated on host trees in Thailand, India and Myanmar [9, 10]. Shellac's chemical structure is composed of hard and soft resin of polyesters and single esters containing hydroxyl and carboxyl groups [11-13]. It is widely used as an adhesive, thermoplastic, insulating material, sealant and as coating in pharmaceutical and agronomical industries [13]. Shellac has excellent film forming and barrier properties. It is soluble in alcohol and alkaline solutions [11]. Therefore it has been widely used in the food and agro industries for gas, moisture, water and microbial protection of food products [11, 13-15].

Chitosan is known as a non-toxic biopolymer derived from the deacetylation of chitin [16]. Due to its high crystallinity, hydrogen bonds between molecular chains, which exhibit good oxygen properties, it has also attracted a lot of interest in packaging field [16-19]. Due to the positive charge on the amino group under acidic conditions, chitosan binds negatively charged molecules and therefore represents a greater barrier against grease [20-22]. Good barrier properties (antimicrobial, mechanical, against grease, oxygen), chitosan coatings can be used also as barriers in packaging [21]. Both chitosan and shellac have certain barrier properties and could be used as films in the packaging filed as replacement of plastic film barriers.

This research shows the preparation, characterisation and comparison of two different types of biopolymers, using different amounts of plasticizers. Our research is focused on film properties that are important for packaging materials. The aim of this work is to investigate moisture barrier properties and tensile properties of chitosan and dewaxed shellac flakes, using 3 different amounts of glycerol and poly (ethylene) glycol as plasticizers, which could be used as packaging materials.

* To whom all correspondence should be sent:
E-mail: urska.vrabic@ntf.uni-lj.si

EXPERIMENTAL

Materials

Shellac, refined product obtained from LAC, the resinous secretion of the female insect *Kerria Lacca (Kerr) Lindinger (Coccideae)*, was supplied from A. F. Suter & Co Ltd. Company, Essex, United Kingdom. In this analysis dewaxed Shellac HS 701 SB was used, which is the purified and bleached lac (by physical absorption) according to Regulation EU 231/2012 and its specification for E904 Shellac. Chitosan, with molecular weight 20 kDa and deacetylation degree higher than 85%, was purchased from Sigma Aldrich, Austria. Poly (ethylene glycol) (PEG), with molecular weight 200, obtained from Acros Organic, Belgium and glycerol, purchased from Sigma Aldrich, Austria were added as plasticizers. Ethanol (96%) was obtained from Sigma Aldrich, Austria.

Preparation of film forming solution and casting of the films

The shellac solution was prepared by dissolving 2 g of shellac flakes in 100 ml of ethanol and different amounts of PEG 200 (2, 5 and 15% w/w) were added as a plasticiser. The solution was mixed at room temperature for 30 min until no flakes were dispersed. After that, the film solution was filtered through a polyester screen (mesh no. 140 with mesh opening of 160 μm) with aspiration to remove small lumps in the solution.

After the aspiration and the treatment, the shellac solution was casted onto petri dishes (50 ml), spread thinly, uniformly and dried at 55 °C for 10 h. After the films were peeled off from the dishes, they were cooled at room temperature (23 °C; 55% RH).

The chitosan solution was prepared by dissolving 2 g of chitosan in 100 ml (2% w/w) acetic acid and glycerol (G) (2, 5 and 15% w/w) was added as a plasticiser. The solution was mixed at 85 °C for 10 min until no chitosan was dispersed. After that it was cooled to room temperature. Before cooling down, the film solution was filtered through a polyester screen (mesh no. 140 with mesh opening of 160 μm) with aspiration to remove small lumps in the solution. After the aspiration, the solution was cast onto petri dishes (50 ml), spread thinly, uniformly and dried at 55 °C for 10 h. After the films were peeled off from the dishes, they were cooled at room temperature (23 °C; 55% RH). The films were stored in desiccators at 60% RH for further investigations.

Methods

Thickness. The thickness of films was measured with a precision digital micrometre Mitutoyo Corporation, Japan, to the nearest 0.0001 mm at 5 random locations on each film.

Water vapour permeability (WVP) and moisture. To determine the WVP of films, the ASTM E96 standard desiccant method was used. The test cups were filled with silica gel (RH = 16% in the cup), where a sample was placed between the cup and the ring cover of each cup. There was an air gap of 11 mm between the silica gel and the underside of the placed film. To ensure the best results of WVP, a silicone sealant was applied around the cup edge. The films with an exposed area of 50 cm^2 were tested at 50 ± 2% RH and 40 ± 2 °C for 24 h. Two replicas per film were tested.

Moisture of the samples was analysed according to the standard method, by measuring weight loss upon drying in a laboratory oven at 105 ± 1°C until constant weight. Five samples per each film were tested and the results were expressed in percentage.

Tensile properties. Tensile strength (TS) and elongation at break (E) of the films were determined on a tensile testing machine Instron 6022. The samples were analysed in standard atmosphere at a temperature of 23 °C ± 1 °C and relative humidity of 55% ± 2%. The cross speed head was 0.15 mm/s. Films of 6 cm in length and 0.7 cm in width were used, and a minimum of five probes for each sample was tested. During sample stretching, several load and elongation data per second were recorded until a break of the sample occurred.

Colour. The film colour was determined using the CIE colorimeter X-rite. The CIE Lab scale was used to determine L*, a* and b* colour values. A standard plate was used as the standard (L* = 92.82, a* = –1.24, b* = 0.5). Fifteen measurements for each specimen at different locations on samples were made. Before the colour measurements, the samples were conditioned at 55% RH and 25 ± 2 °C for 72 h.

The total colour difference (ΔE) was calculated with the following equations [8]:

$$\Delta E = \sqrt{(\Delta L^*)^2 + (\Delta a^*)^2 + (\Delta b^*)^2}$$
$$\Delta L^* = L^* - L_0^*$$
$$\Delta a^* = a^* - a_0^*$$
$$\Delta b^* = b^* - b_0^*$$

Thermal stability. Thermal stability of shellac and chitosan films was determined using a Mettler apparatus, with heating plate Hot stage FP 82 HT. The change of phase was determined, using optical microscope. Measurement conditions were: starting

temperature 25°C, heating speed: 2°C/min and end temperature 150°C. For each sample 25 measurements were done.

RESULTS AND DISCUSSION

Shellac is one of the thermosetting resins of animal origin. The functional properties of films were investigated as function of thickness, water vapour permeability, tensile properties and plasticizer content. Chitosan has been already successfully studied as packaging material. The application of shellac and chitosan films as packaging materials has good potential, still some more research should be done in this direction.

Thickness, moisture and water vapour permeability

The thickness of the films influences water vapour properties. For food packaging materials it is of great importance to achieve water vapour permeability (WVP) as low as possible, where high WVP determines poor moisture and water barrier properties. In our research, the thickness (mean values) of the analysed samples were used in the calculations for WVP.

Table 1. Determination of thickness, moisture content and water vapour permeability (WVP) of shellac and chitosan films with different amounts of plasticizers-glycerol (G) and poly (ethylene glycol) (PEG).

Sample	Plasticizer/ percentage (%)	Thickness (μm)	Moisture content (%)	WVP (g /m^2·day)
Shellac	PEG 200/2	233 ± 3.0a	4.51 ± 0.23a	2.17 ± 0.74b
	PEG 200/5	230 ± 2.9a	3.18 ± 0.28a	1.85 ± 0.08b
	PEG 200/15	232 ± 1.5a	2.55 ± 0.44a	0.82 ± 0.25b
Chitosan	G/2	230 ± 2.5a	10.1 ± 0.71a	7.39 ± 0.09b
	G/5	232 ± 2.0a	9.64 ± 0.15a	6.52 ± 0.63b
	G/15	230 ± 3.1a	8.78 ± 0.49a	5.14 ± 0.17b

[a] Means of five replicas ± standard deviation; [b] Means of three replicas ± standard deviation

The thickness of films influences water vapour properties [23, 24]. The water vapour permeability of films for food packaging should be as low as possible, where high WVP determines poor barrier properties. The nature of the films from biopolymers is mostly hydrophilic; therefore, the thickness influences water barrier and mechanical properties. In our research, the thickness (mean values) of films was used in the calculations for water vapour properties (TS). Table 1 shows a comparison of shellac and chitosan films with different plasticizers and their contents in the films.

From the literature it is known that glycerol is hydrophilic and improves moisture/barrier properties [5]. In our research, glycerol as a plasticiser was added in chitosan films, whereas the shellac is not miscible with glycerol and thus cannot be used as plasticizer of the lacs. Therefore PEG was used as a model plasticizer because of its compatibility with shellac.

From the obtained results it can be seen that the best water vapour properties characterise the shellac film with 15% of PEG (0.82 ± 0.25 g mm/m^2/day kPa, i.e. they are five times lower in comparison with chitosan films with the same amount of plasticizer). The same trend is detected at lower amounts of plasticizer for all samples. The results showed better moisture barrier properties of shellac films and demonstrated that the application as a packaging material in the food area can be effective and at the same time avoiding the use of oil-derived products.

Previous research has explained that chitosan films have good oxygen but poor water vapour barriers, which is due to their hydrophilic character, which was also proved in our research [20–23].

Tensile properties

Good tensile properties such as elongation at break and tensile strength are important parameters for packaging films, due to the handling and shipping of products. Analysed films were flexible, with appropriate manageability.

Tensile strength and elongation at break were determined to estimate the effect of plasticizers on shellac and chitosan films. The results are displayed in figure 1. Compared to the tensile strength of shellac films, which varies from 24.87 to 32.88 MPa, the tensile strength of chitosan films is lower (up to 18.44). The results also show that application of different amounts of glycerol or PEG significantly improved tensile properties of all samples. However, in these cases, the results did not allow displaying the effects of PEG in chitosan films and glycerol in shellac films, which was explained earlier. Consequently, the elongation at break increased for all samples with increased amount of plasticizer. For shellac films it increased by approximately 20% and for chitosan films with 15% of glycerol, elongation increased by 13 %.

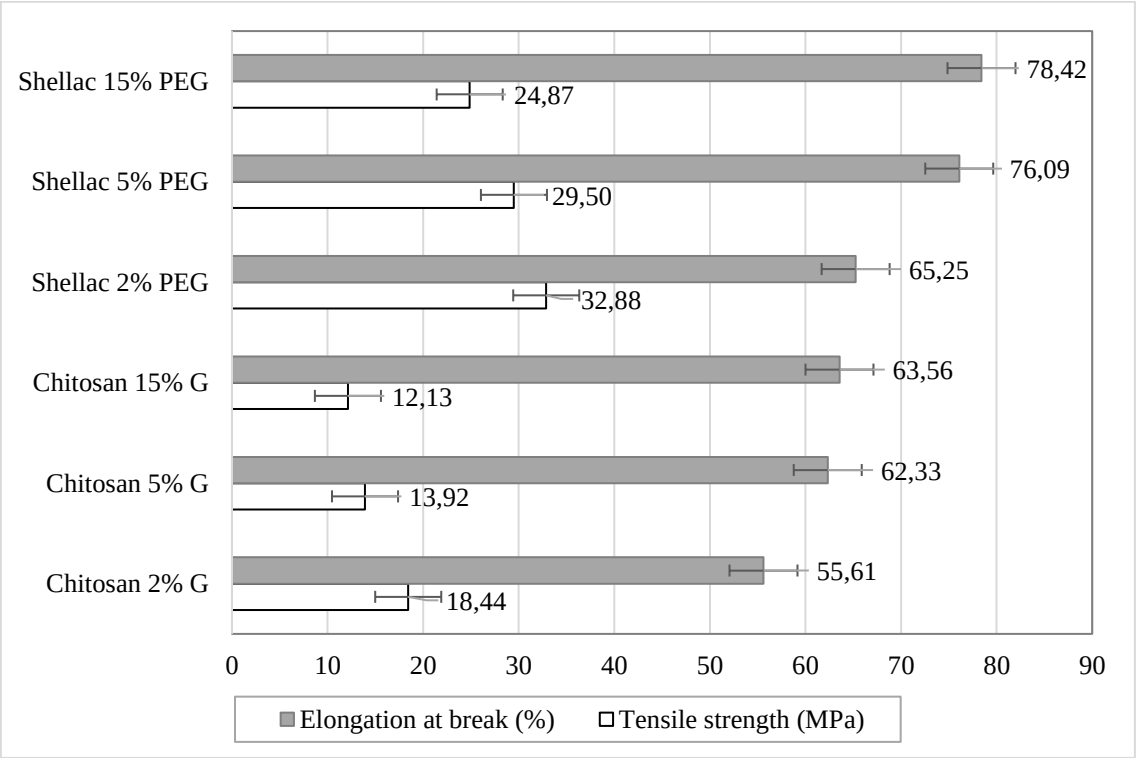

Fig. 1. Tensile strength and elongation at break for shellac and chitosan with different amounts of plasticizers.

Table 2. Colour values (L*a*b*) and colour differences (ΔE), chroma (C) and hue angle (H) of shellac and chitosan films.

	Sample	L*	a*	b*	ΔE	C	H
Shellac	PEG 200/2	84.40	1.12	37.79	/	/	/
	PEG 200/5	78.91	2.83	50.45	12.11	10.80	9.09
	PEG 200/15	77.56	3.09	48.72	11.41	9.14	14.29
Chitosan	G/2	84.06	1.19	32.36	/	/	/
	G/5	83.32	0.93	30.58	1.9	1.80	8.33
	G/15	82.52	1.40	33.02	1.7	0.65	20.01

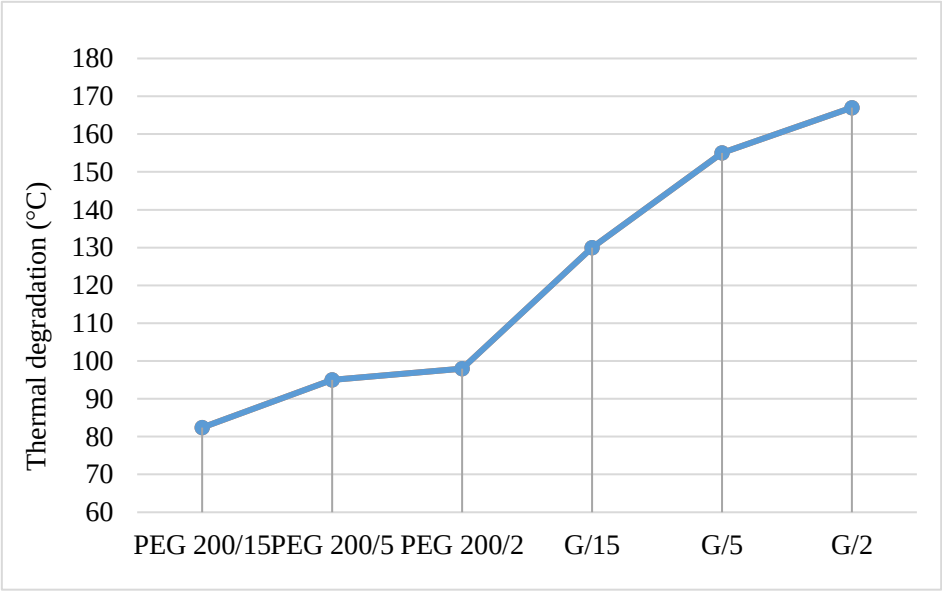

Fig. 2. Thermal stability of shellac and chitosan films with different amounts of plasticizers.

It may be assumed that in the case of the higher amount (15% w/w) of plasticizer it contributes to increased tensile properties which are of great importance for packaging materials. Results show that addition of PEG into shellac increases significantly the stretchability of films. The same results confirm the behaviour of glycerol in chitosan films.

Colour

The colour of films can be a factor in terms of consumer demands and it does not affect other analysed properties. The results are shown in Table 2.

Generally, colour is an important factor of the appearance of packaging materials [3, 8]. The total colour difference, chroma and hue angle were calculated from the colour values, and compared to the samples with the smallest amount of plasticizer. The aim was to compare the appearance of the films with added plasticizer and its effect. As expected, shellac is more yellow compared to chitosan, since the prime component, shellac flakes, are yellow. With added plasticizer to both samples, lightness increased, as seen from table 2. Colour differences between shellac films are bigger, due to uneven flakes colour. Chitosan was applied as powder with more even colour appearance. The a* and b* values significantly vary between all samples. From the colour analysis it was confirmed that shellac films were much more yellow than chitosan films.

Thermal stability

Thermal stability of analysed samples is shown in Figure 2. It can be seen that each film has similar thermal properties. For shellac films with the highest amount of PEG a change in appearance of the films was shown at 82°C. For a sample with 2% of PEG added, the thermal stability was higher. For chitosan films the results were similar. This indicated that the presence of glycerol in the chitosan structure caused the chitosan polymer to break more easily. From the literature it was proven that glycerol reduces intermolecular hydrogen bonding of chitosan backbone, thus weakening the bond between the polymer chains [25]. Compared to shellac films, chitosan is more stable and achieved higher thermal stability, up to 167°C.

CONCLUSIONS

A study on the potential of using shellac and chitosan as packaging films was carried out. The most significant results obtained were: reduction of water vapour permeability and improvement in tensile strength, when the amount of plasticizer increased for both film types. Moreover, the tensile properties of all tested films were good and sufficient for the use in the packaging field. Although the colour of shellac films is quite yellowish, it could be more appropriate from the consumer side as a barrier film. As expected, thermal stability decreased with increased amount of plasticizers in both types of films.

The study demonstrates that the utilization of shellac films with 15% of PEG could be an alternative in the search for a sustainable packaging. Still some more research should be done, regarding barrier properties such as grease, oxygen permeability, migration etc. Compared to chitosan films, shellac is already a food additive and therefore is not harmful for human health and from our research, exhibited better properties.

Acknowledgement: *This research was supported by the COST action CA15216 (ENBA). The author would like to thank Mr. Manfred Penning and Mr. Stephen Hall from the A. F. Suter & Co Ltd. Company, Essex, United Kingdom, for the Shellac supplement. We would also like to thank University of Ljubljana, Faculty of Natural Sciences and Engineering, Department of Textiles Graphic Arts and Design, Ljubljana, Slovenia for financial support.*

REFERENCES

1. G. G. Buonocore, M. A. Del Nobile, A. Panizza, M. R. Corbo, L. Nicolais, *J. Controlled Release*, **90**, 97 (2003).
2. P. Appendini, J. H. Hotchkiss, *Innovative Food Science & Emerging Technologies*, **3**, 113, (2002).
3. U. Vrabič Brodnjak, *Prog. Org. Coat.*, **103**, 93 (2017).
4. W. Zhang, H. Xiao, L. Qian, *Carbohyd. Polym.*, **101**, 401 (2014).
5. P. C. Srinivasa, M. N. Ramesh, K. R. Kumar, R. N Tharanathan, *J. Food Eng.*, **63**, 79 (2004).
6. C. Wu, S. Peng, C. Wen, X. Wang, L. Fan, R. Deng, J. Pang, *Carbohyd. Polym.*, **89**, 497 (2012).
7. D. A Todorova, S. P. Bencheva, *Bulg. Chem. Comm.*, **47**, 45 (2015).
8. U. Vrabič Brodnjak, *Prog. Org. Coat.*, **112**, 86 (2017).
9. S. Soradech, J. Nunthanid, S. Limmatvapirat, M. Luangtana-anan, *Food Control*, **73**, 1310 (2017).
10. Y. Farag, C. S. Leopold, *Dissolut. Technol.*, **16**, 33 (2009).
11. S. Soradech, J. Nunthanid, S. Limmatvapirat, M. Luangtana-anan, *Food Control.*, **108**, 94 (2012).
12. F. Debeaufort, D. Luu, A. Voilley, *J. Membrane Sci.*, **325**, 277 (2008).
13. S. C. Shit, P. M. Shah, *J. Polym.*, **2014**, 13 (2014).
14. M. Penning, *Seifen Öle Fette Wachse,* **6**, 221 (1990).

15. Luangtana-anan, J. Nunthanid, S. Limmatvapirat, *J. Agr. Food. Chem.*, **58**, 12934 (2010).
16. N. Bordenave, S. Grelier, V. Coma, *Biomacromolecules* **11**, 88, (2010).
17. X. Y. Xu, K. M. Kim, M. A. Hanna, D. Nag, *Ind. Crop. Prod*., **21**, 185, (2005).
18. U. Vrabič Brodnjak, A. Jesih, D. Gregor-Svetec, *Coatings*, **8**, 133 (2018).
19. M. S. Rao, S. R. Kanatt, S. P. Chawla, A. Sharma, *Carbohyd. Polym.*, **82**, 1243, (2010).
20. F. Ham-Pichavant, G. Sèbe, P. Pardon, V. Coma, Carbohydr. Polym., **61**, 259, (2005).
21. S. Wang, Y. Jing, *BioResources*, **11**, 1868, (2016).
22. M. Jaworska, K. Sakurai, P. Gaudon, E. Guibal, *Polym. Int.*, **2**, 198 (2003).
23. S. Rivero, M. A. García, A. Pinotti, Composite and bi-layer films based on gelatin and chitosan, *Journal of Food Engineering*, **90**, 531 (2009).
24. K. Cooksey, K. Marsh, L. Doar, Predicting permeability & transition rate for multilayer materials, *Food Technology*, **53**, 60 (1999).
25. E. Susilowati, I. Kartini, S. J. Santosa, S. J., in: IOP Conference Series: Materials Science and Engineering, IOP Publishing, 2016, vol. 107, No. 1, p. 12041.

Acknowledgement to Reviewers for vol. 50 (2018)

The Editors of Bulgarian Chemical Communications would like to take this opportunity to thank you for the effort and expertise that you contribute to reviewing, without which it would be impossible to maintain the high standards of our journal:

A
A. Ahmedova
A. Blanco
A. Hasani
A. Ivanova
A. Mushtaq
A. Reiss
A. S. Hamdy Makhlouf
A. Tachev
A. Tadjer
A. Trendafilova
A.M.A. Hamdy Gomaa

B
B. Banov
B. Shivachev
B. Stamboliyska

D
D. Djonova
D. Paliulis
D. Tasheva

E
E. Kirilova
E. Stanoeva

F
F. Erkec
F. Rabiee
F. Ribarova
F. Sapundji

G
G. Antova
G. Cholakov

H
H. Kaneti

I
I. Grabchev
I. Havezov
I. Ivanov
I. Mihailova
I. Taneva
I. Tsibranska
Iv. Radev
Iv. Uzunov
Iv.Vulchev

K
K. Amoa
K. Balasubramani
K. Kostova
K.K. Petrov
K.M. Petrov

L
L. Ljutzkanov
L. Mitu
L. M. Ming
L. Tancheva

M
M. Angelova-Romova
M. Jaskula
M. Kamenova
M. Nedyalkova
M. Popova
M. Rengasamy
M. Reza Manafi
M. Reza Rasaei
M. S. Loron

N
N. Bancheva
N. Rizov
N. Kosseva
N. Vasilev

O
Og. Ivanov

P
P. Denev
P. Sathiskumar
P. Simeonova

R
R. Amarowicz
Ren Cuirong
R. Kalfin
R. Karvembu
R. Stateva

S
S. Damianova
S. Anguelova
S. Bakalova
S. Boyadzhiev
S. Gomari
S. Hashmi
S. Kitova
S. Momchilova
S. Nenkova
S. P. Aubourg
S. Rangelov
S. Simeonov
S. Vlaev
St. Boyadjiev

T
T. Peev
T. Petrova
T. Traykov
T. Tsoncheva

V
V. Blaskov
V. Boev
V. Georgiev
V. Kancheva
V. Kurteva
V. Sinigerski
Vl. Blaskov

Y
Y. Nikolova
Y. Yalgin Gurkan

Z
Z. Hussain Awan
Z. Peshev
Zl. Alexieva

Instructions about Preparation of Manuscripts

General remarks: Manuscripts are submitted in English by e-mail. The text must be prepared in A4 format sheets using Times New Roman font size 11, normal character spacing. The manuscript should not exceed 15 pages (about 3500 words), including photographs, tables, drawings, formulae, etc. Authors are requested to use margins of 2 cm on all sides.

Manuscripts should be subdivided into labelled sections, e.g. INTRODUCTION, EXPERIMENTAL, RESULTS AND DISCUSSION, *etc*. **The title page** comprises headline, author(s)' names and affiliations, abstract and key words. Attention is drawn to the following:

a) **The title** of the manuscript should reflect concisely the purpose and findings of the work. Abbreviations, symbols, chemical formulae, references and footnotes should be avoided. If indispensable, abbreviations and formulae should be given in parentheses immediately after the respective full form.

b) **The author(s)**' first and middle name initials and family name in full should be given, followed by the address (or addresses) of the contributing laboratory (laboratories). **The affiliation** of the author(s) should be listed in detail (no abbreviations!). The author to whom correspondence and/or inquiries should be sent should be indicated by an asterisk (*) with e-mail address.

The abstract should be self-explanatory and intelligible without any references to the text and containing up to 250 words. It should be followed by keywords (up to six).

References should be numbered sequentially in the order, in which they are cited in the text. The numbers in the text should be enclosed in brackets [2], [5, 6], [9–12], etc., set on the text line. References are to be listed in numerical order on a separate sheet. All references are to be given in Latin letters. The names of the authors are given without inversion. Titles of journals must be abbreviated according to Chemical Abstracts and given in italics, the volume is typed in bold, the initial page is given and the year in parentheses. Attention is drawn to the following conventions: a) The names of all authors of a certain publications should be given. The use of "*et al*." in the list of references is not acceptable; b) Only the initials of the first and middle names should be given. In the manuscripts, the reference to author(s) of cited works should be made without giving initials, e.g. "Bush and Smith [7] pioneered...". If the reference carries the names of three or more authors it should be quoted as "Bush *et al*. [7]", if Bush is the first author, or as "Bush and co-workers [7]", if Bush is the senior author.

Footnotes should be reduced to a minimum. Each footnote should be typed double-spaced at the bottom of the page, on which its subject is first mentioned. **Tables** are numbered with Arabic numerals on the left-hand top. Each table should be referred to in the text. Column headings should be as short as possible but they must define units unambiguously. The units are to be separated from the preceding symbols by a comma or brackets. Note: The following format should be used when figures, equations, *etc*. are referred to the text (followed by the respective numbers): Fig., Eqns., Table, Scheme.

Schemes and figures. Each manuscript should contain or be accompanied by the respective illustrative material, as well as by the respective figure captions in a separate file. As far as presentation of units is concerned, SI units are to be used. However, some non-SI units are also acceptable, such as °C, ml, l, etc. Avoid using more than 6 (12 for review articles) figures in the manuscript. Since most of the illustrative materials are to be presented as 8-cm wide pictures, attention should be paid that all axis titles, numerals, legend(s) and texts are legible.

The authors are required to submit the text with a list of three individuals and their e-mail addresses that can be considered by the Editors as potential reviewers. Please note that the reviewers should be outside the authors' own institution or organization. The Editorial Board of the journal is not obliged to accept these proposals.

The authors are asked to submit **the final text** (after the manuscript has been accepted for publication) in electronic form by e-mail. The main text, list of references, tables and figure captions should be saved in separate files (as *.rtf or *.doc) with clearly identifiable file names. It is essential that the name and version of the word-processing program and the format of the text files is clearly indicated. It is recommended that the pictures are presented in *.tif, *.jpg, *.cdr or *.bmp format.

The equations are written using "Equation Editor" and chemical reaction schemes are written using ISIS Draw or ChemDraw programme.

EXAMPLES FOR PRESENTATION OF REFERENCES

REFERENCES

1. D. S. Newsome, *Catal. Rev.–Sci. Eng*., **21**, 275 (1980).
2. C.-H. Lin, C.-Y. Hsu, *J. Chem. Soc. Chem. Commun*., 1479 (1992).
3. R. G. Parr, W. Yang, Density Functional Theory of Atoms and Molecules, Oxford Univ. Press, New York, 1989.
4. V. Ponec, G. C. Bond, Catalysis by Metals and Alloys (Stud. Surf. Sci. Catal., vol. 95), Elsevier, Amsterdam, 1995.
5. G. Kadinov, S. Todorova, A. Palazov, in: New Frontiers in Catalysis (Proc. 10th Int. Congr. Catal., Budapest (1992), L. Guczi, F. Solymosi, P. Tetenyi (eds.), Akademiai Kiado, Budapest, 1993, Part C, p. 2817.
6. G. L. C. Maire, F. Garin, in: Catalysis. Science and Technology, J. R. Anderson, M. Boudart (eds.), vol. 6, Springer Verlag, Berlin, 1984, p. 161.
7. D. Pocknell, *GB Patent* 2 207 355 (1949).
8. G. Angelov, PhD Thesis, UCTM, Sofia, 2001, pp. 121-126.
9. JCPDS International Center for Diffraction Data, Power Diffraction File, Swarthmore, PA, 1991.
10. CA **127**, 184 762q (1998).
11. P. Hou, H. Wise, *J. Catal.*, in press.
12. M. Sinev, private communication.
13. http://www.chemweb.com/alchem/articles/1051611477211.html.

Texts with references which do not match these requirements will not be considered for publication!!!

CONTENTS